

Long-term observation of rock fracture permeability and structure under various pressure and temperature conditions

2020

Chenlu Song

Declaration

Chenlu Song

The thesis entitled “Long-term observation of rock fracture permeability and structure under various pressure and temperature conditions” is conducted under the supervision of Prof. Kiyoshi Kishida, an instructor of Urban Management Systems, Urban Management at Kyoto University. I hereby declare that except where specific reference is made to the work of others, the contents of this dissertation are original and have not been submitted in whole or in part for consideration for any other degree or qualification in this, or any other University. This dissertation is the result of my own work and includes nothing which is the outcome of work done in collaboration, except where specifically indicated in the text. This dissertation contains less than 41150 words including tables and equations and has less than 110 figures.

Acknowledgements

In the beginning, I would like to express my fortunately to have a good chance that I could study at Kyoto University, Department of Urban Management, Urban Management Systems laboratory for three and a half years. It is a wonderful life experience in my life.

When I wandered over from China looking for a new home and a new direction, Prof. Kiyoshi Kishida gave me a precious opportunity and took me into his group. First and foremost, sincere thanks must go to him for the support and encouragement over the last three and a half years. Without his input, advice, patience and all the effort on the research, I would not have a rare opportunity in the field of rock mechanics academic aesthetics. I am grateful for him a lot of support and help in the research and daily life.

I would like to express my gratitude for Prof. Shinichiro Nakashima, Prof. Hideaki Yasuhara. I am thankful for them a lot of help on my research, and they taught me a lot of knowledge step by step. No matter how busy they are, thanks for them spending a lot of time to modify my paper and always encouraging me never give up. I can learn not only a lot of knowledge but also the spirit of research. Without them, I cannot go further in my study.

I would next like to thanks the sub-supervisor Prof. Mamoru Mimura, Associate Prof. Yosuke Higo. They gave me a lot of ideas on the modification of the thesis. From their questions I can learn more than the current stage. Many thanks for they always care about my research processing.

I would also like to thank Associate Prof. Yasuo Sawamura, Assistant Prof. Yusuke Miyazaki, who helped and encouraged me on the research and daily life. Their infectious enthusiasm for research and their consistent availability to discuss topics in the field of civil engineering are so encouraging that I wish I could become a young researcher like them.

Special thanks shall be sent to Assistant Prof. Ryunosuke Kido for his guidance and continuing support in the last three years. I am grateful for him that he spent his time on many of the discussions.

Special thanks to the technician Takao Yano. Thanks for his kindly help on doing the experiment, a lot of patience in teaching me a lot of knowledge. I am grateful for him a lot of support.

Thanks to lab. secretary Yuko Matsuoka, a lot of help in daily life. Special thanks to all the Urban Management laboratory students. Dr. Sho Ogata (same period), Tanawat Tangjarusritaratorn (Ph.D. student, D2), Kyohei Ambai (Master student, M2), Kaixuan Yuan (Master student, M1), etc. For their help and have a happy memory.

My friends at Kyoto University have been invaluable in the last three years. Sijia Xu (same period, Ph.D. student in Cardiovasclur Medicine, Kyoto university Hospital), my best friend before came to Japan. Nana Kamiya (same period, Ph.D. student in Urban Management), always taught me Japanese culture and enjoyed the amateur cultural life together. Xuzhao Lu (same period, Ph.D. student in Civil Engineering), Jin Wu (same period, Ph.D. student in Urban Management), who always help me in daily life. They contributed a lot to keep me sane during my time in Kyoto. Particular thanks to these friends, who always

help me a lot in life and tolerated me for all the insane moments, though they are social elites with a busy schedule.

To the few, I mention here. Finally, my parents, who are the most important people in my life, dear dad (I miss you forever) and dear mom, played no small role in my getting to this point. It took quite a lot of courage for them to support me here. I will be healthy and happy in my future life as your expectation.

Chenlu Song

June 13, 2019

Abstract

This study examined the evolution of the long-term hydraulic properties of granite specimens with a single fracture under various conditions. The effect of the fracture surface roughness deformation may have been due to the chemical and mechanical compaction, the pressure solution, etc. Moreover, X-ray tomography was utilized to grasp the long-term fracture aperture distribution at arbitrary times. Then a flow simulation was conducted and the results were compared with the CT measured data i.e., the aperture distribution and the fracture contact-area ratio at different times. The hydraulic aperture was compared among different measuring methods. In addition, chemical-mechanical interaction was not only suspected during the experimental work, but was also verified in a simulative study.

Short- and long-term permeability tests were performed under the moderate temperatures of 20, 60, and 90°C and confining stresses ranging from 1.0 – 3.0 MPa. The test results showed that the fracture surface roughness and the contact area were altered under different conditions. Irreversible behavior of the permeability was observed in the test results. Moreover, the element concentrations evaluated from the effluent indicated that a geometrical change in the rough-walled fracture might have occurred in the long-term tests. Mineral concentration increase was confirmed at 90 °C, and it can further explain the permeability decrease and the geochemical response happening in a long-term.

From the permeability test results, it was found that the variation in the fracture surface roughness and the fracture aperture significantly affected the fluid flow behavior. Therefore, in this study, by assembling a triaxial cell with heating capability, microfocus X-ray CT was utilized to intermittently observe the fracture structure under a constant temperature (20°C) and a constant confining pressure (3.0 MPa) (i.e., the same conditions as in the long-term permeability tests). The fracture aperture distribution and the contact-area were then extracted through the X-ray CT scanning results. The change in the contact-area ratio within the granite fracture was also evaluated. A comparison of the hydraulic aperture between the X-ray CT and the permeability tests showed that their decreasing tendencies were quite similar. However, the reduction rates were quantitatively different. Throughout the 180-day test duration, the hydraulic aperture obtained from the X-ray CT decreased by 12%, from 1.37×10^{-4} m to 1.2×10^{-4} m, while that derived from the permeability tests decreased by 53%, from 2.07×10^{-6} m to 9.84×10^{-7} m.

Moreover, the long-term aperture distribution and lower roughness from the CT observation were extracted to conduct a flow simulation. The discharge variation indicated that the flow was controlled by different confining pressures. An aperture color contour map is given with flow vectors clearly representing the contact positions and the variation in flow directions under different conditions. The hydraulic aperture from the flow simulation was also measured and then used to make a comparison with the hydraulic aperture which was obtained from the permeability tests and from the X- ray CT mechanical aperture over the long-term period of 180 days.

Based on the experimental results and the hydraulic aperture variation over the long term under different measuring methods, these different reduction rates indicated that the chemo-mechanical processes might have significantly acted on the rough-walled fracture under the long-term hydro-thermal conditions. Therefore, the geometrical alteration within the fracture, affecting the flow behavior under the coupled processes, was examined by a chemical-mechanical model in this study. The relation between aperture and contact-area ratio change was verified, and was checked by this coupled model. From

experiment and simulation results, it is noted that the fracture geometrical change and the contact-area variation over the long-term were affected by the coupled processes interaction.

Keywords: Permeability, long term, X-ray CT observation, contact-area ratio and aperture distribution, hydraulic properties, chemical-mechanical interaction

Table of Contents

DECLARATION	- 2 -
ACKNOWLEDGEMENTS	- 3 -
ABSTRACT.....	- 5 -
LIST OF TABLES AND FIGURES	- 10 -
CHAPTER1 INTRODUCTION.....	- 15 -
1.1 Background.....	- 15 -
1.2 Objectives	- 17 -
1.3 Structure of the thesis	- 17 -
References.....	- 21 -
CHAPTER2 LITERATURE REVIEW	- 23 -
2.1 Hydro-mechanical characteristics of fractured rocks	- 23 -
2.2 THMC coupling processes of fractured rocks	- 26 -
2.3 Utilization of X-ray CT.....	- 30 -
2.3.1 Utilization of X-ray CT in varied areas	- 30 -
2.3.2 Utilization of X-ray CT in fractured rocks	- 31 -
2.4 Flow simulation of single rock fracture.....	- 32 -
References.....	- 34 -
CHAPTER3 LONG-TERM OBSERVATION OF HYDRAULIC APERTURE AND PERMEABILITY CHANGE UNDER VARIOUS CONDITIONS	- 39 -
3.1 Introduction.....	- 39 -
3.2 Materials and experimental setup	- 41 -
3.3 Methodology.....	- 44 -
3.4 Testing process	- 47 -
3.4.1 Short-term permeability test conditions.....	- 48 -
3.4.2 Long-term permeability test conditions.....	- 48 -
3.5 Permeability experiment results.....	- 49 -
3.5.1 Short-term permeability test results.....	- 49 -
3.5.2 Long-term permeability test results	- 52 -
3.6 Discussions	- 55 -
3.6.1 Discussion of the permeability tests at room temperature	- 55 -
3.6.2 Discussion of the permeability tests at elevated temperatures	- 56 -
3.6.3 Comparison between pre- and post -experiments.....	- 59 -
3.7 Summary.....	- 62 -
References.....	- 65 -
CHAPTER4 LONG-TERM OBSERVATION OF APERTURE DISTRIBUTION AND CONTACT-AREA RATIO CHANGE UNDER VARIOUS CONDITIONS THROUGH MICROFOCUS X-RAY CT	- 68 -
4.1 Introduction.....	- 68 -
4.2 Theoretical of X-ray CT	- 70 -
4.2.1 X-ray micro tomography facility	- 70 -
4.2.2 Composition of X-ray micro tomography facility	- 71 -

4.2.2.1	X-ray source.....	- 71 -
4.2.2.2	Detector.....	- 71 -
4.2.2.3	CT reconstruction	- 71 -
4.2.2.4	CT value and images.....	- 72 -
4.2.2.5	Flat panel detector (FPD).....	- 72 -
4.3	Experimental condition.....	- 73 -
4.3.1	Experimental setup	- 73 -
4.3.2	Testing conditions.....	- 75 -
4.3.3	CT image analytical method	- 76 -
4.4	Results of the X-ray CT observation	- 80 -
4.4.1	Long-term X-ray CT observation at room temperature.....	- 80 -
4.4.2	Long-term X-ray CT observation at elevated temperature.....	- 82 -
4.5	Fracture contact conditions.....	- 83 -
4.5.1	Long-term contact-area ratio change at room temperature.....	- 83 -
4.5.2	Long-term contact-area ratio change at elevated temperature.....	- 84 -
4.6	Discussions	- 85 -
4.6.1	Discussion of long-term hydraulic aperture change between CT observation and permeability tests	- 85 -
4.6.2	Discussion of the effect factors on aperture change	- 86 -
4.6.2.1	Chemical-mechanical influence.....	- 86 -
4.6.2.2	CT resolution influence	- 86 -
4.6.2.2.1	Testing condition of the CT resolution.....	- 87 -
4.6.2.2.2	Results and comparison of the CT resolution.....	- 89 -
4.6.2.2.2.1	Comparison between normal resolution and low resolution	- 89 -
4.6.2.2.2.2	Comparison between normal resolution and high resolution	- 91 -
4.6.2.2.3	Brief summary	- 92 -
4.7	Summary.....	- 93 -
	References.....	- 94 -

CHAPTER5 EFFECT OF DIFFERENT IMAGE PROCESSING METHODS ON ESTIMATING A SINGLE GRANITE FRACTURE UNDER DIFFERENT CONDITIONS..... - 97 -

5.1	Introduction.....	- 97 -
5.2	Experiment setup	- 99 -
5.3	Image processing method	- 100 -
5.3.1	Region growing method (RG)	- 100 -
5.3.2	Edge detection method (ED).....	- 102 -
5.3.3	A comparison analysis of RG and ED	- 104 -
5.4	Analysis results.....	- 106 -
5.4.1	Image processing of CT images without confining stress	- 106 -
5.4.2	Image processing of CT images with confining stress	- 108 -
5.5	Summary.....	- 111 -
	References.....	- 112 -

CHAPTER6 LONG-TERM OBSERVATION OF FLOW BEHAVIOR AND HYDRAULIC PROPERTIES OF A SINGLE ROCK FRACTURE UNDER VARIOUS CONDITIONS..... - 116 -

6.1	Introduction.....	- 116 -
6.2	Methodology.....	- 117 -
6.2.1	Theoretical of the 2-D model	- 118 -
6.2.2	Procedure of the numerical simulation	- 119 -
6.3	Results of the flow simulation	- 120 -

6.3.1	Discharge and aperture change under various conditions	- 120 -
6.3.2	Reynolds number variation under various conditions	- 123 -
6.4	Hydraulic aperture Comparison under different methods	- 124 -
6.5	Summary	- 127 -
	References.....	- 128 -

CHAPTER7 CHEMICAL-MECHANICAL SIMULATION OF A SINGLE ROCK FRACTURE UNDER VARIOUS CONDITIONS..... - 130 -

7.1	Introduction.....	- 130 -
7.2	Matching the laboratory data	- 130 -
7.3	Conceptual model	- 132 -
7.3.1	Pressure solution • free-face dissolution	- 132 -
7.3.2	Relationship between the fracture aperture and the contact area.....	- 136 -
7.3.2.1	Fracture contact condition	- 137 -
7.3.2.2	Procedure of the simulation	- 137 -
7.3.2.3	Parameter <i>a</i>	- 140 -
7.4	Simulation results	- 140 -
7.5	Summary	- 142 -
	References.....	- 143 -

CHAPTER8 CONCLUSIONS AND FUTURE STUDIES..... - 145 -

8.1	Conclusions.....	- 145 -
8.2	Recommendations for future works.....	- 148 -
8.2.1	Long-term permeability tests	- 148 -
8.2.2	CT observation on the fracture information	- 148 -
8.2.3	Image processing methods.....	- 149 -
8.2.4	Model construction and further investigation.....	- 149 -

List of Tables and Figures

- Table 3.1** Mechanical properties of granite specimen
- Table 3.2** Comparison of Z2 and JRC values with profilometer equipment (VR-3200)
- Table 3.3** Permeability experimental conditions
- Table 4.1** Specifications of x-ray micro tomography facility (KYOTOGEO- μ XCT)
- Table 4.2** Experimental conditions at each case (i.e., 20 and 60 °C)
- Table 4.3** Histogram values of CT images
- Table 4.4** CT scanning condition between normal resolution and low resolution
- Table 4.5** CT scanning condition between normal resolution and high resolution
- Table 4.6** Aperture and contact-area ratio results between normal resolution and low resolution
- Table 4.7** Aperture and contact-area ratio results between normal resolution and low resolution
- Table 5.1** Scan conditions under different confining pressures at 20 °C
- Table 5.2** Different conditions of CT images
- Table 5.3** Histogram values of CT images
- Table 6.1** Flow simulation results (0 MPa, 0 day, 20 °C)
- Table 6.2** Flow simulation results (3.0 MPa, 0 day, 20 °C)
- Table 6.3** Flow simulation results (3.0 MPa, 30 day, 20 °C)
- Table 6.4** Flow simulation results (3.0 MPa, 60 day, 20 °C)
- Table 6.5** Flow simulation results (3.0 MPa, 180 day, 20 °C)
- Table 6.6** Long-term hydraulic aperture evolution (water head of 2.5 cm, 3.0 MPa, 180 day, 20 °C)
- Table 7.1** Chemical reaction formula of the ionic activity product
- Table 7.2** Coefficient of the equilibrium constant
- Table 7.3** Simulation result by using the CT observation data
-
- Fig. 1.1** Schematic of deep borehole disposal for nuclear waste in US (Patrick et al., 2009)
- Fig. 1.2** Geological disposal of high-level radioactive waste in Japan (NUMO, 2004; Yamaguchi, 2010)
- Fig. 1.3** Schematic diagram of the objectives of this thesis (illustration of the effect factors which will be introduced in this study)
- Fig. 1.4** Structure of this thesis and the linkage between each chapter
- Fig. 2.1** Permeability tests under different conditions: (a) temperature of 130°C and confining pressure of 15.7 MPa and (b) temperature of 130°C and confining pressure of 57.8 MPa (Kamali-Asl et. al., 2018)
- Fig. 2.2** Permeability evolution with effective confining stress: (a) changes in permeability with confining pressure on aligned fractured and displaced fractured samples (Hofmann et al., 2016) and (b) gas injection tests in which permeability shows reversible behavior in loading–unloading performance (Davy et al., 2007)
- Fig. 2.3** Permeability performance under different conditions in which elastic-plastic transition occurred under different temperatures (Numakura et al., 2015)
- Fig. 2.4** Schematic process of chemical reaction generated within fractured rock (Yasuhara et al., 2004)

- Fig. 2.5** Variation in permeability through use of intact and fractured sandstone: (a) changes in permeability of intact sandstone, (b) changes in permeability of fractured sandstone, and (c) mineral dissolution of Si under different conditions (Yasuhara et al., 2015)
- Fig. 2.6** Relationship between hydraulic aperture and contact-area ratio under numerical prediction: (a) impact of surface topography of fracture channel on permeability evolution: predicted for initial contact-area ratio R_{c0} (Lu et al., 2018), (b) model fitting to measured aperture-contact area relation (Wang, 2017), (c) relationship between mean aperture and contact-area ratio, and (d) variation in contact area when pressure solution occurs (Lang et al., 2015)
- Fig. 2.7** 3-D segmented micro-structures of coal samples (Zhang et al., 2018)
- Fig. 2.8** Scanned CT images of core samples at longitudinal location 665, 85 mm downstream of the inlet: (a) at test initiation (0 hours) and (b) after 1492 hours (Polak et al., 2004)
- Fig. 2.9** Schematic procedure of extraction of micropores using microfocus X-ray CT. A 3-mm cube is imaged in the middle of the rock sample and pore structures are extracted (Yasuhara et al., 2015).
- Fig. 2.10** Flow through high aperture channels between contacts (Stephen, 1987)
- Fig.3.1** Short- and long-term permeability performance under various conditions. (a), (c) short-term permeability tests. (b),(d) long-term permeability tests. (Yasuhara, et al 2010) (Ishikawa,2015)
- Fig.3.2** Long-term permeability performance under different conditions. (a) long-term permeability test about 3200 hours; (Yasuhara, et al.2006), (b) long-term permeability test about 800 days (Yasuhara, et al. 2015)
- Fig.3.3** Sample experiments and fracture surfaces measured by laser profilometer
- Fig.3.4** Sample #1 was set into the triaxial cell
- Fig.3.5** Triaxial apparatus. The upstream and downstream pore water pressures are prescribed to the top and bottom of Sample #1, respectively.
- Fig.3.6** Schematic information of the transient pulse method (Sample #1 physical information)
- Fig.3.7** Conception of the pressure decrement curve (transient pulse method)
- Fig.3.8** Schematic of the process of the short-term permeability tests
- Fig.3.9** Schematic of the process of the long-term permeability tests
- Fig.3.10** Temporal change of the upstream and downstream water pressures during the permeability test
- Fig.3.11** A linear relationship between the logarithm of water pressure difference and time (i.e., $\ln(P_u - P_f)$ and t)
- Fig.3.12** Short-term permeability test results (a) permeability variation at 20 °C, (b) permeability variation at 60 °C, (c) permeability variation at 90 °C and (d) permeability variation in 3rd cycle under different temperature conditions
- Fig.3.13** Permeability variation with time (Sample #1), 20 °C,180 days
- Fig.3.14** Comparison of changes in permeability between (a) current work, and (b) Yasuhara et al. (2013)
- Fig.3.15** Comparison of the permeability variation at the loading confining pressure process between 20 and 60 °C
- Fig.3.16** Permeability variation with time (Sample #1), 60 °C,180 days
- Fig.3.17** Permeability variation with time (Sample #1), 90 °C,120 days
- Fig.3.18** Brief summary of the permeability changes of short-term and long-term tests at 20 °C
- Fig.3.19** The whole summary of the permeability changes under three temperatures (20,60 and 90 °C)
- Fig.3.20** Initial aperture position without confining pressure at pre-experiments. (CT slice 238, at z-direction of 14.04 mm)
- Fig.3.21** CT image comparison of the aperture variation extracted at different length of the sample. (a) pre-experiment, (b) post- experiment

- Fig.3.22** Evolution of the mineral composition at long-term permeability test of 20 °C
- Fig.3.23** Evolution of the mineral composition at long-term permeability test of 60 °C
- Fig.3.24** Evolution of the mineral composition at long-term permeability test of 90 °C
- Fig.4.1** CT scanning images comparison.(a) comparison of the initial dry core, the wet core at 20 °C, 80 °C, and 120 °C. The boxed region illustrates the dissolved masses and the relative displacement of fracture faces,(b) aperture change under different conditions (Polak et al., 2003)
- Fig.4.2** Granite geometric aperture evolution observation through the flow experiments. Stage A-1 = flow-through the granite sample at room temperature, stage A-2 =no flow experiment at 350°C, and stage A-3 = flow-through experiment at 350°C. Stage B-1 = flow-through experiment at room temperature, stage B-2 = flow-through experiment at 350°C (Okamoto, et al., 2017)
- Fig.4.3** Schematic diagram of X-ray micro tomography facility (Kido, 2019)
- Fig.4.4** CT values distribution. (a) horizontal cross-section of a granite CT image, (b) normal distribution of a granite CT image
- Fig.4.5** Granite sample #2 with a single rock fracture (15.23 mm × 33.34 mm)
- Fig.4.6** Triaxial cell coupled with the microfocus X-ray CT
- Fig.4.7** Triaxial cell with heating capabilities was installed on the work table with the microfocus X-ray CT (X-ray CT)
- Fig.4.8** Sample#2 is scanned with several cross-section CT images
- Fig.4.9** Three types of CT voxel connectivity are represented. i.e., 6- connected, 18- connected and 26-connected (in this study, 26-connected neighbourhood was used in 3-D) (Toriwaki, et al., 2002)
- Fig.4.10** Segmentation process for rock phase and void phase by region-growing technique: (a) determination of tolerance of region growing, (b) schematic illustration of region growing in 2-D, (c) segmentation image in 2-D and (d) voxel connectivity of 26-connected neighbourhood
- Fig.4.11** CT image segmentation results. (a) threshold method, and (b) region-growing method
- Fig.4.12** Segmentation procedure for voxels that contain both rock and void: (a) conception of image after segmentation process, (b) voxel that includes rock and void phases (aperture detection method) and (c) contact-area in aperture position
- Fig.4.13** Illustration of the contact position within the fracture
- Fig.4.14** Contour maps of surface roughness and aperture distribution of Sample #2 at confining pressure of 0 MPa obtained through CT observation: (a) surface roughness and (b) aperture distribution
- Fig.4.15** Comparison result of the surface roughness of Sample #2 (Side A) at 0 MPa. i.e., obtained by the VG-3200 pattern projection and by the CT image analysis result
- Fig.4.16** Temporal changes in aperture variation evaluated from CT analysis in long-term tests at 20 °C: (a) initial value of mean aperture at 0 MPa, (b) aperture variation after 0 days at 3.0 MPa, (c) after 90 days and (d) after 180 days
- Fig.4.17** Temporal changes in aperture variation evaluated from CT scanning in long-term tests (comparison of the cross-section images at length direction of 18.7 mm, at 20 °C)
- Fig.4.18** Temporal changes in aperture variation evaluated from CT analysis in long-term tests at 60 °C: (a) initial value of mean aperture at 3.0 MPa, (b) aperture variation after 60 days at 0 MPa, (c) after 120 days at 0 MPa, and (d) after 150 days at 0 MPa
- Fig.4.19** Temporal changes in (a) mean aperture value from CT analysis and (b) contact-area ratio variation at 20 °C
- Fig.4.20** Temporal changes in (a) mean aperture value from CT analysis and (b) contact-area ratio variation at 60 °C

- Fig.4.21** Comparison of changes in hydraulic aperture.(a)Comparison of changes between CT mechanical aperture and hydraulic aperture calculated from CT mechanical aperture.(b)Comparison changes in hydraulic aperture between permeability tests and CT mechanical aperture at 20 °C
- Fig.4.22** Influence of the CT resolution on the tumorous tissue images (a) 100×100 μm², (b) 300×300 μm², (c) 400×400 μm², (d) 500×500 μm² (Braunagel, et al., 2017)
- Fig.4.23** Different CT matrix size represents different resolution (Hata, et al., 2018)
- Fig.4.24** A cross-section of the granite CT image with the matrix size of 1024 × 1024 through CT observation
- Fig.4.25** Comparison between normal resolution and scale transformation resolutions (a)normal resolution, size of the detect element at x, y direction is 0.0151 mm and at z direction is 0.017 mm. The matrix size is 1024×1024, slice number of the sample is 1788, (b) low resolution, size of the detect element at x, y direction is 0.0302 mm and z direction is 0.034 mm. The matrix size is 512×512, slice number of the sample is 896, (c) high resolution, size of the detect element at x, y direction is 0.0886 mm and z direction is 0.011 mm. The matrix size is 1024×1024, slice number of the sample is 3287
- Fig.4.26** CT image comparison between normal resolution and low resolution (at z-direction of 0.6 cm)
- Fig.4.27** Enlarged aperture position, CT image comparison between normal resolution and low resolution (a) 1024 ×1024 (b) 512 × 512. The 512 x 512 looks blurry
- Fig.4.28** Aperture distribution comparison between normal and low resolution (a)1024×1024 matrix, (b) 512×512 matrix
- Fig.4.29** Illustration the process of CT scanning at a high resolution
- Fig.4.30** Aperture distribution comparison between normal and high resolution (a)1024×1024 matrix,(b) 1024×1024 matrix(down-scaled)
- Fig.5.1** Threshold method on identifying the fracture position (Lai et al., 2017)
- Fig.5.2** The granite specimen was fixed into the triaxial cell (transparent to X-ray)
- Fig.5.3** Extracted CT images (#Slice A to Slice E) from the granite specimen
- Fig.5.4** Schematic illustration of region growing method (Kishida et al., 2015)
- Fig.5.5** Gaussian distribution of region growing method
- Fig.5.6** σ value difference on the aperture boundary identification
- Fig.5.7** Edge detection result of a representative slice at 3.0 MPa (removed membrane and mineral)
- Fig.5.8** CT image comparison (a) Original CT image, (b) Image processing under Region growing method (RG), (c) Image processing under Edge detection method (ED)
- Fig.5.9** Aperture boundary profile and a calculation result with RG and ED methods. (a)Comparison of aperture boundary profile, (b)Aperture and contact-area ratio value (RG), (c)Aperture and contact-area ratio value (ED)
- Fig.5.10** Aperture value difference under two image processing methods, (b)Aperture value histogram (RG), (c)Aperture value histogram (ED)
- Fig.5.11** Enlarged views of fracture where difference of extracted aperture by RG and ED is relatively large
- Fig.5.11'** Profile of CT value across the fracture at Line 514 and identification result by RG and ED
- Fig.5.12** CT image comparison under two image processing methods at 0 MPa.(Slice B~E)
- Fig.5.13** Aperture and contact-area ratio value comparison at each case (0 MPa-Slice D~E)
- Fig.5.14** Enlarged view of fracture in Slice D at 0-MPa-confining pressure. (a) original CT image, (b) RG result, and (c) ED result
- Fig.5.15** Enlarged view of fracture in Slice E at 0-MPa confining pressure. (a) original CT image, (b) RG result, and (c) ED result
- Fig.5.16** CT image comparison under two image processing methods at 3MPa-Slice A~E

- Fig.5.17** Aperture and contact-area ratio value comparison at each slice (i.e., 3MPa-Slice A, and 3MPa-Slice E)
- Fig.5.18** CT image comparison under different image processing methods (3MPa-Slice A~E)
- Fig.6.1** Effect factors of the flow behavior within the fracture aperture (a) fluid direction variation on the roughness surface. (Kishida, et al. 2009), (b) fracture width difference and the flow rate change. (Okamoto, et.al. 2017)
- Fig.6.2** Schematic figure of flow through a single fracture (a) flow pass through the rock fracture, (b) cartesian coordinates of Navier-Stokes (Kishida et al., 2013)
- Fig.6.3** Discharge at different water heads (0 day, 0 MPa, 20 °C)
- Fig.6.4** Discharge at different water heads (0 day, 3.0 MPa, 20 °C)
- Fig.6.5** Discharge at different water heads (30 days, 3.0 MPa, 20 °C)
- Fig.6.6** Discharge at different water heads (60 days, 3.0 MPa, 20 °C)
- Fig.6.7** Discharge at different water heads (180 days, 3.0 MPa, 20 °C)
- Fig.6.8** Flow vector distribution under different water heads (0 MPa, 0 day, 20 °C)
- Fig.6.9** Flow vector distribution under different water heads (3.0 MPa, 0 day, 20 °C)
- Fig.6.10** Reynolds number distribution under different water heads (a) 0 MPa, 0 day, 20 °C,(b) 3.0 MPa, 0 day, 20 °C
- Fig.6.11** A linear fitting curve of the discharge changing with different water heads (3.0 MPa, 0 day, 20 °C)
- Fig.6.12** Comparison with hydraulic aperture obtained from CT mechanical aperture and from the flow simulation at 20 °C
- Fig.6.13** Comparison with hydraulic aperture obtained from permeability test, from CT mechanical aperture, and from the flow simulation at 20°C
- Fig.7.1** Schematic of permeability evolution under Chemical-Mechanical coupled processes
- Fig.7.2** Conception figure of the prediction in aperture and the contact-area change
- Fig.7.3** A schematic figure of pressure dissolution
- Fig.7.4** Illustration of the representative elements
- Fig.7.5** Simulation procedure of the Chemical-Mechanical coupled model
- Fig.7.6** Relation between mechanical aperture and contact-area ratio. Circles are evaluated by using the profiling data which has measured from X-ray CT, and the dotted line is the regression curve of $\langle b(t) \rangle_c = b_r + (b_0 - b_r) \exp(-(R_c(t) - R_{c0})/a)$; initial $b_0=0.17$, $R_{c0}=33.4\%$ at 3.0 MPa, 0 day. with the correlation coefficient, $R^2 = 0.95$

Chapter 1 Introduction

1.1 Background

The study of the long-term fluid flow within very low permeable fractured rocks is significant for underground construction in many engineering fields, such as the isolation of nuclear waste, enhanced geothermal systems (Tsang et al., 1987, 1989; Pruess et al., 1990), and petroleum extraction (Pare, 1990, 1991; Chen, 1994; Romele et al., 1997; Gan et al., 2009). In recent years, low permeability reservoirs are being widely developed (Van, 1982; Nelson, 1985; Laubach, 2003; Rutqvist, 2008), such as radioactive waste disposal reservoirs. The safety of these disposal reservoirs depends on the establishment of natural barriers or artificial barriers, which will use low permeability bentonite as the sealing material. Construction of the reservoir barriers may be affected by the combined effects of the hydro-mechanical and the geochemical properties. The heat generated by the radioactive decay and the interaction of the water and the solutes supplied by the surrounding rock are important effect factors. Therefore, it is crucial that the long-term behavior of the low permeable rock masses around sites selected for use as underground disposal reservoirs be evaluated (Tachi et al., 2001; Noiriél, 2015; Gierzynski et al., 2017; Claire et al., 2018).

There are several countries that have initiated underground nuclear waste disposal. In 1957, the US Academy of Sciences Committee considered the deep borehole disposal of nuclear waste (Patrick et al., 2009), as shown in **Fig. 1.1**. Since high overburden pressures contribute to the sealing of waste transport pathways, radioactive waste is emplaced at the bottom of deep (3-5 km) boreholes in crystalline basement rock (granite) with the characteristics of lower water content, lower porosity, and lower permeability of the crystalline basement rock. In this way, the underground water flow and the thermal influence (< 200 m depth) can be prevented. Moreover, the Japanese government is putting forth efforts to establish disposal sites for high-level radioactive waste in order to avoid disasters, such as the 2011 Fukushima nuclear power plant disaster. For the geological disposal of high-level radioactive waste, the stability of the disposal system might be affected by the long-term water flow around the rock fractures (Rutqvist et al., 2002; Tsang, 2012; Yasuhara et al., 2015). In 2000, the Japanese government decided to insulate high-level radioactive waste by vitrifying and burying it 300 m under the ground, as shown in **Fig. 1.2**. Suitable areas were chosen for the storage of this high-level radioactive waste. The appropriate areas were deemed safe and better able to avoid the effects of the long-term underground water flow as well as seismic and volcanic activities (NUMO, 2004; Yamaguchi, 2010).

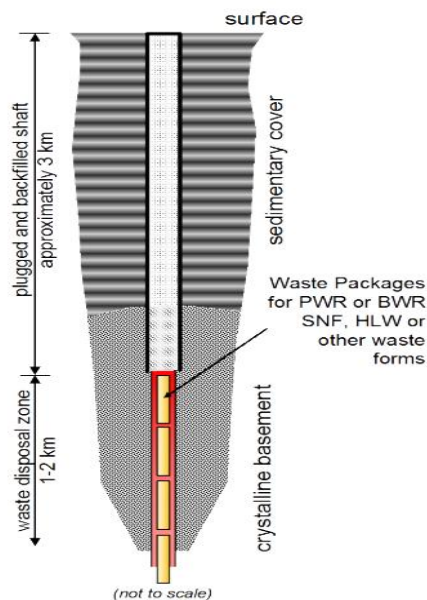


Fig.1.1 Schematic of deep borehole disposal for nuclear waste in US (Patrick et al., 2009)

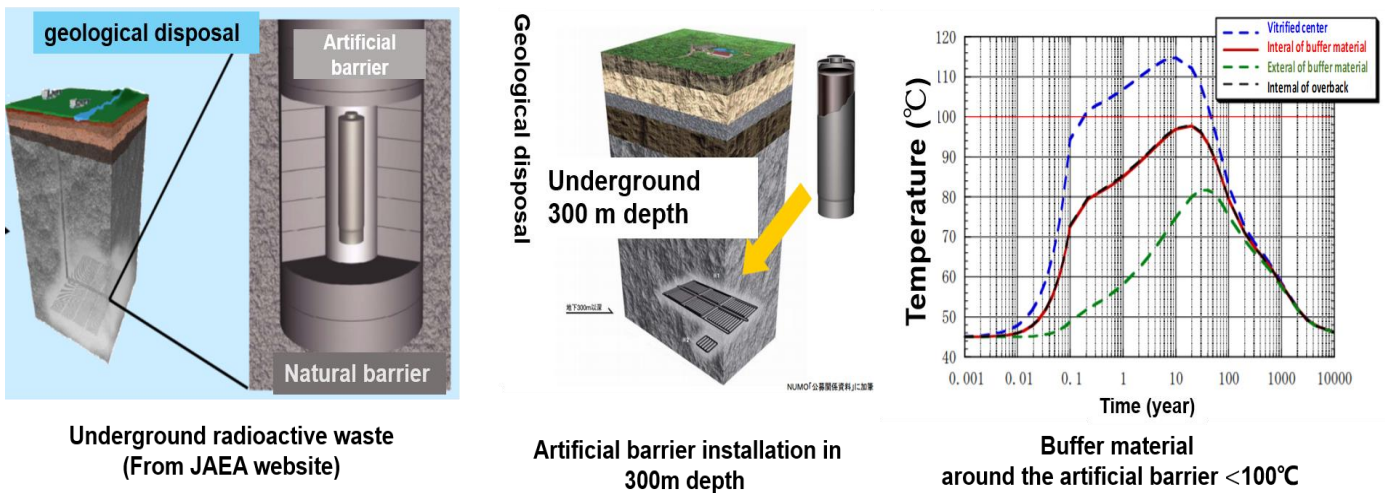


Fig.1.2 Geological disposal of high-level radioactive waste in Japan (NUMO, 2004; Yamaguchi, 2010)

Therefore, considering the underground permeability evolution and the transport of chemical substances that have leaked from around fractured rocks, it is essential to study the permeability evolution of fractured rocks under the coupled processes. However, studies on the long-term permeability evolution of fractured rocks under various conditions are insufficient. Grasping the aperture evolution over the long term under coupled processes is also indispensable. In recent years, microfocus X-ray CT is being utilized to obtain the internal structure of various materials. It is possible to gather various rock samples with fractures or cracks under different conditions. The measured data can be used to reconstruct a microfocus view for illustrating the heterogeneous aperture distribution. Moreover, the changes in the contact-area ratio under the coupled conditions, which were grasped by the X-ray CT, can further illustrate the fluid flow behavior within the fractured rocks and the fracture evolution over the long term.

1.2 Objectives

In general, the long-term underground water flow of fractured rocks under various conditions needs to be further understood. In order to check the permeability evolution under the coupled processes, the focus of the experimental works in this study was to conduct several permeability tests under different conditions, especially for the permeability evolution over the long term under a constant confining stress. An X-ray CT observation was also conducted under the same conditions as the long-term permeability tests. A CT scanner was utilized to obtain the aperture distribution and to grasp the contact-area ratio. Finally, several indexes, such as the contact-area ratio and the aperture distribution, as well as a comparison of the variation in hydraulic aperture, were analyzed to check the factors affecting the permeability evolution over the long term.

In order to better understand the results generated from the experimental works, a flow simulation was also performed based on the CT experimental data. Moreover, the geo-chemical response which will have an effect on the changing permeability and the deformation of the surface roughness over the long term was also conjectured.

1.3 Structure of the thesis

This thesis covers the following subjects:

- (1) Research found in literature on the hydraulic properties of different rocks under various conditions; an approach for grasping the variation in internal rock fractures;
- (2) Investigation of the permeability and hydraulic aperture variation of single-fracture granite samples over the short term under various confining pressure and temperature conditions;
- (3) Study of the permeability and hydraulic aperture variation of single-fracture granite samples over the long term under various confining pressure and temperature conditions;
- (4) Observation of the mechanical aperture variation under various confining pressure and temperature conditions through microfocus X-ray CT (experiment conditions are the same as those in (3) for the long-term permeability tests);
- (5) Effect of different image processing methods on the rock fractures under various confining pressures;
- (6) Investigation of the changes in flow behavior within the granite fracture aperture under different confining pressure conditions. The aperture distribution is verified. Moreover, the hydraulic aperture is compared with the permeability test results in (3) and the CT observation results in (4);
- (7) Linking (2), (3), (4), and (6) from the experimental results and the flow simulation results, the chemical-mechanical interaction is conjectured. Then, a chemical-mechanical numerical simulation is conducted to check the aperture and the contact conditions within the fracture aperture;

(8) Considering the connection between the experimental and the numerical results, the conclusion of this study is summarized, and future work is discussed.

In order to approach the above subjects, a schematic of the objectives of this thesis is drawn in **Fig. 1.3**. The outline of this thesis is summarized as follows:

1.3. The outline of this thesis is summarized as follows:

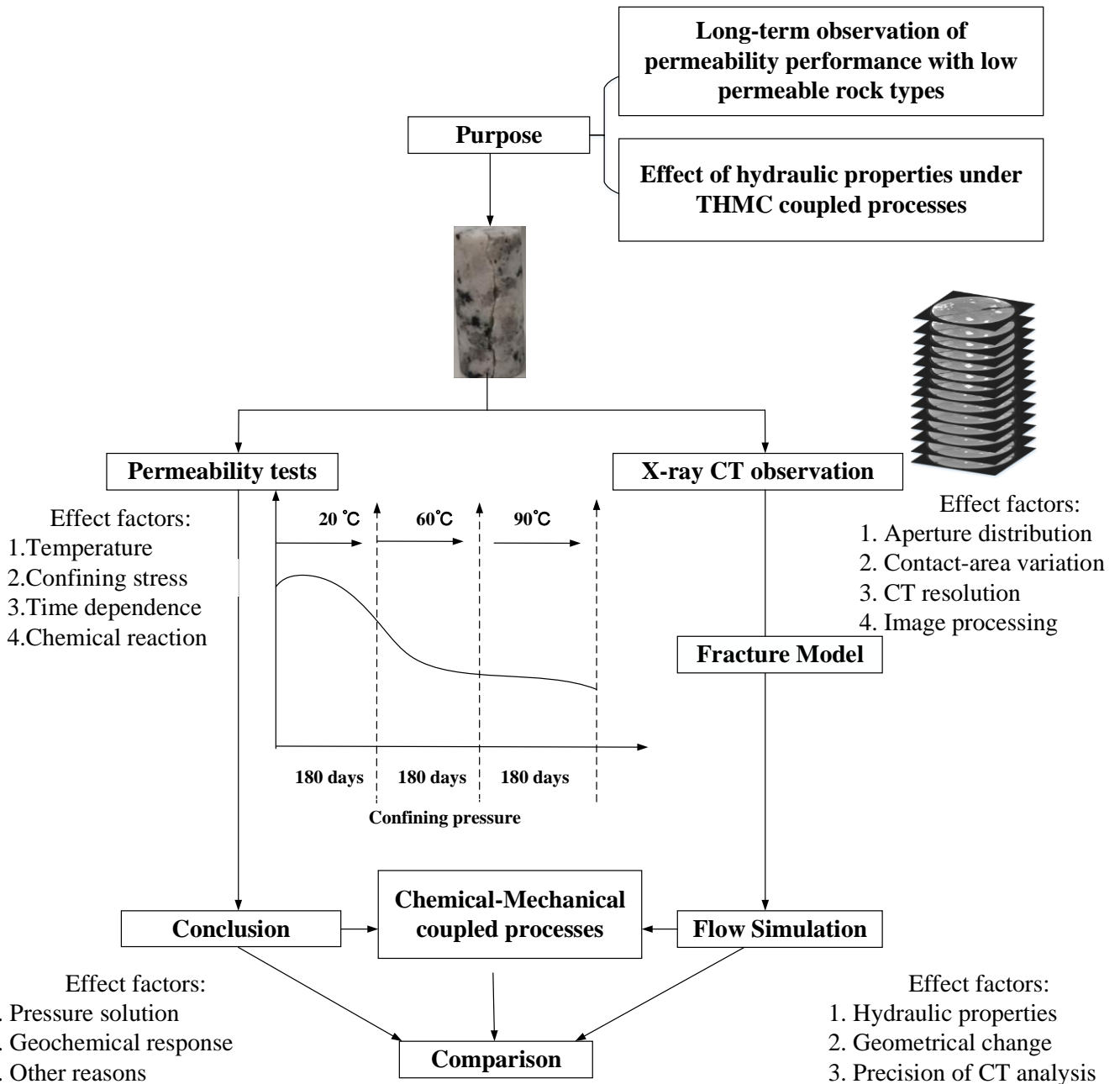


Fig.1.3 Schematic diagram of the objectives of this thesis (illustration of the effect factors which will be introduced in this study)

To achieve the goals presented in this schematic, the thesis was written according to the following structure:

Chapters 1 and 2 provide background information and a literature review of this thesis. The purpose of this study is introduced based on several different focus points and problems taken from the background information and the literature review.

Chapter 3 is the kernel of the experimental tests. A single-fracture rock sample is set into the triaxial cell under a saturated condition. Permeability tests are separated into short-term and long-term tests under different conditions (i.e., different confining pressures and temperatures). The permeability test results are summarized and compared.

Chapter 4 introduces the microfocus X-ray CT experimental tests. Microfocus X-ray CT is combined with the triaxial cell, and the same material is used for another single-fracture granite sample. The experimental conditions are set to be the same as those in the long-term permeability tests. The results illustrate that the mechanical aperture changes under a long-term constant confining stress. Moreover, in order to check the effect factors of the aperture change, different resolutions of the CT scanning conditions are changed and compared.

Moreover, in order to verify the accuracy of the aperture and the contact-area ratio, which are measured by the X-ray CT, several image processing methods are used. Then, the effect of the different image processing methods on the CT images of a single rock fracture under various conditions is discussed and compared in **Chapter 5**.

Chapter 6 investigates the variation in flow behavior through a flow simulation. The numerical flow simulation is conducted based on the data measured in **Chapter 4**. The change in hydraulic aperture, due to the flow simulation under different confining pressures, is checked and compared with the hydraulic aperture which is measured through the permeability tests and the X-ray CT observation. Moreover, the flow discharge and the Reynolds number under different conditions in the long-term are also discussed.

From **Chapter 3**, the experimental results indicate that the variation in permeability might be due to the chemical-mechanical interaction within the fracture. **Chapter 4** further verifies that the aperture is altered over the long term. **Chapter 6** studies the flow variation under different confining pressures. The flow behavior is altered due to the contact-area change within the aperture. From the experiment works and the flow simulation, it is indicated that the fracture asperities under the coupled processes are changed over the long term. In **Chapter 7**, therefore, it is further discussed that the experimental results (i.e., hydraulic aperture and contact-area ratio change) may be due to the chemical-mechanical coupled processes. A chemical-mechanical coupled simulation is performed to check whether or not a geochemical response occurred within the fracture aperture. In addition, the results of the numerical simulation are used to explain the phenomena that occurred in the experimental results in **Chapters 3 and 4**.

By reviewing the entire thesis, several conclusions to this study are finally made and the future work is summarized in **Chapter 8**.

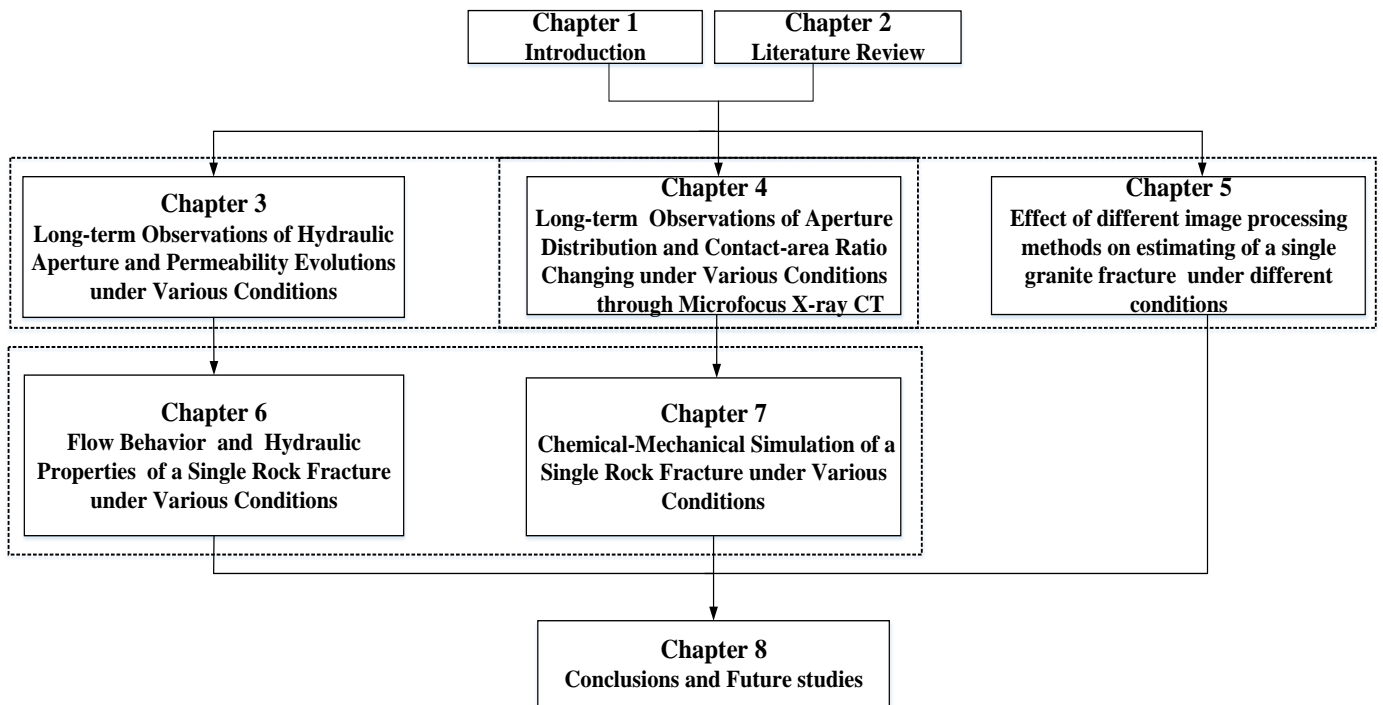


Fig.1.4 Structure of this thesis and the linkage between each chapter

References

- Chen, S. S., Spiro, M.: Study of microwave extraction of essential oil constituents from plant materials. *J Microw Electromagn Energy*. 29:231±241. 1994.
- Gan, S., Lau, E. V., Ng, H. K.: Remediation of soils contaminated with polycyclic aromatic hydrocarbons (PAHs) *J. Hazard. Mater.* 172, pp. 532-549. 2009.
- Claire, W., James, W., David, S., Simon, N.: Coupled reactive transport modelling of the international Long-Term Cement Studies project experiment and implications for radioactive waste disposal. *Applied Geochemistry*, 97, pp: 134-146. 2018.
- Gierzynski, A.O., Pollyea, R.M.: Three-phase CO₂ flow in a basalt fracture network. *Water Resource Research*, 53, pp: 8980-8998. 2017.
- Laubach, S.E.: Practical approaches to identifying sealed and open fractures. *AAPG Bulletin*. 87(4): 561–579. 2003.
- Li, D.P.: The Development of Low-Permeability Sandstone Oilfields. Beijing: *Petroleum Industry Press*. 1997. (in Chinese).
- Nelson, R. A. Tue. "Geologic analysis of naturally fractured reservoirs". United States. OSTI ID: 6000074, 1985.
- NUMO: A technique and safety of the high-level radioactive waste stratum disposal, *Nuclear Waste Management Organization of Japan*. < <https://www.numo.or.jp/> >_Vol. 4~13-37. 2004.
- Noiriel, C.: Resolving time-dependent evolution of pore-scale structure, permeability and reactivity using X-ray microtomography. *Reviews in Mineralogy and Geochemistry*, 80, pp. 247-285. 2015.
- Pare, JRJ.: Microwave extraction of volatile oils and apparatus therefore. Patent no. 90250286.3 (0 485 668A1). 1990.
- Pare, JRJ.: Microwave-assisted natural products extraction. Patent no. 519,588 (5,002,784). 1991.
- Patrick, V., Brady, Bill, W.: Deep Borehole Disposal of High-Level Radioactive Waste. *SANDIA REPORT*. 2009.
- Pruess, K., Wang, J. S. Y., Tsang, Y. W.: On thermo-hydrologic conditions near high-level nuclear wastes emplaced in partially saturated fractured tuff. 2. Effective continuum approximation. *Water Resources Research*, 26 (6) (1990), pp. 1249-1261
- Pruess, K., Wang, J. S. Y., Tsang, Y. W.: On thermohydrologic conditions near high-level nuclear wastes emplaced in partially saturated fractured tuff. Simulation studies with explicit consideration of fracture effects. *Water Resources Research*. 26 (6) (1990), pp. 1235-1248.
- Romele, L., Polesello, S.: How to minimize the use of solvents. *Laboratorio*. 2000. 11:102±110. 1997.

Rutqvist, J., Wu, Y.S., Tsang, C.F.: A modeling approach for analysis of coupled multiphase fluid flow, heat transfer, and deformation in fractured porous rock. *International Journal of Rock Mechanics and Mining Sciences*. 39:429–442. 2002.

Rutqvist, J., Birkholzer, J. T., Tsang, C.F.: Coupled reservoir-geomechanical analysis of the potential for tensile and shear failure associated with CO₂ injection in multilayered reservoir-caprock systems. *International Journal of Rock Mechanics and Mining Sciences*. Volume 45, Issue 2, pp. 132-143. 2008.

Tsang, C. F.: Coupled thermo-hydro-mechanical processes in the near field of a high-level radioactive waste repository in clay formations." *International Journal of Rock Mechanics and Mining Sciences*. 49: 31-44. 2012.

Tsang, Y.W., Pruess, K.: Preliminary Studies of Gas Phase Flow Effects and Moisture Migration at Yucca Mountain. *Nevada. Report: LBL-28819*, Lawrence Berkeley Laboratory, Berkeley, California. 1989.

Tsang, Y. W., Pruess, K.: A study of thermally induced convection near a high-level nuclear waste repository in partially saturated fractured tuff. *Water Resources Research*, 23 (10) (1987), pp. 1958-1966.

Tachi, Y., Shibutani, T., Sato, H., Yui, M.: Experimental and modeling studies on sorption and diffusion of radium in bentonite. *Journal of Contaminant Hydrology*, 47, pp. 171-186. 2001.

Van, G. T. D.: Fundamentals of Fractured Reservoir Engineering. *Development in Petroleum Science*. No. 12. Amsterdam: Elsevier Scientific Pub Co. 1982.

Yamaguchi, S.: The study of the final location choice of the high-level radioactive waste disposal facilities, *Ministry of Economy reference.*, Vol. 97-118. 2010.

Yasuhara, H., Kinoshita, N., Ohfuji, H., Takahashi, M., Ito, K., Kishida, K.: Long-term observation of permeability in sedimentary rocks under high-temperature and stress conditions and its interpretation mediated by microstructural investigations. *Water Resources Research*. 51(7): 5425-5449. 2015.

Chapter 2 Literature review

2.1 Hydro-mechanical characteristics of fractured rocks

The hydrothermal reaction within fractured rocks is an important factor for inducing the fracture geometry and the changes in permeability. High temperatures around fractured rocks will distinctly affect the variation in rock fractures. Thermal expansion may be generated within a fractured rock mass due to higher temperatures, which will result in an aperture reduction. In turn, the aperture reduction will further change the permeability (Hofmann et al., 2006). The permeability evolution within fractured rocks has been studied for many years (Watanabe et al., 2009). Kamali et al. (2018) conducted several permeability tests on fractured rocks under hydrothermal reactions. Kamali-Asl et al. (2018) performed several short permeability tests (i.e., 200 hours) on a single granite fracture under various confining pressures and temperatures, as shown in Fig. 2.1. The results show that the permeability decreased sharply at higher confining pressures, and that the permeability reduction gradient was very significant. This indicated that the closure of the aperture could be attributed to the hydrothermal reactions. Moreover, a chemical analysis of the collected effluent samples, extracted from the rock fracture, showed that the concentration of all the chemical elements became higher. This is an indication that the chemical dissolution occurred within the aperture and reduced the permeability. Other studies have clarified that the permeability of a single fracture decreased monotonically with the increase in confining pressure. In addition, the permeability decreased faster at higher temperatures (Polak et al., 2003; Yasuhara et al., 2015; Farough et al., 2016; Kamali et al., 2018). The fracture geometry was altered under the hydrothermal reactions. In particular, the chemical reaction happened within the fracture over the long term under various conditions, which further changed the permeability (Zimmerman et al., 1996; Farough et al., 2016).

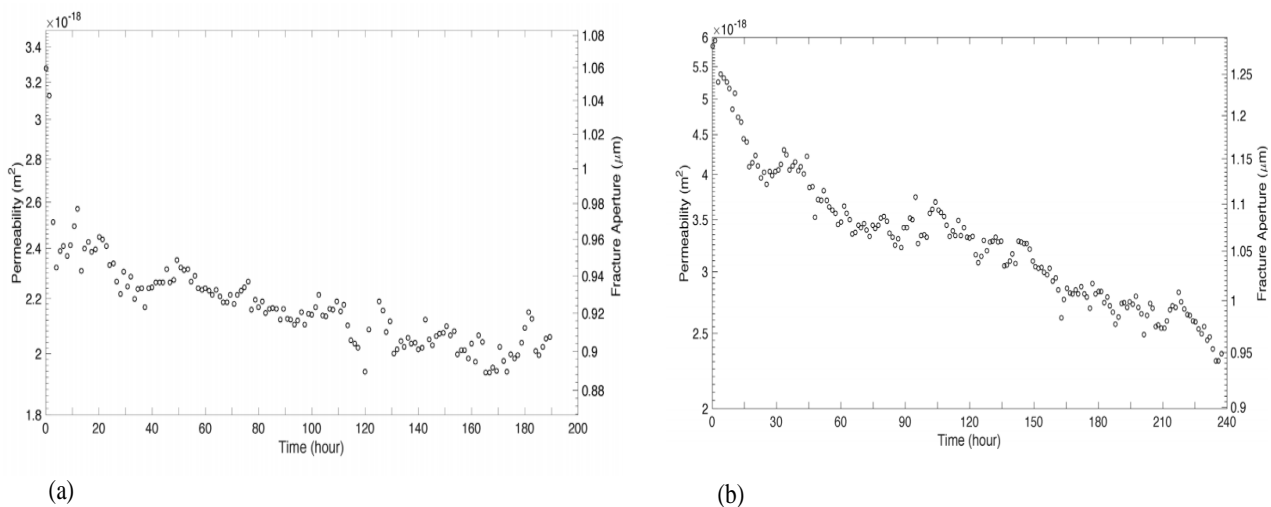


Fig.2.1 Permeability tests under various conditions: (a) temperature of 130°C and confining pressure of 15.7 MPa and (b) temperature of 130°C and confining pressure of 57.8 MPa (Kamali-Asl et al., 2018)

An obvious change in permeability was seen with the change in confining pressure, as depicted in **Fig. 2.1**. In order to check the permeability evolution with the mechanical influence, several permeability tests were conducted under various confining stresses, as illustrated in **Fig. 2.2**. It can be noted that the fracture aperture is sensitive to the confining stress. Davy et al. (2007) and Hofmann et al. (2016) performed several permeability tests through cyclic loading-unloading confining stresses. Hofmann et al. (2016) performed their permeability tests with three different types of granite specimens, i.e., intact, aligned fractured, and displaced fractured samples. The results, seen in **Fig. 2.2 (a)**, illustrate that the permeability had a reversible behavior at each loading-unloading performance, and that the permeability evolution paths at both loading and unloading confining pressures were approximately the same. Moreover, at the 2nd cycle of each experimental case, a relative decrease in permeability was seen from the 1st cycle. The change in aperture of each rock sample was quite similar. Davy et al. (2007) also studied the permeability evolution of different rock fracture samples under different confining pressures, as seen in **Fig. 2.2 (b)**. The permeability was altered with the confining pressure. However, no more prominent changes were seen when the confining pressure was larger than 10 MPa. It can be guessed that the mechanical compaction reduced the aperture. It was difficult for the aperture to be deformed any further and it became narrow when the confining pressure reached a high level. Permeability is sensitive to the confining pressure, and it has a reversible change which is the same as that seen in **Fig. 2.2 (a)**. However, the reduction gradient was different due to different aperture size.

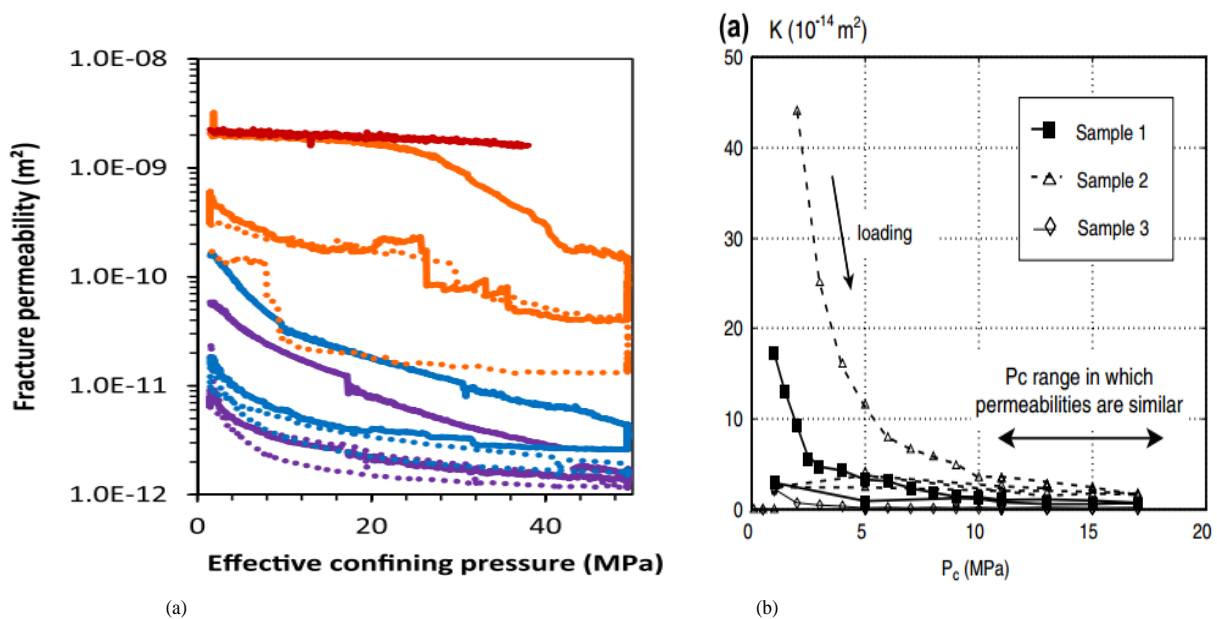


Fig.2.2 Permeability evolution with effective confining stress: (a) changes in permeability with confining pressure on aligned fractured and displaced fractured samples (Hofmann et al., 2016) and (b) gas injection tests in which permeability shows reversible behavior in loading–unloading performance (Davy et al., 2007)

In recent years, a new concept has been proposed, namely, the enhanced geothermal system (EGS) (Pruess, 2008; Zimmermann et al., 2009; Goldstein et al., 2009; Gerber et al., 2012). The change in permeability of the fractured rocks needs to be further studied when the effective confining stress acts on

the thermally fractured rocks. Numakura et al. (2015) clarified that the transition from elastic to plastic deformation of the rock sample occurred at a specific stress point, i.e., the elastic-plastic transition stress depended on the temperature. Therefore, this transition was generated at a much higher confining pressure and temperature level. In this study, several permeability tests were conducted under various temperatures, i.e., from 350°C. ~ 450°C. The permeability decreased with the effective stress. Simultaneously, there was a transition confining stress point generated in each permeability test, which separated the rock deformation from elastic to plastic. The transition points in each permeability test were 70, 50, 40, and 25 MPa at 350, 380, 400, and 450°C, respectively. It can be noted that these transition points decreased with the increase in temperature. The transition point occurred early when the temperature was higher. Then the permeability reduction gradient changed after those transition points. A sharp reduction gradient can be observed in each test, as seen in **Fig. 2.3**.

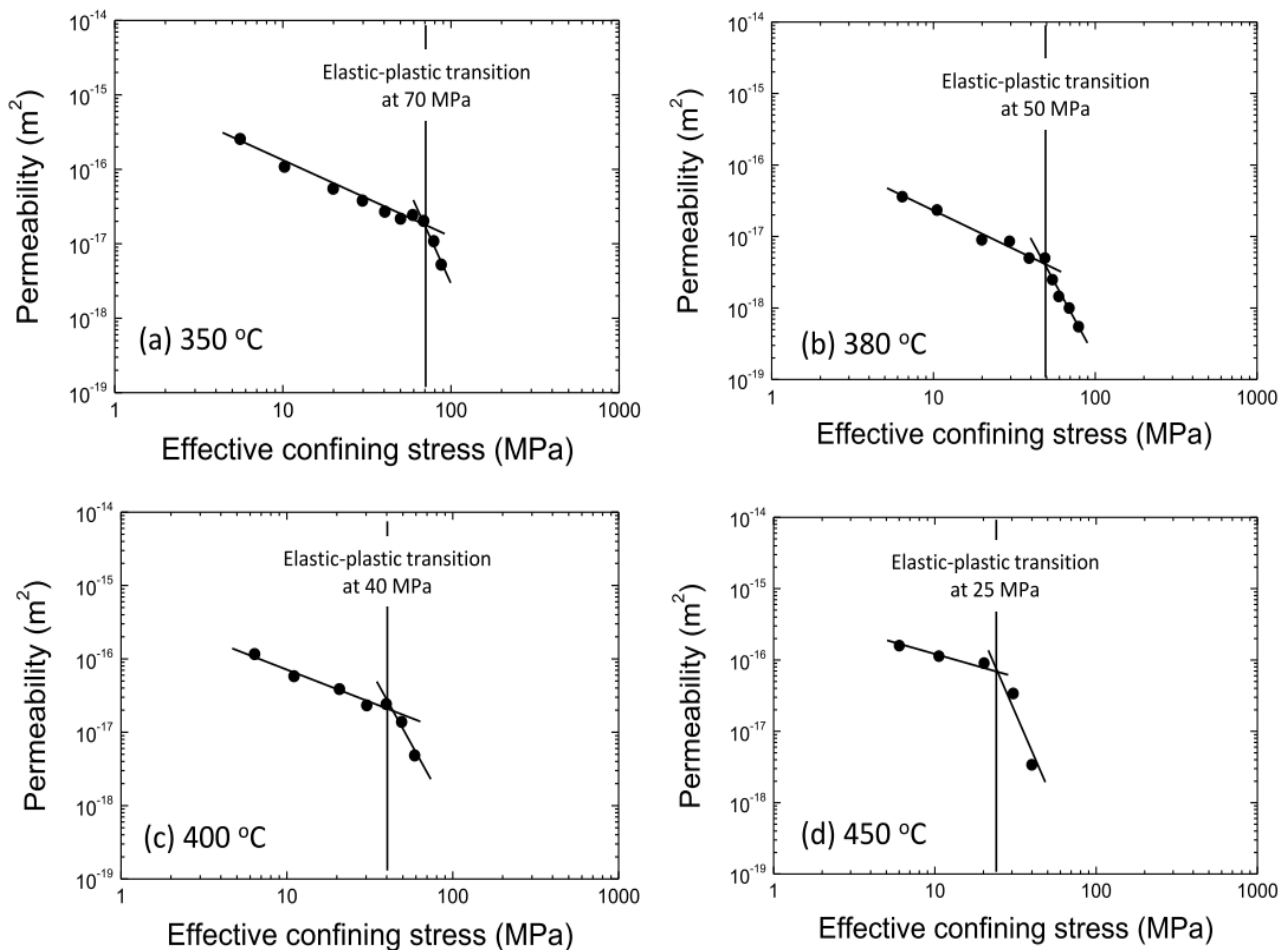


Fig.2.3 Permeability performance under different conditions in which elastic-plastic transition occurred under different temperatures (Numakura et al., 2015)

In general, a much higher temperature and effective confining pressure will induce the plastic change of a rock sample. The permeability first decreases with the effective confining pressure, then it decreases again at a much higher stress level. Therefore, fractured rock under various conditions needs to be fully

understood through laboratory works. However, there is lack of laboratory works which have studied the permeability evolution of fractured rock under coupling processes.

2.2 THMC coupling processes of fractured rocks

Previous studies have indicated that the permeability will be altered under different temperatures and confining stresses. The plastic deformation of fractured rock may occur under a very high stress and temperature level. This deformation may happen due to the chemical reactions that are generated under higher temperature and stress conditions. In recent years, it has been proven that the coupled thermal-hydraulic-mechanical-chemical (THMC) processes have a significant effect on the fluid flow in the deep subsurface (Ghassemi et al., 2007; Taron et al., 2010; Frdric et al., 2017), especially in the construction of geological disposal sites for high-level radioactive waste, petroleum excavation, and the EGS system. The underground water flow within fractured rocks under coupled conditions (THMC coupled processes) may significantly affect the variation in rock fractures (Rutqvist et al., 2002; Yasuhara et al., 2006; Tsang et al., 2012). Moreover, the mineral reactions and the pressure dissolution within the generated fractures may also change the permeability. Then, the transport of radionuclides within the fractured rock would be promoted. Under the coupling processes of the fractured rock, the mechanical creep (i.e., stress corrosion) (Yasuhara et al., 2006; Xu et al., 2016) and the geochemical response (i.e., mineral reaction) (Yasuhara et al., 2004, 2011; Polak et al., 2004; Beeler et al., 2004; Elkhoury et al., 2013) alter the fracture geometry. Pressure dissolution may occur within the aperture, which may change the permeability. Therefore, fractured rock under the THMC coupled processes can be summarized by three main aspects: (i) dissolution of the non-contact fracture asperities due to high localized stresses, (ii) diffusion of the dissolved mass from higher-stressed regions (contacting asperities) to less-stressed regions (free-faces of the fracture surface) due to chemical reactions, and (iii) precipitation of the dissolved minerals at the free-faces of the fracture surface (Yasuhara et al., 2004; Yasuhara et al., 2011). **Fig. 2.4** shows the schematic process of the chemical reaction that occurred within the fractured rock. Mineral dissolution/ precipitation at the grain-to-grain contacts was generated due to the pressure dissolution. Therefore, the fracture aperture and the permeability will be changed with time. The fracture contact area, which became larger, will result in the decrease in permeability (Yasuhara et al., 2011).

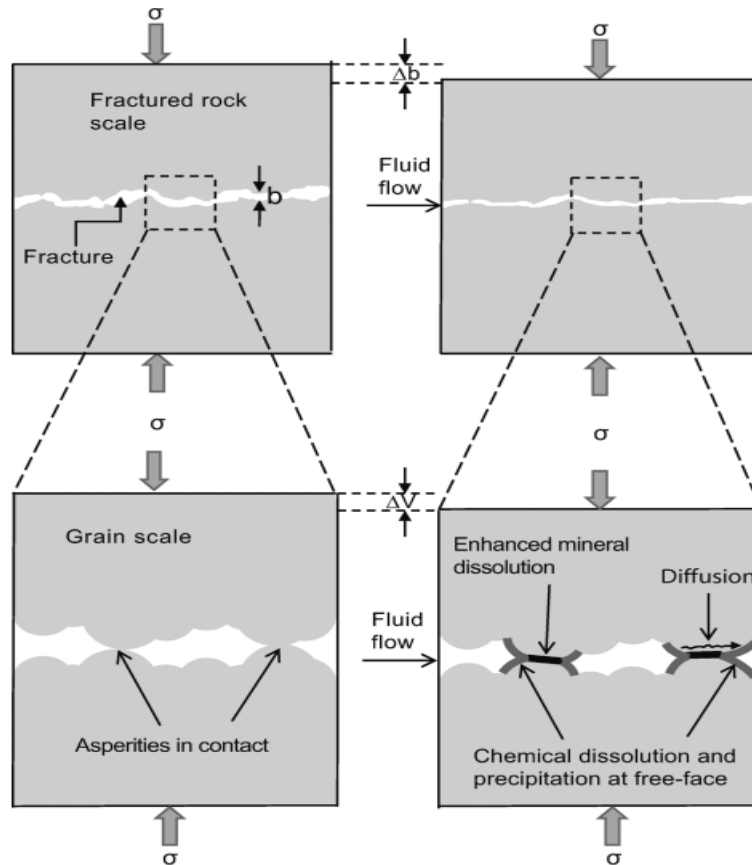


Fig.2.4 Schematic process of chemical reaction generated within fractured rock (Yasuhara et al., 2004)

Several numerical works and a few laboratory works were conducted to predict the variation in permeability under the THMC coupling processes (Li et al., 2008; Taron et al., 2010; Zhang et al., 2013; Yasuhara et al., 2015; Xu et al., 2016; Wang, 2017). Changes in the flow behavior and the fracture aperture, such as the variation in the contact area under coupled processes, are essential. Yasuhara et al. (2015) conducted several long-term permeability tests on many types of rock samples (i.e., intact and fractured sandstone and mudstone samples, respectively) under different conditions, as shown in **Fig. 2.5**. The permeability test on the intact sandstone illustrated that the permeability showed no more obvious changes during the first several days, but it increased sharply at both 20°C and 90°C after 100 days, as seen in **Fig. 2.5 (a)**. However, no distinct difference in permeability can be observed at either temperature. In contrast, the permeability test on the fractured sandstone showed that the permeability decreased after several hundred days at both 20°C and 90 °C, as shown in **Fig. 2.5 (b)**. At 20°C, the permeability decreased more obviously than at 90°C. The permeability did not decrease monotonously at 90°C due to the mineral dissolution generated on the propping asperities. It can be explained as follows. If the effect of the mineral dissolution at the grain contacts is larger at the pore walls (free surface dissolution), the aperture will close and the permeability will decrease with time. This study is different from previous ones in which it was clarified that the permeability decreased monotonously under higher temperatures. Moreover, the mineral variation (Si) of each rock sample with time is depicted in **Fig. 2.5 (c)**. The figure indicates that element

Si dissolved more evidently at 20°C than at 90°C. The reduction rate does not depend on the temperature. However, the concentration depends on the temperature, i.e., the concentration at 90°C is higher than that at 20°C. The dissolved element from the fracture contact asperities shows temperature dependence. Moreover, stress has a slight influence on the mineral dissolution. As shown in **Fig. 2.5 (c)**, the reduction values of Si at 7.5 MPa and 15 MPa are quite similar. It is not easy to say that mineral dissolution is stress dependent. Therefore, the aperture will close or become large, and the pore structure of the rock samples will be changed by the mineral dissolution, as illustrated previously. Moreover, there is a lack of convective studies that can better grasp the changes in the contact area within the fractured rocks. At the present time, the changes in permeability with time cannot be further illustrated. In general, the contact area condition of fractured rock cannot be simply grasped through laboratory work. Several numerical works have been conducted to predict the changes in the fracture's contact area. The results have been used to explain the permeability evolution under the coupled conditions (i.e., THMC processes).

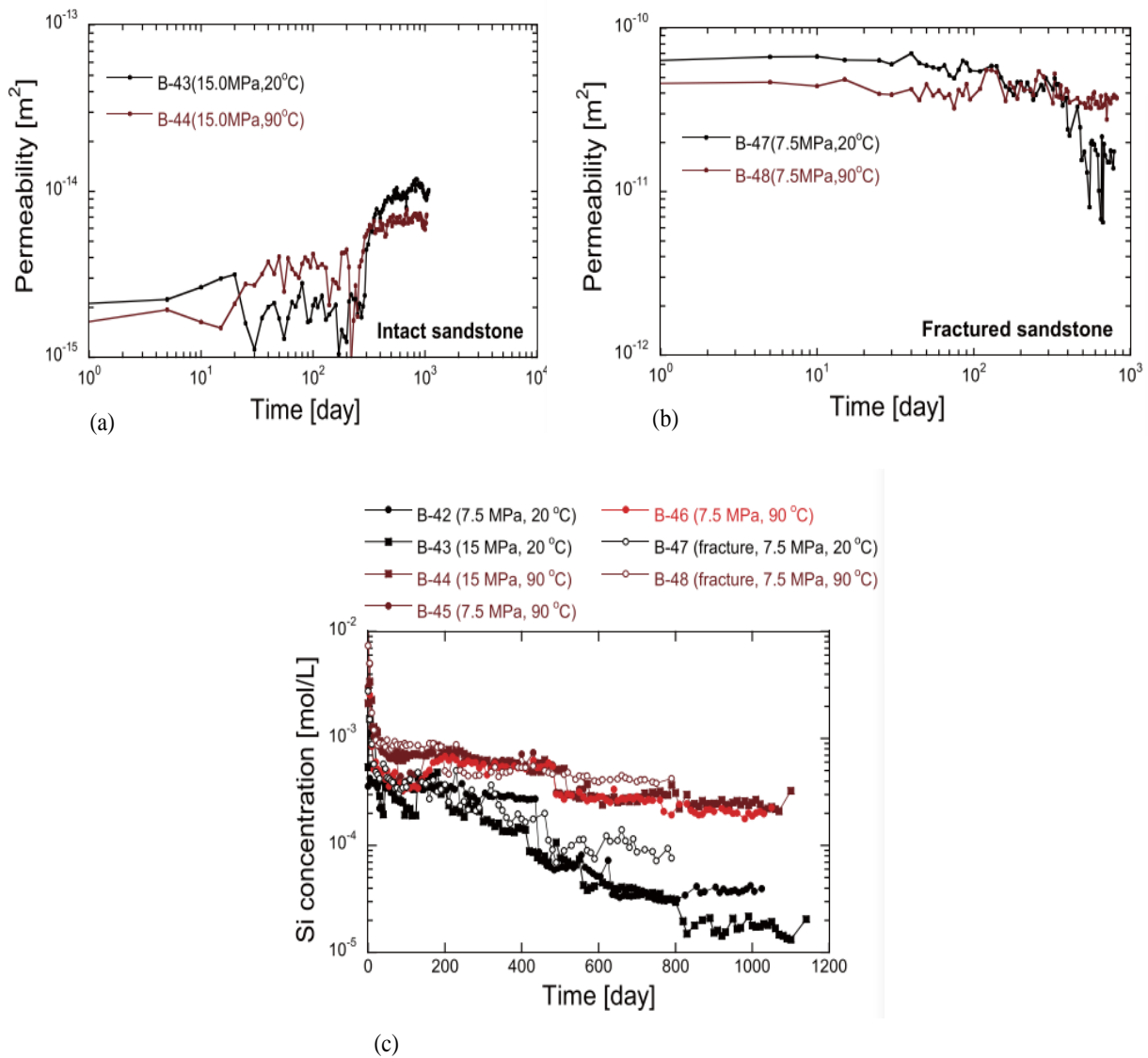


Fig.2.5 Variation in permeability through use of intact and fractured sandstone: (a) changes in permeability of intact sandstone, (b) changes in permeability of fractured sandstone, and (c) mineral dissolution of Si under different conditions (Yasuhara et al., 2015)

Several numerical models were performed to predict the evolution of permeability and the internal contact area conditions under the THMC processes (Lang et al., 2015; Wang, 2017; Lu et al., 2018). Wang (2017) and Lu et al. (2018) conducted numerical works to predict the permeability evolution and the change in the contact area ratio with time. Their theoretical models were used to fit the experimental results from the references. In their numerical models, the pressure solution on the fracture asperities was not considered; the results are shown in **Figs. 2.5 (a) and (b)**. Other numerical works were conducted to predict the permeability and the variation in the contact area ratio without making a comparison with the experimental data, as depicted in **Figs. 2.6 (c) and (d)**.

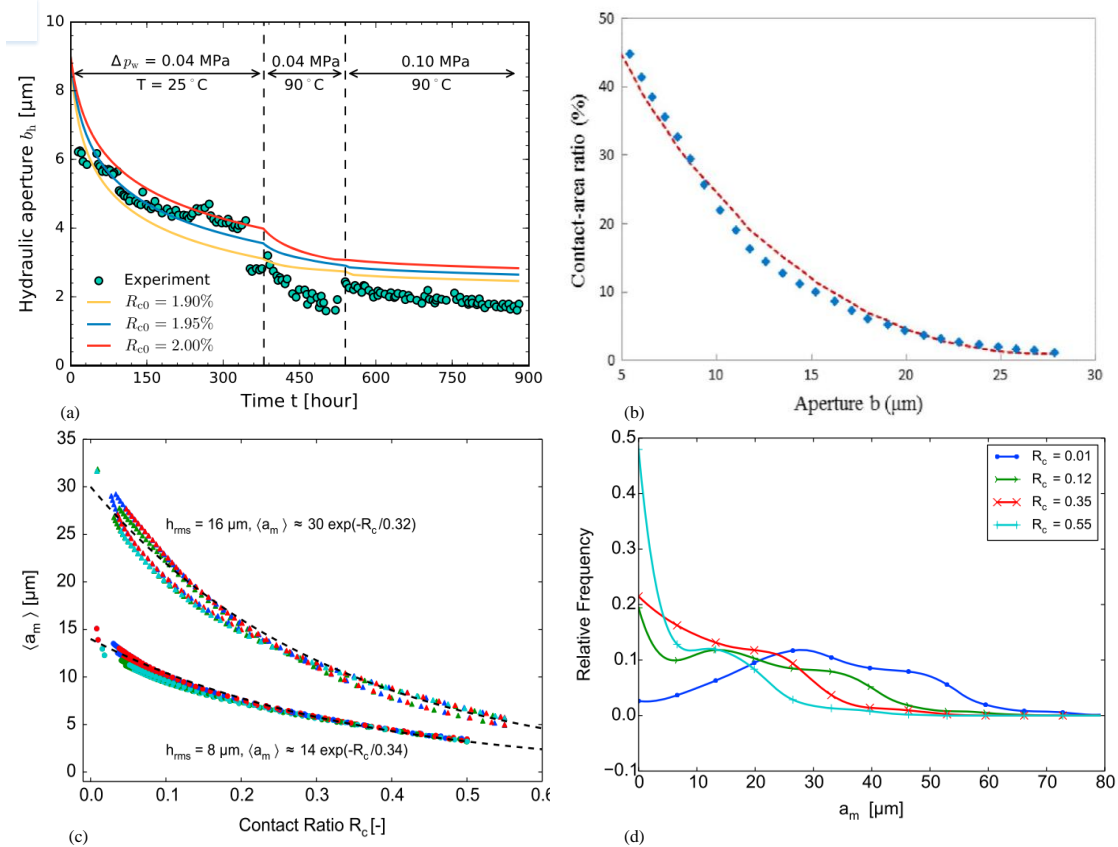


Fig.2.6 Relationship between hydraulic aperture and contact-area ratio under numerical prediction: (a) impact of surface topography of fracture channel on permeability evolution: predicted for initial contact-area ratio R_{c0} (Lu et al., 2018), (b) model fitting to measured aperture-contact area relation (Wang, 2017), (c) relationship between mean aperture and contact-area ratio, and (d) variation in contact area when pressure solution occurs (Lang et al., 2015)

There is a lack of numerical works that can predict the uncertain permeability changes in the experimental results under various conditions (Polak et al., 2004; Yasuhara et al., 2006). Therefore, further investigations of the permeability evolution under various conditions are needed. The contact area condition is a critical factor for clarifying the change in permeability with time. Almost none of the previous studies conducted contact-area ratio estimations through laboratory works, and it is difficult and unpredictable to try to grasp the changes in the contact-area ratio from experimental observations.

2.3 Utilization of X-ray CT

2.3.1 Utilization of X-ray CT in varied areas

Some previous studies utilized microfocus X-ray CT to obtain the internal structure of fractured rocks (i.e., fracture length, position, orientation, etc.). X-ray computed tomography (CT) is an effective technique which is capable of detecting the internal structure non-destructively and three-dimensionally (Robert et al., 1993; Van et al., 2001; Yao et al., 2009; Ketcham et al., 2010; Fan et al., 2018). X-ray was first developed for use in the fields of medical imagery in the early 1970s (Hounsfield, 1972, 1973). Then, other fields, such as paleontology (Haubitz et al., 1988), meteoritics (Arnold et al., 1982), geotechnics (Raynaud et al., 1989), and sedimentology (Kenter, 1989) began to apply it. The X-ray source, detector, and rotation system are the basic components of X-ray CT tomography. The CT images are determined by the sample size and the resolution. The X-ray source needs a higher energy spectrum, which will quantitatively obtain the CT images under radioactive decay. Based on its utilization in the medical field, X-ray CT is now widely used in the research of geological materials and for detecting small-size rock fractures within rock samples. Therefore, it is possible to grasp various rock samples with fractures or cracks under saturation or fluid injection (Stephanie et al., 2001; Karpyn et al., 2007, 2009; Dustin et al., 2017; Kumaria and Lu et al., 2018). The measured data can be used to reconstruct a 3D view for illustrating the heterogeneous fracture distribution, as shown in **Fig. 2.7** (Keller et al., 1998; Kawakata et al., 1999; Mazumder et al., 2006; Yao et al., 2009; Richard et al., 2010; Hamed et al., 2016).

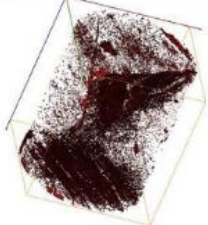

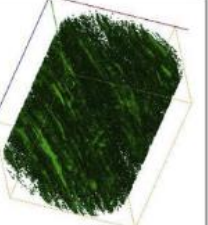



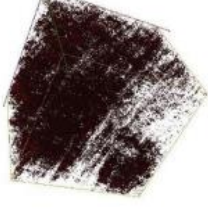

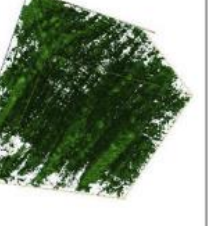
Sample ID	Pore spaces	Macerals	Minerals
B			
J			
Q			

Fig.2.7 3-D segmented micro-structures of coal samples (Zhang et al., 2018)

2.3.2 Utilization of X-ray CT in fractured rocks

Some researchers have used microfocus X-ray CT to observe the aperture changes under varying conditions (Polak et al., 2003; Yasuhara et al., 2015; Okamoto et al., 2017). Polak et al. (2003) studied the changes in fracture aperture under different temperatures (20, 80, and 120°C) through X-ray CT observations of dry and wet core samples. At higher temperatures, the mass removed from the free-face of the fracture surface and the aperture became larger after a long-term test of about 1492 hours, as can be seen in **Fig. 2.8**.

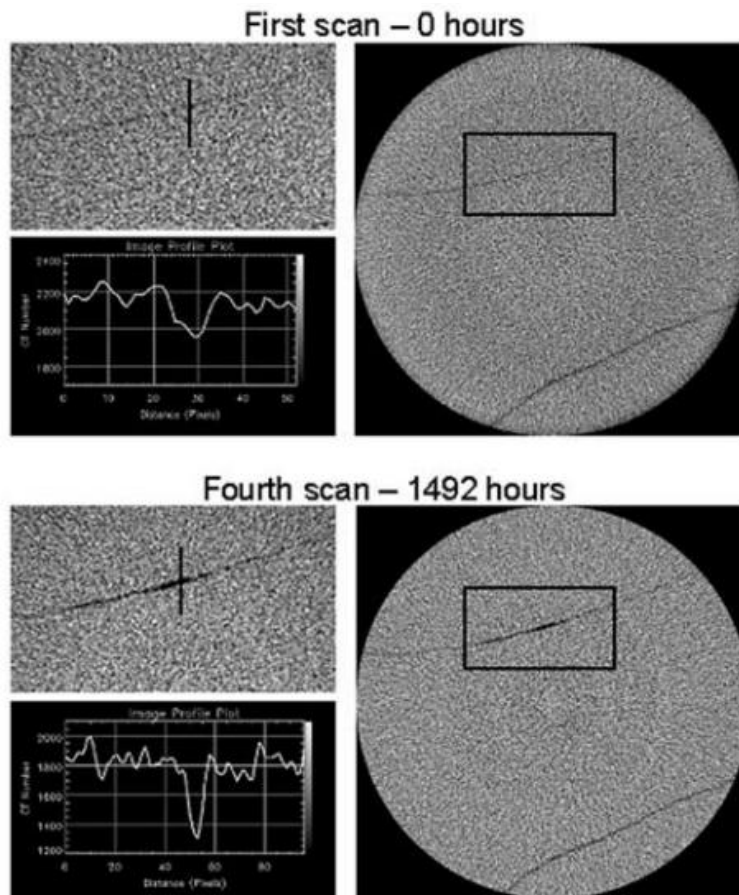


Fig.2.8 Scanned CT images of core samples at longitudinal location 665, 85 mm downstream of the inlet: (a) at test initiation (0 hours) and (b) after 1492 hours (Polak et al., 2004)

Okamoto et al. (2017) showed a comparison of CT scanning images between a sample at room temperature and a sample at the temperature of 350°C. The flow rate changed due to the mineral dissolution or the precipitation generated at 350°C. Yasuhara et al. (2015) conducted a series of permeability tests with several types of rock samples under different temperatures. The pore structures were observed through X-ray CT with a comparison between the pre- and post-experiments, as shown in **Fig. 2.9**. The comparison between the pre- and post-experiments indicated that the changing pore structures might have supported the variation in permeability. Moreover, the geochemical reactions were also confirmed.

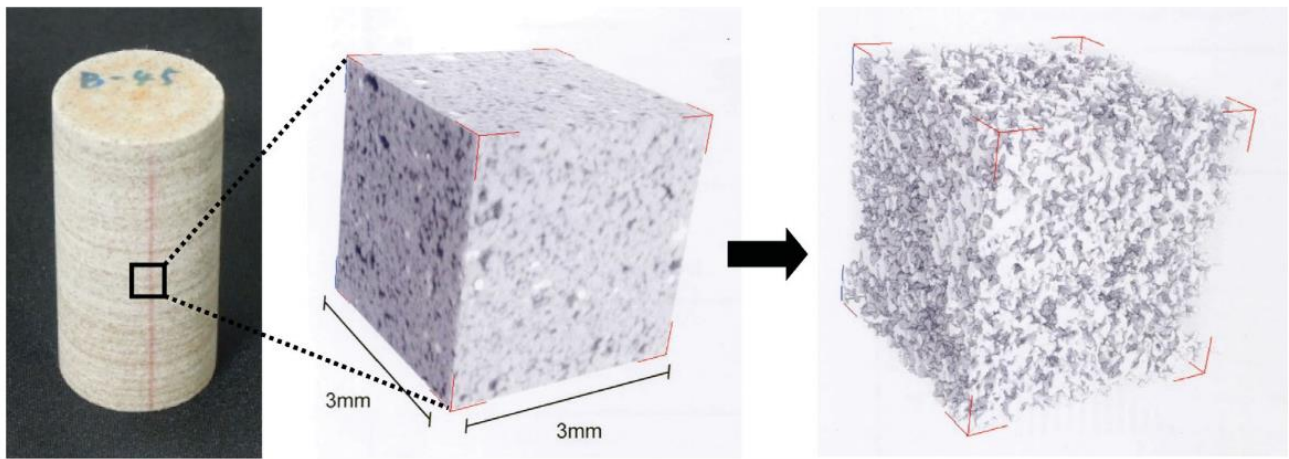


Fig.2.9 Schematic procedure of extraction of micropores using microfocus X-ray CT. A 3-mm cube is imaged in the middle of the rock sample and pore structures are extracted (Yasuhara et al., 2015).

Kamali and Caulk et al. (2016, 2018) found that the aperture would close at higher levels of confining stress. Higher levels of confining stress induced a chemical dissolution on the asperities and resulted in a change in sensitivity of the variable contact-area ratio. In addition, the pressure solution was more significant in accelerating the fracture closure rates.

Therefore, X-ray CT tomography successfully obtained the fracture position, and from the CT image analysis, the fracture aperture change was better understood. It is easier to grasp the performance of the fracture aperture and the permeability within the rock under complex conditions.

2.4 Flow simulation of single rock fracture

Since the fracture geometry of rocks may be altered under various conditions, the fluid flow evolution within the fractured rock is varied and difficult to grasp (Shu et al., 2019). The fluid flow behavior may be influenced by the complex underground environmental conditions. Therefore, the characteristics of the fluid flow within a rock fracture need to be further investigated. Previous studies have reported several laboratory works on the hydraulic properties of different types of fractured rocks (Bing et al., 2017; Farough et al., 2016; Shu et al., 2019). The hydraulic properties of the fractured rocks showed that the fluid flow would be altered under various conditions. Moreover, several numerical works also illustrated that the fluid flow within the fractured rocks was changed under the coupled processes (Konzuk et al., 2004; Li et al., 2008; Zou et al., 2015; Huang et al., 2018). The numerical results indicated that the flow behavior within the rock fracture may be changed due to several factors, such as mechanical compaction, the thermal influence or the pressure dissolution generated on the fracture asperities under long-term high-stress levels, etc. (Yasuhara 2006; 2015).

The flow will be disturbed due to the change in the contact area within the fractured rocks. The condition of the contact area is not easy to estimate through laboratory works. Therefore, the process of

the change in the fracture contact area during the fluid flow through fractured rocks should be fully understood. A rough-walled fracture would be altered, and the variation in the fracture roughness surface would have a significant effect on the flow behavior. It would further change the flow path. Therefore, the flow path within the fracture would become tortuous due to the variation in fracture roughness surfaces and contact area. Moreover, the fluid would be disturbed by the contact area positions within the fractured rock (Zimmerman et al., 1996; Li et al., 2008; Kishida et al., 2013). Numerical works have been aimed at the flow variation under different surface roughness conditions and different aperture sizes (i.e., aperture open or closed). The schematic figure given in **Fig. 2.10** shows that the fluid was disturbed by the fracture contact area (Brown et al., 1987).

A combination of the numerical and laboratory works is important for illustrating the flow change within a fractured rock. Therefore, the flow behavior within fractured rocks under different conditions (i.e., different aperture size, fracture contact-area positions, contact-area variation under coupled conditions) should be further checked.

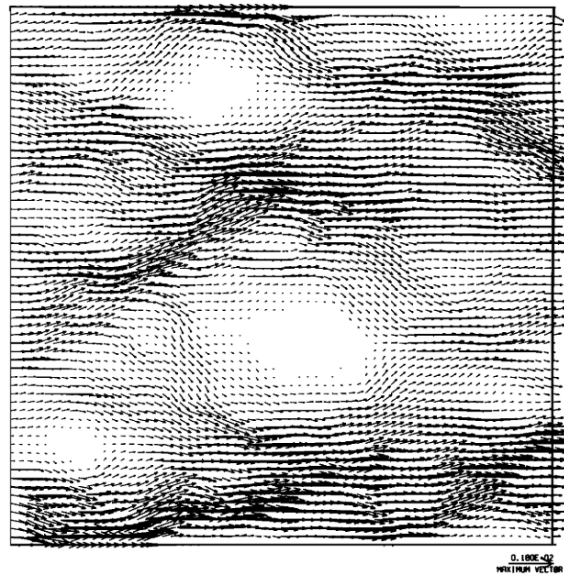


Fig.2.10 Flow through high aperture channels between contacts (Stephen, et al., 1987)

References

- Arnold, J.R., Testa, J.P.J., Friedman, P.J., Kambic, G.X.: Computed tomographic analysis of meteorite inclusions. *Science*, 219, 383-384.1982.
- Beeler, N.M., Hickman, S.H.: Stress-induced, time-dependent fracture closure at hydrothermal conditions. *Journal of Geophysical Research: Solid Earth*. 109(B2).2004.
- Bing, B., Yuanyuan, H., Xiaochun, L., Jun, L., Xiaoxue, H., Jialing, Z.: Experimental and analytical study of the overall heat transfer coefficient of water flowing through a single fracture in a granite core, *Apply. Geochemistry.*, Vol. 116, 79-90.2017.
- Caulk, R.A., Ghazanfari, E., Perdrial, J.N., Perdrial, N.: Experimental investigation of fracture aperture and permeability change within Enhanced Geothermal Systems. *Geothermics*. 62: 12-21.2016.
- Davy, C.A., Skoczylas, F., Barnichon, J.D., Lebon, P.: Permeability of macro-cracked argillite under confinement gas and water testing. *Phys Chem Earth*. Vol. 667–680, 2007.
- Dustin, C., Johnathan, M.B., Magdalena, G.B.: CT scanning and flow measurements of shale fractures after multiple shearing events. *International Journal of Rock Mechanics and Mining Sciences*. 100: 177–187.2017.
- Elkhoury, J.E., Detwiler, R.L., Ameli, P.: Dissolution and deformation in fractured carbonates caused by flow of CO₂-rich brine under reservoir conditions. *International Journal of Greenhouse Gas Control*. 16: S203-S215.2013.
- Fan, H.Z., Jian, C.G., Shou, M.: 3D observations of the hydraulic fracturing process for a model noncemented horizontal well under true triaxial conditions using an X-ray CT imaging technique. *Journal of Natural Gas Science and Engineering*. 52:128-140.2018.
- Farough, A., Moore, D.E., Lockner, D.A., Lowell, R.P.: Evolution of fracture permeability of ultramafic rocks undergoing serpentinization at hydrothermal conditions: An experimental study. *Geochemistry, Geophysics, Geosystems*. 17(1): 44-55.2016.
- Frdric, B., Frank, L., Pierre, D.C., Valr, D. :Implications of safety requirements for the treatment of THMC processes in geological disposal systems for radioactive waste. *Journal of Rock Mechanics and Geotechnical Engineering*. 9(3): 428-434.2017.
- Gerber, L., Maréchal, F.: Environomic optimal configurations of geothermal energy conversion systems: Application to the future construction of Enhanced Geothermal Systems in Switzerland. *Energy* 45(1): 908-923. 2012.
- Ghassemi, A., Kumar, G.S.: Changes in fracture aperture and fluid pressure due to thermal stress and silica dissolution/precipitation induced by heat extraction from subsurface rocks. *Geothermics*. 36: 115-140. 2007.

- Goldstein, B.A., Hill, A.J., Long, A., Budd, A.R., Holgate, F. and Malavazos, M.: Hot Rock Geothermal Energy Plays in Australia. *Proceedings of the Thirty-Fourth Workshop on Geothermal Reservoir Engineering* Stanford University, Stanford, California, February 9-11, SGP-TR-187. 2009.
- Hamed, L.R., Ryan, T., Armstrong, P.M.: Micro-CT image calibration to improve fracture aperture measurement. *Case Studies in Nondestructive Testing and Evaluation*. 6: 4–13. 2016.
- Haubitz, B., Prokop, M., Dthring, W., Ostrom, J.H., Wellnhofer, P.: Computed tomography of Archeopterix. *Paleobiology*, 14, 206-213. 1988.
- Hofmann, H., Blcher, G., Milsch, H., Babadagli, T., Zimmermann, G.: Transmissivity of aligned and displaced tensile fractures in granitic rocks during cyclic loading. *International Journal of Rock Mechanics and Mining Sciences*. Vol. 69-84, 2006.
- Hofmann, H., Blöcher, G., Milsch, H., Babadagli, T., Zimmermann, G.: Transmissivity of aligned and displaced tensile fractures in granitic rocks during cyclic loading. *International Journal of Rock Mechanics and Mining Sciences*. 87: 69-84. 2016.
- Hounsfield, G.N.: A method of and apparatus for examination of a body by radiation such as X- or gamma-radiation. *British Patent*. No 1.283.915, London. 1972.
- Hounsfield, G.N.: Computerized transverse axial scanning (tomography). Part 1: Description of system. *British Journal of Radiology*, 46, 1016-22. 1973.
- Huang, N., Jiang, Y.J., Liu, R.C., Xia, Y.X.: Size Effect on the Permeability and Shear Induced Flow Anisotropy of Fractal Rock Fractures. *Fractals*. 26(02). 2018.
- Kamali, A., Ghazanfari, E., Perdrial, N., Bredice, N.: Experimental study of fracture response in granite specimens subjected to hydrothermal conditions relevant for enhanced geothermal systems. *Geothermics*. 72: 205-224. 2018.
- Karpyn, Z.T., Grader, A.S., Halleck, P.M. Visualization of fluid occupancy in a rough fracture using micro-tomography. *Journal of Colloid and Interface Science*. 307: 181–187. 2007.
- Karpyn, Z.T., Alajmi, B.A., Radaelli, C.F. X-ray CT and hydraulic evidence for a relationship between fracture conductivity and adjacent matrix porosity. *Engineering Geology*. 103: 139–145. 2009.
- Kawakata, H., Cho, B.T., Kiyama, C.T. Three-dimensional observations of faulting process in Westerly granite under uniaxial and triaxial conditions by X-ray CT scan. *Tectonophysics*. 313: 293–305. 1999.
- Keller, A.: High resolution, non-destructive measurement and characterization of fracture apertures. *International Journal of Rock Mechanics and Mining Sciences*. 35: 1037-1050. 1998.
- Kenter, J.A.M.: Applications of computerized tomography in sedimentology. *Marine Geotechnology*, 8, 201-211. 1989.
- Ketcham, R.A., Slottke, D.T., Sharp, J.M.: Three-dimensional measurement of fractures in heterogeneous materials using high-resolution X-ray computed tomography. *Geosphere*. 6:499–514. 2010.

- Kishida, K., Sawada, A., Yasuhara, H.: Estimation of fracture flow considering the inhomogeneous structure of single rock fractures. *Soils and Foundations*. 53(1): 105-116. 2013.
- Konzuk, J. S., Kueper, B.H.: Evaluation of cubic law based models describing single-phase flow through a rough-walled fracture. *Water Resources Research*. 40(2). 2004.
- Kumaria, W.G.P., Ranjith, P.G., Pererab, M.S.A., Li, X.: Hydraulic fracturing under high temperature and pressure conditions with micro CT applications: Geothermal energy from hot dry rocks. *Fuel*. 230:138–154. 2018.
- Lang, P. S., Paluszny, A., Zimmerman, R.W.: Hydraulic sealing due to pressure solution contact zone growth in siliciclastic rock fractures. *Journal of Geophysical Research: Solid Earth*. 120(6): 4080-4101. 2015.
- Li, B., Jiang, Y.J., Koyama, T., Jing, L.R., Tanabashi, Y.: Experimental study of the hydro-mechanical behavior of rock joints using a parallel-plate model containing contact areas and artificial fractures. *International Journal of Rock Mechanics and Mining Sciences*. 45(3): 362-375. 2008.
- Lu, R., Nagel, T., Shao, H., Kolditz, O., Shao, H.B.: Modeling of Dissolution-Induced Permeability Evolution of a Granite Fracture Under Crustal Conditions. *Journal of Geophysical Research: Solid Earth*. 123(7): 5609-5627. 2018.
- Lu, X., Ryan, T., Armstrong.: High-pressure X-ray imaging to interpret coal permeability. *Fuel*. 226: 573–582. 2018.
- Mazumder, S., Wolf, K., Elewaut, K., Ephraim, R.: Application of X-ray computed tomography for analyzing cleat spacing and cleat aperture in coal samples. *Int J Coal Geol*. 68: 205–22. 2006.
- Numakura, T., Watanabe, N., Sakaguchi, K., Kikuchi, T., Tsuchiya, N.: Permeability Measurements of Fractured Granite at 350-450°C Under Confining Stress. *GRC Transactions*. Vol. 39. 2015.
- Okamoto, A., Tanaka, H., Watanabe, N., Saishu, H., Tsuchiya, N.: Fluid Pocket Generation in Response to Heterogeneous Reactivity of a Rock Fracture Under Hydrothermal Conditions. *Geophysical Research Letters*. 44(20): 10,306-310,315. 2017.
- Polak, A., Elsworth, D., Liu, J.: Spontaneous switching of permeability changes in a limestone fracture with net dissolution. *Water Resour. Res*. 40: (W03502). 2004.
- Polak, A., Elsworth, D., Yasuhara, H.: Permeability reduction of a natural fracture under net dissolution by hydrothermal fluids. *Geophysical Research Letters*. Vol. 30. 2003.
- Pruess, K. : On production behavior of enhanced geothermal systems with CO₂ as working fluid. *Energy Conversion and Management*. 49(6): 1446-1454. 2008.
- Richard, A., Ketcham, Donald, T.: Three-dimensional measurement of fractures in heterogeneous materials using high-resolution X-ray computed tomography. *Geosphere*. 2010.

- Robert, A.J., John, S.S., Louis, M.C., Paul, V.R.: Nondestructive Measurements of Fracture Aperture in Crystalline Rock Cores Using X Ray Computed Tomography. *Journal of Geophysical Research*. 98(B2): 1889-1900. 1993.
- Rutqvist, J., Wu, Y.S., Tsang, C.F.: A modeling approach for analysis of coupled multiphase fluid flow, heat transfer, and deformation in fractured porous rock. *International Journal of Rock Mechanics and Mining Sciences*. 39: 429–442. 2002.
- Stephen R. B. : Fluid flow through rock joints: The effect of surface roughness. *Journal of Geophysical Research*. 92(B2). 1987.
- Shu, B., Zhu, R.J., Tan, J.Q., Zhang, S.H., Liang, M.: Evolution of permeability in a single granite fracture at high temperature. *Fuel*, 242: 12-22. 2019.
- Stephanie, P., Bertels. David, A. Measurement of aperture distribution, capillary pressure relative permeability, and in situ saturation in a rock fracture using computed tomography scanning. *Water Resource Research*. 37(3):649-662. 2001.
- Taron, J., Elsworth, D.: Coupled mechanical and chemical processes in engineered geothermal reservoirs with dynamic permeability. *International Journal of Rock Mechanics and Mining Sciences*. 47(8): 1339-1348. 2010.
- Tester, J.W., Anderson, B.J., Batchelor, A.S.: The Future of Geothermal Energy Impact of enhanced Geothermal Systems (EGS) on the United States in the 21st Century. *Massachusetts Institute of Technology*. Accessed April 25.04.16. 2006.
- Tsang, C.F., Barnichon, J.D., Birkholzer, J.: Coupled thermo-hydro-mechanical processes in the near field of a high-level radioactive waste repository in clay formations. *International Journal of Rock Mechanics and Mining Sciences*. 49: 31-44. 2012.
- Van, G. M., Swennen, R., David, P. :Quantitative coal characterisation by means of microfocus X-ray computer tomography, colour image analysis and back-scattered scanning electron microscopy. *Int J Coal Geol*. 46:11–25. 2001.
- Wang, Y.: On subsurface fracture opening and closure. *Journal of Petroleum Science and Engineering*. 155: 46-53. 2017.
- Watanabe, N., Hirano, N., Tsuchiya, N.: Diversity of channeling flow in heterogeneous aperture distribution inferred from integrated experimental-numerical analysis on flow through shear fracture in granite. *J Geophys Res*. 114, 2009.
- Xu, P., Yang, S.Q.: Permeability evolution of sandstone under short-term and long-term triaxial compression. *International Journal of Rock Mechanics and Mining Sciences*. 85: 152-164. 2016.
- Yao, Y.B., Liu, D.M., Che, Y.: Non-destructive characterization of coal samples from China using microfocus X-ray computed tomography. *International Journal of Coal Geology*. 80: 113–123. 2009.
- Yao, Y., Liu, D., Che, Y.: Non-destructive characterization of coal samples from China using microfocus

- X-ray computed tomography. *Int J Coal Geol.* 80:113–23. 2009.
- Yasuhara, H., Kinoshita, N., Ohfuji, H., Lee, D.S., Nakashima, S., Kishida, K.: Temporal alteration of fracture permeability in granite under hydrothermal conditions and its interpretation by coupled chemo-mechanical model. *Applied Geochemistry.* 26: 2074-2088. 2011.
- Yasuhara, H., Kinoshita, N., Ohfuji, H., Takahashi, M., Ito, K., Kishida, K.: Long-term observation of permeability in sedimentary rocks under high-temperature and stress conditions and its interpretation mediated by microstructural investigations. *Water Resources Research.* 51(7): 5425-5449. 2015.
- Yasuhara, H., Polak, A., Mitani, Y., Grader, A.S., Halleck, H.P., Elsworth, D.: Evolution of fracture permeability through fluid-rock reaction under hydrothermal conditions. *Earth Planet Sci. Lett.* 244: 186-200. 2006.
- Yasuhara, H., Elsworth, D.: Evolution permeability in a natural fracture: significant role of pressure solution. *J. Geophys. Res.* (B03204); 109. 2004.
- Zhang, C., Liu, X., Liu, Q.: A thermo-hydro-mechano-chemical formulation for modeling water transport around a ventilated tunnel in an argillaceous rock. *Journal of Rock Mechanics and Geotechnical Engineering.* 5(2): 145-155. 2013.
- Zimmerman, R.W., Bodvarsson, G.S.: Hydraulic conductivity of rock fractures. *Transport in Porous Media*, Vol. 23:1-30. 1996.
- Zimmermann, G. Pressure-dependent Production Efficiency of an Enhanced Geothermal System (EGS): Stimulation Results and Implications for Hydraulic Fracture Treatments. *Pure and Applied Geophysics.* 166(5-7): 1089-1106. 2009

Chapter 3 Long-term Observation of Hydraulic Aperture and Permeability Change under Various Conditions

3.1 Introduction

Permeability within the rock mass in long-term has a great effect on the system of geothermal, radioactive wastes isolation and petroleum reservoirs (e.g., Yasuhara et al., 2006; Ellis et al., 2013; Fridleifsson et al., 2001; Guo et al., 2018; Hooijkaas et al., 2006; Zhang et al., 2014). The permeability evolution of the fractured rock under the THMC coupled processes of the fractured rock had been studied by a few of researchers (e.g., Beydoun et al., 1985; Paillet, 1985; Noorishad et al., 1982; Long et al., 1985; Gamdi, 1978; Kranz et al., 1979; Tsang and Witherspoon, 1981; Schrauf and Evans, 1986). However, the changes of the permeability within the rock fractures under coupled conditions is a significant problem that is not completely resolved. Several previous experimental works were conducted to verify the long-term permeability performance of the fractured rock samples (e.g., Lang et al., 2015; Neretnieks, 2014; Taron & Elsworth, 2010b). Permeability evolution was controlled by long-term fluid flow within the fractured rocks. The effects of the fracture contacts and the fracture channel distributions are undergoing several complexed conditions which have not been fully understood. Therefore, how to quantitative represent the permeability and the fracture aperture variation through the laboratory work is a difficult problem. A few researchers conducted the permeability change in the long-term. (e.g., Yasuhara et al., 2011; Ishikawa, 2015), as shown in **Fig.3.1**. (a) (c) represent the short-term permeability tests. Hydraulic conductivity and permeability are confirmed to have a reversible behavior against the confining pressure. Moreover, it can be observed that hydraulic conductivity decreased with increasing temperature. In **Fig.3.1 (c)**, permeability recovered to the initial value after unloading the confining pressure to 1.0 MPa (i.e., $6.0 \times 10^{-12} \text{ m}^2$). It is inferred that the permeability is sensitive to the confining pressure. Mechanical influence at these two different tests is remarkable. In contrast, long-term permeability tests were depicted in **Fig.3.1 (b) and (d)**. **Fig.3.1 (b)** shows two different long-term permeability tests at 20 and 90 °C. Long-term permeability tests at 20 and 90 °C were conducted under the constant confining stress of 10.0 MPa about 35 days, 18 days, respectively. Permeability at 20 °C showed reversible behavior after unloading the confining pressure after 35 days. However, irreversible behavior of the permeability occurred at 90 °C after unloading the confining pressure. **At Fig.3.1 (d)**, another long-term permeability test around 100 days at 20 °C showed a random variation.

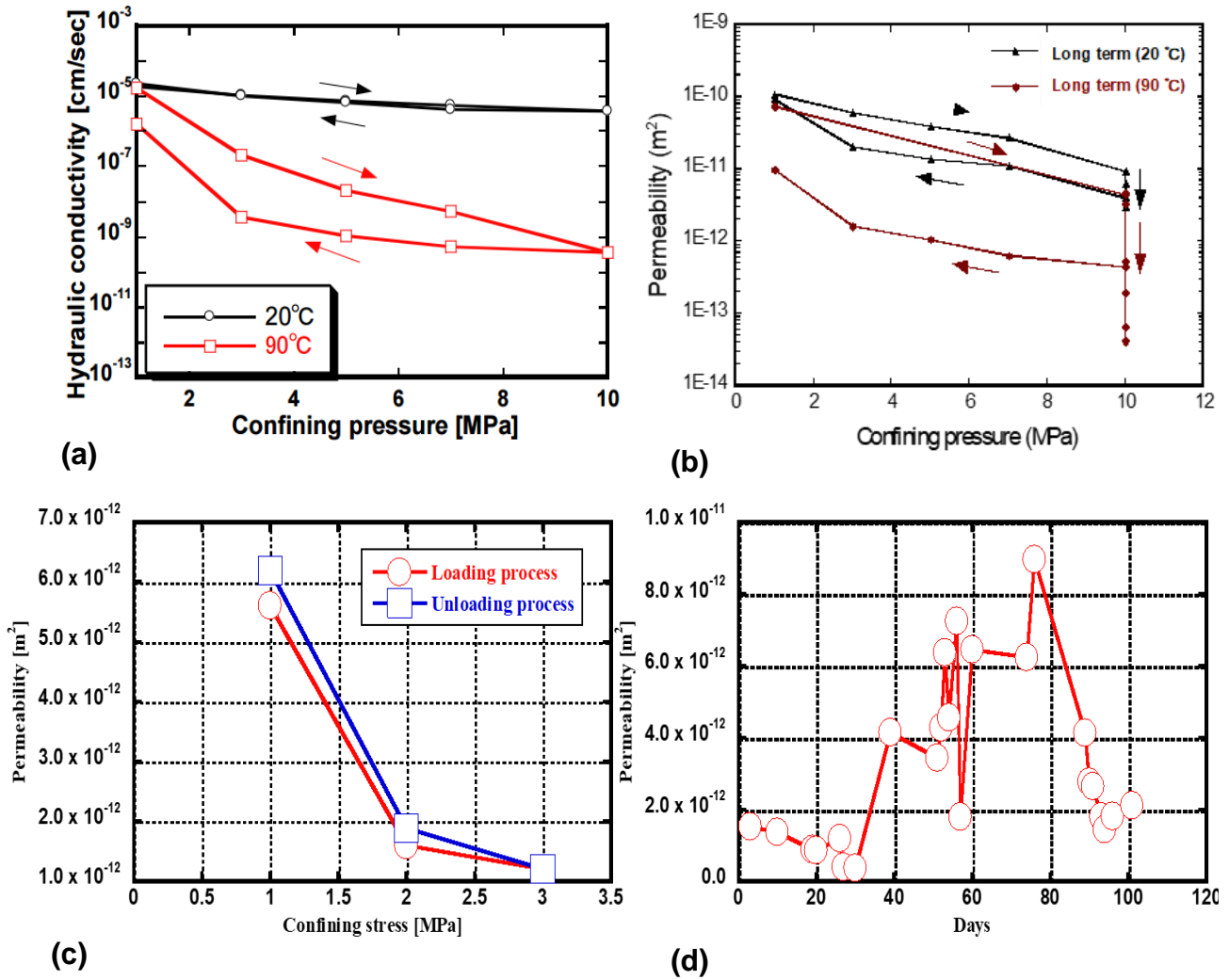


Fig 3.1 Short- and long-term permeability performance under various conditions. (a),(c) short-term permeability tests. (b),(d) long-term permeability tests. (Yasuhara et al 2010) (Ishikawa,2015)

From **Fig 3.1** it is noted that permeability variation is irregular, and internal fracture geometrical change is undiscovered with a thermal influence. In order to further check the long-term permeability evolution under various conditions, Yasuhara et al. (2006, 2015) conducted several long-term permeability tests by using different types of rock samples. (i.e., single fracture of novaculite, intact and fractured sandstone samples), as shown in **Fig. 3.2**. At (a), permeability decreased at first 1300 hours; aperture closed indicates that the internal contact area became larger after 1200 hours testing. Then permeability began to increase after 1200 hours. Mineral dissolution on the fracture surfaces and the free-face dissolution resulted in a different change of the aperture. Permeability did not show a monotonous variation. Moreover, permeability did not decrease monotonously at a higher temperature. (b) showed a long-term permeability result through using a fractured sandstone. At room temperature, permeability showed an obvious reduction after several hundred days. However, at 90 °C permeability increase could be seen obviously after several hundred days. It was almost higher than the permeability value at 20 °C.

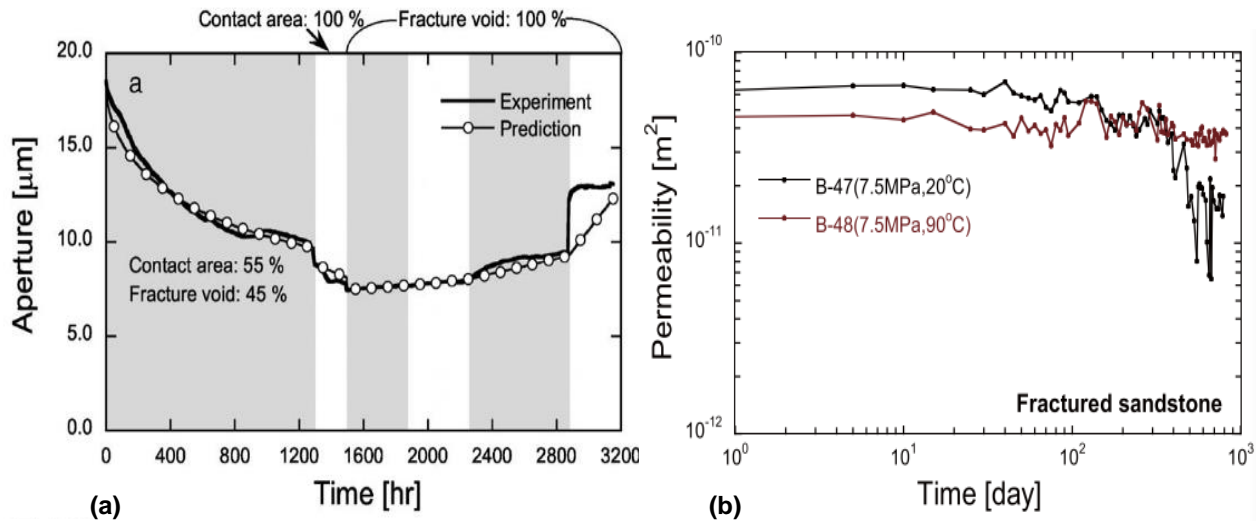


Fig.3.2 Long-term permeability performance under different conditions. (a) long-term permeability test about 3200 hours; (Yasuhara et al.2006) (b) long-term permeability test about 800 days (Yasuhara et al. 2015)

In general, permeability evolution in a long-term under coupled conditions is uncertain. The kernel of the current stage is to verify what altered the permeability change. Therefore, experimental studies in this Chapter focus on several permeability tests under different conditions at different times. (i.e., short- and long term). Granite sample with a single rock fracture was used. Several permeability variations were observed under coupled conditions. Simultaneously, internal aperture change, i.e., open or closed at pre- and post-experiment were checked. Moreover, fracture geometry is considered to be altered by chemical reaction. Therefore, The effluent extracted from the internal granite fracture was checked after each permeability test. Mineral composition results were also used to verify the permeability change with time. The reason for the hydraulic properties variation of a single granite fracture at different period was discussed.

3.2 Materials and experimental setup

In this study, several permeability tests were performed under various conditions over both short- and long terms. Permeability and hydraulic aperture at three different temperatures (i.e., 20, 60, and 90 °C) were compared. Moreover, microfocus X-ray CT was utilized to observe the aperture change of the tested sample. A CT scan was conducted at the pre-experiment. After two long-term permeability tests, the granite specimen was taken out from the triaxial cell and was scanned again as a comparison with the CT image of pre-experiment.

In this study, two cylindrical granite samples, Sample #1 and Sample #2, with a size of 49.3×101.2 mm and 15.2×33.3 mm, respectively, were employed in this study (**Chapter 3** used the Sample #1, **Chapter 4** used the Sample #2). An optical profilometer was employed, using the pattern projection method (VR-3200, Keyence Corporation in Japan), to grasp the morphology of the fracture surfaces. The

profilometer is capable of measuring the surface roughness in a grid pattern through non-contact. The grid size of the elevation measurement is 25 μm and the measurement resolution of the profilometer is 0.1 μm . The color contour maps of the fracture roughness surface morphology is shown in **Fig. 3.3**. Sample #1 was employed for the permeability tests, while sample #2 was primarily used for the X-ray CT observation (in **Chapter 4** will further explain). The granite material is the same. Before the experiments, both samples were split into halves by the Brazilian tensile testing method to create a single fracture along the cylinder axis (Fairurst C. 1964). The mechanical properties of the granite specimens are listed in **Table 3.1**. Moreover, initial granite roughness surface information at pre-experiments was evaluated by the JRC values.

Table 3.1 Mechanical properties of granite specimen

Specimen	Uniaxial compression strength (MPa)	Young's modulus (GPa)	Poisson's ratio	Tensile strength (MPa)
Granite	140.3	55.4	0.2	6.2

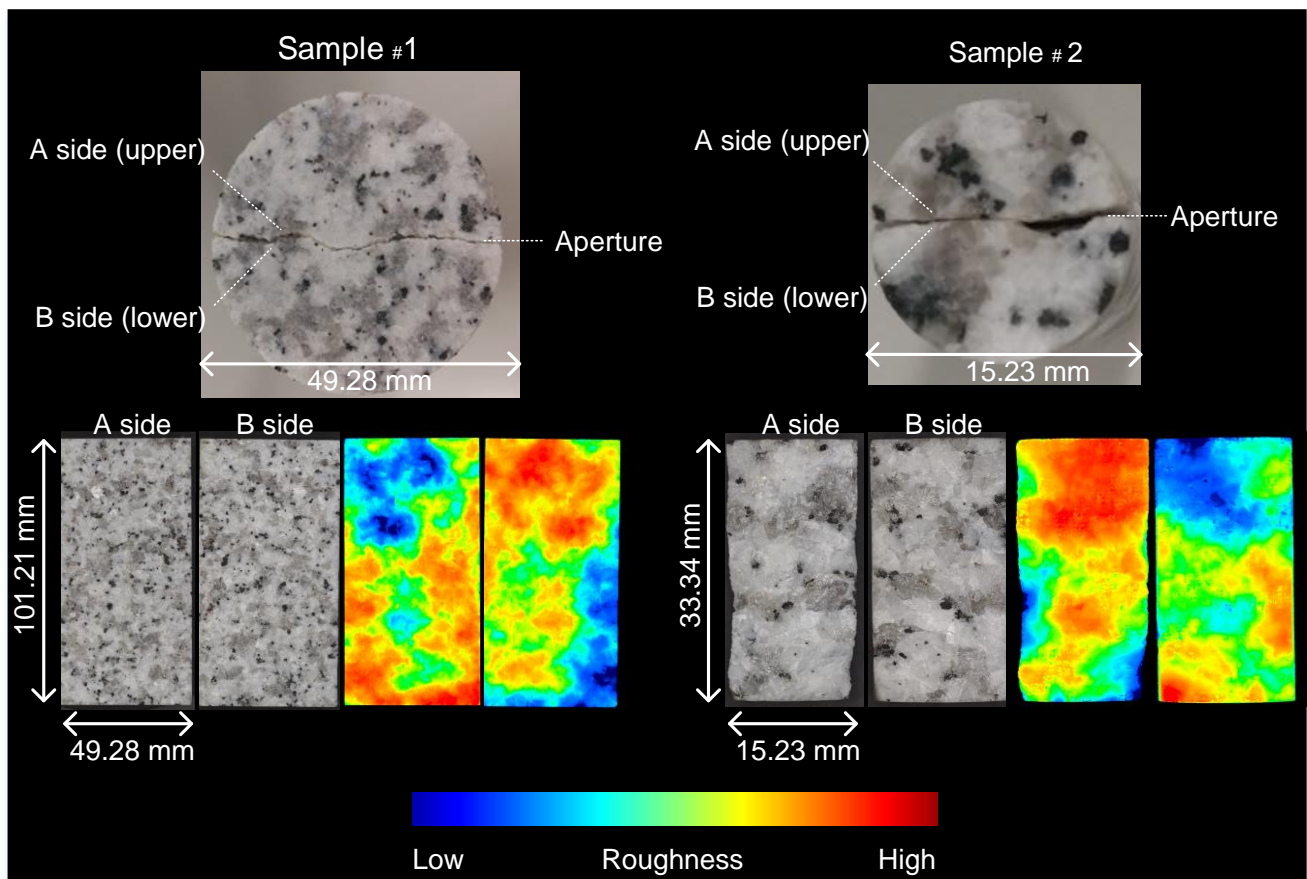


Fig.3.3 Sample experiments and fracture surfaces measured by laser profilometer

In order to clarify the variation in surface roughness, it is necessary to grasp the surface roughness precisely before starting the experiments. Barton's standard of JRC (Joint Roughness Coefficient) profiles was selected as the comparison index. Typically, the JRC value ranges from 0 to 20 in shear behavior of

the rock joints. The JRC values can be calculated with the dimensionless parameter Z_2 which has been widely discussed and is defined as follows (e.g., Barton N et al., 1977.1997; Tse R et al., 1979; Zhang et al.,2014; Dimadis et al.,2014; Yong et al.,2017; Yin et al., 2017):

$$Z_2 = \left[\frac{1}{M-1} \sum_{i=1}^{M-1} \left(\frac{\Delta y}{\Delta x} \right)_i^2 \right]^{\frac{1}{2}} \quad (3.1)$$

where Δx is the sampling interval, Δy is the difference between two adjacent points and M is the number of sampling points along the length of the fracture surface. Subsequently, the JRC values can be evaluated by

$$JRC = 60.32Z_2 - 4.51 \quad (\Delta x = 0.25mm) \quad (3.2)$$

Table 3.2 lists the Z_2 and JRC values for both surfaces of Samples #1 and #2. The obtained JRC values for the two specimens are around 20. The initial values were used to evaluate the difference in the roughness surface between the pre- and post-experiment.

Table 3.2 Comparison of Z_2 and JRC values with profilometer equipment (VR-3200)

	(JRC=60.32* Z_2 -4.51) 0.25 mm	
	A side	B side
Sample #1	19.9	20.2
Sample #2	22.8	20.4

Granite Sample #1 was installed with thermal insulation. A membrane around the granite sample was applied to avoid the thermal damage and leakage, as depicted in **Fig.3.4**. Then the sample was fixed into the triaxial cell under the water-saturated condition as shown in **Fig.3.5**. The maximum pressure and temperature of this triaxial cell that can be prescribed are 20.0 MPa and 200°C, respectively. The granite core was sealed with a heat-shrinkable tube and fixed to pedestals inside the vessel. A thermo-couple was installed to measure the temperature close to the sample. Two water storage tanks supply water that passes through Sample #1. Differential pore water pressure gauges were used to measure the difference in pressure between the upstream and the downstream. Moreover, a small water bottle (at the under of the triaxial cell) was used to storage the effluent which generated from water flow through the internal fracture after each permeability test. The mineral composition will be measured and checked from the effluent at each time. Distilled water was employed as the injection fluid in this experiment in order to accuracy obtain the mineral composition variation in a long-term.

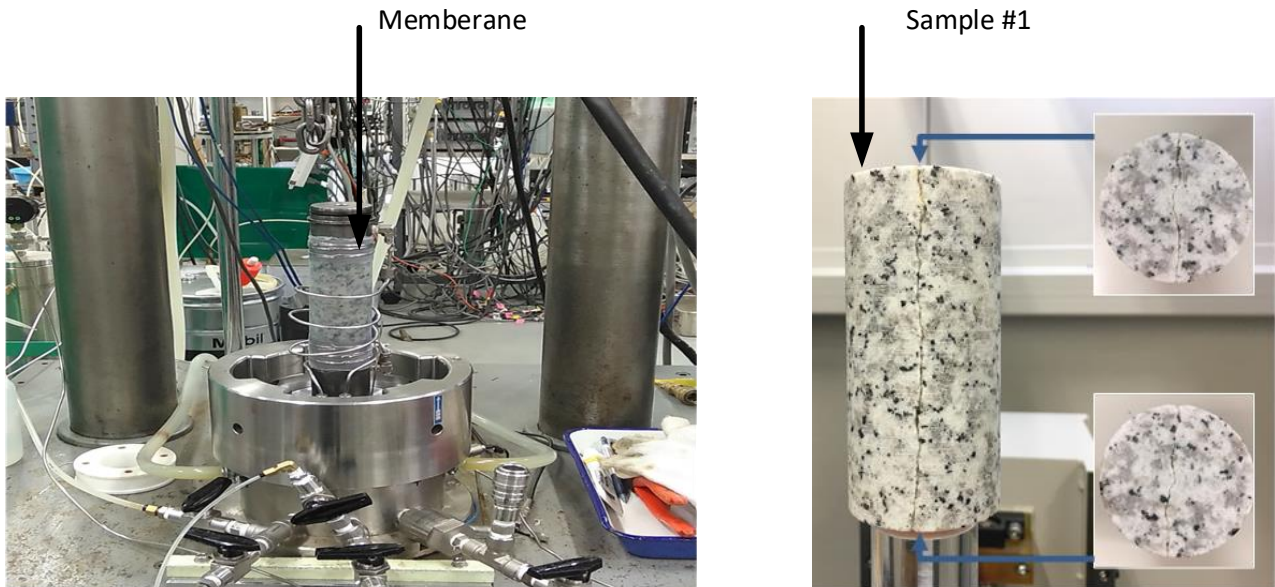


Fig.3.4 Sample #1 was set into the triaxial cell

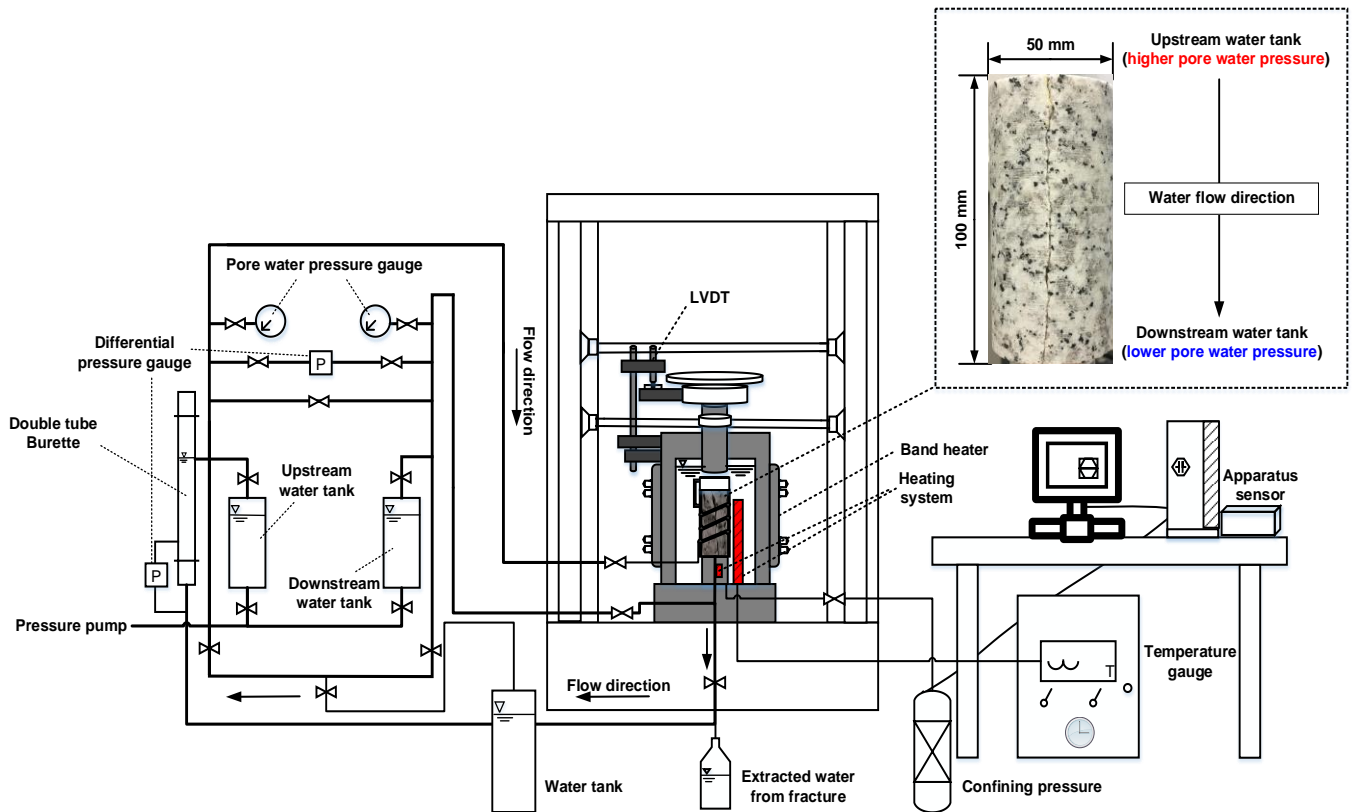


Fig.3.5 Triaxial apparatus. The upstream and downstream pore water pressures are prescribed to the top and bottom of Sample #1, respectively.

3.3 Methodology

To accurately investigate the permeability evolution under various conditions, the transient pulse method (Hsieh et al., 1981) was applied to measure the permeability. Which is suitable for grasping the

permeability coefficient of a single fracture. Two water tanks (i.e., volume is bigger than the sample) are connected with the upper and lower of the rock sample, which produce different pore water pressure, as shown in Fig. 3.6. Then the water pressure difference will generate a one-dimensional water flow. After several seconds, the water pressure will reach a parallel state value under a pressure curve, as illustrated in Fig. 3.7. Simultaneously, the permeability coefficient can be calculated with a linear relationship of the time and a water pressure difference.

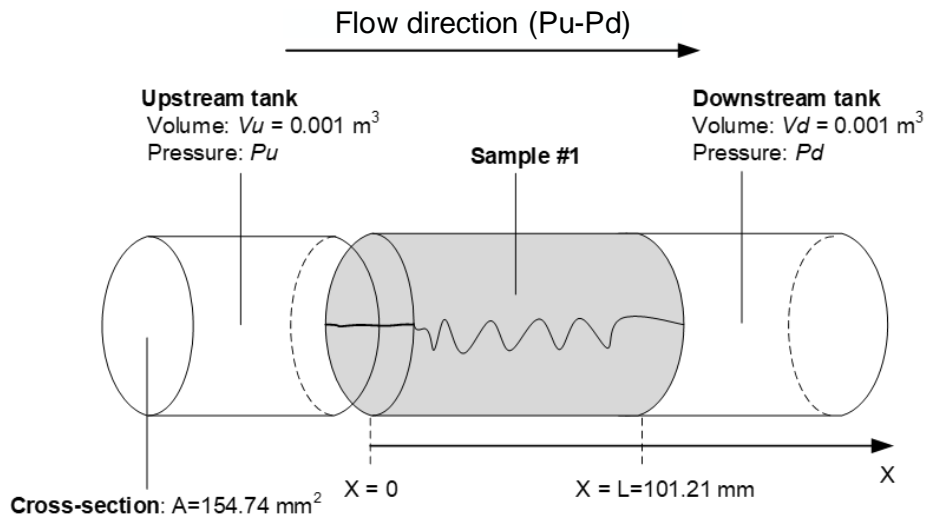


Fig.3.6 Schematic information of the transient pulse method (Sample #1 physical information)

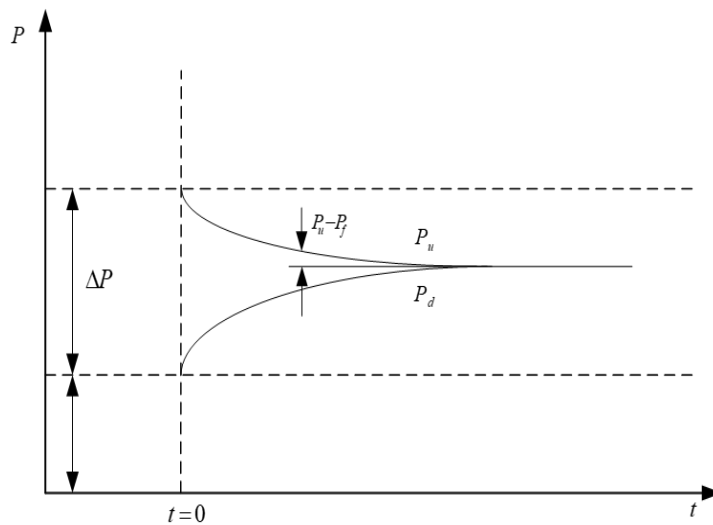


Fig.3.7 Conception of the pressure decrement curve (transient pulse method)

Transient pulse test was explained as follows: the water pressure gradient is generated between the two ends of the sample, then the single phase fluid flow through the sample. The initial boundary condition, i.e., to combine the Darcy's law with mass preservation rules, is written in (3.3)~(3.10). Moreover, fluid compressibility depends on the fluid pressure under different temperatures.

(initial condition)

$$\frac{\partial^2 P}{\partial x^2} - \left(\frac{\mu\beta}{k} \right) \left[\frac{\beta_{eff} - \beta_s}{\beta} + \eta \left(1 - \frac{\beta_s}{\beta} \right) \right] \left(\frac{\partial P}{\partial t} \right) = 0 \quad (3.3)$$

(critical condition)

$$P(x,0) = P_d^0 \quad (3.4)$$

$$P(0,t) = P_d \quad (3.5)$$

$$P(L,t) = P_u \quad (3.6)$$

$$\beta V_d \frac{dP_d}{dt} + A \frac{k}{\mu} \frac{\partial P}{\partial x} \Big|_{x=0} = 0 \quad (3.7)$$

$$P(0,0) = P_d^0 \quad (3.8)$$

$$\beta V_d \frac{dP_d}{dt} + A \frac{k}{\mu} \frac{\partial P}{\partial x} \Big|_{x=L} = 0 \quad (3.9)$$

$$P(l,0) = P_u^0 \quad (3.10)$$

From (3.3), (Brace et al.,1968) mentioned that the pore volume of the permeable fractured rock is generally smaller than the external storage tanks. The rate of fluid compressibility β is larger than the compressibility of mineral particles. Then the compressibility of the whole specimen is written as:

$$\frac{\beta_{eff} - \beta_s}{\beta} + \eta \left(1 - \frac{\beta_s}{\beta} \right) = 0 \quad (3.11)$$

Therefore, (3.3) is written as:

$$\frac{\partial^2 P}{\partial x^2} = 0 \quad (3.12)$$

From (3.7) and (3.8), upper and lower water pressures are written in (3.13):

$$\begin{aligned} \frac{dP_d}{dt} &= \frac{k}{\mu} \frac{A}{V_d \beta} \frac{P_u - P_d}{L} \\ \frac{dP_u}{dt} &= -\frac{k}{\mu} \frac{A}{V_u \beta} \frac{P_u - P_d}{L} \end{aligned} \quad (3.13)$$

The pore water pressure between upstream and downstream in Eq. (3.14) is different. Upstream pressure is increased by the operator in a tiny increments of inject water. Then the permeability is measured by the pressure gradient generated between two ends of the specimen changes with the lapse of time. The pressure difference will reach a new equilibrium, given as follows:

$$\begin{aligned} P_d &= \frac{V_u P_u^0 + V_d P_d^0}{V_u + V_d} - \frac{V_u}{V_u + V_d} (P_u^0 - P_d^0) \exp \left(-\frac{k}{\beta \mu} \frac{A}{L} \frac{V_u + V_d}{V_u V_d} t \right) \\ P_u &= \frac{V_u P_u^0 + V_d P_d^0}{V_u + V_d} - \frac{V_d}{V_u + V_d} (P_u^0 - P_d^0) \exp \left(-\frac{k}{\beta \mu} \frac{A}{L} \frac{V_u + V_d}{V_u V_d} t \right) \end{aligned} \quad (3.14)$$

Where P_u and P_d are the upstream and downstream pressure, respectively, and V_u and V_d are the volume of two reservoirs (0.001 m³ in this study). A and L are the cross-section and the length of the specimen, respectively, as shown in **Fig.3.6**. μ is the viscosity of the fluid and β is the fluid compressibility, η is porosity, β_{eff} is rock effective compressibility, β_s is compressive modulus of minerals. μ and β are temperature-dependent (Bandis et al., 1985). From $P_d = P_u = \frac{V_u P_u^0 + V_d P_d^0}{V_u + V_d}$, it can be noted that $P_f = \frac{V_u P_u^0 + V_d P_d^0}{V_u + V_d}$. Then the difference between P_f and P_d, P_u is written as (3.15) :

$$\begin{aligned} \ln(P_f - P_d) &= \ln\left(\frac{V_u}{V_u + V_d}(P_u^0 - P_d^0)\right) - \frac{k}{\beta\mu} \frac{A}{L} \frac{V_u + V_d}{V_u V_d} t \\ \ln(P_u - P_f) &= \ln\left(\frac{V_d}{V_u + V_d}(P_u^0 - P_d^0)\right) - \frac{k}{\beta\mu} \frac{A}{L} \frac{V_u + V_d}{V_u V_d} t \end{aligned} \quad (3.15)$$

From (3.13), the upper and lower water pressure is transforming with time. Since $(P_u + P_d)/2 = P_f$, Eq. (3.15) is as follows:

$$\ln((P_u - P_d)/2) = \ln\left(\frac{V_d}{V_u + V_d}(P_u^0 - P_d^0)\right) - \frac{k}{\beta\mu} \frac{A}{L} \frac{V_u + V_d}{V_u V_d} t \quad (3.16)$$

$$\alpha = -\frac{k}{\beta\mu} \frac{A}{L} \frac{V_u + V_d}{V_u V_d} \quad (3.17)$$

In Eq. (3.17), A represents the cross-sectional area of the sample. Since the fluid only paths through the aperture, then the cross-section A should be changed as $A=b \times W$, where W is the width of the sample and b is the hydraulic aperture. Consequently, Eq. (3.17) is rewritten as:

$$\alpha = -\frac{b^3}{12\beta\mu} \frac{W}{L} \frac{V_u + V_d}{V_u V_d} \quad (3.18)$$

3.4 Testing process

A series of permeability tests was conducted over both short and long terms to observe the temporal change of permeability. The temperature was set as 20,60 and 90 °C. Short-term permeability tests were conducted about six days; long-term tests were conducted about 180 days at 20 and 60 °C, and 120 days at 90 °C. The temporal change of permeability within the fracture was observed. After finishing the second long-term permeability test (i.e., around 360 days) at 60 °C, X-ray CT was utilized to scan the fracture aperture variation to verify the aperture change. CT image after 60 °C was compared with the pre-experiment CT scan image at 20 °C. Moreover, the temperature was increased as a stepwise of every 5 °C until 90 °C.

3.4.1 Short-term permeability test conditions

At first, short-term permeability tests were carried out at three different temperatures as illustrated in Fig. 3.8. Three cycles of loading-to-unloading confining pressure processes were performed at each temperature. Aperture will become much closed after the short-term permeability tests. At the loading process of a cycle, confining pressure was increased from 1.0 to 3.0 MPa as a step increment of 0.5 MPa. Permeability test was measured at each point of confining pressure. At unloading process, decreased the confining pressure at a stepwise to 1.0 MPa, and measured the permeability. At each test point, permeability was conducted five times. Then the average value of permeability at five times was chosen. Moreover, pore water pressure value was changed with the confining pressure, as the test conditions listed in Table 3.3. Fluid viscosity and fluid compressibility were depended on different temperatures (i.e., 20, 60 and 90 °C). The test process will be repeated three times at each temperature. After the short-term permeability performance, long-term permeability tests will be conducted after reducing the temperature to 20 °C and under a constant confining pressure of 3.0 MPa.

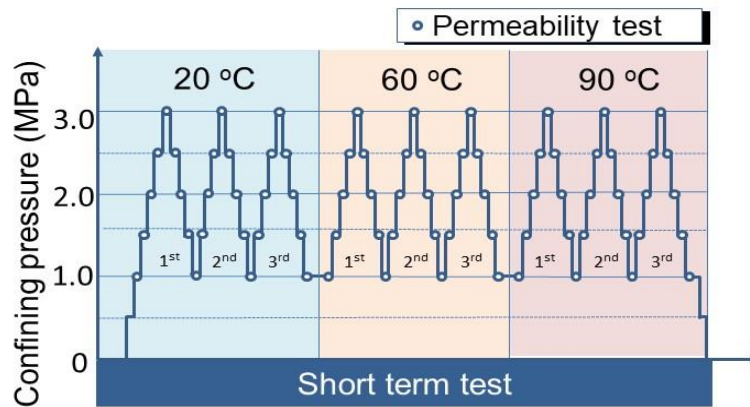


Fig. 3.8 Schematic of the process of the short-term permeability tests

Table 3.3 Permeability experimental conditions

Confining pressure (MPa)	1.0	1.5	2.0	2.5	3.0
Pressure at upstream tank (MPa)	0.200	0.250	0.300	0.350	0.400
Pressure at downstream tank (MPa)	0.150	0.175	0.200	0.225	0.250
Fluid viscosity (10^{-10} Pas)	1.0017 (T=20 °C)	0.467 (T=60 °C)	0.0328 (T=90 °C)		
Compressibility (10^{-3} Pa)	4.5883 (T=20 °C)	4.3 (T=60 °C)	4.6 (T=90 °C)		

3.4.2 Long-term permeability test conditions

Long-term permeability tests were conducted as the same temperature conditions with short-term tests (i.e., 20, 60, and 90 °C). After the short-term test, the confining pressure was unloaded to 1.0 MPa, and the temperature was reduced to 20 °C. Then the confining pressure was reloaded to 3.0 MPa again. First, long-term permeability test was performed under a constant confining pressure of 3.0 MPa, 180 days. Permeability value was measured aperiodically. After each permeability test, the effluent which was extracted from the internal aperture which was used to check the mineral components. After finishing the

long-term permeability test at 20 °C, unloaded the confining pressure to 1.0 MPa as a stepwise. Simoutenously, permeability was conducted at each confining pressure point. Long-term permeability variation at 20 °C was compared with a previous study, which showed that the permeability had a reversible behavior after 35 days.

Second, long-term test at 60 °C was performed. The confining pressure was reloaded to 3.0 MPa again, and temperature was increased every 5 °C from 20 °C to 60 °C. Long-term permeability at 60 °C was performed as the same process with at 20 °C. Moreover, the effluent was checked at each permeability test. After finishing the second test, the sample was taken out from the triaxial cell due to the membrane destroyed by thermal influence. Microfocus X-ray CT was used to grasp the aperture variation after two long-term tests. CT image of aperture and aperture value at pre-(i.e., before starting long-term test at 20 °C) and post-experiment (i.e., after finishing long-term test at 60 °C) were compared. Third, after CT observation, the sample was reset into the cell, and the temperature was increased as a stepwise to 90 °C. Permeability test at 90 °C was conducted about 120 days. A schematic of three long-term permeability tests is depicted in **Fig.3.9**. Permeability value was measured aperiodicity. i.e., each test point.as illustrated in **Fig.3.9**.

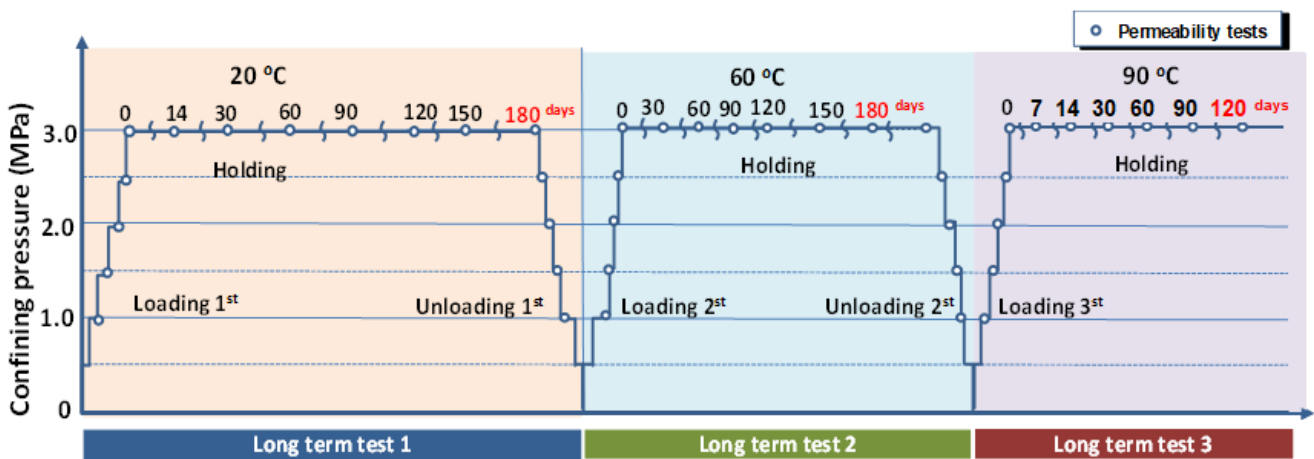


Fig.3.9 Schematic of the process of the everal long-term permeability tests

3.5 Permeability experiment results

3.5.1 Short-term permeability test results

The pore water pressure difference between upper and lower of the Sample #1 was generated a slight pressure change, and then the upstream and downstream water pressure reached to a pressure constant value after a few seconds. The temporal change of the pressure difference elapsing with time (i.e., 600 seconds) is illustrated in **Fig.3.10**. **Fig.3.11** shows a relation between the water pressure difference and elapsed time. Then the permeability value was measured from this linear relationship between them.

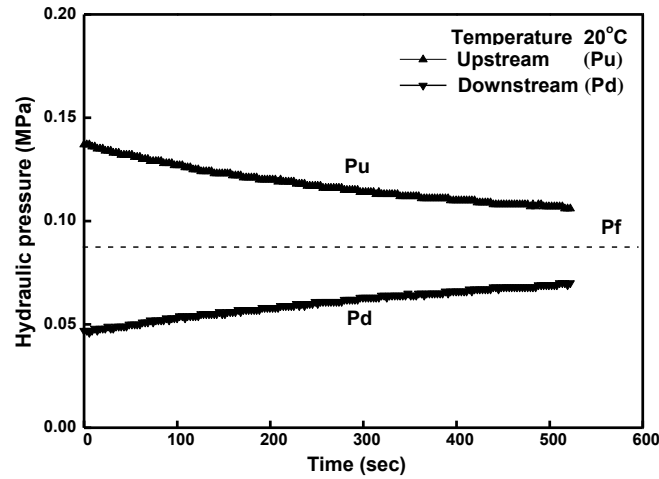


Fig. 3.10 Temporal change of the upstream and downstream water pressures during the permeability test

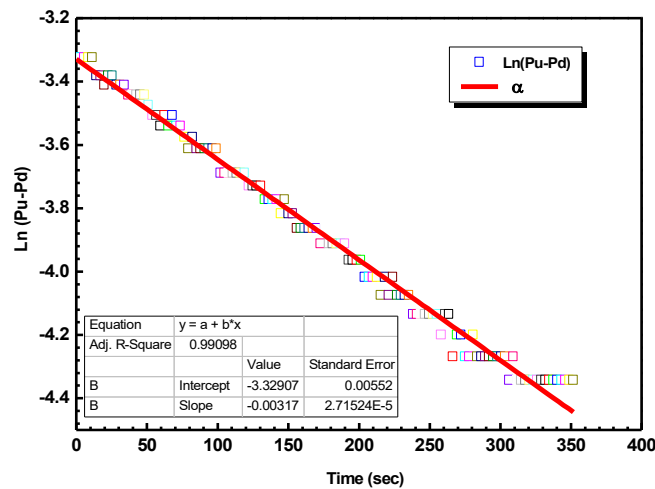


Fig.3.11 A linear relationship between the logarithm of water pressure difference and time (i.e., $\ln(P_u - P_f)$ and t)

Short-term permeability variation under different conditions as illustrate in **Fig. 3.12**. Right and left arrows are loading and unloading processes of the confining pressure, respectively. At 20 °C (**Fig. 3.12 (a)**), First, permeability has a large increase at the first cycle. It can be noted that the fractures may be ill-mated, and the matedness is improved after the first cycle. At 2nd and 3rd cycle, permeability sensitive to the confining pressure and elastic deformation was observed. Result shows that permeability has a slight transformation, and it is not obvious like the first cycle. Permeability had a bit change at 2nd and 3rd cycle. It can be supposed that fracture aperture became closed after this compaction process. Second, at 60 and 90 °C as shown in **Fig.3.12 (b)** and **(c)**, similar changes (i.e., permeability reversible behavior were observed at 20 °C) of the permeability are confirmed. Results indicate that mechanical compaction has a significant effect on the permeability change. Permeability also performed sensitive to the confining pressure, although the temperature was increased. Moreover, permeability also shows a intense temperature-dependence; it decreases with increasing the temperature. **Fig. 3.12 (d)** shows a permeability variation comparison. The 3rd cycle of the permeability values at different temperatures were selected. At

90°C, permeability decreased from 10^{-12} to 10^{-14} m², permeability value is much smaller than at 20 and 60 °C. It is inferred that thermal expansion may enlarge the fracture contact area and then induced aperture decrease. Moreover, fracture geometry was altered under coupled processes. It will lead to the flow behavior and hydraulic properties change under various conditions. Moreover, other potential factors, such as pressure solution or geochemical responses, may function against the mechanical deformation and induce irreversible permeability behavior (e.g., Yasuhara et al.,2004, 2011,2016, 2015; Polak et al.,2003,2004).

Third, it is clarified that mechanical deformation and temperature dependence are the main reasons that induced the permeability evolution. Pressure solution and chemical reaction generated at fracture contact-area are supposed. Permeability is sensitive to the mechanical and temperature variation at short-term tests.

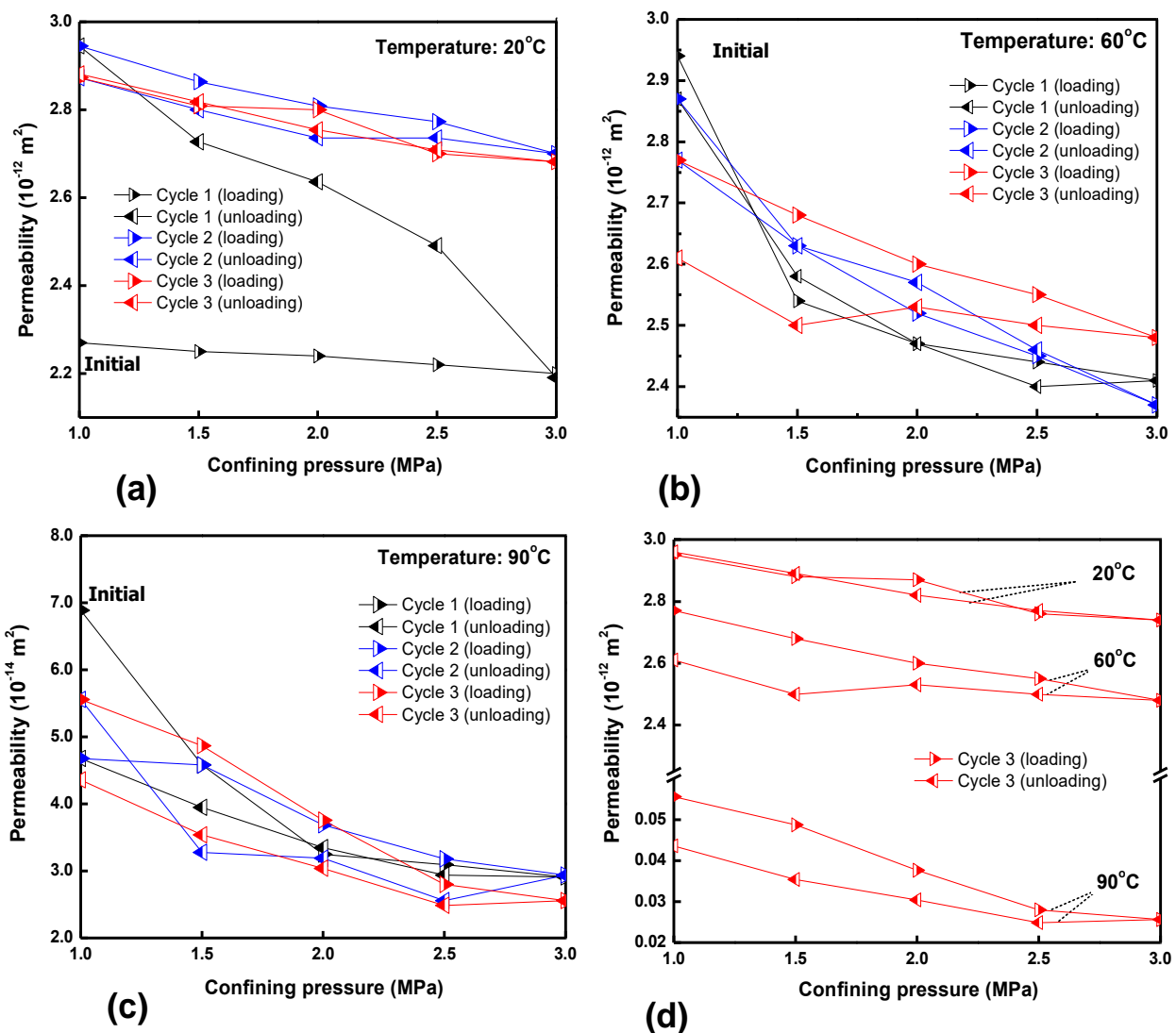


Fig.3.12 Short-term permeability test results: (a) permeability variation at 20°C, (b) permeability variation at 60°C, (c) permeability variation at 90°C and (d) permeability variation in 3rd cycle under different temperature conditions

3.5.2 Long-term permeability test results

Three different long-term permeability tests were conducted under the constant confining pressure of 3.0 MPa. At first, compared with the short-term test at 90°C, permeability increased after the temperature decreased from 90 to 20 °C (i.e., after finishing the short-term permeability tests). Permeability increased from $4.36 \times 10^{-14} \text{ m}^2$ to $4.18 \times 10^{-13} \text{ m}^2$. This change is attributed to the increase in pore volume due to the temperature decrease. Permeability temporal change in 180 days is shown in **Fig. 3.13**. The initial permeability at 0 days is $3.7 \times 10^{-13} \text{ m}^2$. It dropped sharply within several days and decreased about 45 % of the initial value. This change can be interpreted as the mechanical compaction changing the permeability. The hydraulic aperture became narrower at the initial time can be confirmed. Subsequently, the permeability resumed its decrease after a short stable period. The permeability decreased to 87% of the initial value between 30 and 120 days. Creep deformation might lead to the reduction in permeability when the fluid passes through a stressed fracture. From 120 to 180 days, the permeability shows a slight increase. At the end of the 180-day test, the permeability value was $7 \times 10^{-14} \text{ m}^2$. It can not be easily explained the reason for the permeability increase. But the decreasing tendency at the whole test can be confirmed. After 120 days, permeability increase may due to the mineral changing on the fracture surface during the fluid flowing through the aperture at each time. As the possibility of the mineral dissolution from the free-surface of the fracture-wall, the fracture aperture might be enlarged (Yasuhara.et.al. 2004). And the fluid flow pass way became larger to let the fluid pass, then the permeability value might be slightly increased as this result showed.

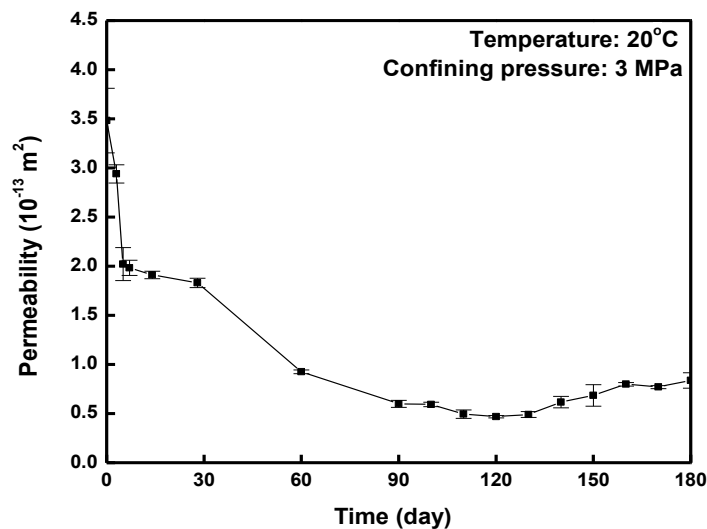


Fig.3.13 Permeability variation with time (Sample #1), 20 °C,180 days

After finishing the long-term test at 20 °C, the confining pressure was unloaded to 1.0 MPa. Permeability variation at a long cycle of the loading-to-unloading confining pressure process is shown in **Fig. 3.14 (a)**. The irreversible change of the permeability was observed between the onset and the end of the test, which is incongruous with the observation made by Yasuhara et al. (2013) as shown in **Fig.3.14**

(b). (i.e., Their long-term permeability test was conducted under a constant confining pressure of 10.0 MPa at 20 °C for 35 days). In this previous research, the permeability value after a long-term keeping period of 35 days showed a reversible behavior.

The long-term permeability test at 20 °C and 180 days is supposed that the propping asperities of the fracture surfaces are truncated under a relatively long confining pressure condition probably induced by mechanical crushing and/or geochemical reactions such as pressure solution occurred on the fracture asperities. It could be used to explain the phenomena that the permeability showed a slightly increasing after keeping the confining stress a hundred of days.

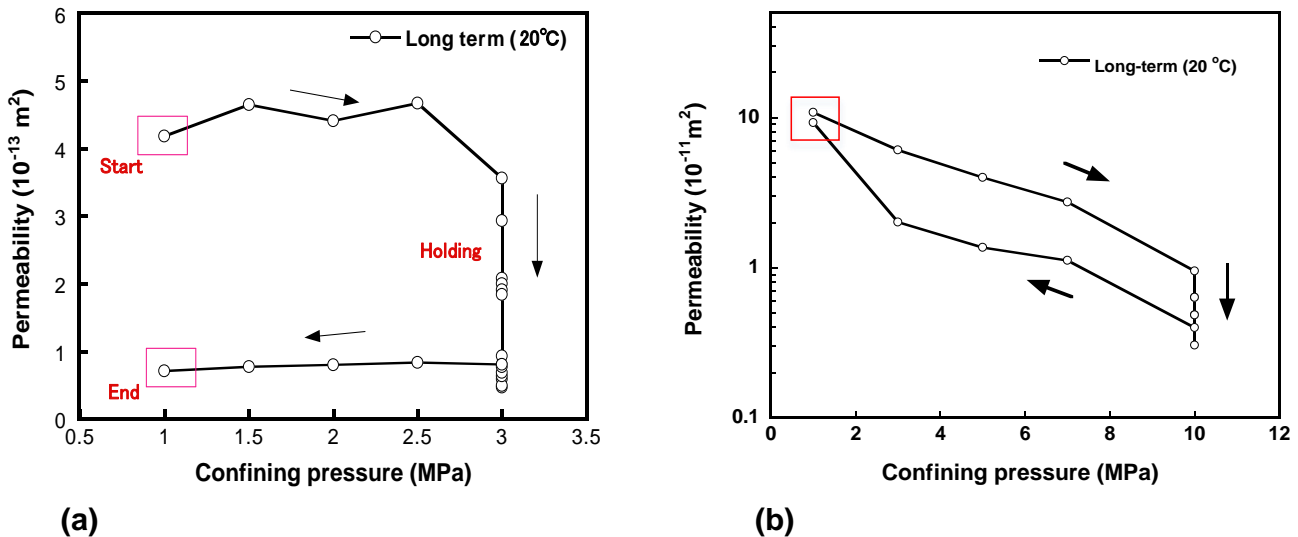


Fig. 3.14 Comparison of changes in permeability between (a) current work and (b) Yasuhara et al. (2013)

Second, the confining pressure was increased from 1.0 MPa to 3.0 MPa again before starting long-term test at 60 °C. In order to examine the permeability variation at 60 °C, permeability tests were conducted the same step as the long-term test at 20 °C (i.e., at 3.0 MPa and 180 days. Permeability tests were conducted intermittently at 20 °C).

At initial time, permeability had an unusual change. Permeability value increased at the loading process of the confining pressure from 1.0 MPa to 3.0 MPa. Permeability value at 60 °C 1.0 MPa is lower than the value at 20 °C, 1.0 MPa. It decreased from $7.13 \times 10^{-14} \text{ m}^2$ to $4.9 \times 10^{-14} \text{ m}^2$. Then the permeability showed an increasing tendency with increasing the confining pressure to 3.0 MPa. The value increased from $4.9 \times 10^{-14} \text{ m}^2$ to $1.2 \times 10^{-13} \text{ m}^2$, as depicted in Fig.3.15. (i.e., permeability evolution at loading process at 60 °C). It is inferred that permeability variation was unstable due to an abrupt temperature increase. Moreover, fluid velocity and viscosity might be accelerated at a higher temperature, then the permeability was increased against the confining pressure. A comparison between the loading performance at 20 °C and 60 °C is shown in Fig.3.15, Permeability value at 60 °C is lower than at 20 °C was confirmed.

Fig.3.16 shows that the initial permeability value at 0 day is $1.2 \times 10^{-13} \text{ m}^2$. With an opposite change of the permeability at 20 °C, it dropped slightly after several days and decreased about 47 % from the

initial value. Permeability changing is slightly until 60 days, and it is always lower than the value at 20 °C. Permeability decrease with increasing the temperature which is congruent with short-term test. This change could be interpreted that the mechanical compaction or the thermal expansion decreased with permeability. Subsequently, permeability appeared an increase tendency after 60 days. It increased about 28 % from 60 to 120 days. Moreover, permeability value reached to $8.7 \times 10^{-14} \text{ m}^2$ at the end of 180 days.

This long-term test showed that it didn't decrease significant as the same with the permeability at 20 °C. Moreover, permeability at 60 °C performed a chaotic variation in 180 days. This is contradictory to some other researchers who claimed that the permeability decreased monotonously at a higher temperature. In contrast, it is similar to the previous study, previous researchers clarified that permeability variation under a constant confining pressure at first decreased for dozens of days and then increased at a higher temperature. (e.g., Li et al.,2008; Xu et al., 2016). The fluid velocity and the viscosity might be altered at a higher temperature and result in a chaotic change of the permeability. (Yasuhara et al., 2006,2015) found that mineral dissolution generated on the fracture asperities at a higher temperature. The geochemical response will further alter the permeability in long-term.

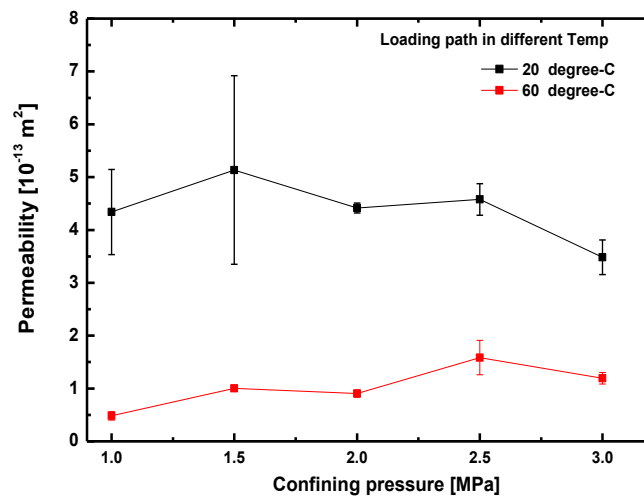


Fig.3.15 Comparison of the permeability variation at the loading confining pressure process between 20 and 60 °C

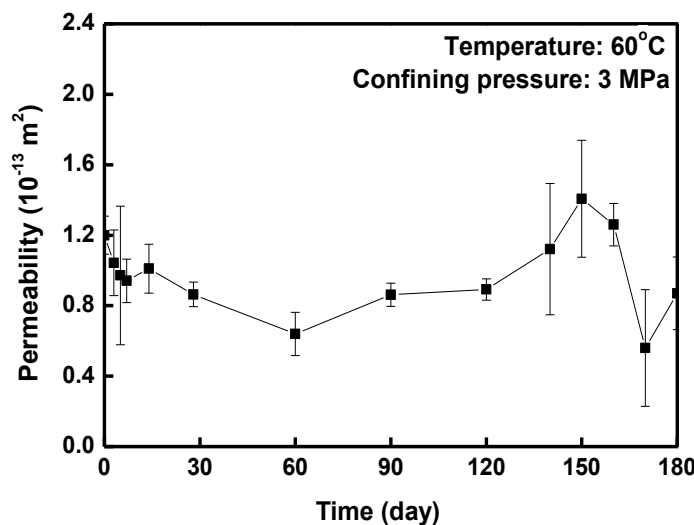


Fig.3.16 Permeability variation with time (Sample #1), 60 °C,180 days

Third, permeability not sensitive to the confining pressure was confirmed at the long-term loading and unloading process at 20 °C. Therefore, before starting the long-term test at 90 °C, the stepwise increasing the confining pressure was omitted. The confining pressure was increased to 3.0 MPa immediately after resetting the membrane and sample into the triaxial cell.

At 90 °C, permeability value is much lower than it at 20 and 60 °C, as depicted in **Fig.3.17**. It showed a quite similar phenomena with the short-term test at 90 °C. Permeability is one order of magnitude lower than it at 20 and 60 °C. After finishing the long-term permeability test of 60 °C, permeability value reached around $8 \times 10^{-14} \text{ m}^2$. Permeability dropped sharply to $5.8 \times 10^{-15} \text{ m}^2$ after increasing the temperature to 90 °C. Permeability has a fluctuant and unstable change until 120 days. The permeability value shows it increased or decreased. After 120 days, permeability value reaches to $8.7 \times 10^{-15} \text{ m}^2$. Comparing with the initial value at 90 °C, permeability increasing was confirmed. Which can be guessed that the chemical reaction may significant happen on the fracture surfaces. Aperture was enlarged may due to the free-face dissolution generated. The mineral may dissolve from the free surface of the aperture and transport with the fluid, then the effluent was exported outside of the aperture. Therefore, the fracture geometry may be changed and suffered a long-term transformation. Moreover, an enlarged aperture will increase the permeability.

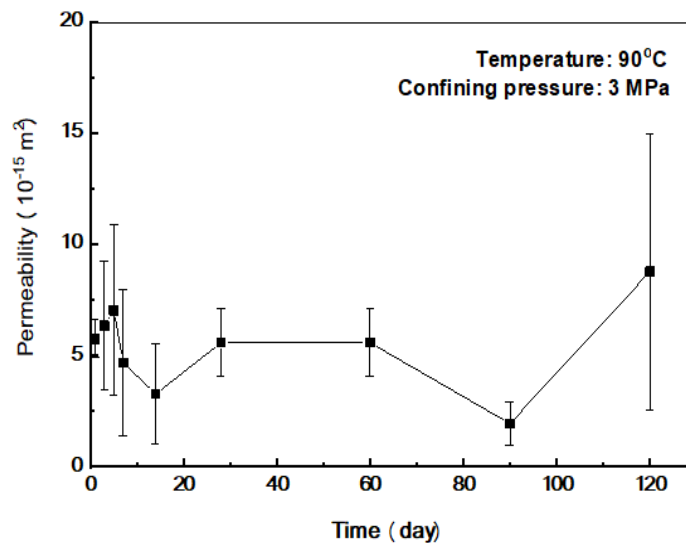


Fig.3.17 Permeability variation with time (Sample #1), 90 °C, 120 days

3.6 Discussions

3.6.1 Discussion of the permeability tests at room temperature

Fig.3.18 shows a summary of the permeability test results. i.e., short-term tests at various temperatures and long-term at the room temperature. From observing the short-term permeability test results, the permeability reversible behavior against the confining pressure can be confirmed. Additionally, thermal expansion may enlarge the fracture contact area, then the flow path became narrow. A relative high

temperature may result in the mineral dissolution happen and further changes the permeability. Based on the variation of the short-term permeability tests, permeability evolution under various conditions needs to be checked further. After finishing the short-term tests, the temperature was reduced to 20 °C and long-term permeability test was conducted at a constant confining stress of 3.0 MPa for 180 days. The permeability decreased remarkably in the early period, which may mainly result from the mechanical compaction. Then the permeability reached a stable value in a short period of time (7~28 days) and decreased again. After 100 days, the permeability oscillated slightly with an irregular fluctuation. Irreversible crushing and/or dissolution at the contacting asperities might be a reason for the phenomena in the long-term test. The chemical reaction might happen at this period, mineral dissolution may occur on the fracture free-surface and then the fracture aperture became larger. It will also result in the fluid flow velocity become faster than the initial value. Permeability value showed a slight increasing during 100 ~ 180 days. Moreover, the confining pressure was unloaded after 180 days permeability tests. The permeability shows an irreversible variation which is not sensitive to the confining pressure (see **Fig. 3.14 (b)**). Geochemical reactions, such as pressure solution, may occur on the fracture surfaces and alter the permeability.

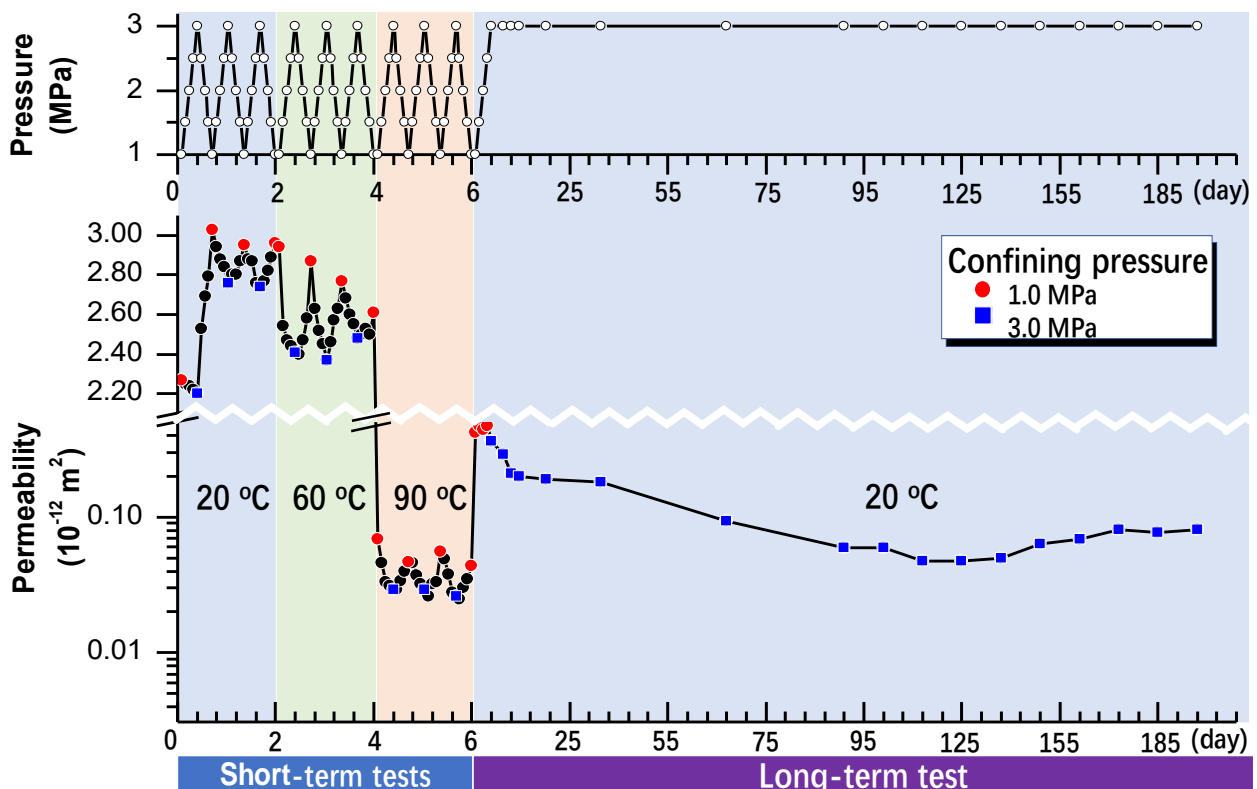


Fig.3.18 Brief summary of the permeability changes in short-term and long-term tests at 20 °C

3.6.2 Discussion of the permeability tests at elevated temperatures

Fig.3.19 shows the whole process of permeability tests under three different temperatures. (i.e., 20,60 and 90 °C). Redpoint represents the permeability value at the confining pressure of 1.0 MPa. Bluepoint is

the value at 3.0 MPa. Permeability showed reversible behavior against the confining pressure at the short-term tests; at the beginning of the long-term test, permeability showed irregular change at the loading process of the confining pressure. i.e., it has been illustrated in **Fig.3.14**. Permeability decreased remarkably could be confirmed at the long-term test of 20 °C. Then the confining pressure was unloaded. Permeability change at the unloading performance also showed an irreversible variation and not sensitive to the confining pressure, which has been discussed in **Fig. 3.14 (b)**.

At the second long-term permeability test, reloaded the confining pressure before starting the long-term test at 60 °C. Contrary to the short-term tests, the permeability increased at this loading process, and the value is higher than the permeability value at 20 °C. It can be noted that the permeability is unstable at a higher temperature of 60 °C. A higher temperature induced the plastic deformation occur on the fracture surfaces, which will result in the geometrical change. At the initial time, permeability decreased sharply, and it is consistent with the permeability variation at 20 °C. At the first 60 days, permeability value is lower than at 20 °C due to the thermal influence. Moreover, mechanical compaction may also significantly decreased the permeability. Then the permeability decreased again after a short stable period. However, the permeability shows an inverse change after 100 days. It increased gradually. Permeability value almost reached to the initial value after 180 days. (i.e., permeability value at 0 days, 60 °C). This result is different from the short-term test results, which showed that the permeability reduced at a higher temperature. However, this result is similar to the results of the previous studies. (Yasuhara et.al., 2015) confirmed that the permeability and aperture decreased at the first several hundred days and then increased significantly after this reduction.

Then at 90 °C. Previous research (Hasegawa, 2010) shows that permeability value is lower than 20 °C. However, the permeability test was only conducted for 18 days. In this study, permeability decreased significantly at the initial time of 90 °C, and it reaches to $5.7 \times 10^{-15} \text{m}^2$. Moreover, permeability showed a fluctuant tendency in 120 days. Finally, permeability shows a significant increase to $8.7 \times 10^{-15} \text{m}^2$. Which is much higher than the initial value of 90 °C.

From several permeability tests, it can be noted that at a higher temperature, an irreversible crushing or dissolution at the contacting asperities, reversible compaction, and the plastic deformation occurred on the fracture surfaces might be a reason for the phenomena in the long-term tests. The free surface dissolution might happen and then result in the aperture open. Therefore, the permeability value will become higher. Moreover, the roughness surfaces might be changed under the repeated flow experiments. Geochemical reactions, such as pressure solution, might alter the fracture geometrical characteristics and altered the permeability evolution in the long-term.

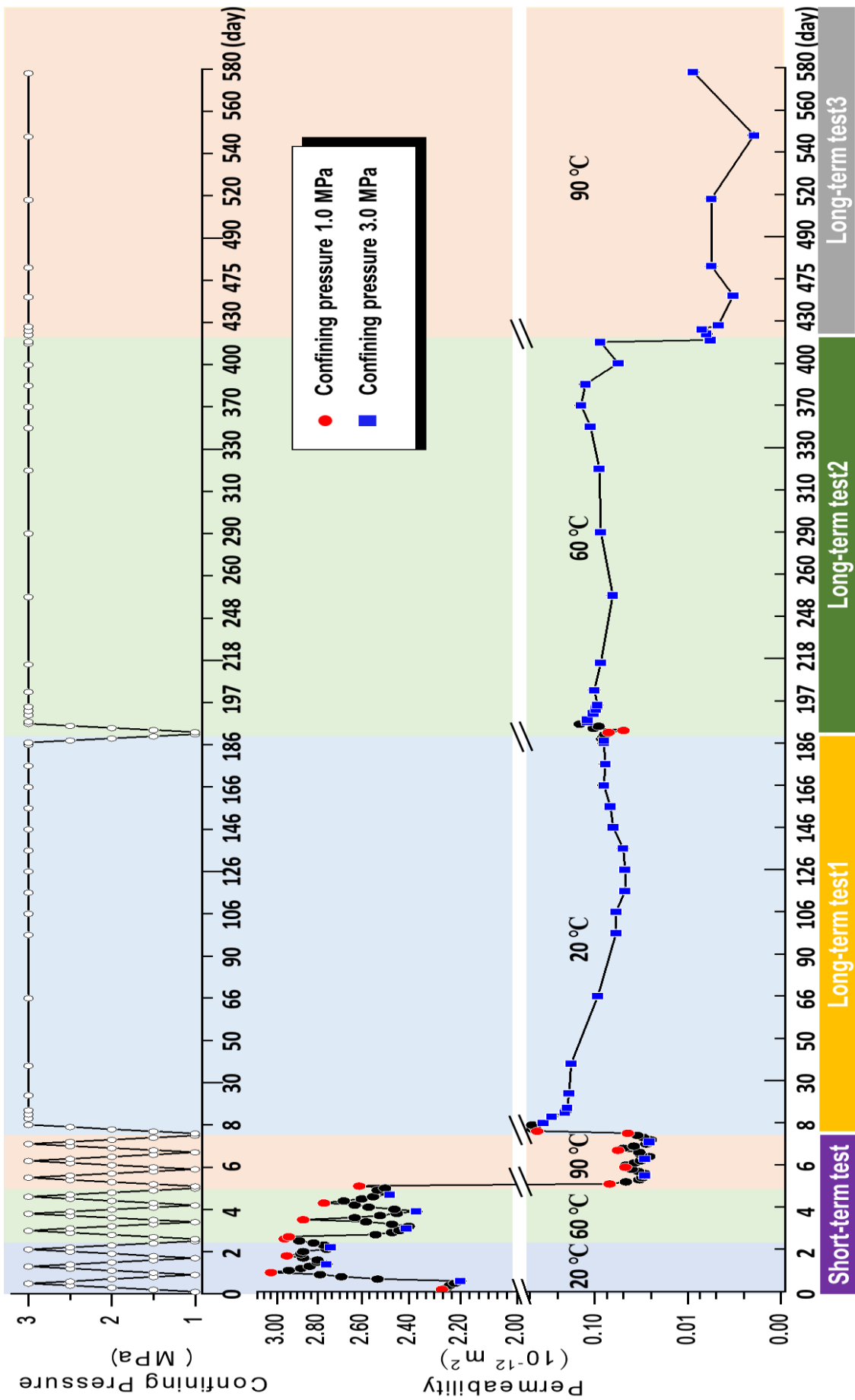


Fig.3.19 The whole summary of the permeability changes under three temperatures (20,60 and 90 °C)

3.6.3 Comparison between pre- and post -experiments

Aperture variation of the pre- and post- experiments (i.e., before long-term permeability test at 20 °C and after long-term permeability test at 60 °C), which were obtained from X-ray CT observation were compared. Granite sample #1 was first measured without confining pressure before starting the permeability experiments. 1811 slices of CT cross-section images were scanned. One slice of the cross-section (i.e., slice 238, at z-direction of 14.04 mm) is depicted in **Fig.3.20**. Aperture position was distinct observed from the CT image. Then the sample was scanned again after finishing the second long-term permeability test of 60 °C. **Fig.3.21** illustrated a comparison between pre- and post-experiments. Several CT images were extracted from different positions(i.e., different positions at the length of the sample) and made a comparison (i.e., pre- and post-experiment CT images). A distinct difference between the two CT images can be observed. After two long-term permeability testing processes, aperture closure is confirmed from this CT observation. However, it is difficult to say that the aperture became narrow will reduce permeability. Permeability evolution at 60 °C showed the value was not decreasing monotonously. Several factors may contribute to influence the permeability change, such as the mineral dissolution along the fractured walls, free-surface dissolution, or precipitation. Moreover, permeability had an increasing tendency after several hundred days was observed from both of long-term experiments. It can be supposed that the fracture geometry change at different positions is uncertain. Therefore, the aperture comparison result may difficult to explain the reason of the permeability variation. However, aperture decrease was confirmed from the CT observation.

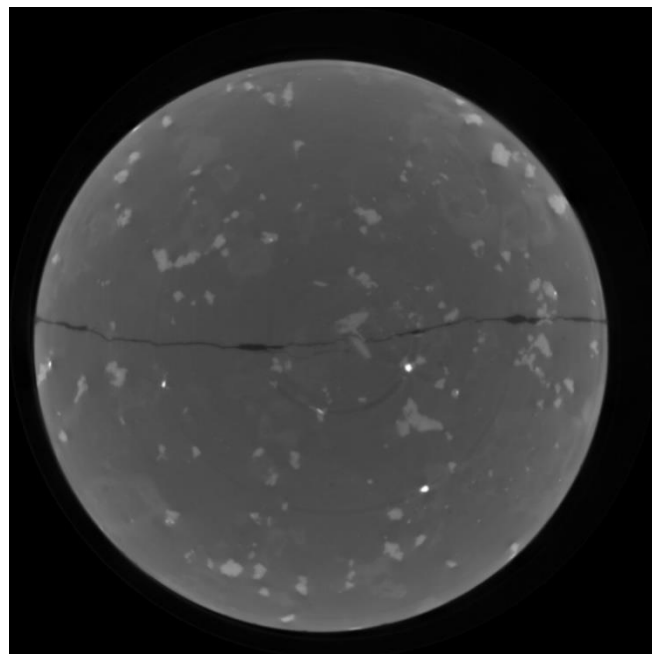
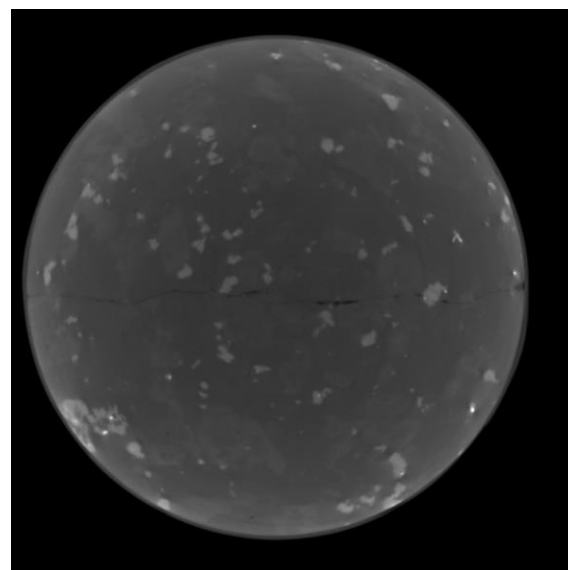
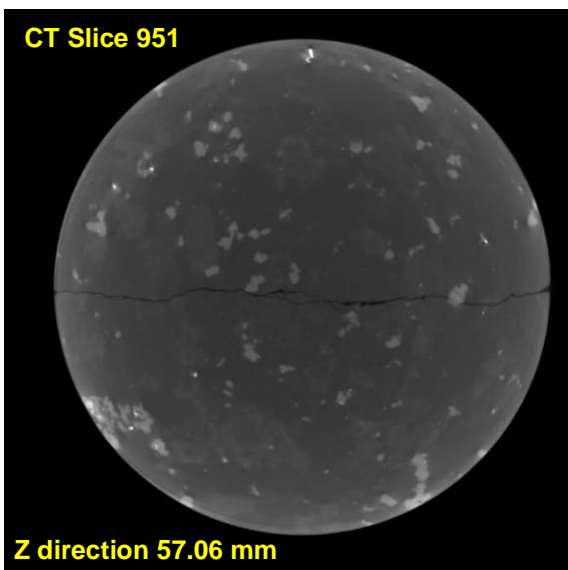
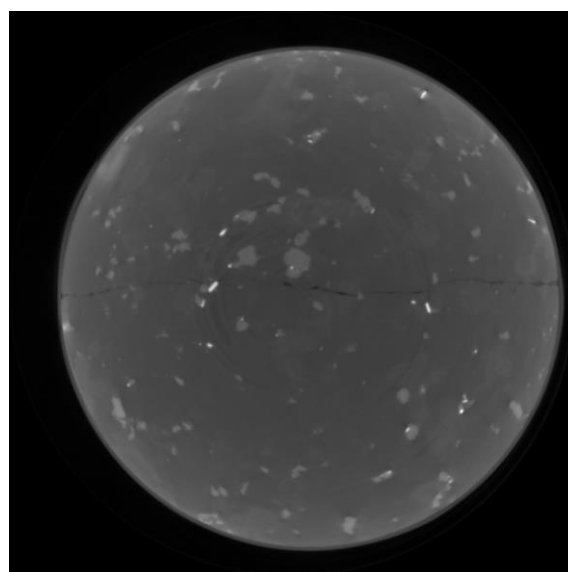
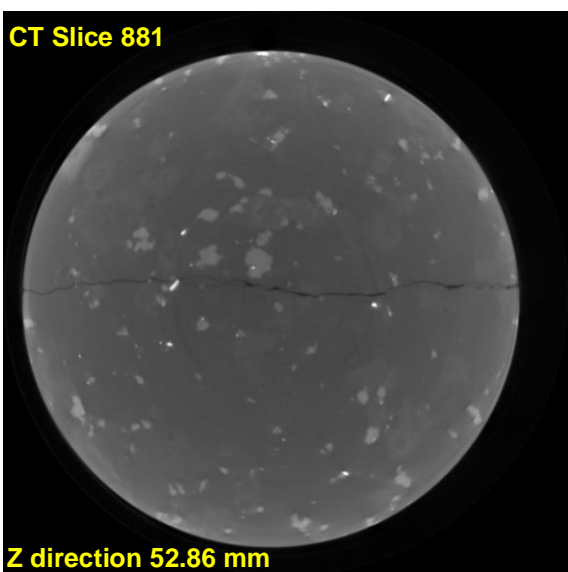
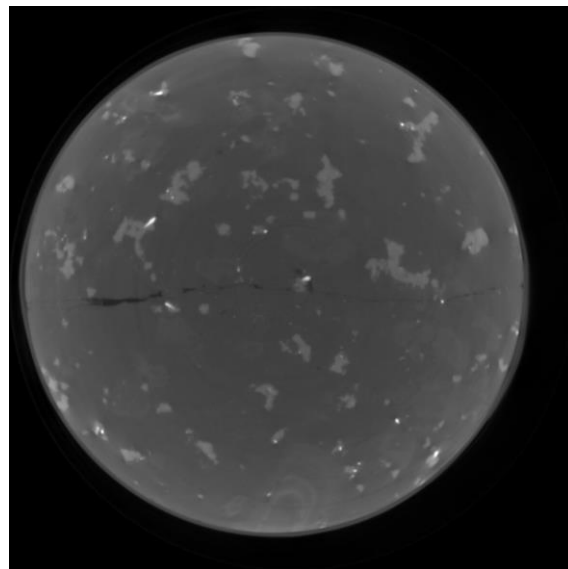
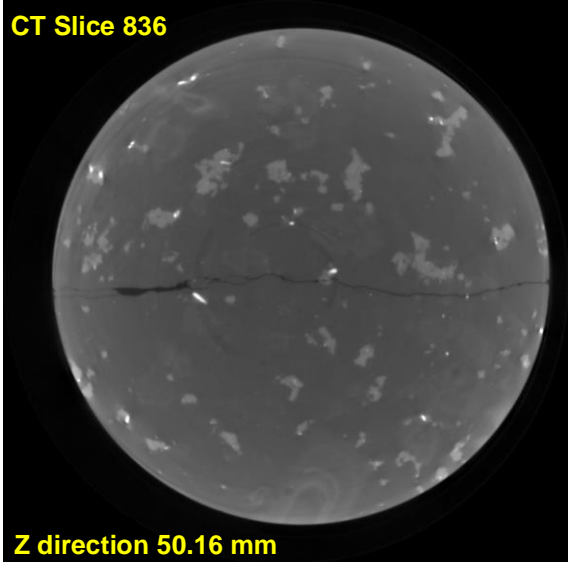
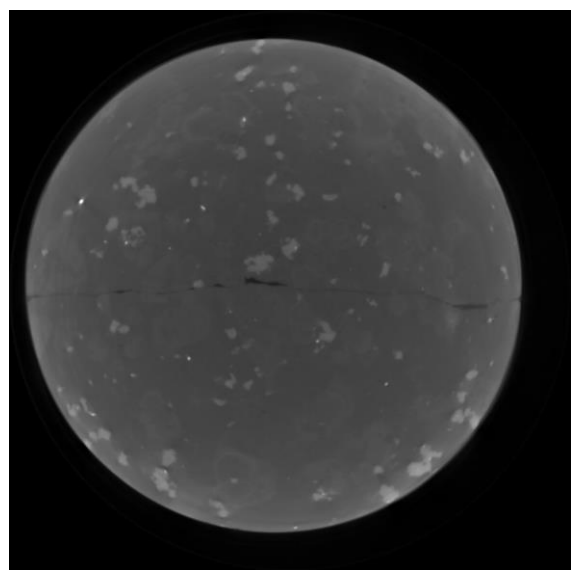
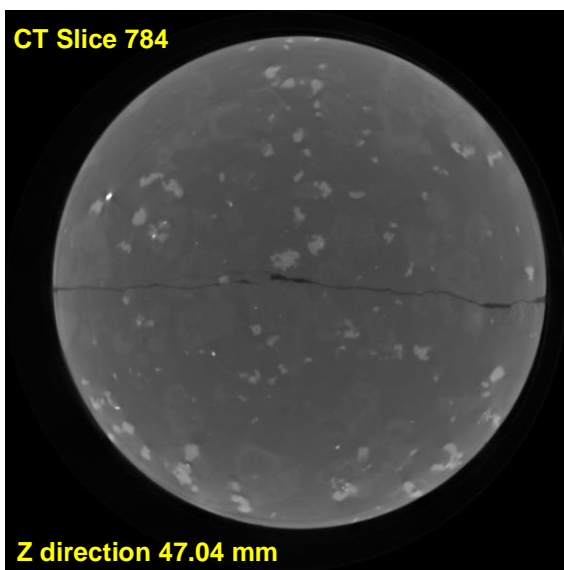
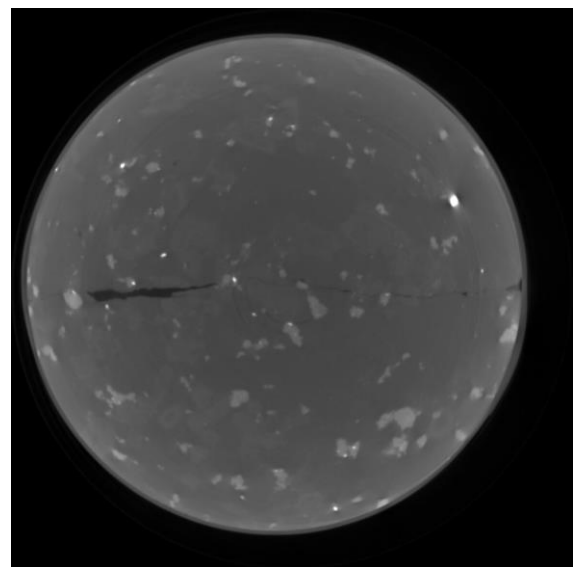
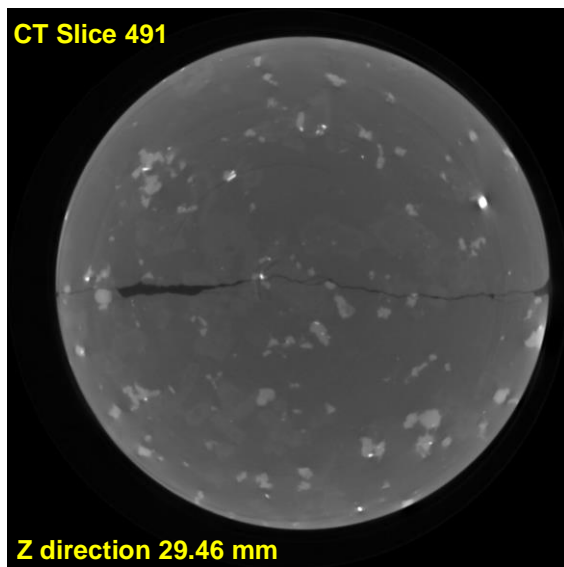
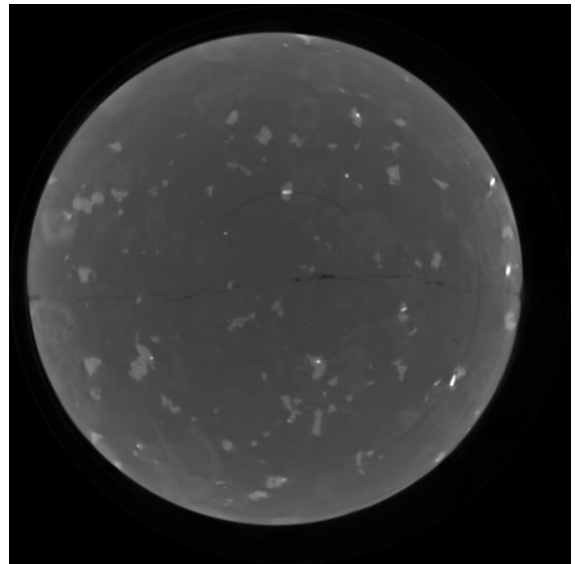
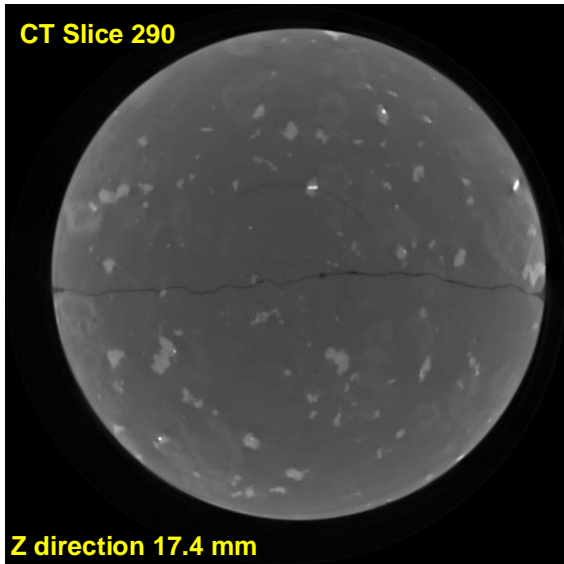


Fig.3.20 Initial aperture position without confining pressure at pre-experiments. (CT slice 238, at z-direction of 14.04 mm)



(a)

(b)



(a)

(b)

Fig.3.21 CT image comparison of the aperture variation at different length of the sample. (a) pre- experiment (b) post- experiment

3.7 Summary

In this study, short- and long-term permeability tests were conducted under various conditions. There are some conclusions are summarized as follows:

Short-term permeability tests show that permeability is sensitive to the confining pressure and temperature. However, it became a slow response to the confining pressure when the long-term permeability at 20 °C was started. It should be guessed that the internal fracture morphology was changed after the short-term permeability tests under various conditions. Permeability has an significant decrease after finishing the long-term test at 90 °C. Which indicated that the fracture aperture became much closed after a long-term. Moreover, the geochemical response may happen within the aperture.

Aperture variation was observed after two long-term permeability tests through the CT observation. A significant difference between the pre- and post-experiment is confirmed. Fracture aperture became closed after several hundred of days. Fracture roughness surfaces may be altered and have an irreversible variation under the coupled processes, and the fracture contact-area became larger. Yasuhara et al. (2015) demonstrated the theoretical about the fracture variation. i.e., if the effects of the dissolution at the contact asperities is larger than the free-face dissolution, it is thought to explain the decrease of the permeability and the increase of fracture contact-area; if the effects are smaller, that means the free-surface dissolution will enlarge the fracture aperture, and the fluid velocity will become faster.

In this study, it can be supposed that the pressure solution may happen within the fracture, and drive to the mineral dissolution happen on the contact asperities. The mineral precipitation generated within the fracture, which will further result in the aperture closure. Therefore, the reason for the permeability decrease should be verified.

However, experiment results show that the permeability neither decreased with the elevated temperature nor changed monotonously. In order to further verify the long-term permeability variation, the effluent from the flow outlet at regular intervals was checked after each permeability test in the long-term. The element Si, Al, K, Fe, Ca, Na, and Mg concentrations were illustrated. The chemical analysis assayed by inductively-coupled plasma atomic emission spectrometry (ICP-AES) (Thermo Scientific iCAP6300, Ehime University). Prior to analysis, the effluent solutions were diluted by 50 times with 2 % concentrated HNO₃.

The element concentration result at 20 °C is shown in **Fig.3.22**. The concentration of Si, Na, and Ca are larger than the others. The element concentrations became larger can be confirmed before 30 days. After 30 days, the elements didn't show an obvious variation. However, at 60 °C, the effluent analysis result showed that the element concentration of Si is higher than the value at 20 °C, see in **Fig.3.23**. Moreover, the element concentration of K, Fe, and Mg showed a slight undulation, which is corresponded

to the permeability test results at 60 °C. Permeability value shows an irregular change at 60 °C. It can be guessed that internal fracture may happen the chemical reaction. i.e., the mineral element may dissolve from the fracture surfaces and then was transported with the fluid within the aperture. Therefore, the element concentration shows a slight fluctuation with a comparison of the value at 20 °C.

The element concentration at 90 °C can further explain the permeability change, as depicted in **Fig.3.24**. From observing the element concentration at 90 °C, it can be noted that the value of each mineral element became much higher than the value at 20 and 60 °C. Especially the element concentration of Si, it increased two order of magnitude than the value at 20 °C, and presented a stepwise increasing with the temperature. Which is also corresponding to the permeability test result, the permeability at 90 °C decreased two order of magnitude. Moreover, the element concentration at 90 °C shows that the mineral solution increased with time. Moreover, each mineral concentration shows an unstable change, which is also reflected to the irregular change of the permeability at 90 °C.

From observing the permeability test results, the reduction of the hydraulic aperture, the irreversible behavior of the permeability, and the element concentration increasing at 90 °C, it is supposed that pressure solution may generate on the fracture contact-area. Which acted to decrease the permeability. Mineral solution increase at a higher temperature indicated that the geochemical response happened during the permeability tests. Mineral dissolution and precipitation may generate on the rough-walled fracture, which will result in the aperture decrease. Therefore, the permeability reduction and irregular change at a higher temperature, especially at 90 °C was verified.

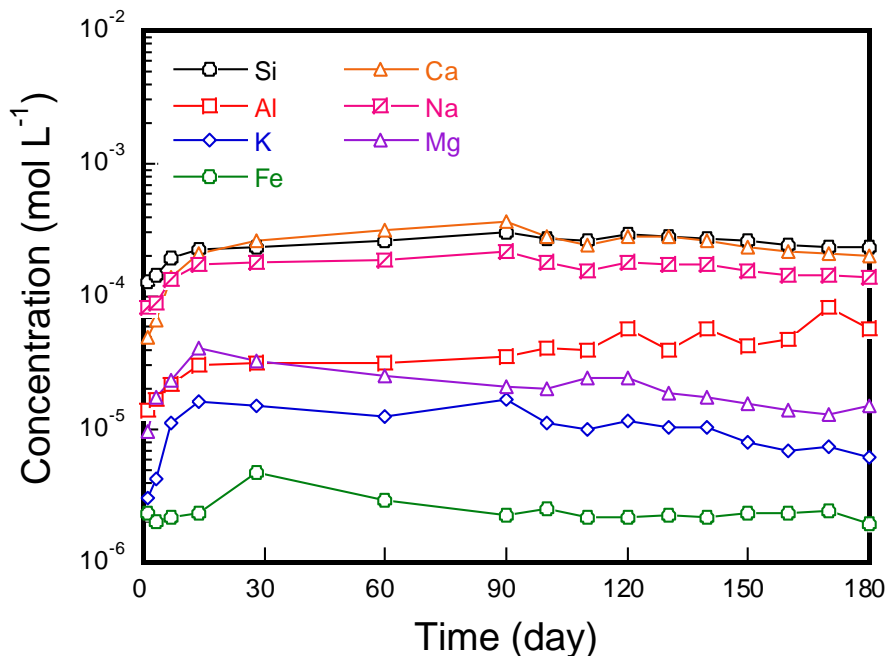


Fig. 3.22 Evolution of the mineral composition at long-term permeability test of 20 °C

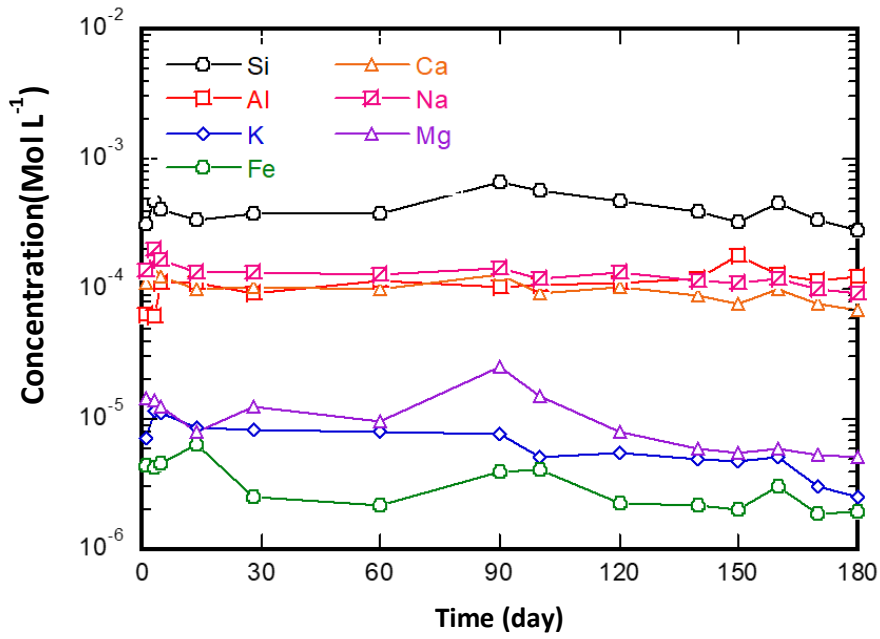


Fig. 3.23 Evolution of the mineral composition at long-term permeability test of 60 °C

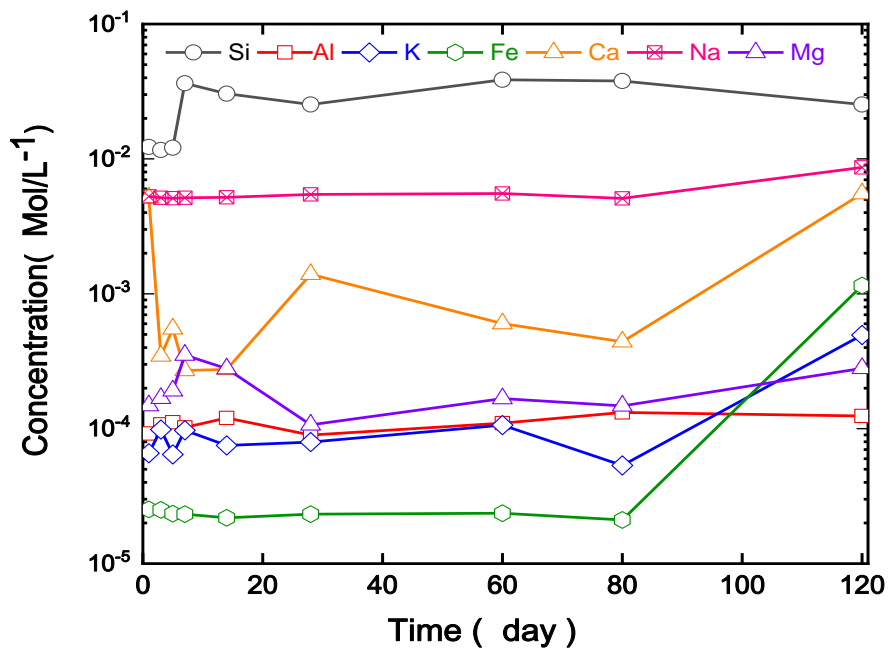


Fig. 3.24 Evolution of the mineral composition at long-term permeability test of 90 °C

References

- Bandis, S., Makurat, A., Vik, G.: Predicted *and* measured hydraulic conductivity of rock joints. *Int. Symp. Fundamentals of Rock Joints*, Bjørkliden. pp. 269–280. 1985.
- Barton, N., Choubey, V. :The Shear Strength of Rock Joints in Theory and Practice. *Rock Mechanics*. 10: 1-65. 1977.
- Barton, N., Quadros, D.E.F. :Joint aperture and roughness in the prediction of flow and groutability of rock masses. *International Journal of Rock Mechanics and Mining Sciences*. 34: 3-4.1997.
- Beydoun, W. B., Cheng, C. H., and Toksoz, M.N. :Detection of open fractures with vertical seismic profiling, d. *Geophysical. Research*. 90, 45574566.1985.
- Brace, W. F., Walsh, J. B. & Frangos, W. T.: Permeability of granite under highpressure, *Journal of Geophysical Research*, Vol.73, pp.2225-2236.1968.
- Dimadis, G., Dimadi, A., Bacasis, I.: *Influence of fracture roughness on aperture fracture surface and in fluid flow on coarse-grained marble, experimental results. Journal of Geoscience and Environment Protection*. 2: 59-67.2014.
- Ellis, B.R., Fitts, J.P., Bromhal, G.S.: Dissolution-driven permeability reduction of fractured carbonate caprock. *Environment. Engry. Sci*. 30, 187–193.2013.
- Fairhurst C. : On the validity of the ‘Brazilian’ test for brittle materials. *International Journal of Rock Mechanics and Mining Sciences*. 1(4): 535–546.1964.
- Fridleifsson, I.B. : Geothermal energy for the benefit of the people, *Renew. Sustain. Energy Rev*. 2001;5, 299-312.
- Guo, L.L., Zhang, Y.B., Zhang, Y.Z. :Experimental investigation of granite properties under different temperatures and pressures and numerical analysis of damage effect in enhanced geothermal system, *Renew. Energy* 126,107-125.2018.
- Hasegawa.: Experimental evaluation of fracture permeability in granite under temperature and stress controlled conditions. Master Thesis,2010.
- Hooijkaas, G.R., Genter,A., Dezayes,C.: Deep-seated geology of the granite intrusions at the Soultz EGS site based on data from 5km-deep boreholes, *Geothermics*. 35,484-506.2016.
- Hsieh, P. A., Tracy, J.V., Neuzil, C.E.: A transient laboratory method for determining the hydraulic properties of ‘tight’ rocks—I. Theory. *International Journal of Rock Mechanics and Mining Sciences & Geomechanics Abstracts*. 18: 245-252.1981.
- Ishikawa. :Rock aperture distribution and permeability test through triaxial cell coupled with X-ray CT microfocus observation.Mater thesis.2016.2.

Kranz, R. L., Frankel, A.D., Engelder, T., and Scholz, C.H.: The permeability of whole and jointed Barre granite. *International Journal of Rock Mechanics and Mining Sciences*. 16, 225-234.1979.

Lang, P., Paluszny, A., Zimmerman, R. : Hydraulic sealing due to pressure solution contact zone growth in siliciclastic rock fractures. *Journal of Geophysical Research: Solid Earth*, 120, 4080–4101. <https://doi.org/10.1002/2015JB011968>.2015.

Li, B., Jiang, Y.J., Koyama, T., Jing, L.R., Tanabashi, Y. :Experimental study of the hydro-mechanical behavior of rock joints using a parallel-plate model containing contact areas and artificial fractures. *International Journal of Rock Mechanics and Mining Sciences*. 45(3): 362-375.2008.

Long, J. C. S., Gilmour, P., Witherspoon, P.A. :A model for steady fluid flow in random three-dimensional networks of discshaped fractures. *Water Resource Research*. 21, 1105-1115.1985.

Neretnieks, I. : Stress-mediated closing of fractures: Impact of matrix diffusion. *Journal of Geophysical Research: Solid Earth*, 119, 4149–4163. <https://doi.org/10.1002/2013JB010645>.2014.

Noorishad, J., Ayatollahi, M.S., Witherspoon, P.A. :A finiteelement method for coupled stress and fluid flow analysis in fractured rock masses, *International Journal of Rock Mechanics and Mining Sciences*. 19, 185-193.1982.

Paillet, F. L. :Problems in fractured-reservoir evaluation and possible routes to their solution. *Log Anal.* 26, 26-41.1985.

Polak, A., Elsworth, D., Yasuhara, H. : Permeability reduction of a natural fracture under net dissolution by hydrothermal fluids. *Geophysical Research Letters*. Vol. 30.2003.

Polak, A., Elsworth, D., Liu, J.: Spontaneous switching of permeability changes in a limestone fracture with net dissolution. *Water Resource Research*. 40: (W03502).2004.

Schrauf, T. W., Evans, D.D.: Laboratory studies of gas flow through a single natural fracture, *Water Resource Research*. 22, 10381050.1986.

Taron, J., Elsworth, D. :Constraints on compaction rate and equilibrium in the pressure solution creep of quartz aggregates and fractures: Controls of aqueous concentration. *Journal of Geophysical Research*, 115, B07211. <https://doi.org/10.1029/2009JB007118>.2010.

Tsang, Y. W., and P. A. Witherspoon, Hydromechanical behavior of a deformable rock fracture subject to normal stress, *J. Geophysical Research*. 86, 9287-9298.1981.

Tse, R., Cruden, D.M. :Estimating joint roughness coefficients, *International Journal of Rock Mechanics and Mining Sciences* . 303-307. 1979.

Xu, P., Yang, S.Q.: Permeability evolution of sandstone under short-term and long-term triaxial compression. *International Journal of Rock Mechanics and Mining Sciences*. 85: 152-164.2016.

Yasuhara, H, Elsworth, D.: Evolution permeability in a natural fracture: significant role of pressure solution. *J. Geophysical Research*. (B03204); 109.2004.

- Yasuhara ,H., Hasegawa, D., Nakashima, S.Kishida,K.: Experimental evaluation of fracture permeability in granite under temperature and stress controlled conditions. *Japanese Geot.-Journal*. Vol. 71-79.2013.
- Yasuhara, H., Kinoshita, H., Kishida,K. :Temporal alteration of fracture permeability in granite under hydrothermal conditions and its interpretation by coupled chemo-mechanical model. *Applied Geochemistry*, 2011.
- Yasuhara, H., Kinoshita, N., Ohfuji, H.,Kishida, K. Long-term observation of permeability in sedimentary rocks under high-temperature and stress conditions and its interpretation mediated by microstructural investigations. *Water Resources Research*. 51(7): 5425-5449.2015.
- Yasuhara, H., Polak, A., Elsworth, D. :Evolution of fracture permeability through fluid-rock reaction under hydrothermal conditions. *Erath Planet Sci. Lett.* 244, 186–200.2006.
- Yin, Q., Ma,G.W., Jing, H.W. :Hydraulic properties of 3D rough-walled fractures during shearing: An experimental study. *Journal of Hydrology*. 555: 169-184.2017.
- Yong , R., Ye, J., Liang, Q.F. :Estimation of the joint roughness coefficient (JRC) of rock joints by vector similarity measures. *Bull Eng Geol Environment*. 2017.
- Zhang, G.C., Karaku,s M., Tang, H.M. :A new method estimating the 2D Joint Roughness Coefficient for discontinuity surfaces in rock masses. *International Journal of Rock Mechanics and Mining Sciences*.72: 191-198.2014.
- Zhang, Y.Z, Li, Z.W., Guo, L.L. : Electricity generation from enhanced geothermal systems by oilfield produced water circulating through reservoir stimulated by staged fracturing technology for horizontal wells: a case study in Xujiaweizi area in Daqing Oilfield, China, *Energy*.78, 788-805.2014.

Chapter 4 Long-term Observation of Aperture Distribution and Contact-area Ratio Change under Various Conditions through Microfocus X-ray CT

4.1 Introduction

It is well known that microfocus X-ray CT tomography has been utilized in a lot of fields such as in the medical field and in the geotechnical engineering etc. Some researchers have used microfocus X-ray CT to observe the fracture variation under varying conditions (Polak et al., 2003;Yasuhara et al., 2015; Okamoto et al.,2017). Polak et al. studied about the aperture change under different temperatures (20, 80 and 120 °C) by using X-ray CT and different fracture rock samples. The mass removed from the fracture contact area, and the fracture became narrow was confirmed. Moreover, the aperture decreased under higher temperatures was illustrated in **Fig.4.1** (Polak et al., 2003). Aperture variation can be reflected through using the CT observation.

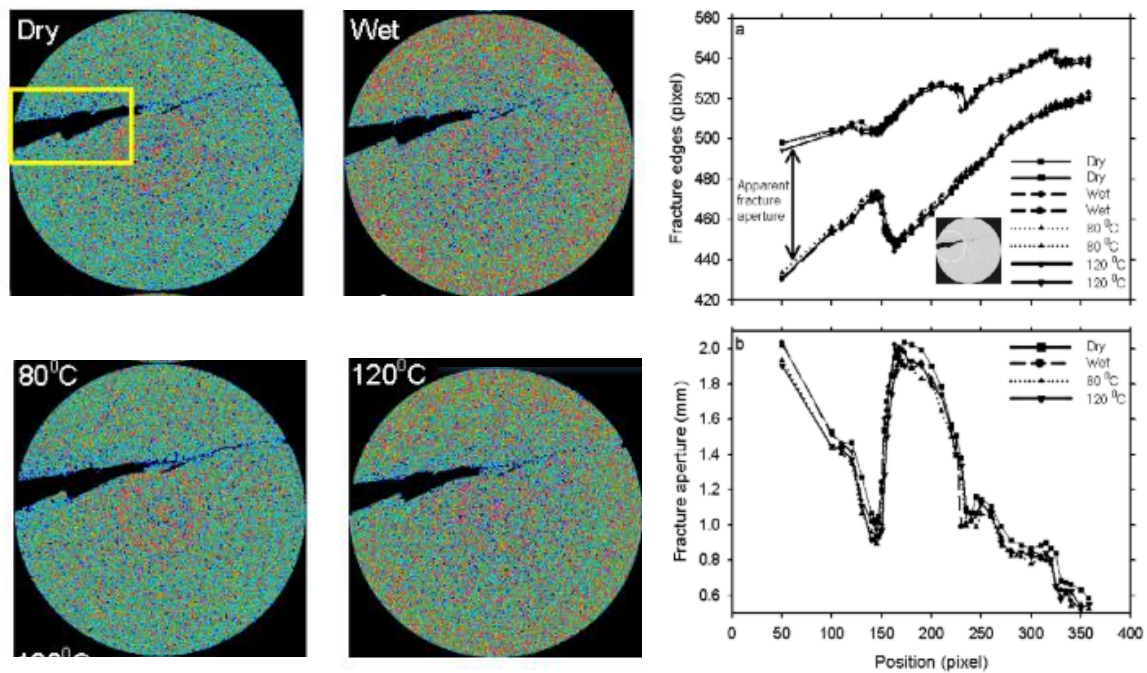


Fig.4.1 CT scanning images comparison.(a) comparison of the initial dry core, the wet core at 20 °C, 80 °C, and 120 °C. The boxed region illustrates the dissolved masses and the relative displacement of fracture faces.(b) aperture change under different conditions (Polak et al., 2003)

(Okamoto et al., 2017) showed a CT scanning image comparison of the aperture variation between the rock sample at room temperature and at 350 °C. Aperture decreasing under a higher temperature was distinct observed. Moreover, the quartz distribution illustrates that the aperture was altered under the

coupled processes. The chemical reaction happened and resulted in the quartz distribution change. The flow rate within the rock fracture was also changed. It was altered within the fracture may due to the mineral dissolution or the precipitation generated at 350 °C, as depicted in **Fig.4.2**. Therefore, CT observation of the rock sample can better explain the aperture variation under various conditions. However, a 2-D CT cross-section image can not better illustrate the aperture variation of the whole sample. Aperture variation at 3-D should be further studied.

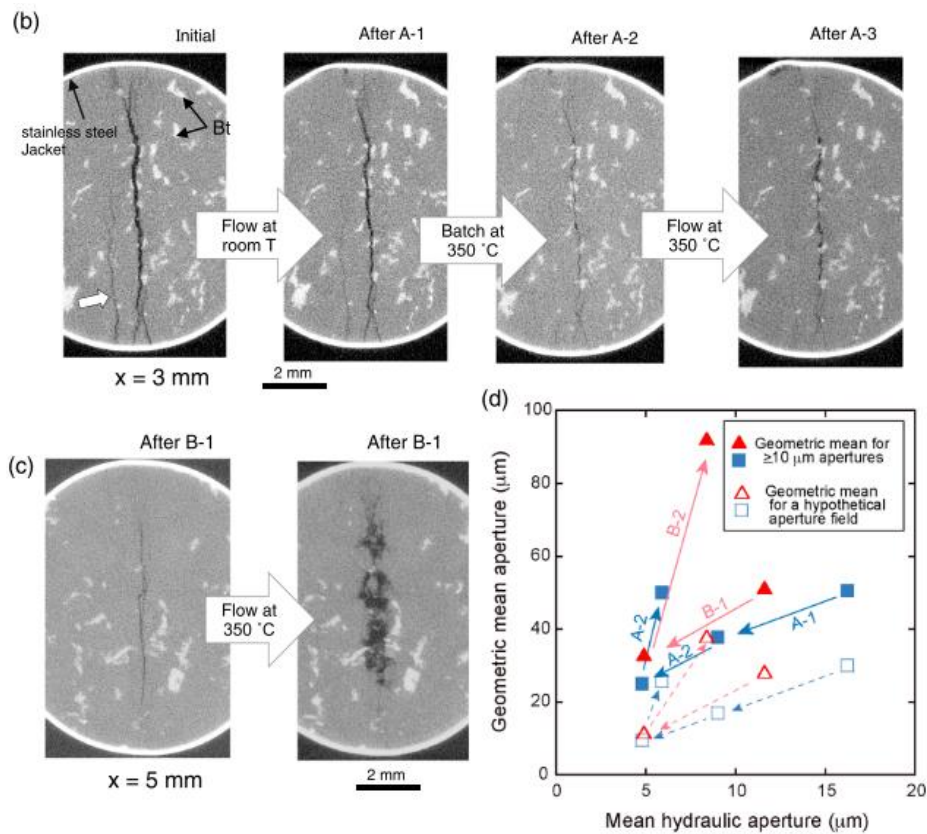


Fig.4.2 Granite geometric aperture evolution observation through the flow experiments. Stage A-1 = flow-through the granite sample at room temperature, stage A-2 =no flow experiment at 350°C, and stage A-3 = flow-through experiment at 350°C. Stage B-1 = flow-through experiment at room temperature, stage B-2 = flow-through experiment at 350°C (Okamoto et al., 2017)

(Yasuhara et al., 2015) conducted a series of permeability tests with several types of rock samples under different temperatures. Pore structures of rock samples were observed through X-ray CT with a comparison between the pre- and post-experiment. The comparison indicated that the changing pore structures might support the variation of the permeability. Moreover, the geochemical reactions were also confirmed from the experiment results. (Caulk et al., 2016; Kamali-Asl et al., 2018) found that the fracture aperture would close at high levels of confining stress. High levels of confining stress induced chemical dissolution happen on the fracture asperities and resulted in the contact ratio change. Besides, the pressure solution generated on the fracture asperities is more significant on accelerating the fracture closure rates.

In general, long-term flow behavior within the rock fractures under various conditions needs to be further understood. Moreover, the contact-area condition is also a lack of fully grasping. In order to check

the aperture evolution with time under coupled processes, the experimental works in this study focus on measuring the aperture changing under different conditions through microfocus X-ray CT in a long-term. CT experiments were conducted with the same condition of the long-term permeability tests. The CT scanner was utilized to obtain the aperture distribution change within the granite fracture and the contact-area ratio variation in long-term. Finally, several indexes, such as the contact-area ratio, the aperture distribution, a comparison of hydraulic aperture difference and the CT resolution difference were analysed and discussed.

4.2 Theoretical of X-ray CT

4.2.1 X-ray micro tomography facility

X-ray micro tomography facility which is composed of an X-ray source, a detector and a work table. The specimen on the work table will be 360 degree rotated when it is being scanned. The attenuation of X-ray energy is obtained after the X-ray reaches to the detector. X-rays are exponentially attenuated with the transparent length as shown in Eq.4.1. It shows the X-rays which are generated from the X-ray source are attenuated into the object. **Fig 4.3** shows a schematic diagram of the X-ray micro tomography facility (Kido, 2019).

$$I = I_0 \exp(-\mu x) \quad (4.1)$$

where x (m) is the transparent length, I is the X-ray intensity after transparence into the material by x (m), I_0 is the incident X-ray intensity and μ (1/m) is the X-ray absorption coefficient. μ is defined by the following equation:

$$\mu = \mu_m \rho \quad (4.2)$$

where μ_m (m^2/Mg) is the mass absorption coefficient that depends on each material and ρ (Mg/m^3) is the material density. This equation clarified that a higher the material density result in a larger of the X-ray attenuation. μ_m (m^2/Mg) is dependent on the incident X-ray energy; it is an element that constitutes the target object, i.e., an atomic number.

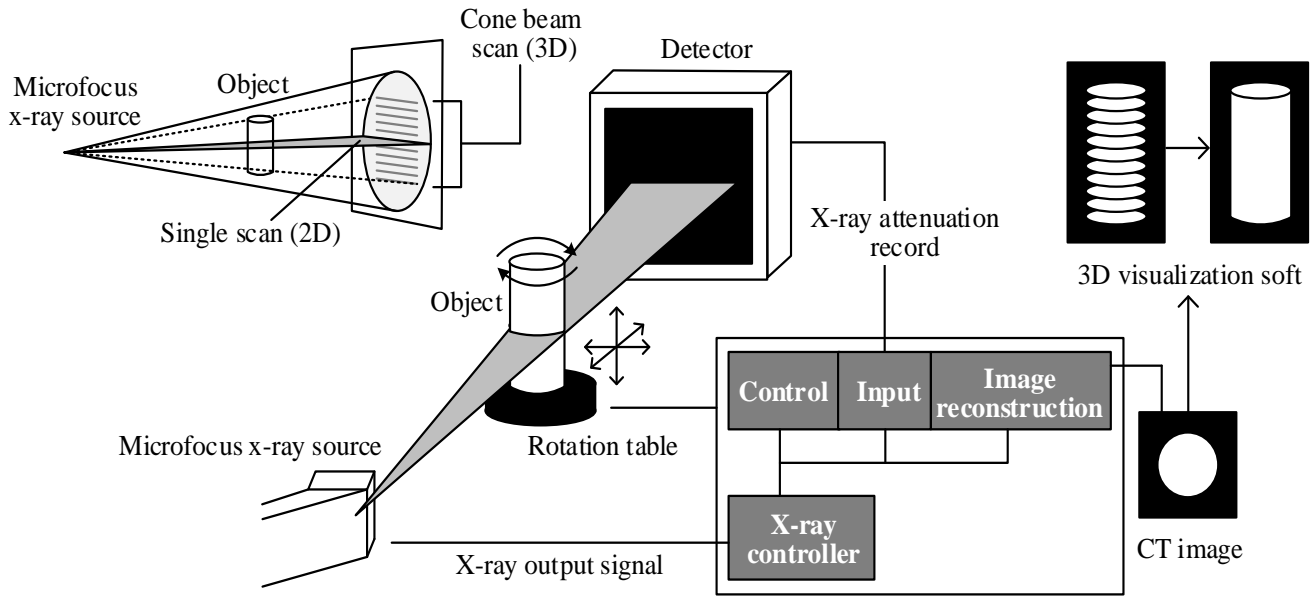


Fig.4.3 Schematic diagram of x-ray micro tomography facility (Kido, 2019)

4.2.2 Composition of X-ray micro tomography facility

4.2.2.1 X-ray source

The X-ray source generates continuous X-rays with various wavelengths, i.e., different levels of X-ray energy. The discharge which is produced by air is prevented to enter the X-ray tube by vacuum pressure. Synchrotrons provide characteristic X-rays, which are represented by Spring-8 in Japan. X-rays with uniform wavelengths are generated by synchrotrons because no attenuation characteristics occur involving X-ray energy, which becomes easy to provide higher resolution images.

4.2.2.2 Detector

The X-rays reach to the detector through the object and then the attenuation energy of the X-rays is recorded. The detector is composed of a scintillator which converts the X-rays into visible light; it is represented by a flat panel detector (FPD). Which converts incident X-rays directly into the electronic signals. Therefore, the FPD provides higher resolution CT images and becomes widely used.

4.2.2.3 CT reconstruction

Reconstruction is a type of computer process for making tomographic images based on the amount of X-ray attenuation recorded by the detector. The absorption of X-rays for an object with X-ray absorption coefficient μ_i ($i=1, \dots, N$) in a certain direction yields is written as follows:

$$I = I_0 \exp\{-x(\mu_1 + \mu_2 + \dots \mu_N)\} \quad (4.3)$$

Therefore, huge of data from multiple directions and a large number of simultaneous equations are obtained at two dimensional. Then the other unknown numbers (X-ray absorption coefficients) can be calculated. It indicates that a larger number of projections provide better spatial resolution.

4.2.2.4 CT value and images

The CT image is composed by the discrete CT values. CT values are determined as follows:

$$CT\ value = af(\mu) + b \quad (4.4)$$

Where a and b are certain constant values. $f(\mu)$ is a value with respect to μ ; each facility has its own value. Generally, the CT value is represented by a 16-bit signed integer. Different materials such as the granite sample, the rock, mineral and the air, are distinguished from each other based on different CT values.

A CT image cross-section is a two-dimensional slice. The numerous regions are composed of the pixel, while the thickness in the vertical direction of a CT image which is so-called the voxel. Both pixel and voxel numbers compose a two-dimensional CT image. Then thousands of 2-D CT image slices will rebuild a three-dimensional sample through the CT 26-Connectivity. A cylindrical shape of the granite sample at the cross-section is obtained through X-ray CT is shown in **Fig 4.4(a)**. Then aperture and contact-area ratio value are measured through a CT segmentation method as illustrated in **Fig.4.4(b)**. A CT segmentation image can be conducted through this Gaussian distribution.

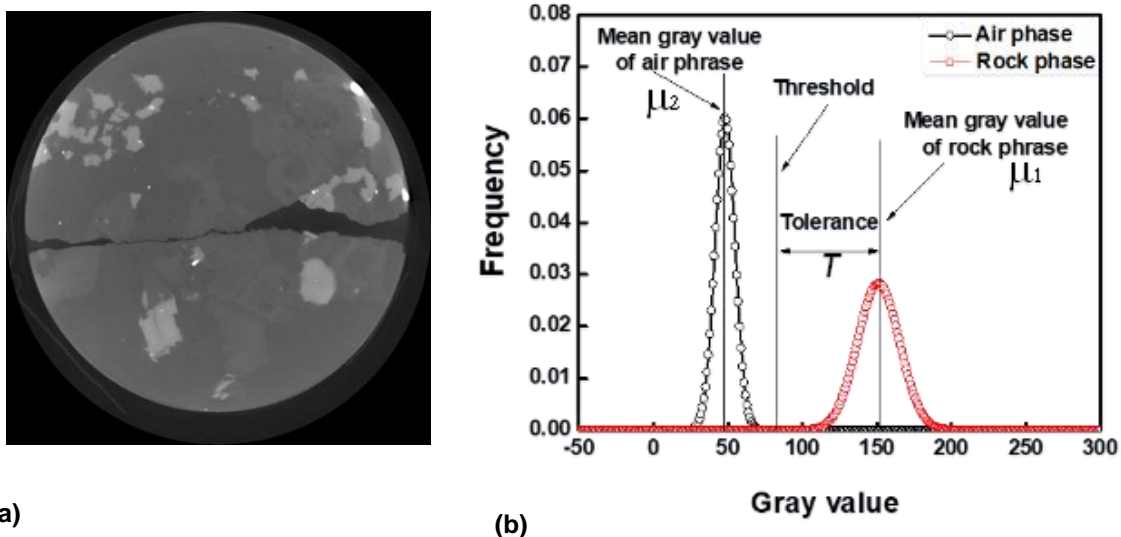


Fig.4.4 CT values distribution (a) horizontal cross-section of a granite CT image, (b) normal distribution of a granite CT image

4.2.2.5 Flat panel detector (FPD)

The CT image matrix is set as 512^2 , 1024^2 or 2048^2 , which are used to determine how many voxels in one tomographic slice. The larger image matrix i.e., 2048^2 provides CT images with a higher resolution,

it costs a relative long time at the CT image reconstruction. The flat panel detector (FPD) was utilized from 2013. (Kido, 2019). The greatest characteristic of the FPD is that the incident X-rays are converted directly into visible light, and a higher CT resolution image can be obtained. The feedback capacitance (gain) and integration time are needed to be set when using the FPD. Then a relative clearer perspective CT image can be measured through a longer integration time.

4.3 Experimental condition

4.3.1 Experimental setup

Granite sample 2# with a single rock fracture was used in this experiment, see in **Fig 4.5**. The physical properties and the morphology information have already illustrated in **Chapter 3** (i.e., the same material of sample 1#).The CT scanner is KYOTOGEO- μ XCT (TOSCANER-32250 hdk, TOSHIBA IT and Control Systems Corporation) as shown in **Fig 4.6** (Kido et al., 2017). The condition of X-ray micro tomography facility (KYOTOGEO- μ XCT) is listed in **Table 4.1**.

In order to observe the fracture variation under various conditions, the granite Sample #2 was fixed on the pedestal with a heater and a sensor inside, as shown in **Fig 4.7 (a)**. The triaxial cell is coupled with two water tanks which are used to ensure the water supply of the specimen as shown in **Fig 4.7 (b)**. Then the triaxial equipment was set on the rotate table and faced to the X-ray source. The external conditions of Sample #2 is set the same with granite Sample #1, as illustrated in **Chapter 3**. Then the Sample #2 was set into the triaxial cell and was scanned aperiodically.

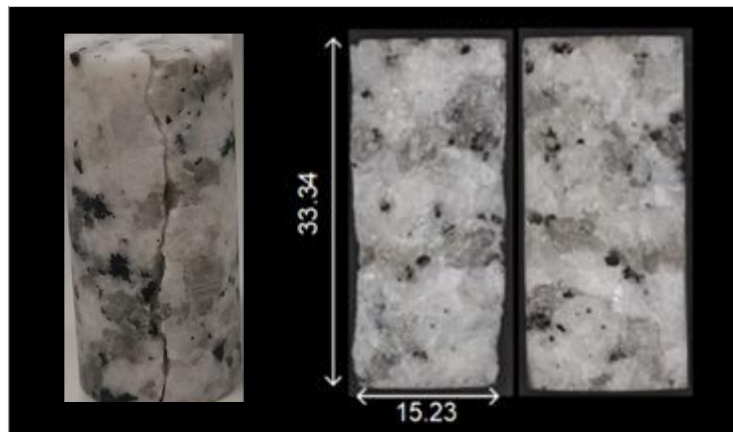


Fig.4.5 Granite sample #2 with a single rock fracture (15.23 mm × 33.34 mm)

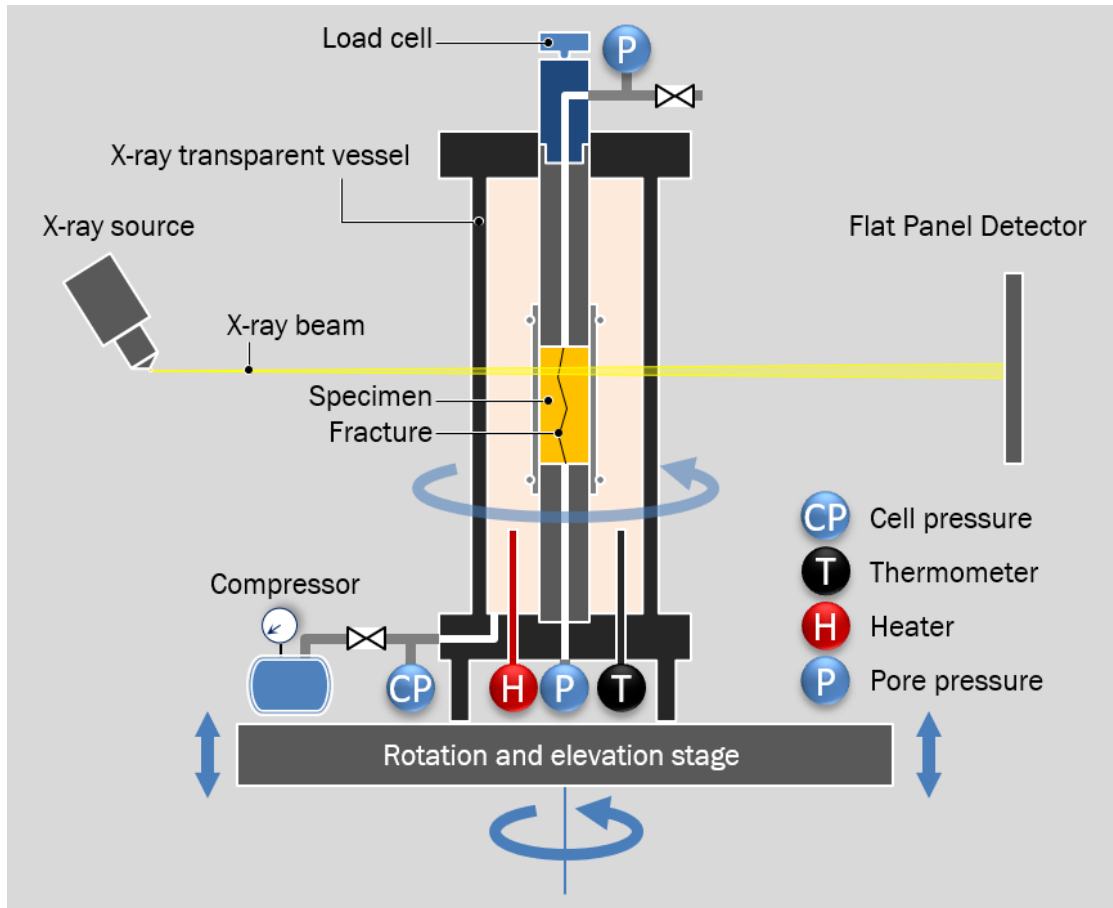


Fig.4.6 Triaxial cell coupled with the microfocus X-ray CT

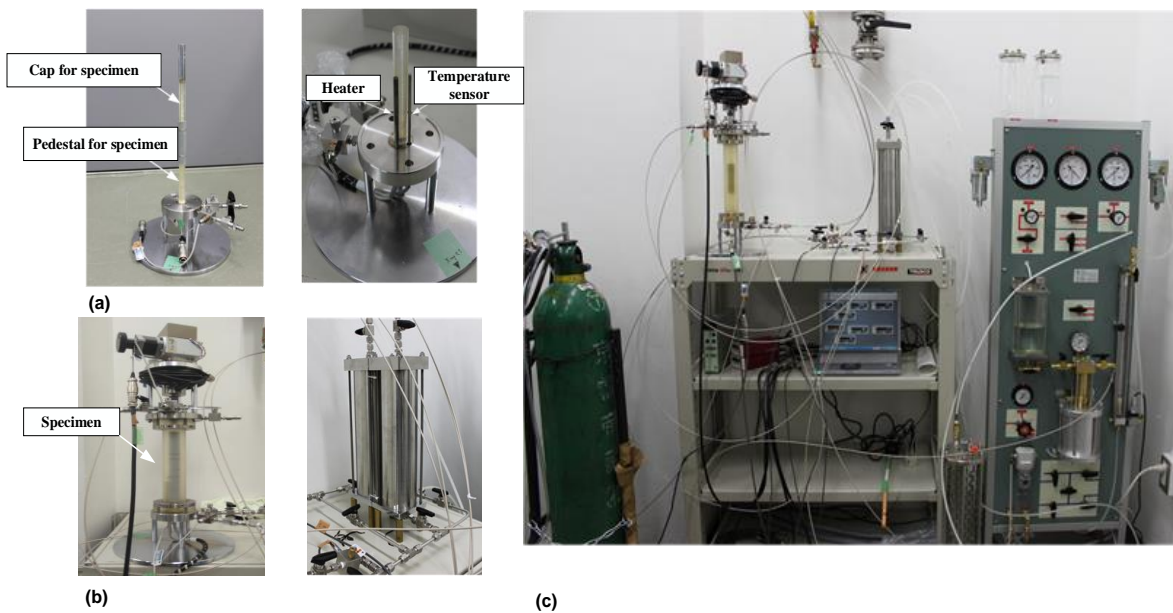


Fig.4.7 Triaxial cell with heating capabilities was installed on the work table with the microfocus X-ray CT (μ X-ray CT)

Table 4.1 Specifications of x-ray micro tomography facility (KYOTOGEO- μ XCT)

X-ray source	Maximum voltage (kV)	225
	Maximum current (mA)	0.888
	Maximum electric consumption power (W)	200
	Minimum spot size (μm)	4
Work table	Maximum scan area (mm)	200
	Maximum size of specimen (mm)	ϕ : 700 / h: 700
	Maximum weight of specimen (kgf)	45
Image intensifier (I.I.) (2007~2013)	Size of detector	9 / 6 / 4.5 inch (114.3 / 152.4 / 228.6 mm)
	Image matrix	512 ² / 1024 ² / 2048 ²
Flat panel detector (FPD) (2013~)	Feedback capacitance (gain) (pF)	0.25 - 8.0
	Image matrix	1024 ²
	Resolution performance (μm)	5
	Integration time (ms)	66 - 999
	Pixel size (μm)	200
	Projection view	600 - 4800
	Integration images	1 - 50
Total area (mm ²)	204 ²	
CT image	Spatial resolution performance (μm)	5
	Scanning method	Single beam (2D) Cone beam (3D)

4.3.2 Testing conditions

CT scan condition of each case is listed in **Table 4.2**. In a CT slice, the voxel size is $18.4 \times 18.4 \times 21.0$ micrometers in X , Y and Z directions, respectively. One CT slice is composed of 1024×1024 voxels. The total CT slices are composed to a three-dimensional, which is equivalent to the height of the whole sample (Sample #2: 33.34 mm) as shown in **Fig 4.8**. The initial mechanical aperture was obtained at the as-received (dry) condition of 0 MPa, and then the sample was fixed into the triaxial cell under the water-saturated condition. The confining pressure was increased up to 3.0 MPa and the temperature was set at 20 and 60 °C. At 20 °C, Sample #2 was scanned as the same time interval with the long-term permeability test. However, the CT scan conditions were changed after finishing the long-term CT observation at 20 °C. Various confining pressure conditions were applied during the second long-term CT scan at 60 °C.

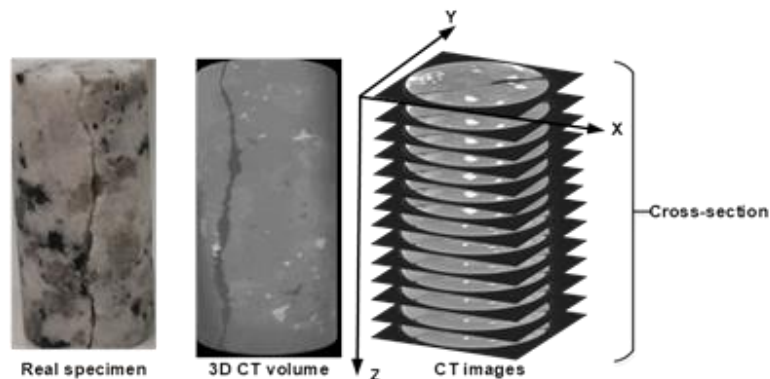
**Fig.4.8** Sample #2 is scanned with several cross-section CT images

Table 4.2 Experimental conditions at each case (i.e., 20 and 60 °C)

	Confining pressure (MPa)	Time (Day)	Voltage (kV)	Current (μ A)	Voxel size (μm^3)	Projection view	Scan area (mm)	Integrated images for one projection
20 °C	0	0	150	65	15.1 ² x17.0	4506	15.462	10
	3	0	160	90	18.4 ² x21.0	2253	18.824	15
	3	14	160	90	18.4 ² x21.0	2253	18.791	15
	3	30	160	90	18.4 ² x21.0	2253	18.798	15
	3	60	140	140	18.4 ² x21.0	2253	18.787	15
	3	90	160	90	18.4 ² x21.0	2253	18.728	15
	3	120	160	90	18.4 ² x21.0	2253	18.747	15
	3	150	150	140	18.4 ² x21.0	2253	18.695	15
	3	180	150	140	18.4 ² x21.0	2253	18.791	15
60 °C	3	0	150	140	18.4 ² x21.0	2253	18.784	15
	0	60	150	140	18.4 ² x21.0	2253	18.792	15
	0	120	150	140	18.4 ² x21.0	2253	18.785	15
	0	150	150	140	18.4 ² x21.0	2253	18.788	15

4.3.3 CT image analytical method

In a CT cross-section image, the fracture aperture position is an analytical object. In order to accurately achieve the fracture aperture, a segmentation of each material is required in the CT images. A CT image is an assembly of discrete voxels including representative CT values for each material; Therefore, the segmentation can be performed based on the CT values. In the present study, the rock phase and the void phase in the CT images of Sample #2 are distinguished from each other using a region-growing method (Rosenfeld., 1982). The method is implemented with the 3D image analysis software VGstudioMax3.1 (Volume Graphics GmbH) (Higo et al., 2014). This method examines the CT values of the neighbouring voxels around the initial seed voxels and determines whether the voxel neighbours are added into the region of seed groups. The regions are grown from the seed voxels to the adjacent voxels depending on a region membership criterion. This process is iterated until there are no change in two successive iterative stages. The essential factors in the region-growing method are initial seed voxel selection (3D location and CT value), a region membership criterion (range in CT values), and voxel connectivity for examination (26- connected neighborhood in 3-dimensional) as shown in **Fig 4.9**.

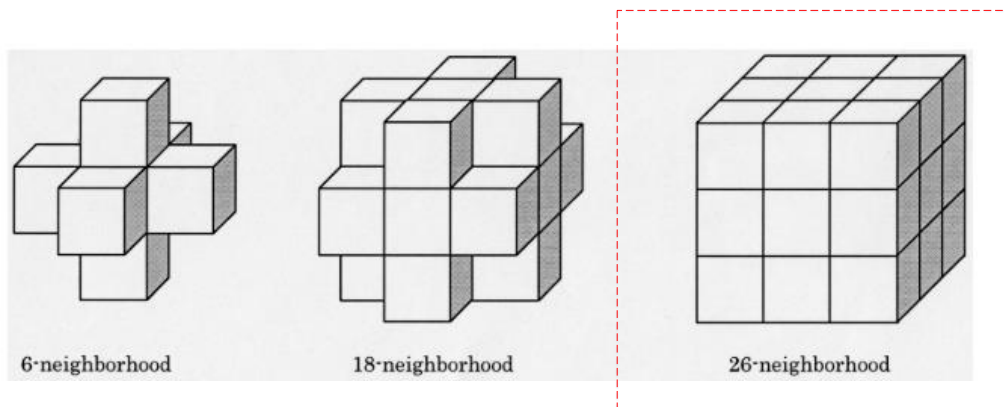


Fig.4.9 CT voxel connectivity for examination. Three types of connectivity are represented. i.e., 6- connected, 18- connected and 26- connected (in this study, 26- connected neighbourhood was used in 3-D) (Toriwaki et al., 2002)

Fig 4.10 shows the segmentation procedure of the rock phase using this method. Assuming that the distribution of the CT values for a homogeneous material follows a normal distribution, the mean values of the rock phase and the void phase are μ_1 and μ_2 , respectively, and their standard deviations are σ_1 and σ_2 , as shown in **Table 4.3**. A threshold of 82 between the void phase and the rock phase is consistent with the intersection of the histogram of the CT values for the two phases, as shown in **Fig 4.10 (a)**. A tolerance T to extract the rock phase using the region-growing technique is given by the difference between the mean value of the histogram of rock phase and the threshold. In this case, tolerance T is equal to 69.34.

The region growing process of the CT image in this study is explained as follows:

- 1) An initial seed voxel selection of which the CT value corresponds to the mean CT value of rock phase, i.e., 151, is chosen as shown in **Fig 4.10 (b)**. Region membership criterion determines whether the neighboring voxels of initial seed voxel are assimilated into the region of rock phase seed groups or not. Namely, the adjacent voxels of the initial seed voxel in the CT values that are more than $\mu_1 \pm T$, i.e., 82 would assimilate into the region of rock phase seed groups.
- 2) This process is iterated on until all of the neighboring voxels are assimilated and no further significant changing in two successive iterative stages. As a result, the representative segmentation image in 2-dimensional was obtained as shown in **Fig 4.10 (c)**. Red and black colors represent the rock phase and the void phase, respectively.
- 3) Voxel connectivity of the region-growing technique is 26-connected neighborhood in 3-dimensional, which ensures the continuity of adjacent voxels of the initial seed voxel at different orientations, i.e., X, Y and Z directions. Then the segmentation image in 3-dimensional is depicted in **Fig 4.10 (d)**.

Table 4.3 Histogram values of CT images

	Mean value of rock μ_1	Mean value of void μ_2	Standard distribution of rock σ_1	Standard distribution of void σ_2	Tolerance T
Sample #2	151.34	48.17	14.11	6.63	69.34

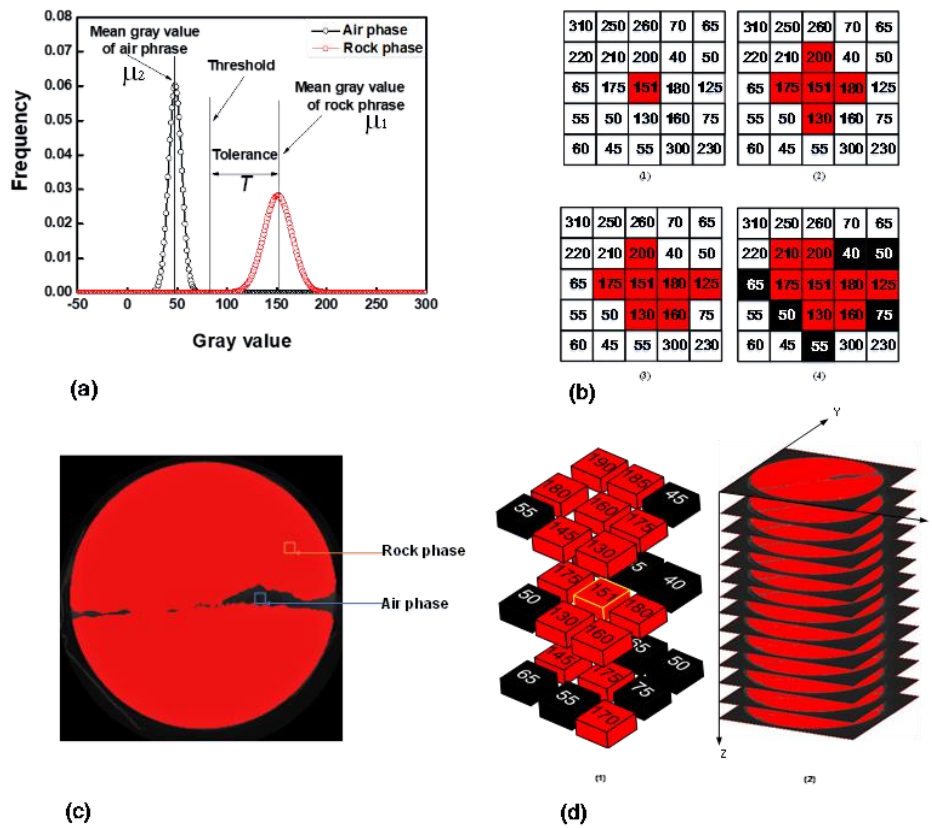


Fig.4.10 Segmentation process for rock phase and void phase by region-growing technique: (a) determination of tolerance of region growing, (b) schematic illustration of region growing in 2-D, (c) segmentation image in 2- D and (d) voxel connectivity of 26-connected neighbourhood.

The greatest characteristic of the region-growing technique is that it can extract the edges of the target material more clearly than other methods. **Fig 4.11** shows a comparison with two different CT segmentation methods, namely, the threshold method (Otsu et al., 1979) and the region-growing technique. In the former method, the CT value of 82 was only used as a threshold to distinguish the rock phase and the void phase. In this case, there are some voxels with CT values larger than 82 which are misrecognized as the rock phase, although they are obviously discontinuous with the real rock body. It is difficult to identify the aperture position correctly. In contrast, in the latter method, the adjacent voxels around the initial seed voxel selection of the rock phase are assimilated as the rock phase. In other words, only material which is physically continuous can be extracted, resulting in a reduction in the misidentification of the aperture position in the CT image.

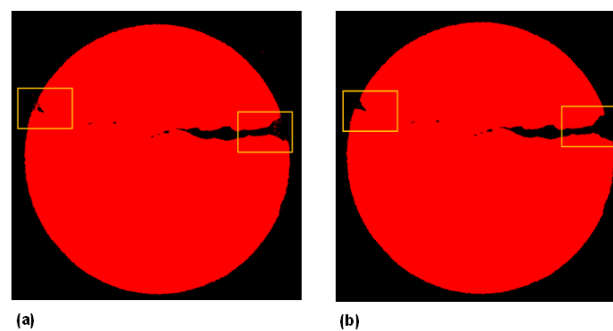


Fig.4.11 CT image segmentation results. (a) threshold method, and (b) region-growing method

Fig 4.12 (a) shows the identification of the aperture position using a segmentation image, in which the yellow rectangle, including the aperture of Sample #2, is chosen as the analytical region for the extracting aperture position. The coordinate of this analytical region is applied for all of the segmentation images. **Fig 4.12 (b)** illustrates the detection of the void phase, the position where a red voxel (a voxel for the rock phase), which is located above a black voxel (a voxel for the void phase), is detected by searching for voxels from the upper to the lower part of the image, i.e., in a negative direction to the y-axis. Then, the position of a black voxel, which is located above a red voxel, is also detected from the direction of the lower to the upper part of the image. From this detection, the aperture width is given by the number of voxels in the void phase, which are located between the upper surface roughness and the lower surface roughness. The same procedure is repeated for each X coordinate, and the position where there is no black voxel is identified as the contact area. **Fig 4.12 (c)** shows the enlarged area of the analytical region. As a result of the above search for a CT slice, the contact parts are found in the X direction. The same procedure is repeated for each slice, providing the contact-area ratio for Sample #2 by the same calculation as that mentioned above. A 3-D profile of the aperture distribution is shown in **Fig 4.13**. The black position denotes the rock contact-area, while the white position denotes the non-contact area.

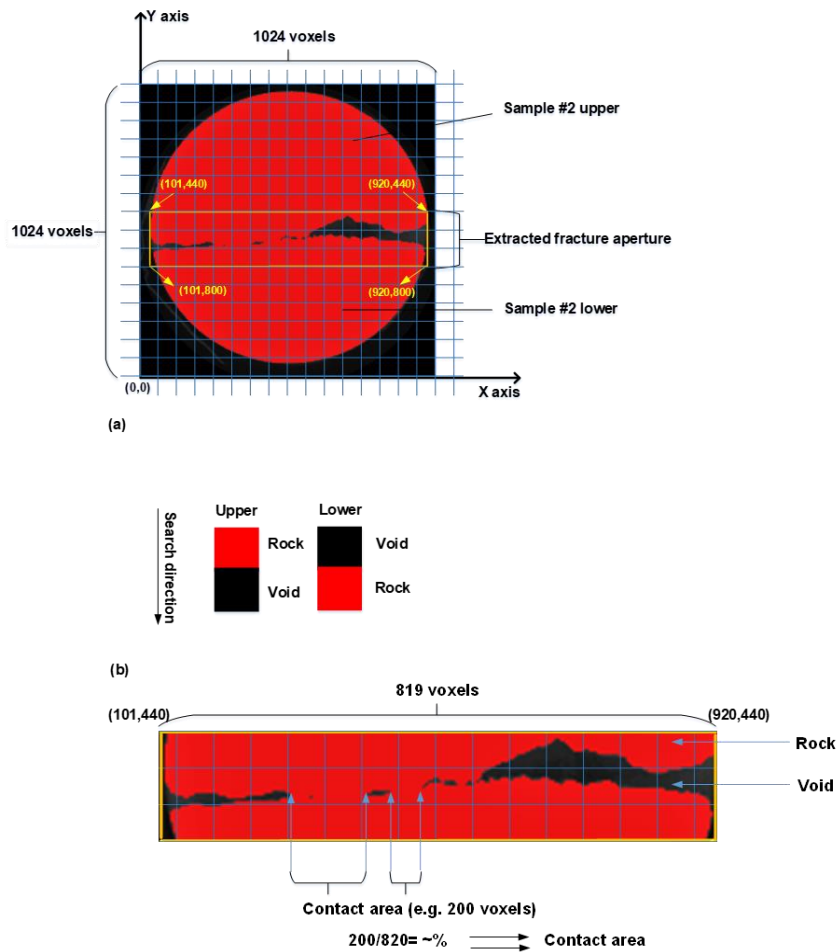


Fig.4.12 Segmentation procedure for voxels that contain both rock and void: (a) conception of image after segmentation process, (b) voxel that includes rock and void phases (aperture detection method) and (c) contact-area in aperture position

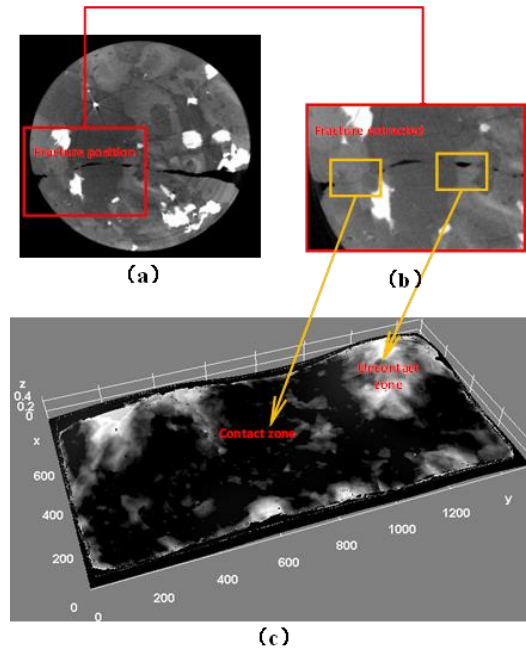


Fig.4.13 Illustration of the contact position within the fracture

4.4 Results of the X-ray CT observation

4.4.1 Long-term X-ray CT observation at room temperature

The irreversible behaviour of permeability variation has been verified at the long-term permeability tests in **Chapter 3**. It indicates that aperture was changed with time. The geometries of the fracture surfaces and the aperture distribution are important parameters for characterizing the flow paths within the fracture. **Fig 4.14** illustrates the contour maps of the CT image analysis results at 0 MPa. i.e., the fracture roughness of side A and the fracture aperture distribution. The extracted surface roughness (side A) of Sample #2 (**Fig 4.14 (a)**) is quite similar to which was measured from the optical profilometer using the pattern projection in **Chapter 3, Fig. 3.3**. The blue part at **Fig 4.14 (b)** represents the fracture contact-area. It is noted that the initial arithmetical mean aperture (hereinafter called the mechanical aperture) and the contact-area ratio without the confining pressure are 0.253 mm and 5.4%, respectively.

Moreover, the surface roughness of sample #2 (Side A) which are measured by the pattern projection of VG-3200 and by the CT analysis result is compared in **Fig.4.15**. The morphology comparison of down-roughness surface shows quite similar. Morphological similarity of the surface roughness also verified the accuracy of the CT analysis result.

Fig 4.16 shows the temporal change in the aperture variation using the CT image analysis in the long-term test. In **Fig 4.16 (a)** and **(b)**, the aperture distribution at 3.0 MPa shows a significant difference from that at the confining pressure of 0 MPa. The change in aperture under different confining stresses can be confirmed. It is also congruent with the permeability test results whereby the permeability is dependent on the confining stress conditions. In **Fig 4.16 (c)**, the blue areas become larger, which indicates that the contact area was enlarged after 90 days. Moreover, a further reduction of the aperture can be seen in **Fig**

4.16 (d). The fracture aperture gradually became narrower under the constant confining stress in 180-day holding period. **Fig 4.17** illustrates an enlarged comparison of the aperture variation in the original CT image. The locations of the cross-sections are at the same position, i.e., in the Z-direction of 18.7 mm. From the extracted fracture aperture images, a significant difference between the confining pressure at 0 MPa and that at 3.0 MPa was observed. The yellow arrows in **Fig 4.17** demonstrate that the aperture becomes smaller with time under the constant stress condition, which also indicates that the fracture surfaces should be deformed under the compaction condition.

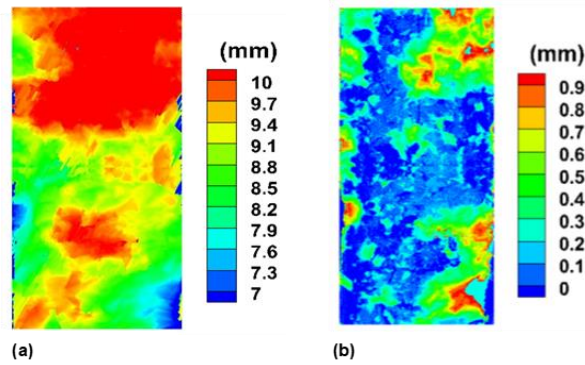


Fig 4.14 Contour maps of surface roughness and aperture distribution of Sample #2 at confining pressure of 0 MPa obtained through CT observation: (a) surface roughness and (b) aperture distribution

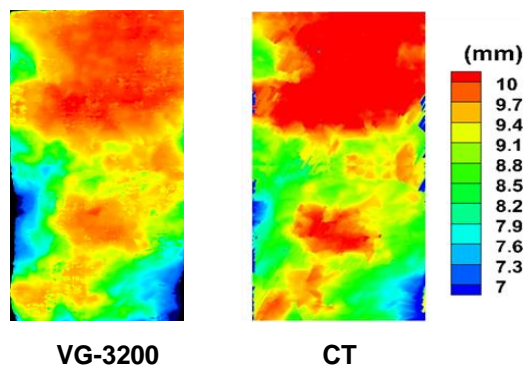


Fig.4.15 Comparison result of the surface roughness of Sample #2 (Side A) at 0 MPa, i.e., obtained by VG-3200 pattern projection and by the CT image analysis result

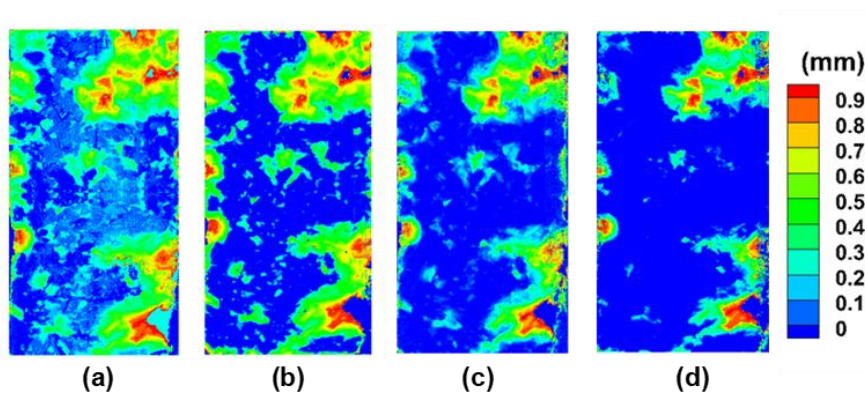


Fig.4.16 Temporal changes in aperture variation evaluated from CT analysis in long-term tests: (a) initial value of mean aperture at 0 MPa, (b) aperture variation after 0 days at 3.0 MPa, (c) after 90 days and (d) after 180 days

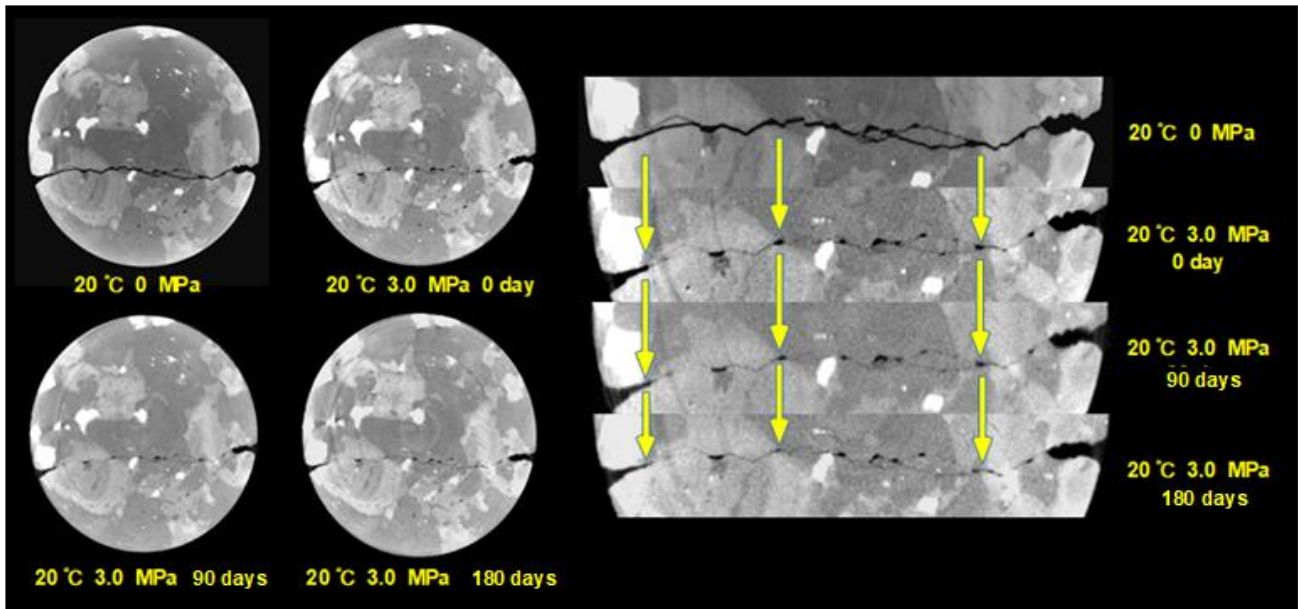


Fig.4.17 Temporal changes in aperture variation evaluated from CT scanning in long-term tests (comparison of the cross-section images at length direction of 18.7 mm, at 20 °C)

4.4.2 Long-term X-ray CT observation at elevated temperature

Aperture distribution at elevated temperature needs to be checked, then the temperature was increased to 60 °C and confining pressure was increased to 3.0 MPa. From 30 to 180 days, the confining pressure became 0 MPa. At 60 °C, aperture distribution and the contact-area ratio were measured aperiodically, results are shown in **Fig 4.18**. Aperture became narrower was confirmed at initial time. However, the contact area isn't have a significantly increase as the result at 20 °C,180 days. Aperture variation is not sensitive as it at 20 °C. Thermal expansion is not the determining role on the aperture reduction. It may due to the irreversible change of the fracture surfaces after a long-term. Moreover, the contact-area at 0 MPa has a random variation from 30 to 180 days. It should be noted that the aperture became open or closed at this period. Aperture values at 0 MPa, 60 °C was the approach to the value at 20 °C, 3.0 MPa. This also indicated that the aperture was not further influenced by the confining pressure. It is also corresponding to the permeability tests at 60 and 90 °C. The permeability had a random variation at a relatively high temperature.

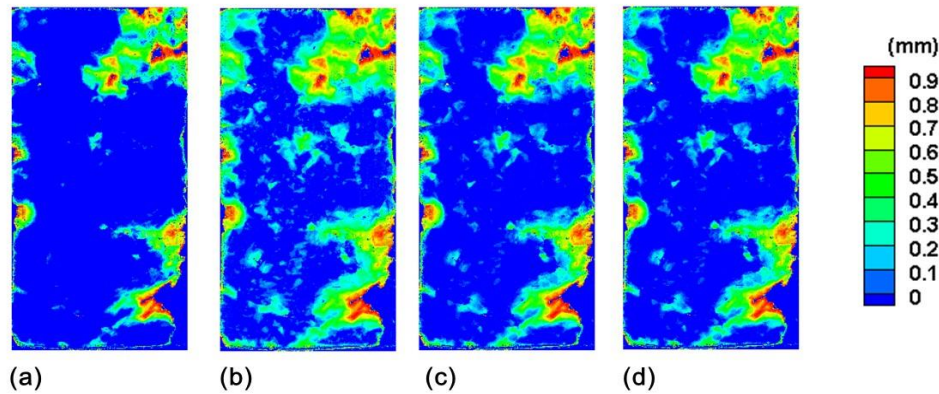


Fig.4.18 Temporal changes in aperture variation evaluated from CT analysis in long-term tests at 60 °C: (a) initial value of mean aperture at 3.0 MPa, (b) aperture variation after 60 days at 0 MPa, (c) after 120 days at 0 MPa, and (d) after 150 days at 0 MPa

4.5 Fracture contact conditions

4.5.1 Long-term contact-area ratio change at room temperature

Some researchers have studied about the contact-area ratio change through data prediction (Polak et al., 2003; Dimadis et al., 2014). Generally, it is hard to grasp the aperture distribution immediately. Some studies have illustrated that the aperture change at a cross-section, but it is difficult to comprehend the variation in the aperture distribution under various conditions (Stephanie et al., 2001). In this study, the aperture value and contact-area ratio were measured from a 3-D calculation. **Fig 4.19** shows the temporal changes in the mechanical aperture and the contact-area ratio from the CT analysis at 20 °C. The aperture value drastically decreases from 0 MPa to 3.0 MPa (**Fig 4.18(a)**). Simultaneously, the contact-area ratio increases from 5 % to 33 % (**Fig 4.18(b)**), which is consistent with the permeability test results in which the permeability shows a sharp decrease with the increase in the confining pressure. At the confining pressure of 3.0 MPa, the mechanical aperture decreases gradually to 7.5 % from 0 to 90 days. Then, it further decreases to 10 % from 90 to 180 days. Moreover, the tendency for the contact area to become larger can be confirmed. The contact-area ratio reaches approximately 37 % at 180 days. Geochemical reactions, such as the pressure solution, might also occur under the constant stress condition. The complex reaction on the fracture surfaces and the irreversible behavior of the aperture distribution in the long-term test under various conditions need to be further examined.

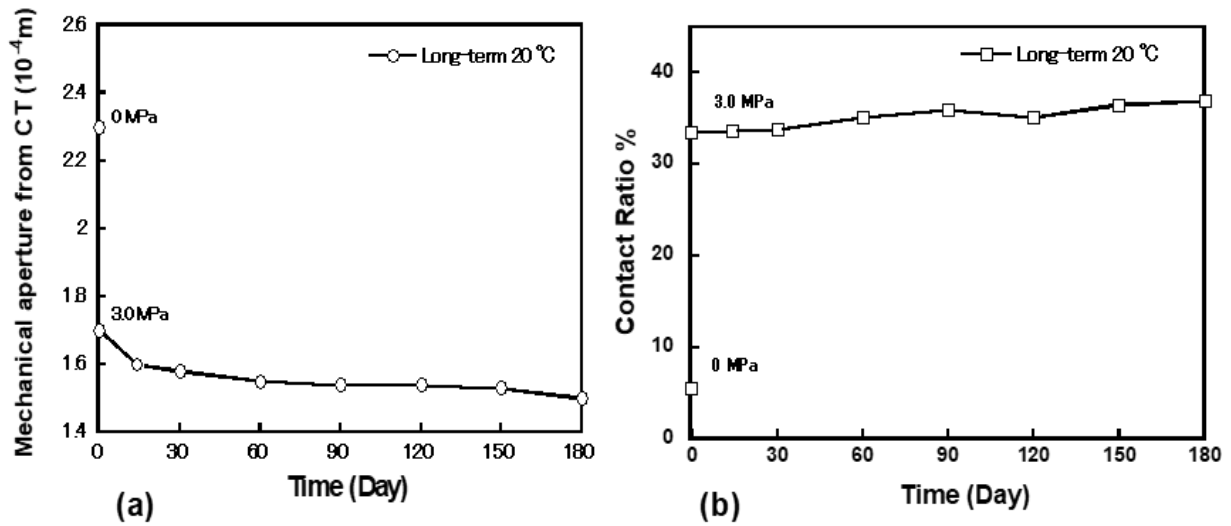


Fig.4.19 Temporal changes in (a) mean aperture value from CT analysis and (b) contact-area ratio variation at 20 °C

4.5.2 Long-term contact-area ratio change at elevated temperature

Aperture and the contact-area ratio variation at 60 °C are shown in Fig 4.20. At the initial time, the contact-area ratio reaches to 55 %. From 30 to 150 days, it decreased and changed randomly due to unloaded the confining pressure. The contact-area ratio value reached to 20 % after unloading the confining pressure to 0. However, before starting the long-term CT observation at 20 °C, CT observation at 0 MPa shows that the contact-area ratio was almost equal to 0 %. It can be noted that the fracture aperture was reduced under a higher temperature and various confining pressures. Moreover, fracture aperture has an irreversible change, and it is not sensitive to the temperature after a long-term. This result also shows a similar variation with the long-term permeability test at 60 °C, which presents that the permeability evolution became randomly and didn't decrease monotonously under a higher temperature.

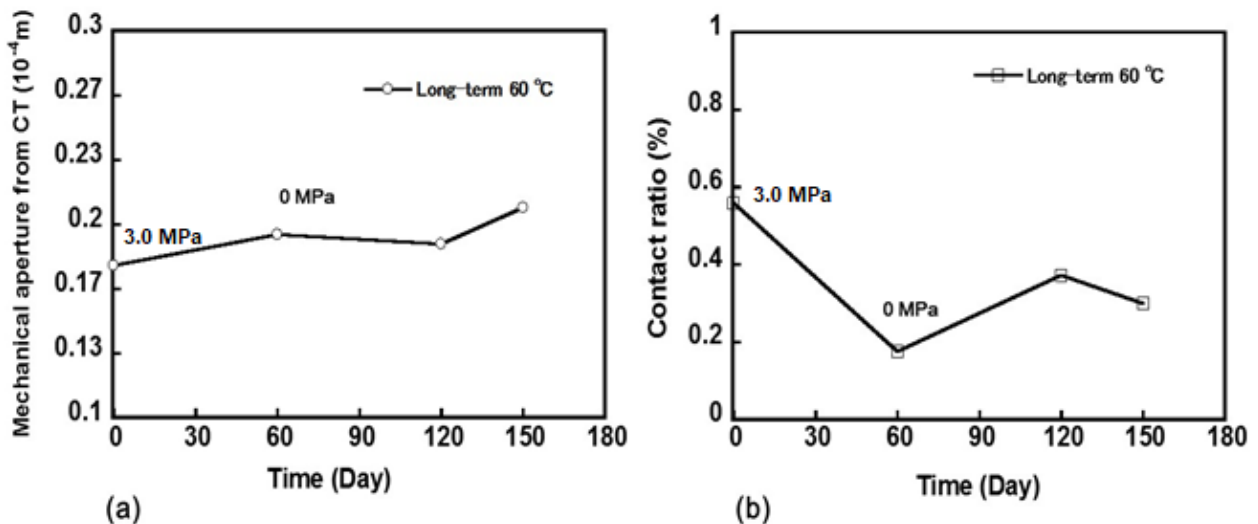


Fig.4.20 Temporal changes in (a) mean aperture value from CT analysis and (b) contact-area ratio variation at 60 °C

4.6 Discussions

4.6.1 Discussion of long-term hydraulic aperture change between CT observation and permeability tests

In order to examine the alteration of the internal aperture distribution, the confining pressure condition and the holding period were set to be the same as in the permeability test to investigate the mechanism of change in aperture in the long term at 20 °C. Furthermore, the aperture distribution and the contact-area ratio of the fracture surfaces under various confining pressures were analysed and compared.

Fig 4.21(a) shows a comparison of the mechanical aperture and the hydraulic aperture. The mechanical aperture shows a relationship between the hydraulic aperture and the contact-area ratio, as defined by (Walsh, 1981; Zimmerman, 1996; Li et al.,2008):

$$b_H^3 = b_M^3(1-R_C)/(1+R_C) \quad (4.5)$$

where b_H is the hydraulic aperture and b_M is the mechanical aperture. In the present study, the contact-area ratio and the mechanical aperture value are measured from the long-term CT observation. The results show that hydraulic aperture is lower than the mechanical aperture. Although cubic law assumes that the flow is ideal as smooth parallel plates, the real surface of rock joints is rough (Bandis et al., 1985). Moreover, the contact area disturbs the flow and the flow concentrates in a wide aperture area (Kishida et al., 2013). Therefore, the hydraulic aperture is always lower than the mechanical aperture (Renshaw, 1995; Zimmerman et al.,2004; Liu, 2005). The roughness characteristics influence the fluid passing through the aperture and lead to a hydraulic aperture that is lower than the mechanical aperture.

The hydraulic aperture obtained from the permeability tests and from the CT observation were compared, as shown in **Fig 4.21 (b)**. Their variation tendencies qualitatively match each other well. Although the two specimens are different in size, the material and the experimental conditions are set to be the same. However, the hydraulic aperture obtained from the permeability test is always lower. From the initial hydraulic aperture value to the end value after 180 days, the decreasing gradient of the hydraulic aperture obtained from the permeability test is about 52 % and the decreasing gradient from the CT observation is about 12 %. The hydraulic aperture from the permeability test had a more significant decrease than the value obtained from the CT observation. It can be inferred that the granite Sample #1 was applied in the short-term tests under different temperatures before the long-term test, but that the granite Sample #2 was applied under the same conditions as the long-term permeability test. During the short-term tests, the fracture surface roughness might be altered by the geo-chemical response, which may result in making the long-term hydraulic aperture value lower. From the long-term aperture distribution of the CT observation, the decreasing aperture and the increasing contact area can be confirmed, which also corresponds to the variation in the long-term permeability test results at 20 °C.

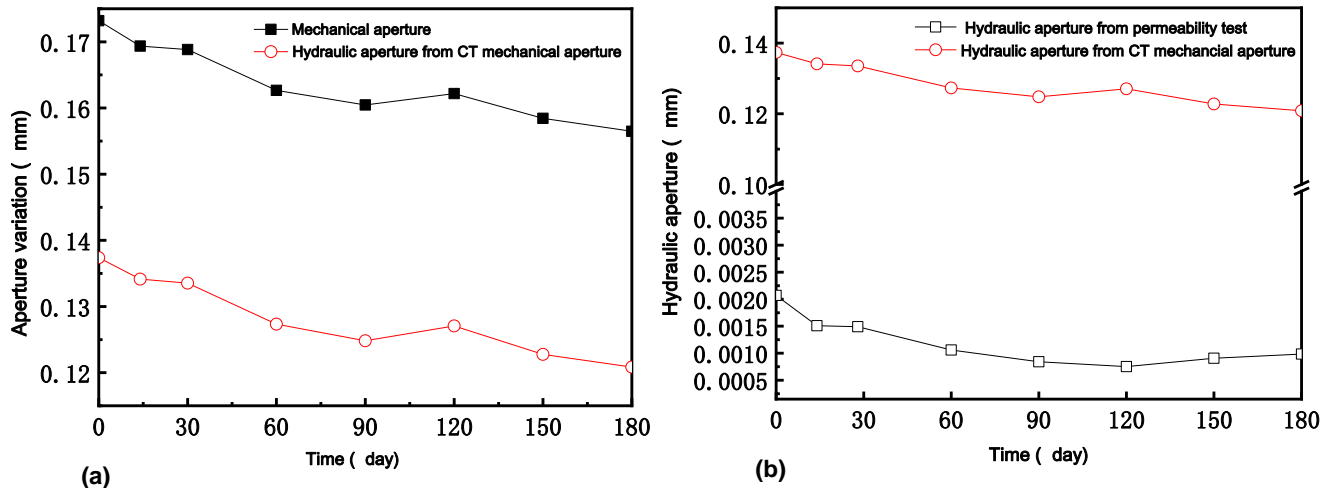


Fig.4.21 Comparison of changes in hydraulic aperture.(a)Comparison of changes between CT mechanical aperture and hydraulic aperture calculated from CT mechanical aperture.(b)Comparison changes in hydraulic aperture between permeability tests and CT mechanical aperture at 20 °C

4.6.2 Discussion of the effect factors on aperture change

4.6.2.1 Chemical-mechanical influence

The contact-area ratio was found to be an important factor to illustrate the aperture and permeability change in a long-term. The contact area variation may due to the pressure solution generated on the fracture asperities, and geochemical reactions occurred within the fracture in the long term. In this study, results showed that the contact-area increase, and the aperture decrease are congruent with the permeability test results. Moreover, the contact-area change indicated that the mineral dissolution and the precipitation might occur on the rough-walled fractures. Therefore, the hydraulic aperture and permeability were changed under various conditions in the long-term.

4.6.2.2 CT resolution influence

In order to check the accuracy of the contact-area ratio value, which was obtained from the X-ray CT observation, CT scanning resolution was considered as a pivotal effect factor. CT resolution may have a great influence on the calculation result. Therefore, in this section, different resolutions were chosen to verify the contact-area ratio difference. Since the CT images were widely analysed and applied in the medical field, current clinical images which were scanned by CT are well utilized in detecting the different subtypes of cell carcinoma at human organs (. Woodard et al., 1986; Mayo et al., 1987; Murata et al., 1988; Willner et al., 2015). It has a significant influence on the therapy and prognosis of cancer. Some research indicated that a lower clinical image resolution is hard to ensure the border delineation between the healthy and the tumorous tissue (Wildberger et al., 1997). A significant difference between the healthy and

tumorous tissue can be observed in **Fig 4.22**. e.g., A ($100\times 100\mu\text{m}^2$) and D ($500\times 500\mu\text{m}^2$). (Braunagel et al., 2017).

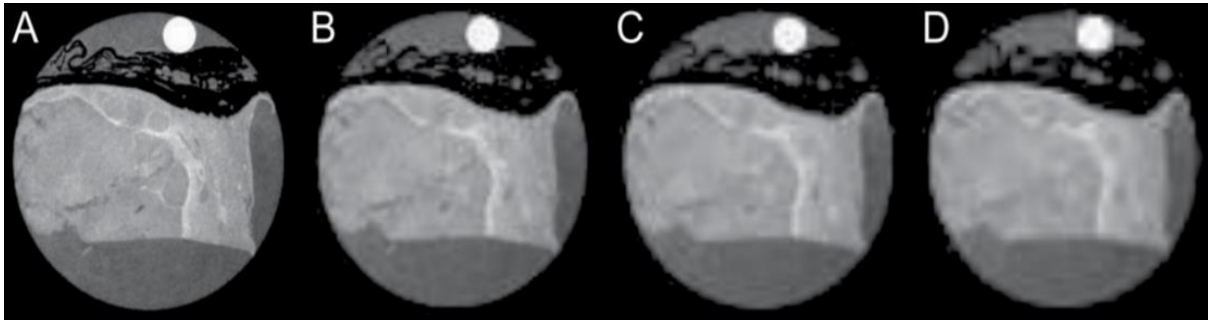


Fig.4.22 Influence of the CT resolution on the tumorous tissue images. (a) $100\times 100\mu\text{m}^2$, (b) $300\times 300\mu\text{m}^2$, (c) $400\times 400\mu\text{m}^2$, (d) $500\times 500\mu\text{m}^2$ (Braunagel et al., 2017)

Medicinal researches indicate that different matrix size of the CT images have a great influence on the quality of CT images, and the image analysis results may be different due to the different size of the matrix, as shown in **Fig 4.23**. There are separated three different matrix sizes. Larger matrix sizes (i.e., 1024×1024 , 2048×2048) are utilized for getting a relatively high resolution of CT images while small matrix (i.e., 512×512) represents the lower resolution (Hata et al., 2018). Therefore, the CT image resolution difference was considered as a key point which may have a great effect on the analysis result.

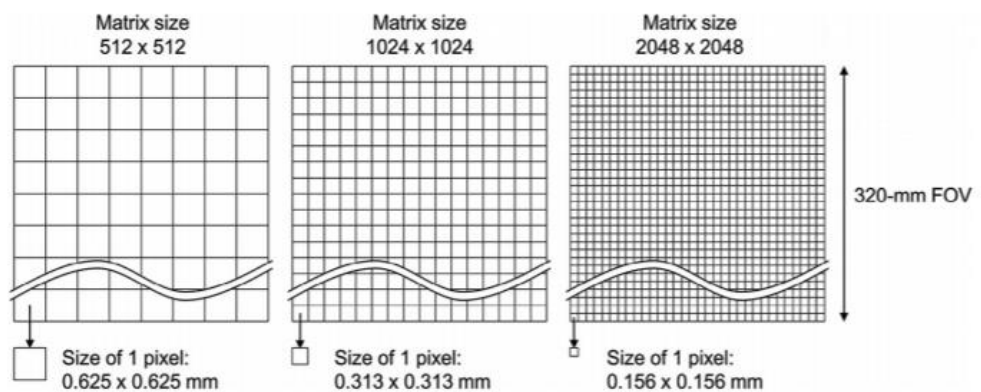


Fig.4.23 Different CT matrix size represents different resolution (Hata et al., 2018)

4.6.2.2.1 Testing condition of the CT resolution

Considering to check the CT resolution influence, the checking process is separated into two steps. At the first step, the normal resolution and the low-resolution CT images were compared. Pre-experiment CT images (i.e., without confining pressure) were used in this step. The CT scan condition is listed in **Table 4.4**. **Fig 4.24** illustrates the matrix size of one cross-section CT image. First, the granite specimen was scanned with a 1024×1024 matrix size in *X*- and *Y*-direction. i.e., the normal resolution. The whole slices are 1788 in *Z*-direction, which are corresponding to the length of the sample. Second, the matrix

size was reduced from the normal scale image (i.e., 1024×1024 matrix size) to a low scale image (i.e., 512×512 matrix size), then the voxel size at each X and Y direction was enlarged and the CT resolution became lower.

After that, the normal resolution and the high-resolution CT images were compared. At this step, the post-experiment (i.e., after long-term CT observation of $60\text{ }^{\circ}\text{C}$, 0 MPa) CT images were used. The CT image scan condition is listed in **Table 4.5**. In order to get a high-resolution CT image, the voxel size at each X and Y direction was reduced twice smaller than the normal voxel size. **Fig 4.25** is a schematic figure which represents the different resolutions comparison. i.e., the normal resolution, lower and higher resolution.

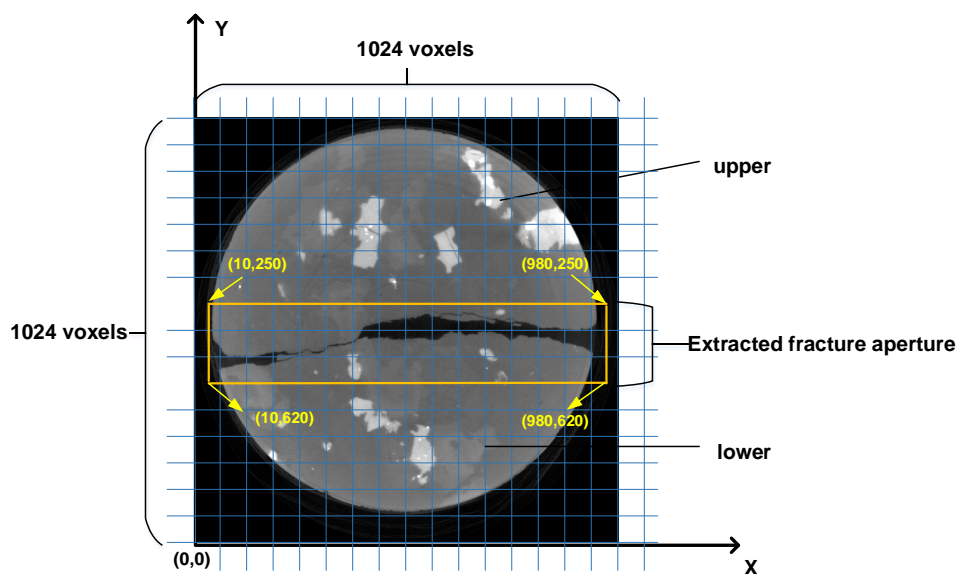


Fig.4.24 A cross-section of the granite CT image with the matrix size of 1024×1024 through CT observation

Table 4.4 CT scanning condition between normal resolution and low resolution

	Matrix size	Confining pressure (MPa)	Time (Day)	Voltage (kV)	Current (μA)	Voxel size (μm^3)	Slice number
Normal resolution	1024×1024	0	0	150	65	$15.1^2 \times 17.0$	1788
Low resolution	512×512	0	0	150	65	$30.2^2 \times 34.0$	896

Table 4.5 CT scanning condition between normal resolution and high resolution

	Matrix size	Confining pressure (MPa)	Scan Time (Day)	Voltage (kV)	Current (μA)	Voxel size (μm^3)	Slice number
Normal resolution	1024×1024	0	May.28th	150	65	$18.30^2 \times 21.0$	1788
High resolution	1024×1024	0	June.03th	150	65	$8.86^2 \times 11.0$	3287

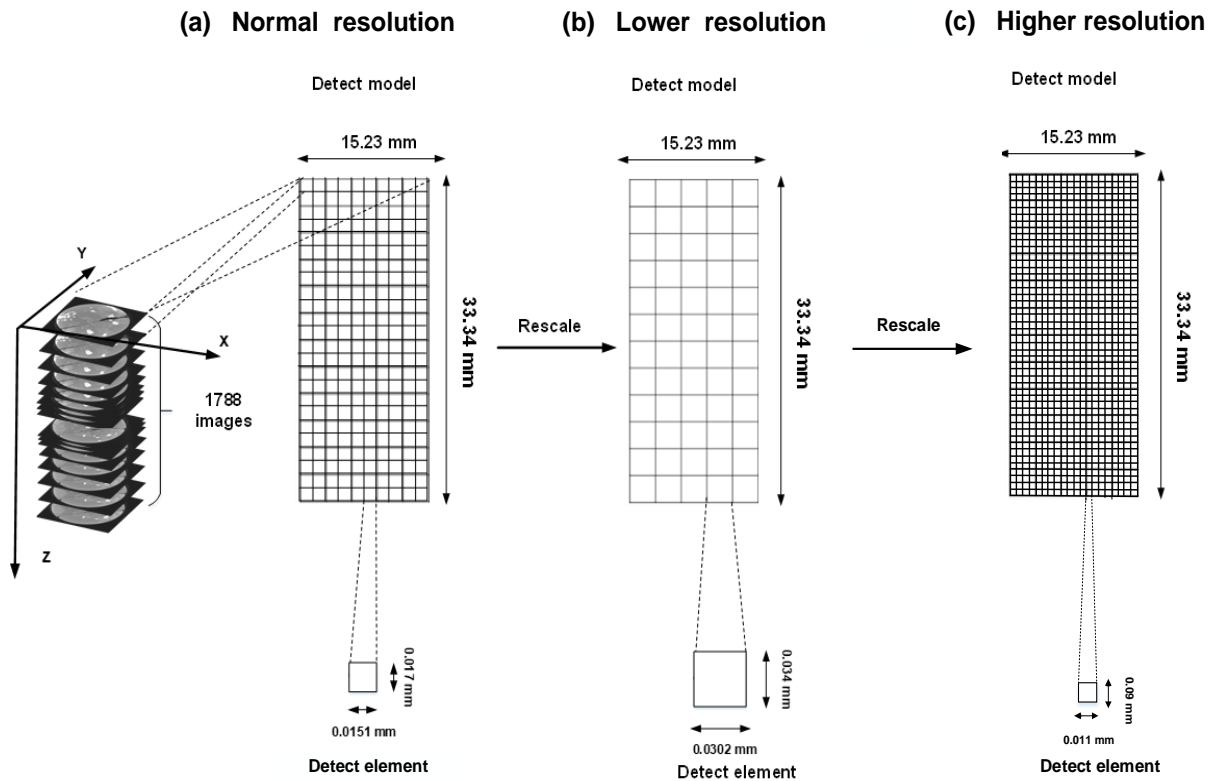


Fig.4.25 Comparison between normal resolution and scale transformation resolutions (a)normal resolution, size of the detect element at x, y direction is 0.0151 mm and at z direction is 0.017 mm. The matrix size is 1024×1024 , slice number of the sample is 1788, (b) low resolution, size of the detect element at x, y direction is 0.0302 mm and z direction is 0.034 mm. The matrix size is 512×512 , slice number of the sample is 896, (c) high resolution, size of the detect element at x, y direction is 0.0886 mm and z direction is 0.011 mm. The matrix size is 1024×1024 , slice number of the sample is 3287.

4.6.2.2.2 Results and comparison of the CT resolution

4.6.2.2.2.1 Comparison between normal resolution and low resolution

Fig 4.26 shows the original CT image comparison between the normal and low-resolution. i.e., the cross-section CT image was picked up from Z -direction of 0.6 cm. There is no obvious difference from observing this cross-section comparison. **Fig 4.27** shows the magnified aperture position comparison based on **Fig. 4.26**. The low-resolution image, i.e., see in (b). i.e., the matrix size of 512×512 shows blurred and poor quality with a comparison of the normal resolution image (a). i.e., matrix size of 1024×1024 .

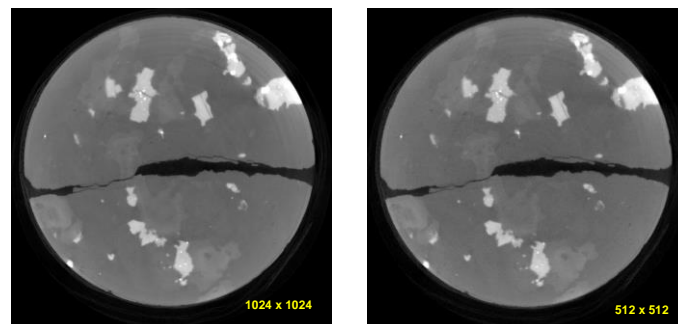


Fig.4.26 CT image comparison between normal resolution and low resolution (at z -direction of 0.6 cm)

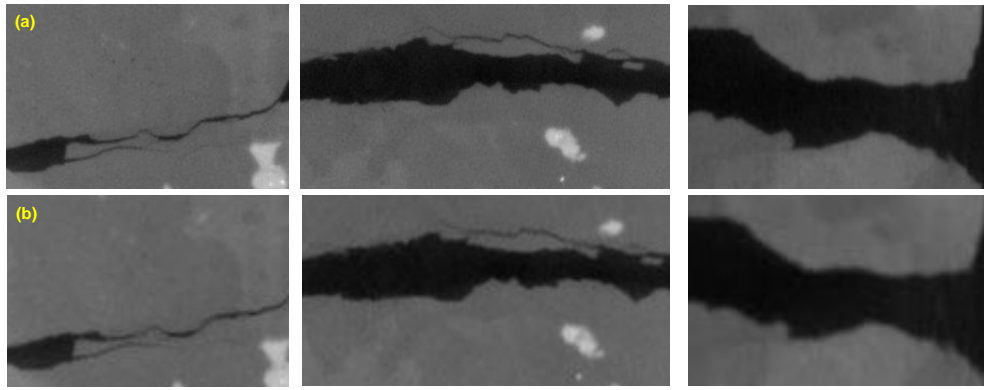


Fig.4.27 Enlarged aperture position, CT image comparison between normal resolution and low resolution (a) 1024×1024 (b) 512×512 . The 512×512 looks blurry

Moreover, aperture distribution which were obtained from the normal resolution and the low-resolution are compared. Aperture distribution is quite similar although the resolution is different. From the CT analysis result in **Fig 4.28**, it can be seen that the pixel number at X - and Y -direction of low-resolution is smaller. However, the calculation result shows that the contact-area ratio values of the two resolutions have no significant difference, as listed in **Table 4.6**. Aperture and contact=area ratio value are equal to 0.25 mm,0.26 mm, and 5.6%, 5%,respectively. Therefore, the low-resolution CT image has a slight influence to the calculation result.

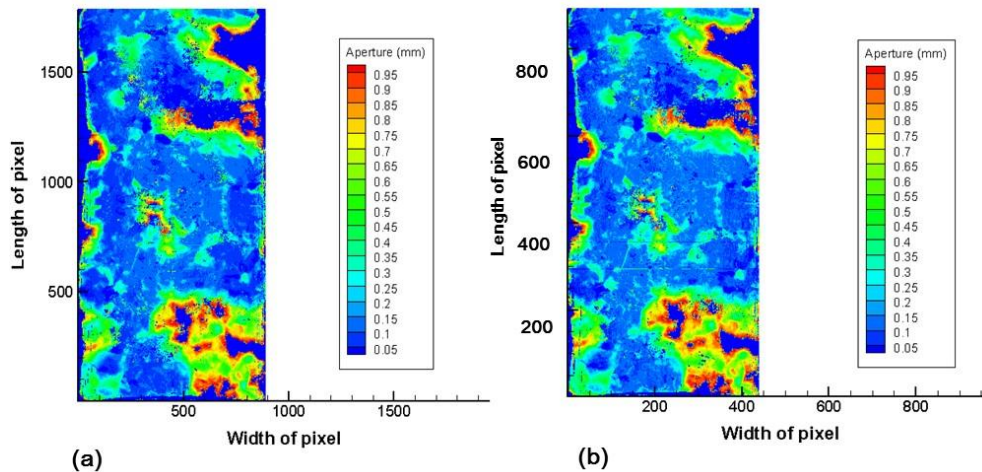


Fig.4.28 Aperture distribution comparison between normal and low resolution (a) 1024×1024 matrix, (b) 512×512 matrix

Table 4.6 Aperture and contact-area ratio results between normal resolution and low resolution

	Matrix size	Aperture value (mm)	Contact ratio (%)
Normal resolution	1024×1024	0.25 mm	5.6 %
Low resolution	512×512	0.26 mm	5.0 %

4.6.2.2.2 Comparison between normal resolution and high resolution

The experiment process of normal resolution and high-resolution are conducted as follows:

The sample was taken out from the device after finishing the CT observation test of 60 °C. The sample was scanned as two steps. At first, it was scanned as the normal resolution (2019.05.28). Second, it was scanned as a high-resolution (2019.06.03). The CT scan condition of the high-resolution has been illustrated in **Table 4.5**. In order to achieve a high-resolution CT image, the CT X-ray source was concentrated on the center of the sample, as shown in **Fig 4.29**. The high-resolution CT images were scanned about 3287 slices. Aperture distribution comparison of the normal and high-resolution is shown in **Fig 4.30**, the pixel number of aperture distribution at the length and width in *X*- and *Y*- direction is different. Then the aperture and contact-area ratio values are calculated, as listed in **Table 4.7**. CT analysis result shows that the CT resolution has an obvious difference on the calculation result. Under these two resolutions, the aperture and the contact-area ratio value difference are about 0.01 mm and 5 %, respectively.

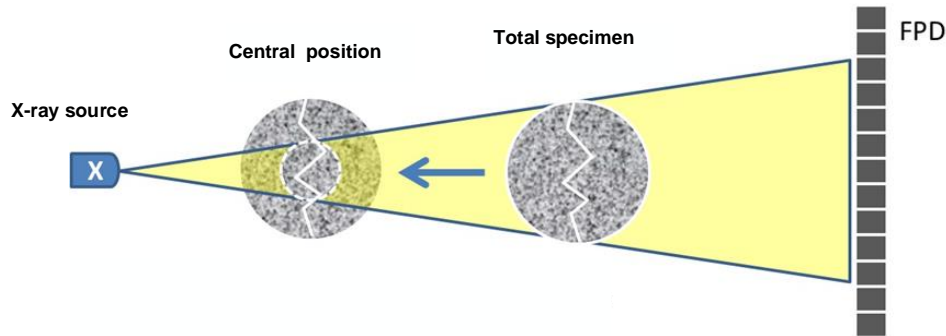


Fig.4.29 Illustration the process of CT scanning at a high resolution

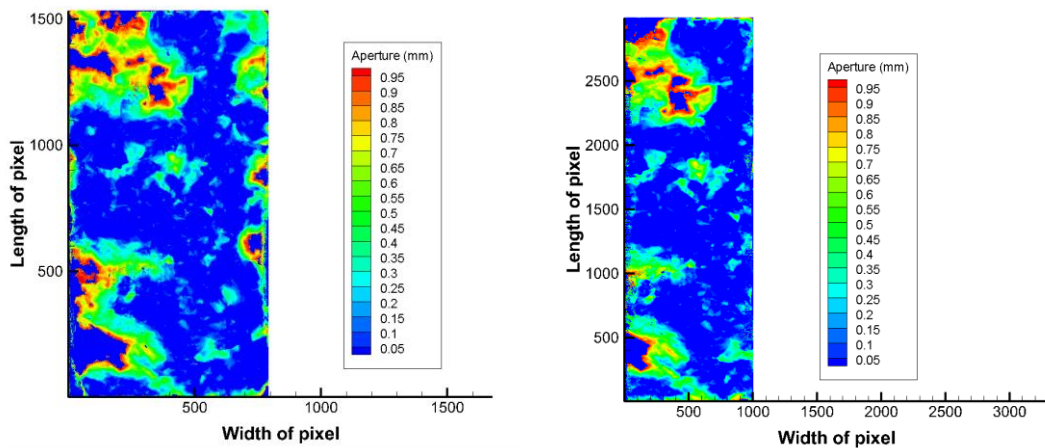


Fig.4.30 Aperture distribution comparison between normal and high resolution (a)1024×1024 matrix, (b) 1024×1024 matrix

Table 4.7 Aperture and contact-area ratio results between normal resolution and low resolution

	Matrix size	Aperture value (mm)	Contact ratio (%)
Normal resolution	1024 × 1024	0.174	55.9 %
High resolution	1024 × 1024	2.162	50.2%

4.6.2.2.3 Brief summary

In this study, different CT resolution analysis results show that different CT resolution has influence on the calculation result. There is no obvious distinction between the normal resolution and the low-resolution. However, there is some difference between the normal resolution and high-resolution. Results show that the contact-area ratio which was calculated from a high-resolution CT image has an obvious difference from the normal resolution. The contact-area ratio decreased about 5% by analysing a higher CT resolution image. Therefore, different CT resolutions of CT image should be further checked.

4.7 Summary

In this section, X-ray CT was used to observe the fracture aperture change under different conditions. Granite sample 2# was fixed into the triaxial cell and coupled with the X-ray CT scanning system.

1. The granite sample 2# was set the same condition with the long-term permeability test at 20 °C. Mechanical aperture and contact-area ratio change were calculated through the CT image analysis. Result showed that the aperture decrease has a similar variation with the permeability at 20 °C.
2. Hydraulic aperture from the permeability tests and from the CT observations were compared. Hydraulic aperture is lower than the mechanical aperture. This is also consistent with the reason that the flow channel within the fracture aperture is much narrower than the mechanical aperture; From the hydraulic aperture comparison result, it is noted that hydraulic aperture from the CT mechanical aperture has the same decreasing tendency with from the permeability test at 20°C. It can be summarized as two reasons. First, the experimental conditions of the permeability test and CT observation were set as the same. Second, granite Sample #2 is used the same material with Sample #1 although the size of them is different. Therefore, the hydraulic aperture variation from the permeability test and from the CT mechanical aperture have a similar variation. Moreover, hydraulic aperture value from the permeability test result shows much lower than from the CT mechanical aperture. It might be due to the variation of the fracture roughness surface after the short-term permeability tests. Short-term tests under various conditions were conducted before starting the long-term permeability test at 20 °C. Therefore, the fracture surface was altered under a hydro-thermal coupled processes, and the aperture became much narrower before conducting the long-term tests.
3. CT observation of granite sample #2 was conducted under different confining stress conditions at 60 °C. Aperture distribution and the contact-area ratio change under different confining pressure conditions were discussed. Results showed that the aperture was changed irregular after unloading the confining pressure. It can be inferred that the fracture roughness surfaces might be altered at a higher temperature, and the geochemical reaction may generate within the fracture aperture under a high temperature in the long-term. Which will procedure a random change of the aperture and contact-area ratio.
4. From the experiment result, we found that the CT resolution may have a significant influence on the calculation result. Therefore, different CT resolutions were chosen and were discussed. Result showed that the low-resolution CT image has a slight influence on the calculation result. However, the high-resolution analysis result makes a difference with the normal resolution. Contact-area ratio decreased under a high CT resolution CT analysis. It can be supposed that different CT image resolution and analysis method may have a big influence on achieving the accuracy information of internal fracture.

References

- Bandis, S., Makurat, A., Vik, G. :Predicted *and* measured hydraulic conductivity of rock joints. *Int. Symp. Fundamentals of Rock Joints, Bjørkliden*. pp. 269–280.1985.
- Braunagel, M., Birnbacher,L., Willner,M.: Qualitative and Quantitative Imaging Evaluation of Renal Cell Carcinoma Subtypes with Grating-based X-ray Phase-contrast CT. *Scientific Reports*. 7: 45400.2017.
- Caulk, R.A., Ghazanfari, E., Perdrial, J.N., Perdrial, N.: Experimental investigation of fracture aperture and permeability change within Enhanced Geothermal Systems. *Geothermics*. 62: 12-21.2016.
- Dimadis, G., Dimadi, A., Bacasis, I. :Influence of fracture roughness on aperture fracture surface and in fluid flow on coarse-grained marble, experimental results. *Journal of Geoscience and Environment Protection*. 2: 59-67.2014.
- Hata,A., ,Yanagawa,M., Osamu,H.,Noriko,K.,Tomo,M.,Tsukagoshi,S.,Uranishi,A.,Tomiyama,N. : Effect of Matrix Size on the Image Quality of Ultra-high-resolution CT of the Lung: Comparison of 512×512 , 1024×1024 , and 2048×2048 . *Academic Radiology*, Vol 25, No 7, July 2018.
- Higo,Y.,Oka, F.,Morishita, R.,Matsushima, Y.,Yoshida, T. : Trinarization of μ X-ray CT images of partially saturated sand at different water-retention states using a region growing method. *Nuclear Instruments and Methods in Physics Research Section B: Beam Interactions with Materials and Atoms*. 324: 63-69.2014.
- Kamali-Asl, A., Kc, B., Foroutan, M., Ghazanfari, E., Cladouhos, T. : Experimental study of fracture response in granite specimens subjected to hydrothermal conditions relevant for enhanced geothermal systems. *Geothermics*. 72: 205-224.2018.
- Kido, R. : Microscopic Characteristics of Partially Saturated Soil and their Link to Macroscopic Responses. *doctoral thesis*.2019.
- Kido, R., Higo, Y.: Evaluation of distribution of void ratio and degree of saturation in partially saturated triaxial sand specimen using micro x-ray tomography. *Japanese Geotechnical Society Special Publication*. 5(2): 22-27.2017.
- Kishida, K.,Sawada,A.,Yasuhara,H.,Hosoda,T.:Estimation of fracture flow considering the inhomogeneous structure of single rock fractures. *Soils and Foundations*. 53(1): 105-116.2013.
- Li, B., Jiang, Y.,J, Koyama, T., Jing, L.R., Tanabashi, Y. :Experimental study of the hydro-mechanical behavior of rock joints using a parallel-plate model containing contact areas and artificial fractures. *International Journal of Rock Mechanics and Mining Sciences*. 45(3): 362-375.2008.

Liu, E.: Effects of fracture aperture and roughness on hydraulic and mechanical properties of rocks: implication of seismic characterization of fractured reservoirs. *Journal of Geophysics and Engineering*. 2(1): 38-47.2005.

Mayo, J.R., Webb, W.R., Gould, R., Stein, M.G., Bass, I., Gamsu, G., Goldberg, H.I.: High-resolution CT of the lungs: an optimal approach. *Radiology*. 163:507–510.1987.

Murata, K., Khan, A., Rojas, K.A., Herman, R.G.: Optimization of computed tomography technique to demonstrate the fine structure of the lung. *Invest Radiol*. 23:170–175.1988.

Okamoto, A., Tanaka, H., Watanabe, N., Saishu, H., Tsuchiya, N.: Fluid Pocket Generation in Response to Heterogeneous Reactivity of a Rock Fracture Under Hydrothermal Conditions. *Geophysical Research Letters*. 44(20): 10,306-310,315.2017.

Otsu, N.: A Threshold Selection Method from Gray-Level Histogram. *IEEE Trans. Systems Man, and Cybernetics*. 9: 62-66.1979.

Polak A, Elsworth D, Yasuhara H. : Permeability reduction of a natural fracture under net dissolution by hydrothermal fluids. *Geophysical Research Letters*. Vol. 30.2003.

Renshaw, C.E.: On the relationship between mechanical and hydraulic apertures in rough-walled fractures. *Journal of Geophysical Research: Solid Earth*. 100(B12): 24629-24636.1995.

Rosenfeld, A., Kak, A.C. :Digital Picture Processing, San Diego, CA: *Academic Press*.1982.

Stephanie, P., Bertels, David, A. Measurement of aperture distribution, capillary pressure relative permeability, and in situ saturation in a rock fracture using computed tomography scanning. *Water Resource Research*. 37(3):649-662.2001.

Toriwaki, V.J., Yonekura, T.: Euler Number and Connectivity Indexes of a Three Dimensional Digital Picture. *Forma*. 17(3): 183-209.2002.

Walsh, J.B. :The Effect of Pore Pressure and Confining Pressure on Fracture Permeability. *International Journal of Rock Mechanics and Mining Sciences*. Vol. 18, No. 5, pp. 429-435.1981.

Wildberger, J.E., Adam, G., Boeckmann, W., Münchau, A., Brauers, A., Günther, R.W., Füzesi, L.: Computed tomography characterization of renal cell tumors in correlation with histopathology. *Invest Radiol*. 32, 596–601.1997.

Willner, M., Fior, G., Marschner, M., Birnbacher, L., Schock, J., Braun, C., Fingerle, A.A., Noël, P.B., Rummeny, E.J., Pfeiffer, F., Herzen, J.: Phase-Contrast Hounsfield Units of Fixated and Non-Fixated Soft-Tissue Samples. *PLoS One*. 10, e0137016, doi: 10.1371/journal.pone.0137016.2015.

Woodard, H. Q., White, D. R. :The composition of body tissues. *Br J Radiol*. 59, 1209–1218.1986.

Yasuhara H, Kinoshita N, Ohfuji H, Takahashi, M., Ito, K., Kishida, K: Long-term observation of permeability in sedimentary rocks under high-temperature and stress conditions and its interpretation mediated by microstructural investigations. *Water Resources Research*. 51(7): 5425-5449.2015.

Zimmerman, R.W., Bodvarsson, G.S. :Hydraulic conductivity of rock fractures. *Transport in Porous Media*, Vol. 23:1-30.1996.

Zimmerman, R.W.,Main, I.G.: Hydromechanical behaviour of fractured rocks. *Mechanics of Fluid-Saturated Rocks ed Y Gueguen and M Bouteca (London: Elsevier)*. 361–419.2004.

Chapter 5 Effect of different image processing methods on estimating a single granite fracture under different conditions

5.1 Introduction

Estimating the fluid behavior within the fractured rocks in deep subsurface (Tsang et al., 2005; Ellis et al., 2013) is essential on rock engineering fields, such as on the underground nuclear waste repositories and on the enhanced geothermal systems. Flow behavior within the fractured rock is controlled by fracture evolution (McGuire et al., 2013). Fracture aperture change within the rocks under complexed conditions would alter the flow direction, and it may result in the leakage of radioactive waste. Then the radionuclide transports within the fractured rocks in a long-term will further destroy the environment (Silveira et al., 2013). Some laboratory works focused on the hydraulic aperture variation under various conditions. The experiment results clarified that fracture aperture was altered by the interaction of various conditions (i.e., THMC process, thermal-hydraulic-mechanical-chemical coupled process) (Elsworth et al., 2006; Danko and Ghassemi, 2012). Moreover, fracture geometry was changed in a long-term under the coupled conditions (Polak et al., 2003; Yasuhara et al., 2006; 2008), which is a fundamental problem on influencing the underground water flow within the fractured rock mass.

Microfocus X-ray CT scanning has been widely applied on the medical field (Joseph et al., 1978; Vig et al., 2012, Hata et al., 2018). It has the capability to detect internal structures of the material and to measure the rock aperture, length, void, contact-area, and orientation immediately (Van et al., 2001; Ketcham et al., 2010; Farough et al., 2016; Okamoto and Dustin, 2017; Kumaria, 2018). Previous studies showed that the rock fracture geometry was observed by X-ray CT. Internal rock pore structure at pre- and post- experiments were compared (Polak et al., 2003; 2004). Moreover, mineral dissolution and precipitation reactions within the internal fracture were also observed (Yasuhara et al., 2015; Farough et al., 2016). Therefore, fracture aperture reduction and tortuosity of the flow path within the fractured rock can be verified by the CT observation.

In general, a 2-D fractured rock sample CT image is composed by three primary regions, i.e., the void phase of the fracture position, the rock phase, and the mineral composition on the rock surface (Bertels et al., 2001; Gouze et al., 2003). Those components are quantified and distinguished by several image processing technologies such as threshold method (Otsu, 1979), which has been used to detect the rock fracture. In recent years, several studies applied the threshold method to segment the fracture from

the rock region in a CT image (Karpyn et al., 2009; Deng et al., 2016; Tachi et al., 2018). A certain CT value is chosen at each component, then the neighboring voxels, which has a similar CT number around this value would be considered as the same region. Therefore, this specific value which is used to distinguish different regions is a decisive factor in threshold method. However, it also has some limitations such as it would result in the misidentification of neighboring voxels. Lai et al. (2017) used the CT threshold method to identify the rock fracture from a CT image (as shown in **Figure 1**). It shows that the extracted fracture position has several misidentifications, i.e., within the red square was misidentified as the white part, i.e., rock phase after the CT image segmentation. It is noted that threshold method is not suitable for a relative low resolution CT image.

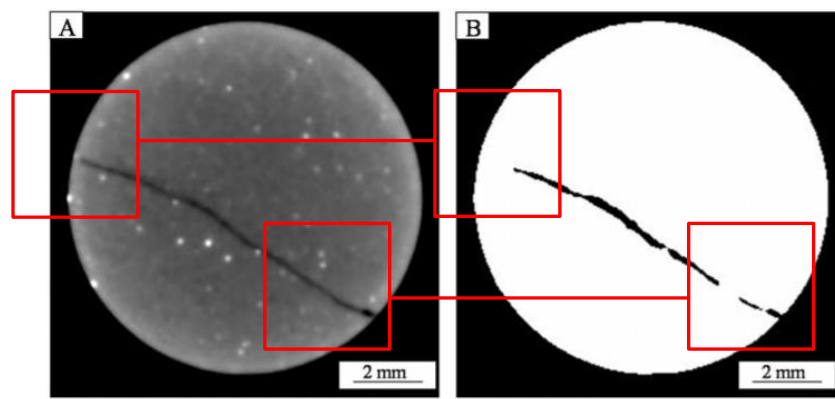


Fig.5.1 Threshold method on identifying the fracture position (Lai et al., 2017)

The misidentification results has a great effect on grasping the rock fracture information accurately. Some previous researchers verified the rock fracture permeability evolution and established the numerical model through the CT image analysis (Li, 2017; Fathani, et al. 2017). Therefore, an efficient image processing technology and image analysis method on analyzing the rock fracture CT image are critical. Edge detection is a common method on identifying medical CT image, such as human tissues and bone structures (Vig, Shubhangi, Mahendran, 2012). The characteristic of this method is focusing on the discontinuity and similarity region in a CT image with high efficiency (Jiang et al., 1999). The common process of edge detection includes three steps: the differentiation of the different regions, enhance the boundary and removing the unwanted voxels (Rong et al., 2014). The overlapping line which locates around the perimeter can be removed subtly. Canny deduced the best Canny edge detection algorithm in 1986, which was widely utilized (Canny, 1986). A high-quality detection and sifting the image noises are the advantage of this method. Particularly, a relative low CT resolution image is unaffected.

Not many researches aim at the image processing on the rock fracture. Moreover, none of the previous studies clarified that different image processing methods have an influence on the rock aperture and fracture contact-area value change. Therefore, in this study, two different image processing methods (i.e., region growing technique and edge detection, respectively.) are applied on identifying the single granite fracture. Several CT images under various stress conditions (i.e., at 0 MPa and at 3.0 MPa, respectively.)

were extracted from different granite rock positions. The critical factors (i.e., aperture value and contact-area ratio) were analysed and compared under two different methods. Then characteristic of different image processing methods on rock fracture were discussed from several comparison results. Aperture and fracture contact-area variation were further verified.

5.2 Experiment setup

A cylindrical granite rock sample with diameter and length 15.2×33.3 mm was split by the Brazilian tensile test to make a single fracture along the cylindrical axis. The sample was set into a triaxial cell. The triaxial cell with the granite sample inside was mounted on the rotation table and was faced to the X-ray source, as shown in **Fig 5.2**. The microfocuss X-ray CT scanner in this study is the KYOTOGEO-XCT (TOSCANER-32250 hdk, TOSHIBA IT and Control Systems Corporation) (Higo et al.,2014; Kido et al., 2017). This CT scanner has an X-ray focal spot size of 4 micrometers and a resolution of $5 \mu\text{m}$. The maximum current and voltage are 1 mA and 225 kV, respectively. The scan condition is listed in **Table 1**. The granite sample was scanned with two steps through the microfocuss X-ray CT. First, it was scanned as-received (i.e., dry condition) without confining stress. The sample was scanned into 1788 CT slices with the pixel size and the slice thickness of $15.1 \times 15.1 \times 17.0$ micrometers at each direction. Second, the sample was fixed into the water-saturated triaxial cell, and was scanned with the confining stress of 3.0 MPa. In this step the sample was scanned into 1736 slices with the pixel size and the slice thickness of $18.4 \times 18.4 \times 21.0$ micrometers. The cross-section CT image matrix is 1024×1024 at X and Y direction. The CT images are output as 16-bit grayscale.

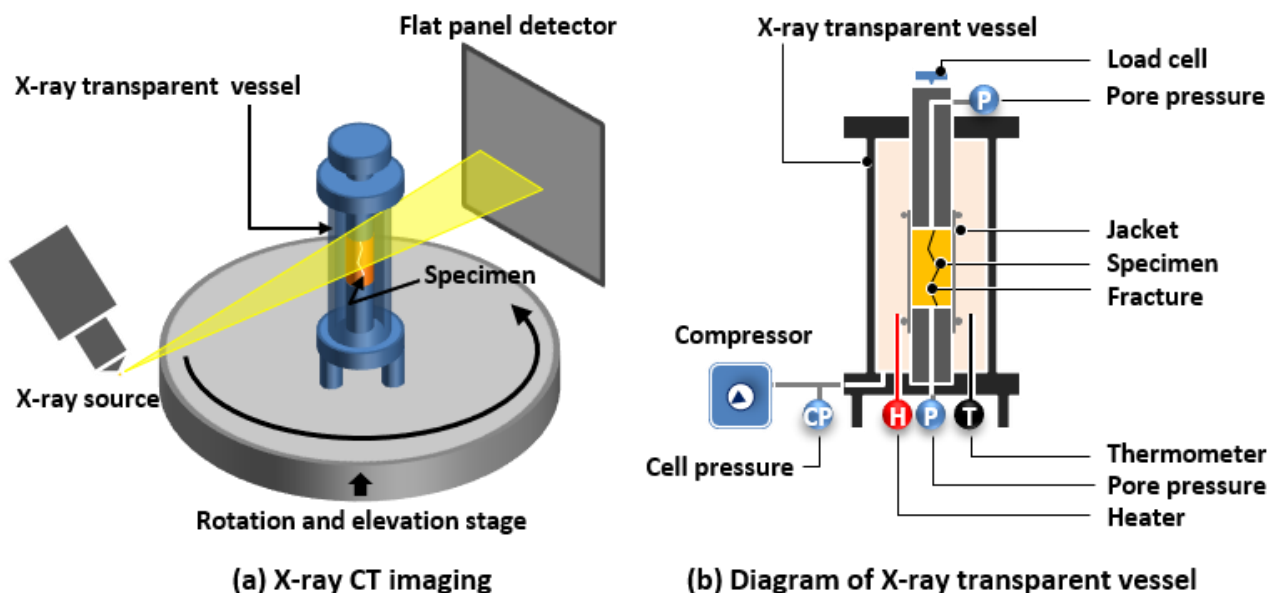
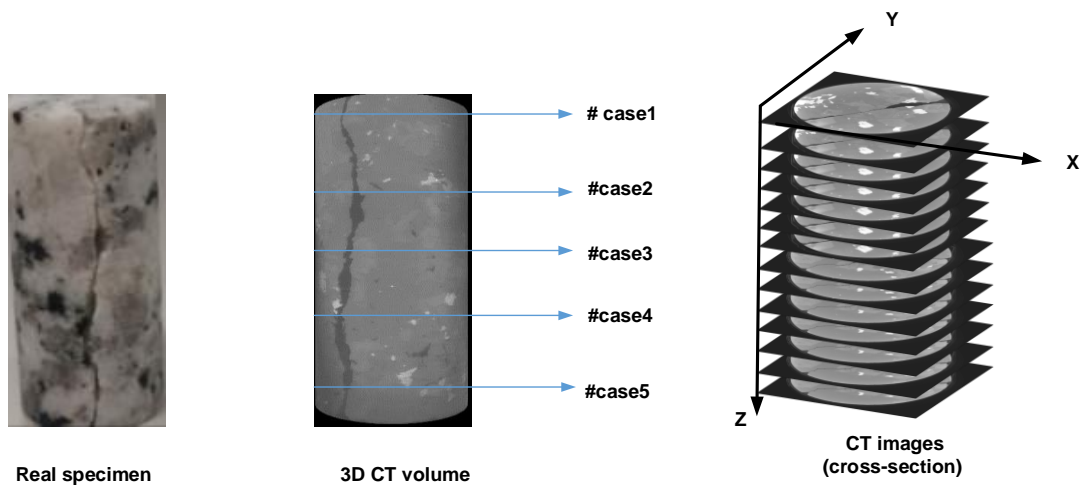


Fig.5.2 The granite specimen was fixed into the triaxial cell (transparent to X-ray)

Table 1 Scan conditions under different confining pressures at 20 °C

Confining pressure (MPa)	Voltage (kV)	Current (μ A)	Voxel size (μm^3)	Projection view	Scan area (mm)	Integrated images for one projection
0	150	65	15.1 ² ×17.0	4506	15.462	10
3	160	90	18.4 ² ×21.0	2253	18.824	15

Several 2-D cross-section CT images (i.e., Slice A to E, were picked up from different length of the sample) at each confining stress condition, as depicted in **Fig 5.3**. The extracted CT images were used to check the fracture variation, **Table 2** lists the extracted CT image numbers and positions at each stress condition. Two different image processing methods (i.e., region growing and edge detection) were applied to identify the fracture variation by the measured CT images. Moreover, aperture and contact-area ratio value at each cross-section were calculated under the two image processing methods.

**Fig.5.3** Extracted CT images (#Slice A to Slice E) from the granite specimen**Table 2** Different conditions of CT images

Analysis condition	CT image slice number.	0 MPa	CT image slice number.	3.0 MPa
		Z-direction (mm)		Z-direction (mm)
Slice A	161	2.7	161	2.7
Slice B	361	6.1	361	7.6
Slice C	661	9.9	661	13.9
Slice D	1261	18.9	1261	26.5
Slice E	1561	23.4	1561	32.8

5.3 Image processing method

5.3.1 Region growing method (RG)

CT images were segmented by the region growing method (*Rosenfeld, 1982*). An image analysis software VGstudioMax3.1 (Volume Graphics GmbH) (Higo et al., 2014) was used to conduct the region growing process. Region growing has the characteristic of aggregating the specific range and similar value of voxels into a region. The separation and unification are best conducted through a region growing. The

voxel of an image will be aggregated to the same region when the voxel is satisfying with a criterion of homogeneity (Zucker 1976; Abdelsamea 2014). A criterion of homogeneity depends on selecting the initial seed point and criteria utilized to stop the region growing process. When we chose the criteria, the object size, boundary, color, and the average intensity are the characteristic of the regions in a CT image. Which has a dominant rule on region growing. Moreover, several drawbacks of region growing may also exist. If the initial seed point selection is not appropriate, it will lead different image segmentation results. Therefore, an effective voxel selection at region growing process is essential . (Adams et al.,1994; Fan et al., 2005; Mahbubun et al., 2018). A process of region growing method is schematically illustrated in **Fig 5.4** (Kishida et al., 2015). In this example, tolerance criterion of ± 50 is used. Firstly, a representative voxel, for example the yellow voxel in **Fig 5.4 (a)**, value 400 was is chosen as the initial seed. The 8 voxels adjacent to the seed are scanned and integrated into the seed group for the next step, as shown in **Fig 5.4(b)**. if their values are within the range of the seed value \pm tolerance, which is 400 ± 50 in this example, in the next step, the 12 yellow voxels in **Fig 5.4 (c)** are new seed group, and 8 voxels adjacent to each seed voxel are scanned to see whether the voxel values are within the seed value \pm tolerance. If the value of scanned voxel does not meet the criteria, the voxel is not integrated into the seed group for the next step, as shown in **Fig 5.4 (d)** which means the region growing stops in that direction. These steps are repeatedly conducted and the neighbour voxels are judged by the criteria, as illustrated in **Fig 5.4 (e)**, until the total number of seed voxels stops increasing and get the final segmentation image, as shown in **Fig 5.4 (f)**.

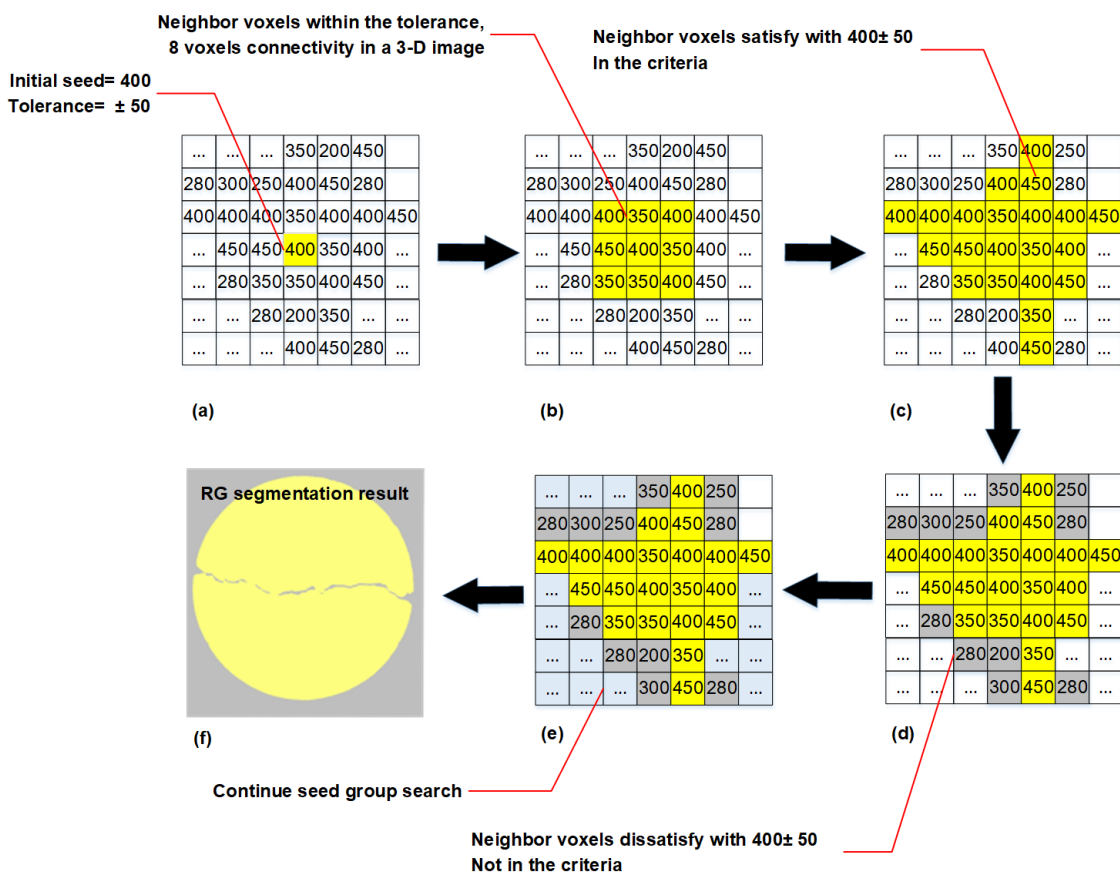


Fig.5.4 Schematic illustration of region growing method (Kishida et al., 2015)

Adjacent voxel at X , Y and Z direction which existed around the initial seed voxel would be assimilated into the initial seed voxel in three-dimensional, which will ensure the voxel connectivity in 3-D. If the CT voxel membership probability is over the threshold, those voxel value can be distinguished. The value of different region in a CT image is listed in **Table 3**. It includes the mean value of each phase (i.e., σ_1 and σ_2); the standard of the mean value (i.e., μ_1 and μ_2); A threshold value of 82 was decided through this Gaussian distribution, as shown in **Fig 5.5**. The representative voxel value 151 was chosen as the represent rock initial value. The neighbouring voxels were assimilated through the distance (i.e., the tolerance T 69.34) between the threshold value and the mean value of the rock region. If the adjacent voxels around the initial value are more significant than the threshold value of 82, these voxels will also be assimilated into the rock phase seed groups with this region growing.(i.e., the same procedure has been introduced in **Chapter 4**) Then the rock aperture is distinguished from this segmentation process.

Table 3 Histogram values of CT images

Mean value of rock μ_1	Mean value of void μ_2	Standard distribution of rock σ_1	Standard distribution of void σ_2	Tolerance T	Threshold
151.34	48.17	14.11	6.63	69.34	82

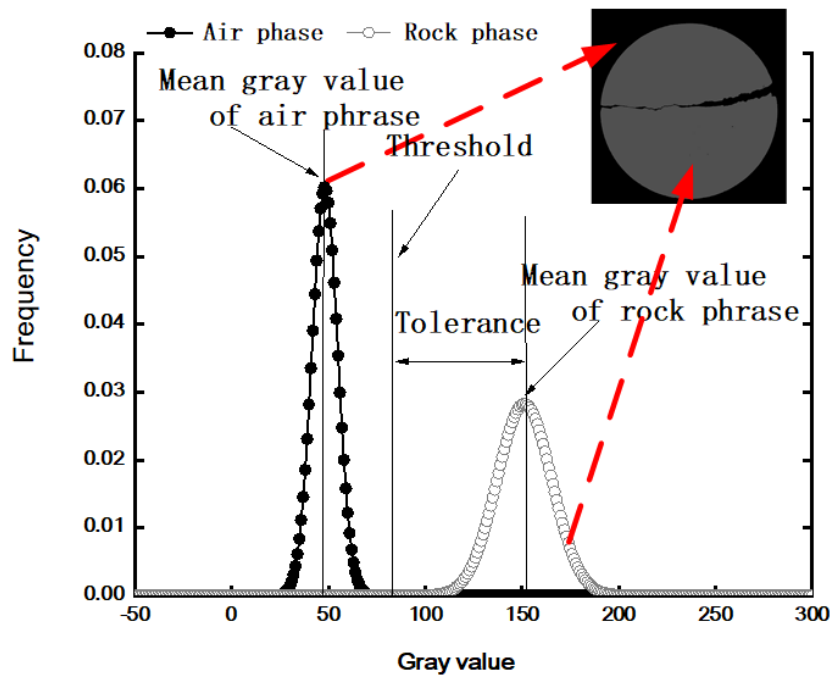


Fig.5.5 Gaussian distribution of region growing method

5.3.2 Edge detection method (ED)

Edge detection method is an efficient operation on object recognition and boundary extraction at image processing. This method has a characteristic on reducing the neighborhood voxel noises which exist around the object structure boundary. Several edge detection methods such as Prewitt, Roberts, Sobel, and

Canny (Rahim et al., 2004) are applied on the image processing. Canny edge detection (Canny, 1986) deduced the best approximation of the optimal edge detection operation through the algorithm of the first derivative of Gaussian function. It was regarded as the optimal filter and contributed to the image processing. This algorithm generally has a significant advantage on weakening the image noise, then the smooth image is successfully achieved through deducing the 2-dimensional Gaussian function:

$$G(x, y) = \frac{1}{\sqrt{2\pi}\sigma} e^{-\frac{(x^2+y^2)}{2\sigma^2}} \quad (5.1)$$

where σ represents the scale of smoothing, the image will be smoothed when the value becomes larger. However, superfluous noise suppression may produce the image lack fidelity. Edge in an image will become phantom and smooth when a large filter variance of σ is chosen. A comparison figure is shown in **Fig 5.6** In this study, the value of σ is set as $\sigma=0$. Although a relatively small value of σ will lead to a superfluous noise suppression, it can keep the aperture boundary accuracy. i.e., as the same shape with the original image. If an unsuitable σ is chosen equal to 4, the aperture boundary became smooth. However, the aperture is fuzzy and it is not the same shape as the original CT image.

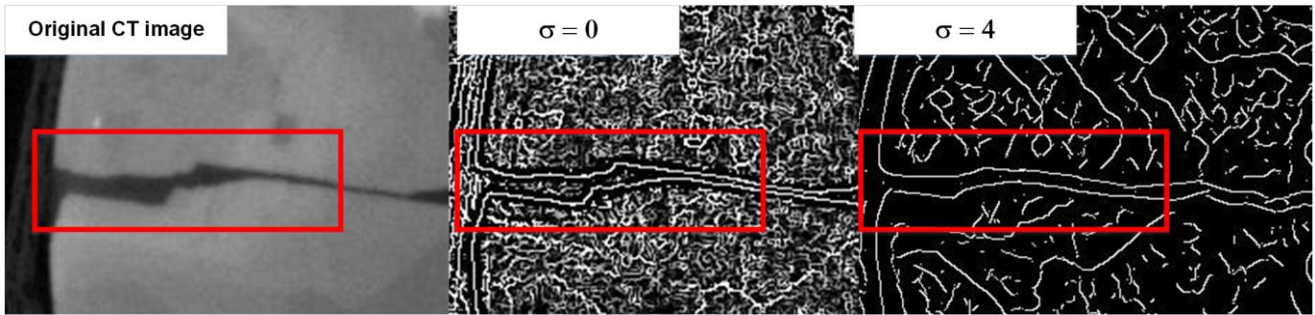


Fig.5.6 σ value difference on the aperture boundary identification

In a CT image, if a value is larger than the threshold value, the pixel at each direction can be recognized as an edge. An edge gradient is a vector which depends on the magnitude and direction. The edge strength (magnitude) is calculated through the first-order derivative expression at X and Y direction; then the second-order derivatives is written as:

$$L = \sqrt{\left(\frac{\partial f}{\partial x}\right)^2 + \left(\frac{\partial f}{\partial y}\right)^2} \quad (5.2)$$

where L is the first-order image derivative (the gradient magnitude) and f is the CT value at coordinates (x, y) in a CT image. $\partial f/\partial x$ and $\partial f/\partial y$ are the vector in the maximum rate change of f at X and Y directions.

Then the vector at X and Y directions is calculated by the Sobel operator equation as follows:

$$\begin{bmatrix} -1 & -2 & -1 \\ 0 & 0 & 0 \\ 1 & 2 & 1 \end{bmatrix} \quad \begin{bmatrix} -1 & 0 & 1 \\ -2 & 0 & 2 \\ -1 & 0 & 1 \end{bmatrix} \quad (5.3)$$

Gradient direction ϕ is computed as:

$$\varphi = \tan^{-1} \left(\frac{\partial f}{\partial y} / \frac{\partial f}{\partial x} \right) \quad (5.4)$$

Therefore, a CT image processing result after this calculation is shown in **Fig 5.7**, which has filtered the nonsignificant regions, and only concentrated on the fracture aperture boundary.

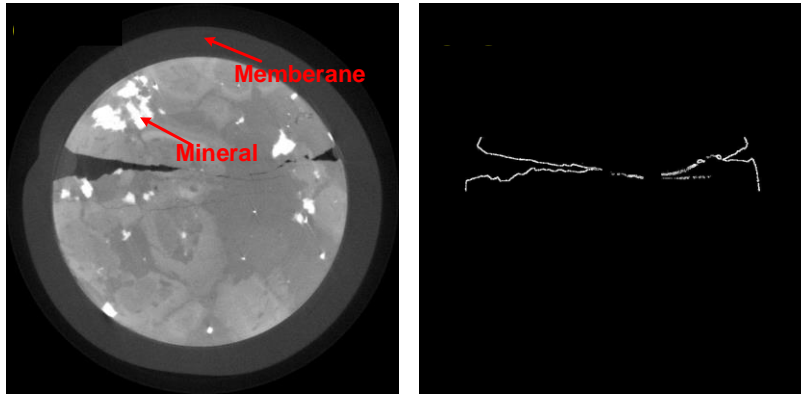


Fig.5.7 Edge detection result of a representative slice at 3.0 MPa (removed membrane and mineral)

5.3.3 A comparison analysis of RG and ED

The region growing method (RG) and the edge detection method (EG) were applied to the CT image of Slice A that was scanned under unconfined condition. **Fig 5.8** shows the result. From this figure, it is confirmed that the boundary of upper and lower fracture is successfully identified with these two methods.

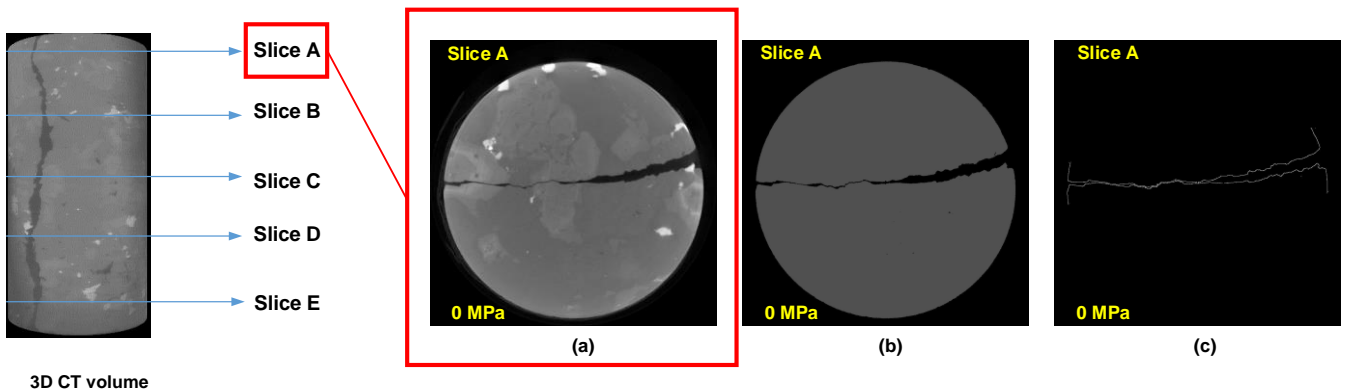


Fig.5.8 CT image comparison (a) Original CT image, (b) Image processing under Region growing method (RG), (c) Image processing under Edge detection method (ED)

Fig 5.9 shows aperture boundary of Slice A (i.e., upper and lower fracture surface) with RG and ED methods. The calculated mean aperture of RG and ED methods are 18 pixel and 18.61 pixel, and the contact-area ratios are 0% and 0.1%, respectively, which means RG and ED provide almost the same result in extraction of aperture boundary.

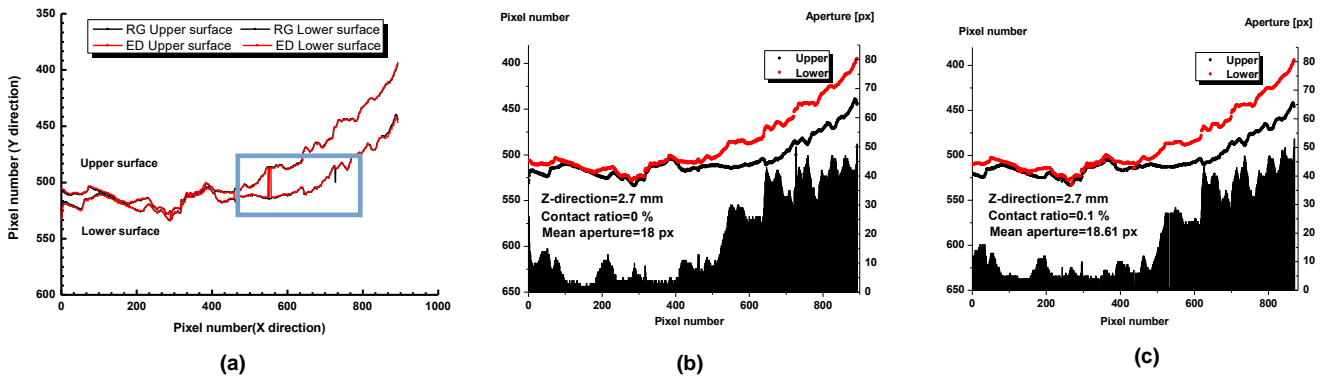


Fig.5.9 Aperture boundary profile and a calculation result with RG and ED methods. (a)Comparison of aperture boundary profile, (b)Aperture and contact-area ratio value (RG), (c)Aperture and contact-area ratio value (ED)

Fig 5.10 shows the difference of extracted apertures between RG and ED. The average of the difference was calculated as 1.52 pixel. Aperture difference histogram of RG and ED methods are shown in **Fig 5.10 (b)** and **(c)**. The result shows that aperture value has an apparent difference from the value 0 to 20. It can be guessed that aperture closure position may result in the slight image processing difference. RG result shows aperture value at 0~5 is larger than ED.

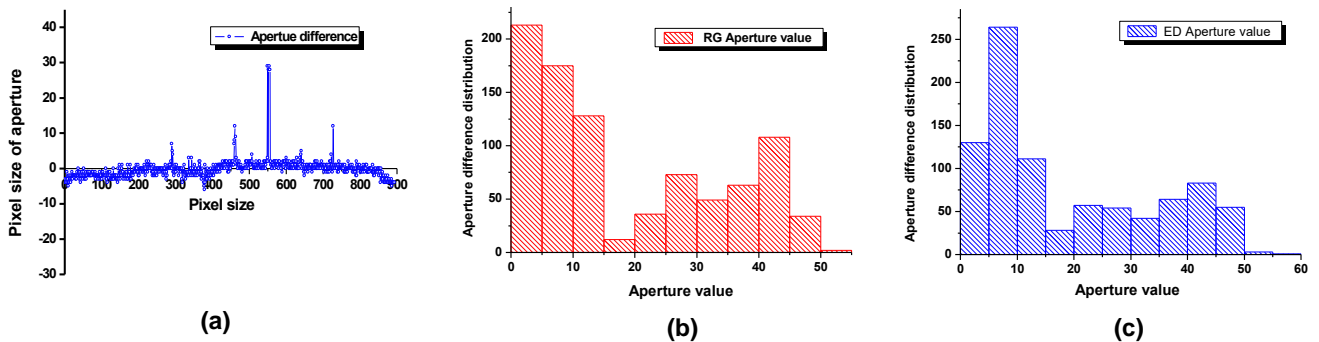


Fig.5.10 Aperture value difference under two image processing methods, (b)Aperture value histogram (RG), (c)Aperture value histogram (ED)

Fig 5.11 is enlarged views where difference of extracted aperture is relatively large in Figure 9. We can see that some part of aperture boundary is missing or mis-identified in ED result, especially where boundary of rock part and void part is blurry in the original image.

Fig 5.11' shows profile of CT value across the fracture at Line 514 and identification results by RG and ED. In RG method, the pixels having the CT value of less than 82, namely, lower than the threshold CT value, are identified as void part as indicated with red line. In ED method, on the other hand, the pixels where gradient of CT value is largest around are identified as boundary of void part and rock part. Therefore, extracted aperture is slightly different between the two methods.

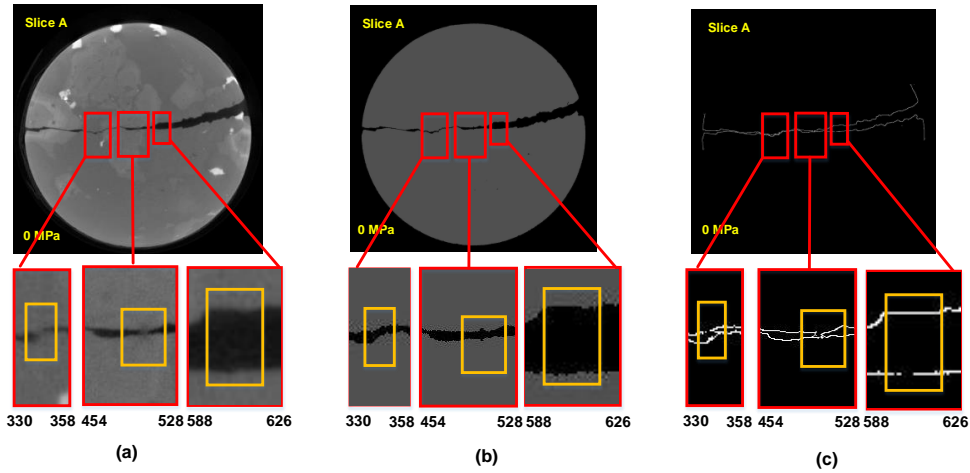


Fig.5.11 Enlarged views of fracture where difference of extracted aperture by RG and ED is relatively large

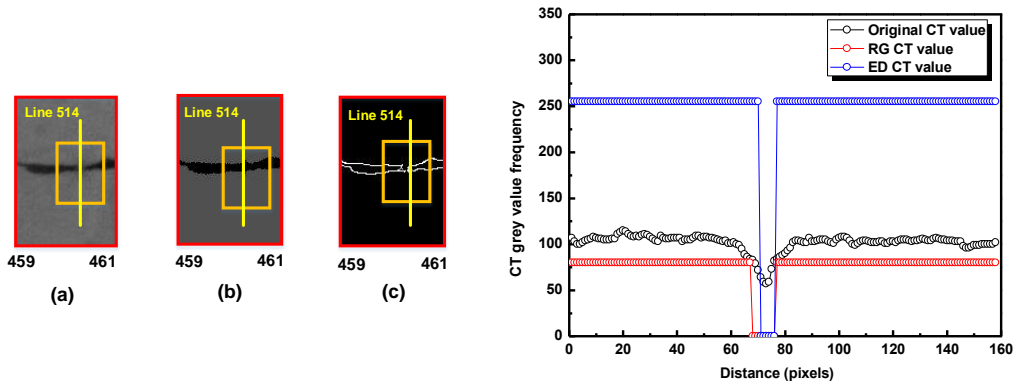


Fig.5.11' Profile of CT value across the fracture at Line 514 and identification result by RG and ED

5.4 Analysis results

5.4.1 Image processing of CT images without confining stress

Fig 5.12 shows the result of fracture extraction by RG and ED for Slices B to E at the confining pressure of 0 MPa. In these slices, secondary fractures that are hidden below the major fracture surface can be seen. These hidden secondary fractures are also successfully detected by RG and ED.

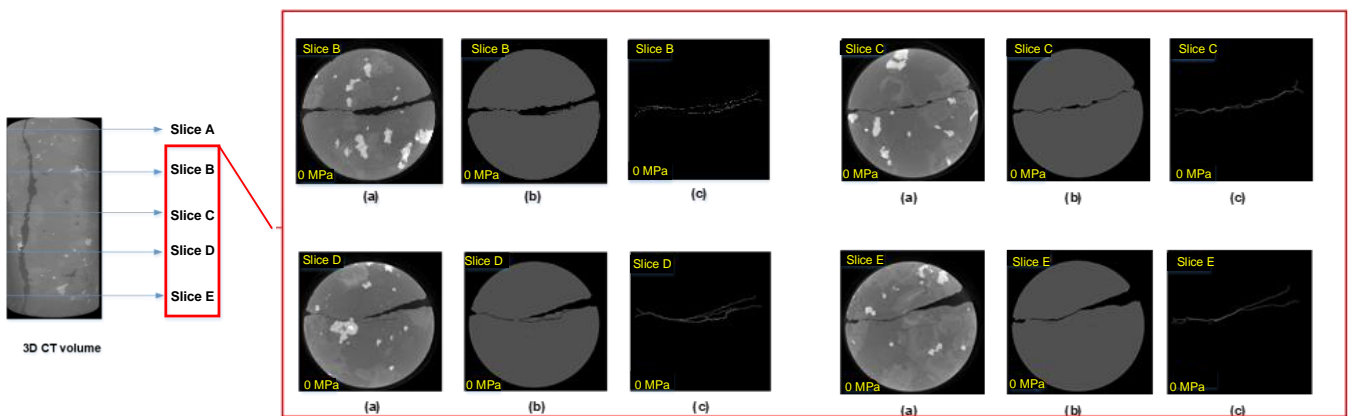


Fig.5.12 CT image comparison under two image processing methods at 0 MPa.(Slice B~E)

Fig 5.13 shows fracture boundary shape and aperture width in Slices D and E. The differences of mean aperture width between RG and ED are almost within 2 pixels, which mean good agreement between the two methods. On the other hand, contact ratios are different by the methods. In these slices, contact ratios are several percent in RG result, while almost zero percent in ED result. The contact-area ratio shows a relative larger at RG method. It can be understood that the RG method has the characteristic on the voxel-connectivity. A high-density voxels may locate on the rock discontinuity positions, which will result in the voxel misallocation. Then the rock discontinuity positions was misidentified as the rock connectivity due to the voxel-connectivity under RG segmentation. Therefore, the contact-area ratio of RG shows a bit higher. In contrast, ED method is sensitive to the high CT value, and it is easy to concentrate on the aperture boundary. Which will keep an accuracy on the boundary extracting. Therefore, the contact-area ratio shows lower than RG.

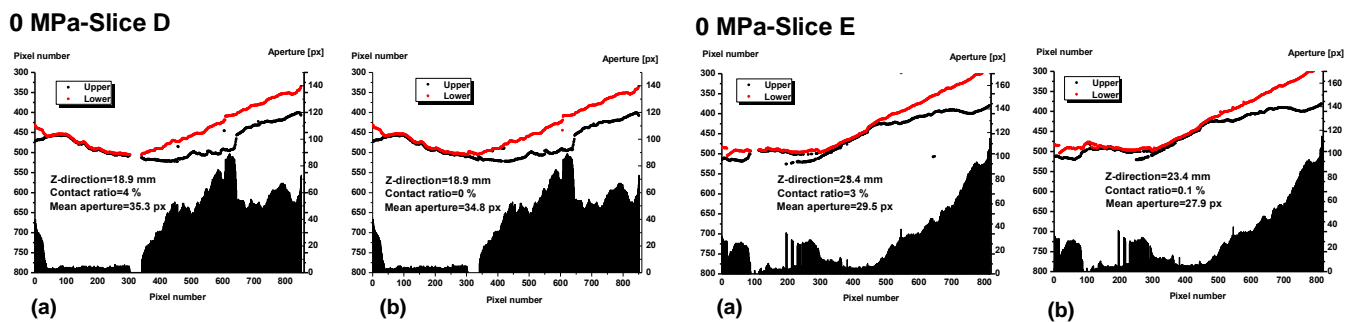


Fig.5.13 Aperture and contact-area ratio value comparison at each case (0 MPa-Slice D~E)

Fig 5.14 and **Fig 5.15** show enlarged views of fracture in Slices D and E where results of RG and ED are largely different. We can clearly see narrow cracks in the original CT images and they are detected in EG results. On the other hand, RG fails to detect these cracks. As seen in Figure 15(a), the cracks penetrate very high density mineral (white pattern). The CT value within the fracture can be dragged into higher by the surrounding high density mineral, and it did not exceed the threshold value of rock and void. This result implies that RG method is not good at detecting narrow fractures penetrating very high density mineral in our cases. It is not matter in ED method because the edge (boundary of materials) is identified not by the CT value itself but by the spatial gradient of the CT value.

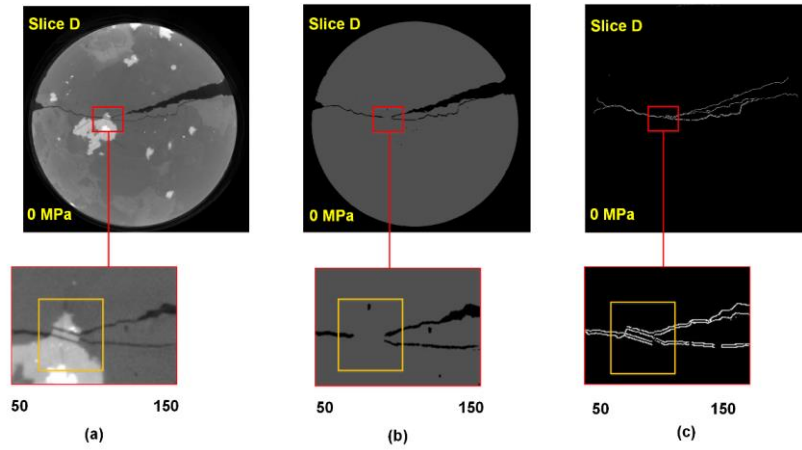


Fig.5.14 Enlarged view of fracture in Slice D at 0-MPa confining pressure. (a) original CT image, (b) RG result, and (c) ED result

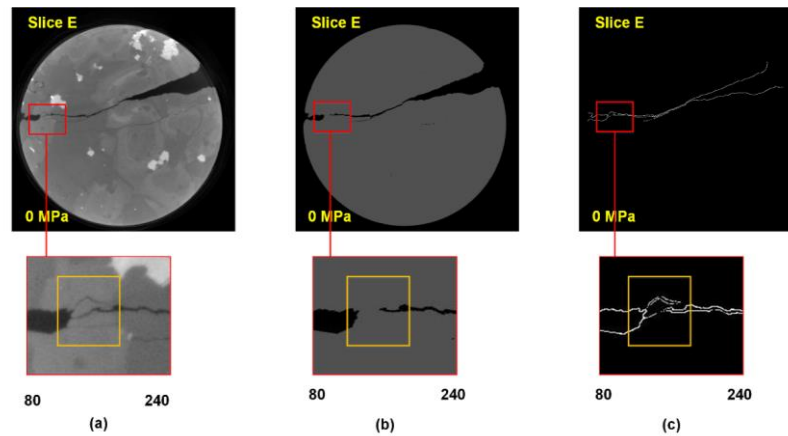


Fig.5.15 Enlarged view of fracture in Slice E at 0-MPa confining pressure. (a) original CT image, (b) RG result, and (c) ED result

5.4.2 Image processing of CT images with confining stress

From image processing of CT images at 0 MPa, it can be noted that some image identification difference may easily generate at aperture closed position. Therefore, image processing methods of RG and ED are used to check the CT images with confining stress influence. 3MPa-Slice A~E were extracted from the sample under the confining stress of 3MPa.

Fig 5.16 shows the original CT images and the results of RG and ED for the same slices with the previous section at confining pressure of 3 MPa. Comparing these images with those in the previous section, we can clearly see that the fractures are closing due to the confining pressure. These are much harder cases from the viewpoint of fracture detection.

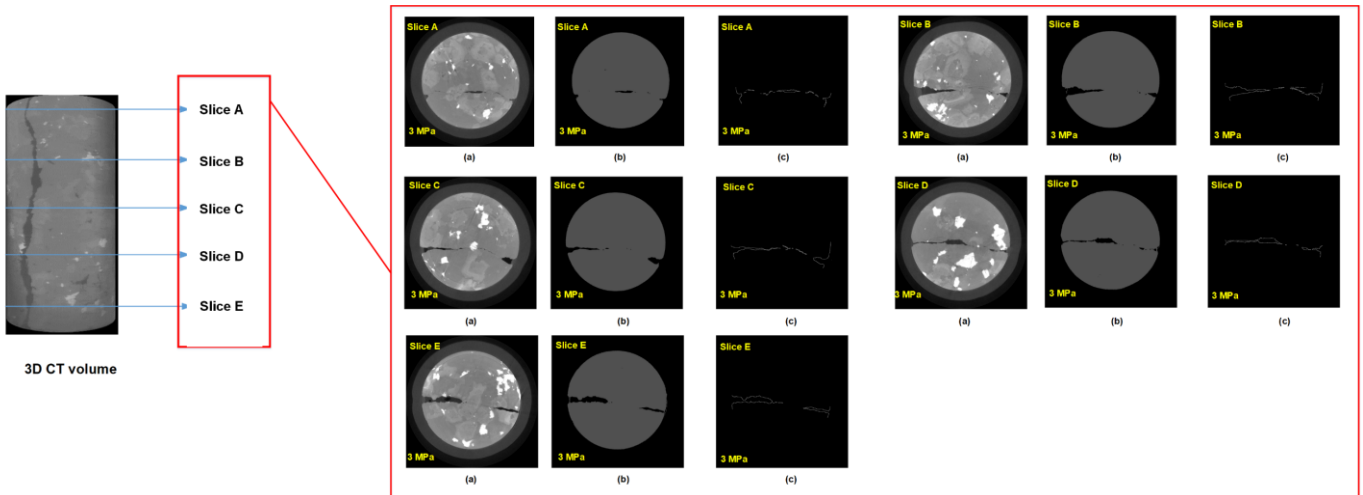


Fig.5.16 CT image comparison under two image processing methods at 3MPa-Slice A~E

Aperture and contact-area ratio value results are shown in **Fig 5.17**. In Slice E, mean aperture width and contact ratio are almost the same values between RG and ED. On the other hand, a significant difference is seen in Slice A. The contact-area ratio value of 3MPa-Slice A is 68.5% and 6.5% at RG and ED segmentation, respectively, which shows almost 10 times difference.

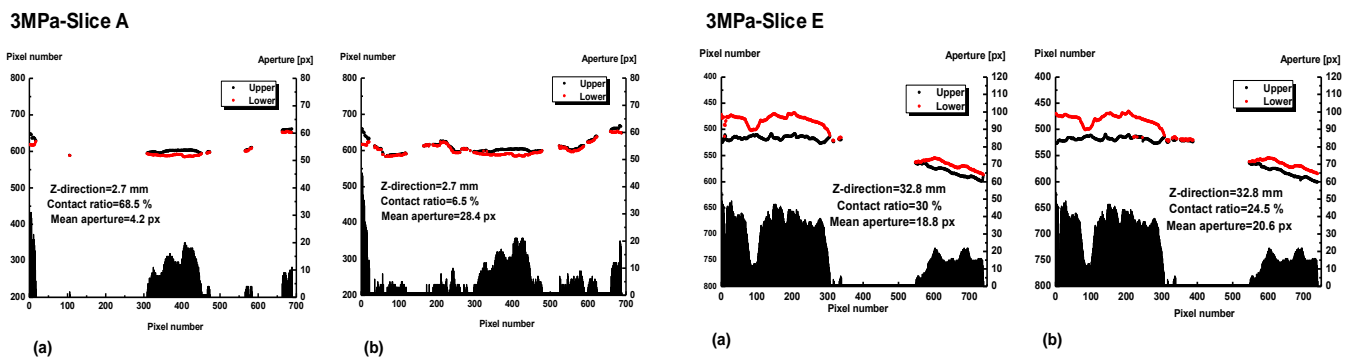


Fig.5.17 Aperture and contact-area ratio value comparison at each slice (i.e., 3MPa-Slice A, and 3MPa-Slice E)

Several aperture positions were picked up and made a comparison as shown in **Fig 5.18**. After RG segmentation, results indicate that some void positions are difficult to be distinguished due to an ill-suited threshold value chosen. Different regions were misrecognized and assimilated into the rock region and resulted in the image misidentification. Moreover, it will influence the inaccurate calculation of the contact-area ratio.

Image misidentification positions were also depicted. i.e., aperture position of 3MPa-Slice A at X-direction pixel number of 100~335, and 3MPa-Slice E, 80~220. Original CT image and the CT segmentation image of RG and ED were compared at these positions. The result shows that 3MPa-Slice A had a large difference between the two segmentation results. RG segmentation misrecognized some different regions around the narrow void region as a rock voxel continuity, and the aperture boundary was neglected. In contrast, ED only concentrated on the boundary, and segmented result is quite similar to the original CT image.

In order to further check the aperture identification difference, yellow profile line was compared at these two CT slices. i.e., 3MPa-Slice A, profile line 275 at X-direction, and 3MPa-Slice E, 142. 3MPa-Slice A presents the ED profile lines is well reflected the original CT image. However, the RG profile line value is equal to 0, which is corresponding to the CT segmentation results. A relative aperture narrow position was misrecognized as a connectivity of the rock region. 3MPa-Slice E presents a significant difference in the profile line due to the misidentification of the different regions into the rock region after RG segmentation. The profile line of RG shows an oscillation variation. However, profile line value of ED is range from 40 to 85, which is the same to the original CT image.

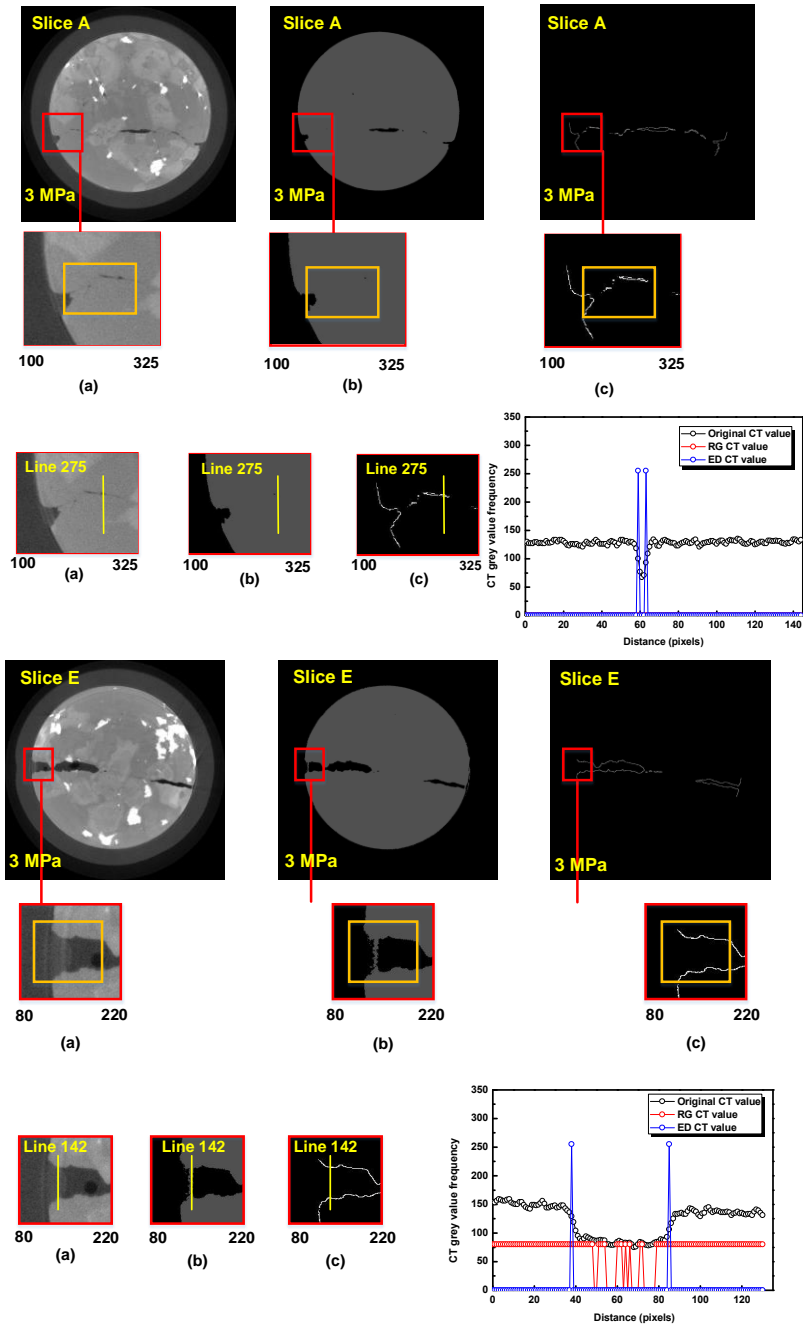


Fig.5.18 CT image comparison under different image processing methods (3MPa-Slice A~E)

5.5 Summary

Different from previous studies, it is a new attempt on identifying the rock fracture aperture boundary under various confining stresses through using different image processing methods in this study. Two image processing methods are applied to estimate the aperture and the fracture contact conditions under different confining stress. Some conclusions are summarized as follows:

Different image processing methods (RG and ED methods) have a significant difference on the aperture boundary identification. Aperture boundary became difficult to be identified when the aperture was reduced by confining stress. Two kinds of CT images (i.e., the CT image slices at 0 and 3.0 MPa were picked up from different positions of the rock sample) are used for image processing. Aperture value generated a bit difference at 0 MPa. In contrast, aperture difference presents more significant at 3.0 MPa when the aperture became much narrower. Therefore, image processing result shows a large difference on the aperture identification and on the calculation result due to the confining stress influence.

RG segmentation method concentrated on the voxel connectivity of the same region. However, it will result in several image misidentifications. Aperture boundary was omitted under the confining stress influence. It can be guessed that a high density CT value voxel existing within the aperture will lead to the voxel misallocation, especially this misallocation is much easier to happen on a narrow aperture.

ED segmentation method has a good property on recognizing the fracture aperture boundary at fine scales. It has a good advantage on avoiding the noise of the neighboring voxel. Moreover, ED identified the aperture boundary not only by the CT value itself but also by the spatial gradient of the CT value. Which will avoid the voxel misallocation although the high density CT value voxel existing around the narrow aperture.

Aperture and the contact-area ratio are the two representation parameters on estimating of the fracture variation. Both of the two image processing methods are great and impactful on analyzing the fracture variation. Especially, edge detection has advantage of detecting the fracture boundary and it should be widely applied on the rock engineering field.

References

- Abdelsamea, M.: An Automatic Seeded Region Growing for 2D Biomedical Image Segmentation. *Computer Vision and Pattern Recognition*, ar Xiv:1412.3958. 2014.
- Adams, R., Bischof, L.: Seeded region growing. *IEEE Trans. Pattern Analysis Machine Intelligence*, 16(6): 641–647, Jun, 1994.
- Bertels, S. P., Dicarolo, D.A., Blunt, M.J.: Measurement of aperture distribution, capillary pressure, relative permeability, and in situ saturation in a rock fracture using computed tomography scanning. *Water Resources Research* 37(3): 649-662. 2001.
- Canny, J.: A computational Approach to Edge Detection, *IEEE Trans. Pattern Analysis and Machine Intelligence*, vol. 8, no. 6, pp. 679-698. 1986.
- Danko, G., Bahrami, D. A.: new T-H-M-C model development for discrete-fracture EGS studies. *GRC Trans.* 36:383–392. 2012.
- Deng, H., Fitts, J.P., Peters, C.A.: Quantifying fracture geometry with X-ray tomography: Technique of Iterative Local Thresholding (TILT) for 3D image segmentation. *Computational Geosciences*. 20(1): 231-244. 2016.
- Dustin, C., Johnathan, M.B., Magdalena, G.B.: CT scanning and flow measurements of shale fractures after multiple shearing events. *International Journal of Rock Mechanics and Mining Sciences*. 100: 177–187. 2017.
- Ellis, B.R., Fitts, J.P., Bromhal, G.S., McIntyre, D.L., Rappero, R., Peters, C.A., .: Dissolution-driven permeability reduction of fractured carbonate caprock. *Environ. Eng. Sci.* 30, 187–193. 2013.
- Elsworth, D., Yasuhara, H.: Short-Timescale Chemo-Mechanical Effects and their Influence on the Transport Properties of Fractured Rock. *Pure and Applied Geophysics*. 163(10): 2051-2070. 2006.
- Fan, J.P., Zeng, G.H., Mathurin, B., Mohand, S.H.: Seeded region growing: an extensive and comparative study. *Pattern Recognition Letters*. 26, 1139–1156. 2005.
- Fathani, T.F., Legono, D., Karnawati, D.: A Numerical Model for the Analysis of Rapid Landslide Motion [J]. *Geotechnical & Geological Engineering* 35(2), 1- 16, 2017.
- Farough, A., Moore, D. E., Lockner, D.A., Lowell, R. P. : Evolution of fracture permeability of ultramafic rocks undergoing serpentinization at hydrothermal conditions: An experimental study. *Geochemistry, Geophysics, Geosystems* 17(1): 44-55. 2016.
- Ghassemi, A.: A review of some rock mechanics issues in geothermal reservoir development. *Geotech Geol Eng.* 30:647–664. 2012.
- Gouze, P., Noiriél, C., Bruderer, C., Loggia, D., Leprovost, R.: X-ray tomography characterization of fracture surfaces during dissolution." *Geophysical Research Letters* .30(5). 2003.

- Hata, A., Yanagawa, M., Honda, O., Kikuchi, N., Miyata, T., Tsukagoshi, S., Uranishi, A., Tomiyama, N.: Effect of Matrix Size on the Image Quality of Ultra-high-resolution CT of the Lung: Comparison of 512 x 512, 1024 x 1024, and 2048 x 2048. *Acad Radiol.* 25(7): 869-876.2018.
- Higo, Y., Oka, F., Morishita, R., Matsushima, Y., Yoshida, T.: Trinarization of μ X-ray CT images of partially saturated sand at different water-retention states using a region growing method." *Nuclear Instruments and Methods in Physics Research Section B: Beam Interactions with Materials and Atoms.* 324: 63-69.2014.
- Jiang, X.Y., Binke, H.: Edge Detection in Range Images Based on Scan Line Approximation . *Computer Vision and Image Understanding.* Vol. 73, No. 2, February, pp. 183–199, 1999.
- Joseph, P.M., Spital, R.D.: A method for correcting bone induced artifacts in computed tomography scanners. *Journal of Computer Assisted Tomography.* vol. 2, pp. 100-108, January 1978.
- Karpyn, Z. T, Alajmi, A., Radaelli, F., Halleck, P.M., Grader, A.S.: X-ray CT and hydraulic evidence for a relationship between fracture conductivity and adjacent matrix porosity. *Engineering Geology.* 103(3-4): 139-145.2009.
- Ketcham, R.A., Slottke, D.T., Sharp, J.M.: Three-dimensional measurement of fractures in heterogeneous materials using high-resolution X-ray computed tomography. *Geosphere.* 6:499–514.2010.
- Kido, R., Higo, Y. : Evaluation of distribution of void ratio and degree of saturation in partially saturated triaxial sand specimen using micro x-ray tomography. *Japanese Geotechnical Society Special Publication.* 5(2): 22-27.2017.
- Kishida, K., Ishikawa, T., Higo, Y., Sawada, A., Yasuhara, H.: Measurements of fracture aperture in granite core using microfocus X-ray CT and fluid flow simulation. *49th US Rock Mechanics / Geomechanics Symposium.* San Francisco, CA, USA, 15-0485, 2015.
- Kumaria, W.G.P., Ranjith, P.G., Pererab, M.S.A., Li, X.: Hydraulic fracturing under high temperature and pressure conditions with micro CT applications: Geothermal energy from hot dry rocks. *Fuel.* 230:138–154.2018.
- Lai, J., Wang, G.W., Fan, Z., Chen, J., Qin, Z.Q., Xiao, C.W., Wang, S.C., Fan, X.Q.: Three-dimensional quantitative fracture analysis of tight gas sandstones using industrial computed tomography. *Scientific Reports* 7(1).2017.
- Li, B., Jiang, Y. J., Koyama, T., Jing, L. R., Tanabashi, Y.: Experimental study of the hydro-mechanical behavior of rock joints using a parallel-plate model containing contact areas and artificial fractures. *International Journal of Rock Mechanics and Mining Sciences.* 45(3): 362-375. 2008.
- Li, M.Y.: Creep characteristics analysis of asphalt mixture in meso-scale based on Drucker-Prager model. *Journal of North China Institute of Science & Technology,* 14(6), 96-100, 2017.
- Mahendran, S.K. : A Comparative Study on Edge Detection Algorithms for Computer Aided Fracture

- Detection Systems. *International Journal of Engineering and Innovative Technology (IJEIT)*. Volume 2, Issue 5, November. 2012.
- Mahbubun.,N.M.,Sujan., A., Dr., M., Mijanur., R.: Improvement of single seeded region growing algorithm on image segmentation. *Global Journal of Computer Science and Technology*. Graphics & vision. Vol.18.2018.
- McGuire,T.P., Elsworth , D., Karcz, Z.: Experimental measurements of stress and chemical controls on the evolution of fracture permeability. *Transp. Porous Med.* 98, 15–34.2013.
- Okamoto, A., Tanaka, H., Watanabe, N., Saishu, H., Tsuchiya, N.: Fluid Pocket Generation in Response to Heterogeneous Reactivity of a Rock Fracture Under Hydrothermal Conditions. *Geophysical Research Letters*. 44(20): 10,306-310,315.2017.
- Otsu, N.: A threshold selection method from gray-level histograms. *IEEE Trans. Syst. Man Cybern.* SMC-9(1), 62-66.1979.
- Polak, A., Elsworth, D., Liu, J.H., Grader, A.S.: Spontaneous switching of permeability changes in a limestone fracture with net dissolution. *Water Resources Research*. 40(3).2004.
- Polak,A., Elsworth Elsworth, D., Yasuhara, H., Grader, A., Halleck, P.: Permeability reduction of a natural fracture under net dissolution by hydrothermal fluids, *Geophys. Res. Lett.* 30 (20).2003.
- Rahim, M.S.M., Ismail, N.I.N., and Idris, M.A.S.: The use of hybrid technique : thresholding and edge detection for identifying river from arial photo, *Jurnal Teknologi*, 41(B), Pp.1-25, 2004.
- Rong, W.B., Li, Z.J., Zhang, W.: An Improved Canny Edge Detection Algorithm. *International Conference on Mechatronics and Automation*. August 3 - 6, Tianjin, China.2014.
- Rosenfeld, A., Kak, A.C.: Digital Picture Processing, San Diego, CA: *Academic Press*.1982.
- Shubhangi, D.C., Chinchansoor, R.S., Hiremath, P.: Edge Detection of Femur Bones in X-ray images – A comparative study of Edge Detectors. *International Journal of Computer Applications*. (0975 – 8887) Volume 42– No.2, March 2012.
- Silveira, C. S. d., Alvim, A.C.M., Oliva, J.d.J.R.: Radionuclide Transport in Fractured Rock: Numerical Assessment for High Level Waste Repository. *Science and Technology of Nuclear Installations*. 1-17.2013.
- Tachi,Y., Ito, T., Akagi, Y., Satoh, H., Martin, A.J.: Effects of Fine-Scale Surface Alterations on Tracer Retention in a Fractured Crystalline Rock From the Grimsel Test Site. *Water Resources Research*. 54(11): 9287-9305.2018.
- Tsang, C.F., Bernier, F., Davies, C.: Geo-hydromechanical processes in the excavation damaged zone in crystalline rock, rock salt, and indurated and plastic clays - in the context of radioactive waste disposal. *Int. J. Rock Mech. Min. Sci.* 42, 109–125. 2005.
- Van, G.M., Swennen, R., David, P. : Quantitative coal characterisation by means of microfocus X-ray computer tomography, colour image analysis and back-scattered scanning electron microscopy. *Int J Coal*

Geol. 46:11–25.2001.

Vig.R.,Agrawal.S.,Kaur,J: A Comparative Analysis of Thresholding and Edge Detection Segmentation Techniques. *International Journal of Computer Applications* 39(15): 29-34.2012.

Yasuhara, H., Elsworth,D. :Compaction of a Rock Fracture Moderated by Competing Roles of Stress Corrosion and Pressure Solution. *Pure and Applied Geophysics.* 165(7): 1289-1306.2008.

Yasuhara, H., et alKinoshita, N., Lee, D.S., Choi, J.H., Kishida. K.: Long-term observation of permeability in sedimentary rocks under high-temperature and stress conditions and its interpretation mediated by microstructural investigations. *Water Resources Research.* 51(7): 5425-5449.2015.

Yasuhara, H., Polak, A, Mitani, Y., Grader, A.S., Halleck, P.M.H., Elsworth, D.: Evolution of fracture permeability through fluid–rock reaction under hydrothermal conditions. *Earth and Planetary Science Letters.* 244(1-2): 186-200.2006.

Zucker,S.W.: Region growing: Childhood and adolescence. *Computer Graphics and Image Processing.* vol. 5, pp. 382- 399, 1976.

Chapter 6 Long-term Observation of Flow Behavior and Hydraulic Properties of a Single Rock Fracture under Various Conditions

6.1 Introduction

Fluid flow within the rock mass always controlled by the fracture aperture geometry variation. The flow path within a fractured rock mass is altered under various conditions. Polak et al. (2004) and Min et al. (2009) clarified that the fluid behavior within the fractured rock under the coupled THMC (thermal-hydraulic-mechanical-chemical) processes exert a significant effect on the deep subsurface of the geological systems. The complex processes may alter the fracture surface roughness and may change the flow direction. Yasuhara et al. (2004, 2006) performed several flow tests, which proved that the pressure dissolution on the fracture asperities resulted in the changing of the fracture aperture. Several previous experimental and numerical works are assumed that the fracture contact-area within the aperture might be altered by the complexed conditions. Then the hydraulic aperture was transformed. The previous researches, such as Barton et al. (1985) and Pyrak et al. (1987), clarified that the fluid behavior within the rock fractures was changed under normal and shear stress. Raven et al. (1985) illustrated that the normal loading and shear displacement have an effect on the fluid flow within the rock fractures. Moreover, Kishida et al. (2009, 2013) and Li et al. (2008) performed several studies about the flow path within the fracture. It indicated that the flow path within the fracture channels may be changed due to the contact-area variation. The fluid may be disturbed by the fracture contact-area. Moreover, mineral dissolution also has a great influence on the flow direction. Then the flow direction was transformed due to the fracture variation under different conditions, as shown in **Fig 6.1** (Kishida et al., 2013; Okamoto et al., 2017).

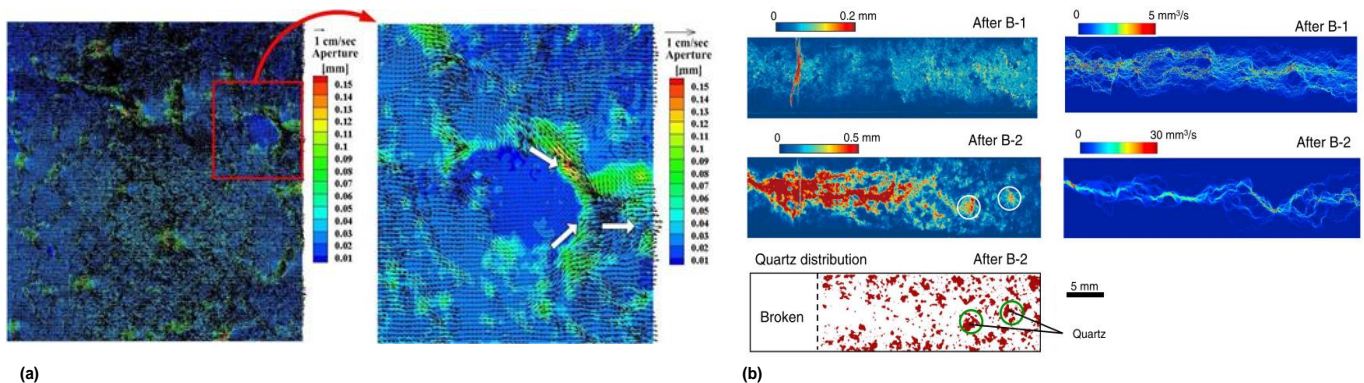


Fig.6.1 Effect factors of the flow behaviour within the fracture aperture (a) fluid direction variation on the roughness surface. (Kishida.et al.2009),(b) fracture width difference and the flow rate change. (Okamoto.et.al. 2017)

Most previous studies assumed that the fluid within a single fracture was considered as a smooth parallel flow. However, the real fracture surface was relatively rough and bumpy. Fracture aperture was confirmed as an essential factor that will affect the flow behavior, and the fracture asperities may be changed under various conditions. The fracture contact-area may be enlarged due to the rock particles filled into the nearby void, and then it will narrow the flow path. The complex internal topography of a fracture and its evolution under different conditions should be verified.

In this Chapter, the purpose is to verify the CT observation result as mentioned in Chapter 4. And to better understand the flow behavior within the fractured rock mass. Aperture distribution and the contact-area ratio under various confining conditions were picked up from the X-ray CT observation result at 20 °C. Based on the X-ray CT data, the flow simulation within the rock fracture is conducted to verify the flow direction change and to check the influence of the contact-area variation within the fracture. Finally, the flow behavior under different confining stress conditions is discussed.

6.2 Methodology

The cubic law was applied to check the flow behavior and the hydraulic properties of the fractured rock. Moreover, the cubic law was suitable for the Re number less than 1 and the inertia term can be ignored. However, the real rough-walled fracture cannot be considered ideal as a smooth parallel plate. Therefore, the fluid passes through the rough-walled fracture should not be identified as the smooth parallel plate. The relative rough fracture surface may produce the hydraulic resistance, and the coefficient of the resistance should be considered as a factor that will influence the flow behavior. In this study, a 2-D flow simulation model was established involving the inertia term, pressure term, and the diffusion term (Mgaya et al., 2004; Kishida et al., 2009, 2013, 2015). Then the flow simulation of a single rock fracture was conducted based on the cubic law and the Navier-Stokes equations.

In this study, the flow discharge distribution and the hydraulic aperture variation under different confining stresses, the Re number were calculated to verify the flow behavior. Different water heads (i.e., 0.25, 0.5, 1.0, 1.5, 3.0, 4.5, 6 cm) were chosen. Moreover, the permeability coefficient was also calculated under different water heads and different conditions. The data which was used in this flow simulation was obtained from the X-ray CT observation, as mentioned in **Chapter 4** (i.e., aperture distributions and the roughness surfaces variation under different confining pressures). A Schematic figure was illustrated in **Fig 6.2**. One-dimensional water flow was generated due to the water head difference between the two sides of the sample. The different flow directions were considered within the rough-walled fracture surfaces, which will also generate the hydraulic resistance and further affects the fluid flow within the fracture.

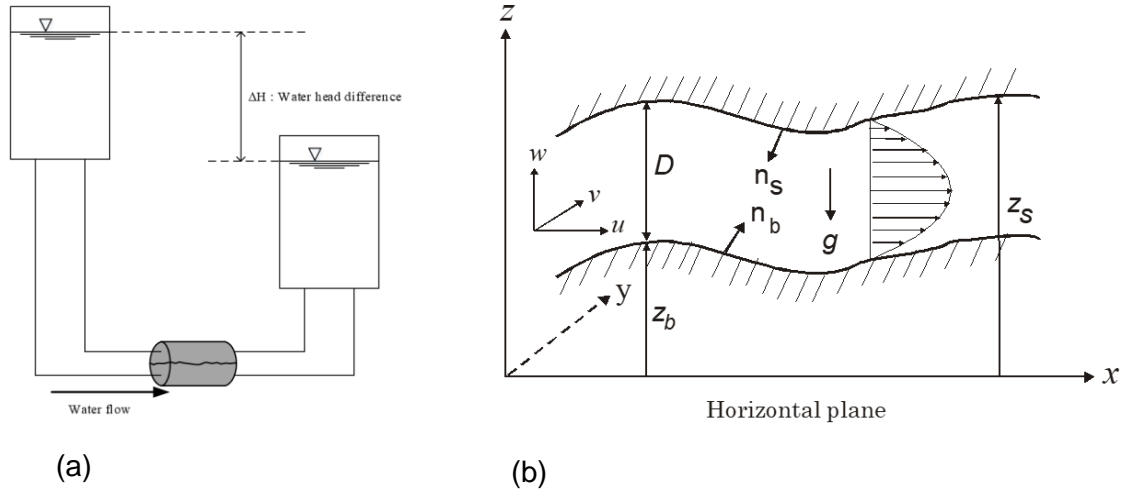


Fig.6.2 Schematic figure of flow through a single fracture (a) flow pass through the rock fracture, (b) cartesian coordinates of Navier-Stokes (Kishida et al., 2013)

6.2.1 Theoretical of the 2-D model

Fig 6.2 has illustrated the orthogonal coordinate which represents the internal fluid flow within the aperture of a single rock fracture. The 2-D flow model shows the momentum conservation equation, which is also used to solve the 3-D problem. The continuation equation and momentum equation of this 2-D model (Mgaya et al.,2004; Kishida et al., 2013) are illustrated as follows:

(Continuity equation)

$$\frac{\partial DU}{\partial x} + \frac{\partial DV}{\partial y} = 0 \quad (6.1)$$

(Momentum equation at X-direction)

$$\begin{aligned} \frac{\partial UD}{\partial t} + \beta \frac{\partial DU^2}{\partial x} + \beta \frac{\partial DUV}{\partial y} = & -D \frac{\partial}{\partial x} \left(\frac{P_D}{\rho} \right) - gD \frac{\partial (Z_b + D)}{\partial x} \\ & - \frac{\tau_{bx}}{\rho} \sqrt{1 + \left(\frac{\partial Z_b}{\partial x} \right)^2 + \left(\frac{\partial Z_b}{\partial y} \right)^2} - \frac{\tau_{sx}}{\rho} \sqrt{1 + \left(\frac{\partial Z_s}{\partial x} \right)^2 + \left(\frac{\partial Z_s}{\partial y} \right)^2} \\ & + \frac{\partial}{\partial x} \left(\nu D \frac{\partial U}{\partial x} \right) + \frac{\partial}{\partial y} \left(\nu D \frac{\partial U}{\partial y} \right) \end{aligned} \quad (6.2)$$

(Momentum equation at Y-direction)

$$\begin{aligned} \frac{\partial VD}{\partial t} + \beta \frac{\partial DUV}{\partial x} + \beta \frac{\partial DV^2}{\partial y} = & -D \frac{\partial}{\partial y} \left(\frac{P_D}{\rho} \right) - gD \frac{\partial (Z_b + D)}{\partial y} \\ & - \frac{\tau_{bx}}{\rho} \sqrt{1 + \left(\frac{\partial Z_b}{\partial x} \right)^2 + \left(\frac{\partial Z_b}{\partial y} \right)^2} - \frac{\tau_{sy}}{\rho} \sqrt{1 + \left(\frac{\partial Z_s}{\partial x} \right)^2 + \left(\frac{\partial Z_s}{\partial y} \right)^2} \\ & + \frac{\partial}{\partial x} \left(\nu D \frac{\partial V}{\partial x} \right) + \frac{\partial}{\partial y} \left(\nu D \frac{\partial V}{\partial y} \right) \end{aligned} \quad (6.3)$$

where U and V are the depth-averaged velocities in the X- and Y-directions, respectively;

D is the distance between the upper roughness surface to lower roughness surface;

$(D=z_s-z_b)$. z_s and z_b are the upper and the lower fracture surface from the standard horizontal plane;

p_D is the pressure of $z = z_b + D$;

g is the gravitational acceleration.

τ_s and τ_b are the shear stress on the upper and the lower walls, respectively. (τ_{bx}, τ_{by}) is the stress vector of the down roughness, (τ_{sx}, τ_{sy}) is the stress vector of the upper roughness;

ν is the kinematic viscosity;

β is introduced here as a momentum correction factor for the laminar flow. In this study, $\beta=1.2$.

The shear stress values on the fracture walls are calculated through using the resistance law, then (τ_{bx}, τ_{by}) and (τ_{sx}, τ_{sy}) are calculated as bellow:

$$\frac{\tau_{bx}}{\rho} = \frac{\tau_{sx}}{\rho} = 6\frac{\nu U}{D}, \quad \frac{\tau_{by}}{\rho} = \frac{\tau_{sy}}{\rho} = 6\frac{\nu W}{D} \quad (6.4)$$

6.2.2 Procedure of the numerical simulation

The fracture roughness surface was considered as an idealized sinusoidal surface (Mgaya et al., 2004;). Therefore, the flow within the aperture is determined as the fluid under a slight amplitude-to-wavelength ratio, then the flow behavior was thought as a laminar flow. For an incompressible fluids, the numerical analysis procedure is explained as follows (Mgaya et al., 2004; Kishida et al., 2009;2013;2015):.

In order to calculate the velocity and the pressure, the HSMAC (Highly Simplified Marker and Cell) method was used (Hirt and Cook, 1972).At the initial condition, When the time $t = n\Delta t$, the flow flux M, N ($M=UD, N=UD$) and the p_D are already known. When at the time step $t = (n+1)\Delta t$, the hydraulic variables are obtained as below:

- 1) N^* and M^* represent the hydraulic variables. At $t = (n+1)\Delta t$, they will be calculated as:

$$\frac{M^* - M^n}{\Delta t} = -(\text{Inertia term})^n - (\text{Pressure term})^n - (\text{remaining term})^n \quad (6.5)$$

$$\frac{M^* - M^n}{\Delta t} = -(\text{Inertia term})^n - (\text{Pressure term})^n - (\text{remaining term})^n \quad (6.6)$$

- 2) N^* and M^* are the important factors which are used to satisfy the equation of (6.1). (6.7) is a correction factor of the pressure p_D and p_D^* , as shown below:

$$P_{Di,j}^* = P_{Di,j}^n + \delta P_D^* \quad (6.7)$$

Then δP_D^* is calculated by Eq. (6.8):

$$\delta^* P_{Di,j} = -\frac{\omega \varepsilon_{i,j}^*}{2gD_{(i,j)}\Delta t \left(\frac{1}{\Delta x^2} + \frac{1}{\Delta y^2} \right)} \quad (6.8)$$

where ω is the convergence parameter, in this study it is equal to 0.5.

Then from the continuation equation, the error ε^* can be calculated as illustrated in Eq. (6.9):

$$\varepsilon^* = \frac{M_{i+1,j}^* - M_{i,j}^*}{\Delta x} + \frac{N_{i,j+1}^* - N_{i,j}^*}{\Delta y} \quad (6.9)$$

- 3) P_D^* was calculated from Eq. (6.7), then the N^* and M^* can be calculated by using the value of P_D^* is inputted into the momentum equations in X- and Y-directions of (6.2), (6.3).
- 4) If the absolute values of N^* and M^* which are obtained from the continuation equation are less than the average value, when $t = (n+1)\Delta t$, N^* , M^* and P_D^* can be calculated again from the procedure 2) and 3).
- 5) 4) will be repeated when the error value of ε^* is satisfied (Kishida et al., 2009);.

6.3 Results of the flow simulation

6.3.1 Discharge and aperture change under various conditions

At 20 °C, flow simulation was conducted under different stress conditions through using the obtained data of X-ray CT. Flow variation was affected both of the confining pressure and the water head difference. Flow simulation results are listed in **Table 6.1~6.5**. Moreover, the flow discharge distributions under different conditions are depicted in **Fig 6.3~Fig 6.7**.

From the simulation results, it is noted that the flow discharge became larger under a higher water head. In contrast, the flow discharge at the confining pressure of 3.0 MPa was lower than the value at 0 MPa, which indicates that the apertures became smaller under a higher confining pressure. The flow velocity was larger at 0 MPa, in contrast, the velocity decreased sharply when the confining pressure was applied immediately. This result is also corresponding to the permeability test results. Which showed that the permeability decreased with increasing the confining pressure. i.e., at the short-term tests, the permeability is sensitive to the confining stress influence. Moreover, it can be confirmed that hydraulic aperture obtained from the simulation result is decreased after 180 days. It is congruent with the long-term permeability test result, the permeability has a decreasing tendency after keeping the confining pressure at 3.0 MPa for 180 days. It is also congruent with the CT observation result, which showed that the fracture aperture became narrower after 180 days.

Table 6.1 Flow simulation results (0 MPa, 0 day, 20 °C)

Water head [cm]	0.25	0.5	1.0	1.5	3.0	4.5	6.0
Discharge [cm ³ /s]	7.98×10^{-3}	1.57×10^{-2}	3.05×10^{-2}	4.45×10^{-2}	8.35×10^{-2}	0.12	0.15
Hydraulic aperture[mm]	0.19893	0.19784	0.19593	0.19413	0.19005	0.18735	0.18337
Permeability [m ²]	3.30×10^{-9}	3.26×10^{-9}	3.20×10^{-9}	3.14×10^{-9}	3.01×10^{-9}	2.93×10^{-9}	2.80×10^{-9}
Reynolds number	0.54	1.06	2.06	3.00	5.63	8.09	10.10

Table 6.2 Flow simulation results(3.0 MPa, 0 day, 20 °C)

Water head [cm]	0.25	0.5	1.0	1.5	3.0	4.5	6.0
Discharge [cm ³ /s]	4.359×10^{-3}	8.690×10^{-3}	1.728×10^{-2}	2.578×10^{-2}	6.157×10^{-2}	9.105×10^{-2}	0.120
Hydraulic aperture[mm]	0.16261	0.16244	0.16213	0.16183	0.17169	0.17088	0.17022
Permeability [m ²]	2.20×10^{-9}	2.20×10^{-9}	2.48732×10^{-9}	2.45789×10^{-9}	2.45656×10^{-9}	2.43336×10^{-9}	2.41462×10^{-9}
Reynolds number	0.294	0.586	1.16	1.74	4.15	6.14	8.09

Table 6.3 Flow simulation results (3.0 MPa,30 day, 20 °C)

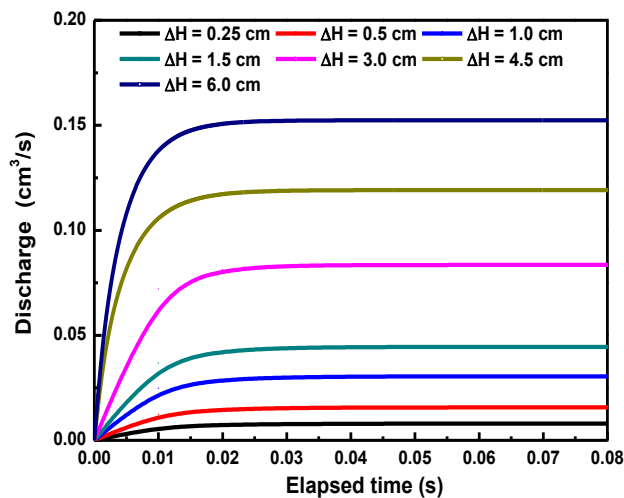
Water head [cm]	0.25	0.5	1.0	1.5	3.0	4.5	6.0
Discharge [cm ³ /s]	4.318×10^{-3}	8.605×10^{-3}	1.71×10^{-2}	2.55×10^{-2}	5.00×10^{-2}	7.39×10^{-2}	9.71×10^{-2}
Hydraulic aperture[mm]	0.16210	0.16191	0.16156	0.16125	0.16018	0.1594	0.15862
Permeability [m ²]	2.19×10^{-9}	2.18×10^{-9}	2.17517×10^{-9}	2.16668×10^{-9}	2.13826×10^{-9}	2.1173×10^{-9}	2.09672×10^{-9}
Reynolds number	0.291	0.58	1.15	1.72	3.37	4.98	6.55

Table 6.4 Flow simulation results (3.0 MPa, 60 day, 20 °C)

Water head [cm]	0.25	0.5	1.0	1.5	3.0	4.5	6.0
Discharge [cm ³ /s]	4.359×10^{-3}	8.690×10^{-3}	1.73×10^{-2}	2.58×10^{-2}	5.07×10^{-2}	7.51×10^{-2}	9.88×10^{-2}
Hydraulic aperture [mm]	0.16261	0.16244	0.16219	0.16188	0.16093	0.16026	0.15954
Permeability [m ²]	2.20×10^{-9}	2.20×10^{-9}	2.19209×10^{-9}	2.18364×10^{-9}	2.15817×10^{-9}	2.14016×10^{-9}	2.12112×10^{-9}
Reynolds number	0.294	0.586	1.17	1.74	3.42	5.06	6.66

Table 6.5 Flow simulation results (3.0 MPa, 180 day, 20 °C)

Water head [cm]	0.25	0.5	1.0	1.5	3.0	4.5	6.0
Discharge [cm ³ /s]	4.447×10^{-3}	8.868×10^{-3}	1.76×10^{-2}	2.63×10^{-2}	5.19×10^{-2}	7.68×10^{-2}	1.01×10^{-1}
Hydraulic aperture[mm]	0.16370	0.16354	0.16324	0.16295	0.16217	0.16146	0.16083
Permeability [m ²]	2.23×10^{-9}	2.22×10^{-9}	2.2205×10^{-9}	2.21274×10^{-9}	2.19153×10^{-9}	2.17234×10^{-9}	2.1556×10^{-9}
Reynolds number	0.3	0.598	1.19	1.77	3.50	5.18	6.81

**Fig.6.3** Discharge at different water heads (0 day,0 MPa,20 °C)

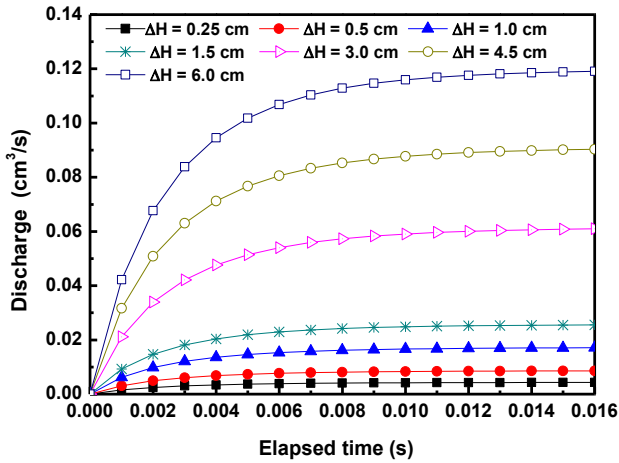


Fig.6.4 Discharge at different water heads (0 day, 3.0 MPa, 20 °C)

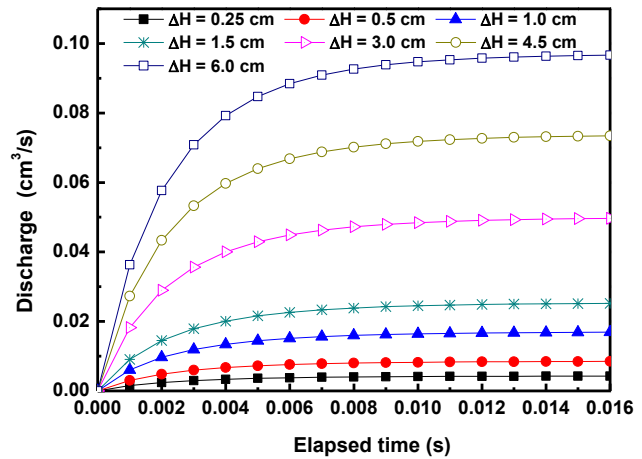


Fig.6.5 Discharge at different water heads (30 day, 3.0 MPa, 20 °C)

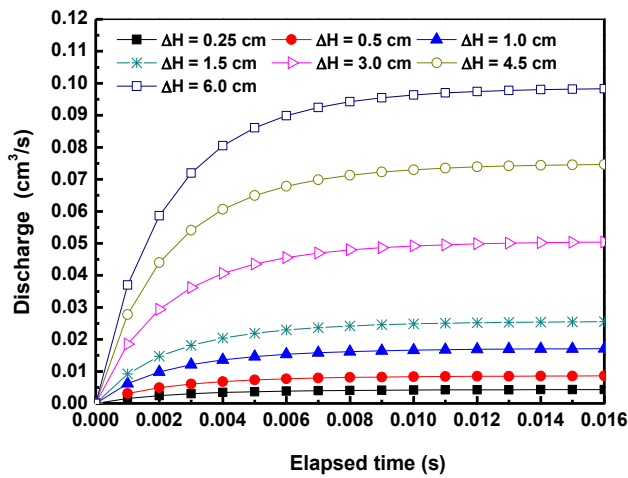


Fig.6.6 Discharge at different water heads (60 day, 3.0 MPa, 20 °C)

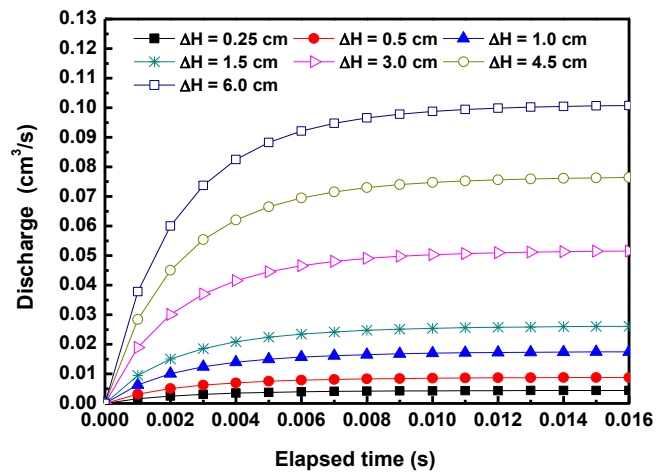


Fig.6.7 Discharge at different water heads (1800 day, 3.0 MPa, 20 °C)

The flow vector variations are shown in Fig 6.8~Fig 6.9. The flow vector distribution illustrates that the flow velocity and direction are different under different conditions. i.e., different water heads (i.e., 0.25,~6.0 cm), and different confining stresses (i.e., 0 and 3.0 MPa). The flow vectors became larger at a higher water head. However, it decreased at 3.0 MPa, as shown in Fig 6.9. Moreover, the fracture aperture reduction can be observed from the color contour map. Aperture decreasing will change the flow path, and the flow concentrates on the aperture open positions. It can be noted that the flow bypassed the fracture contact-areas under the confining stress of 3.0 MPa. The flow vector distributions demonstrate that the flow became more tortuous and random around the fracture contact-areas at a higher confining pressure.

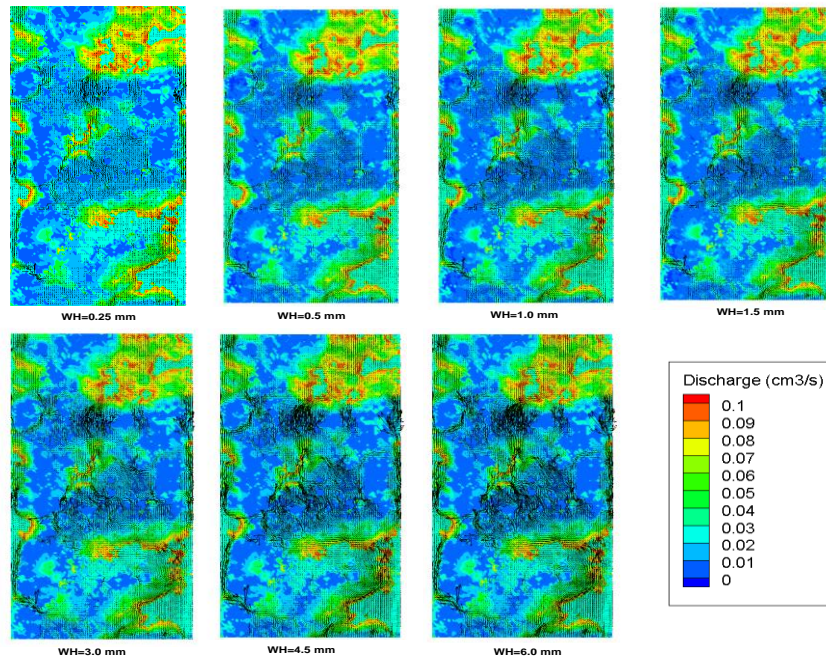


Fig.6.8 Flow vector distribution under different water heads (0 MPa, 0 day, 20 °C)

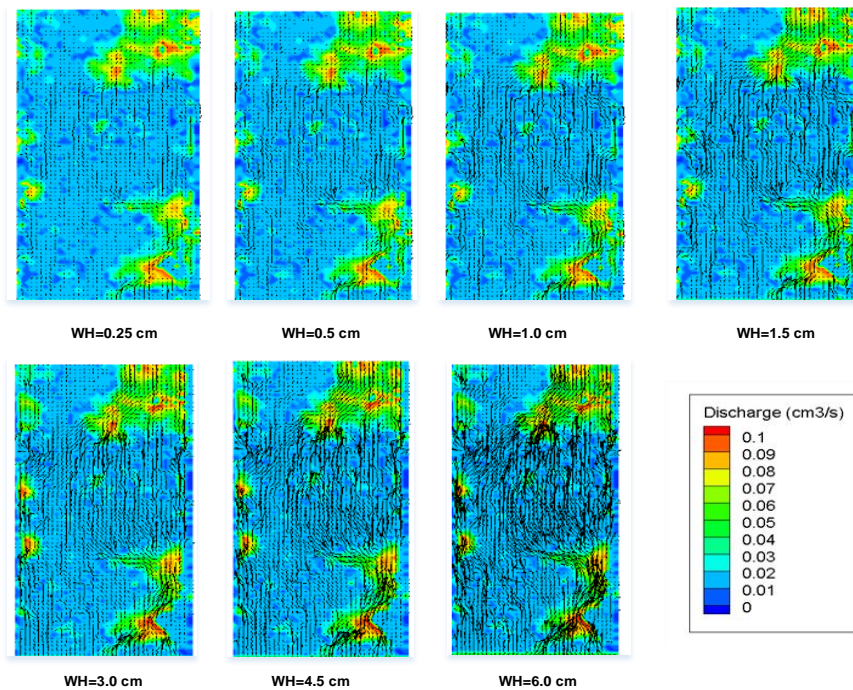


Fig.6.9 Flow vector distribution under different water heads (3.0 MPa, 0 day, 20 °C)

6.3.2 Reynolds number variation under various conditions

In general, flow within a single rock fracture was considered as laminar flow. Flow simulation results showed that the Re number is less than 10 when the water heads are less than 1.5 cm. The weak inertia regime exists when the Reynolds number is range from 1.0~10.0, and the hydraulic transmissivity nonlinearly will decrease when the Re values becomes larger. From the simulation results, it can be observed that Re number is smaller under a relative lower water head. In contrast, a larger Reynolds

number exists when the water head becomes higher, i.e., the water heads equal to 3.0~6.0 cm. The Re values in **Table 6.1~6.5** are almost ranging from 1~8. However, some fracture positions, as illustrated of the red color in the Re contour map in **Fig.6.10**, which shows that the value is larger than 10.0. Therefore, it can not be recognized as a linear flow. The flux and the pressure gradient became nonlinear under a relative high Reynolds number. A Forchheimer flow regime (Vafai, et al., 1995) should be considered when the Reynolds number is larger than 10. Which clarified that the flow was inclined to be a turbulence. Therefore, a larger Re value may correspond to the flow behavior within the aperture, it became tortuous and random under the different conditions.

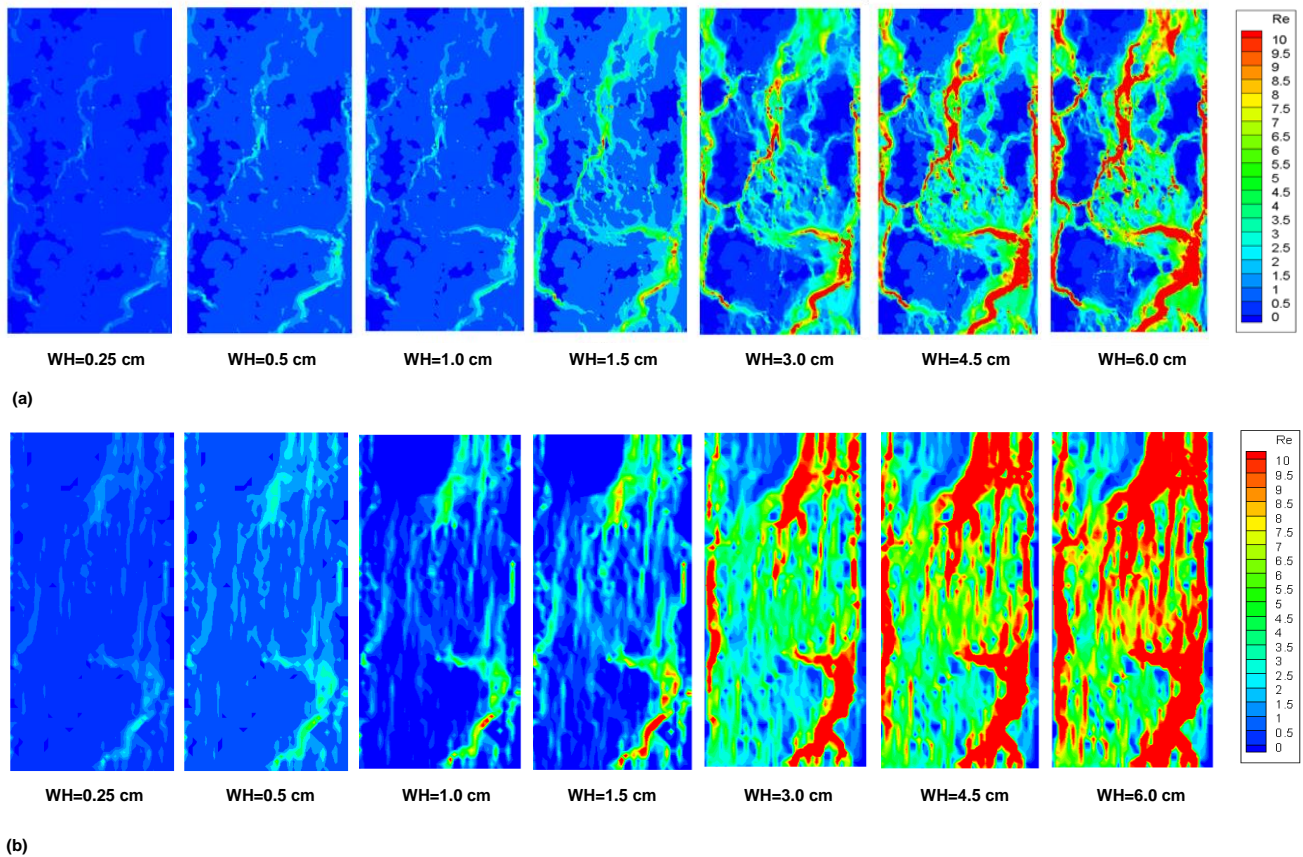


Fig.6.10 Reynolds number distribution under different water heads (a) 0 MPa, 0 day, 20 °C;(b) 3.0 MPa, 0 day, 20 °C

6.4 Hydraulic aperture Comparison under different methods

The flow discharge under different water heads can be linearized as a fitting curve as shown in **Fig.6.11**. i.e., the flow discharge value can be calculated when the water head is 2.5 cm. Therefore, the discharge and the hydraulic aperture value at different period (i.e., 0, 30, 60 and 180 days) at the water head is 2.5 cm are listed in **Table 6.6**. Moreover, hydraulic aperture results from the CT observation are extracted aperiodicity. i.e., hydraulic aperture value at 0, 14, 28, 60, 90, 120, 150, 180 days. Therefore, hydraulic aperture comparison between the flow simulation and the CT experiment results is shown in **Fig 6.12**.

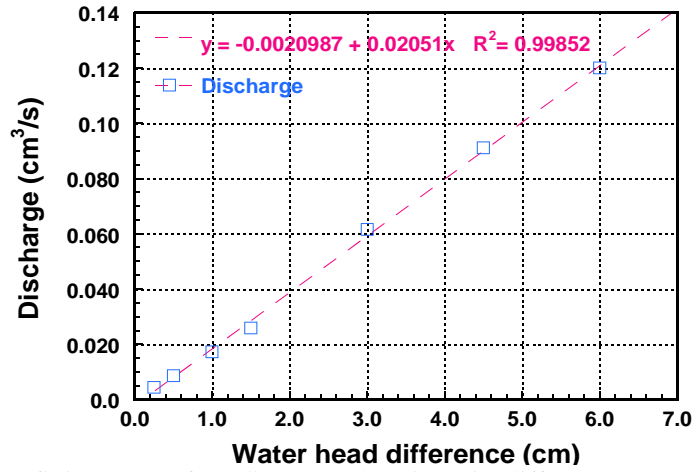


Fig.6.11 A linear fitting curve of the discharge changing with different water heads (3.0 MPa, 0 day, 20 °C)

Table 6.6 Long-term hydraulic aperture evolution at the water head of 2.5 cm, 3.0 MPa, 180 day, 20 °C)

Water head difference (2.5 cm)	Discharge (cm ³ /s)	Hydraulic aperture (mm)
3 MPa, initial 0 day, 20 °C	4.904×10^{-2}	0.169
3 MPa, 30 day, 20 °C	3.97×10^{-2}	0.158
3 MPa, 60 day, 20 °C	4.02×10^{-2}	0.158
3 MPa, 180 day, 20 °C	4.13×10^{-2}	0.160

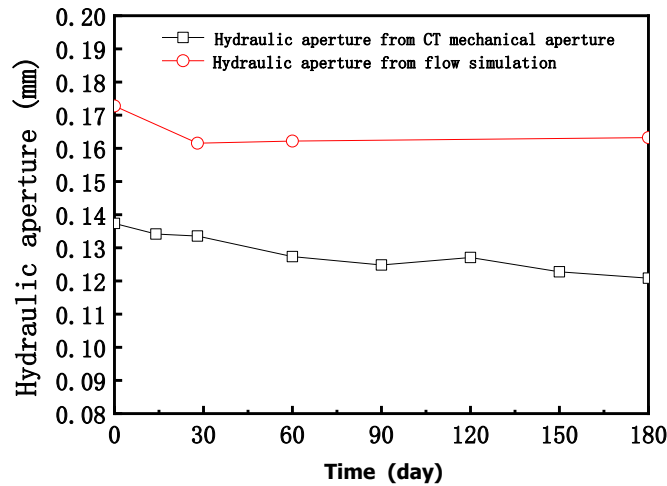


Fig.6.12 Comparison with hydraulic aperture obtained from CT mechanical aperture and from the flow simulation

Hydraulic aperture obtained from the CT mechanical aperture, and from the flow simulation were compared. Hydraulic aperture from the flow simulation is slightly larger than the value from the CT mechanical aperture, as depicted in **Fig.6.12**. After 180 days, hydraulic aperture decreasing is confirmed. Moreover, after 30 days, both of two results (i.e., hydraulic aperture value from the CT mechanical aperture and the flow simulation) are decreased about 0.01. The decreasing tendency is quite similar. It also indicates that the fracture aperture before 30 days generated an aperture deformation under the mechanical compaction. After 30 days, the aperture deformation is not obvious. The fracture asperities generated an irreversible change, and the flow behavior was altered as this deformation. After 90 days,

the hydraulic aperture shows that it is a slight increase. The same variation indicates the aperture may be enlarged. Moreover, the fracture roughness surfaces variation and the aperture change in the long-term illustrated that the flow within the fracture might not defer to the Cubic law. It becomes randomly when the fracture roughness surface was deformed. Therefore, the Reynolds number shows the value is larger than 10. The transform of fracture roughness surfaces may produce the hydraulic resistance, then the flow within the rough-walled fracture became slowly.

Fig 6.13 shows the hydraulic aperture comparison of three different results. i.e., hydraulic aperture obtained from the flow simulation, from the CT mechanical aperture, and from the permeability tests. Result shows that there is no significant difference on the hydraulic aperture obtained from the flow simulation and from the CT mechanical aperture. However, hydraulic aperture from the permeability tests showed that it was 2 orders of magnitude lower than the other two results. Which can be supposed that the sample size is different. i.e., the sample which was used in the permeability test has a larger size than in the CT observation test. However, the decreasing tendency of hydraulic aperture is quite similar. It indicates that the fracture roughness surfaces of the two samples generated a similar deformation under the same experimental condition although the size is different. The simulation result corresponds to the experimental results, as mentioned in **Chapter 3 and 4**.

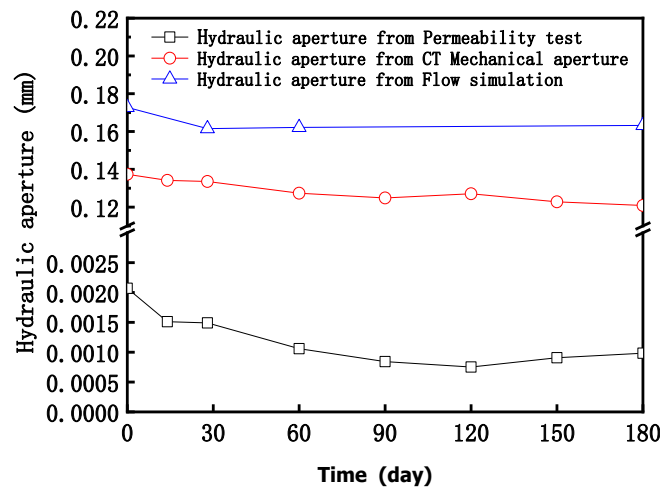


Fig.6.13 Comparison with hydraulic aperture obtained from permeability test, from CT mechanical aperture, and from the flow simulation at 20 °C

6.5 Summary

In this Chapter, numerical flow simulation was conducted using the CT experimental data at 20 °C. Aperture distributions and the roughness surfaces at different periods at 0 and 3.0 MPa were picked up. i.e., long-term CT observation of 180 days. Flow simulation was conducted and compared at each experiment point. Several conclusions are summarized as follows:

1. The flow vector distributions show that the flow velocity at 0 MPa is more significant than the value at 3.0 MPa. Mechanical compaction has a significant influence on the flow velocity. The flow discharge distribution demonstrates that the flow decreased at 3.0 MPa, which indicates that a closed aperture will restrict the fluid flow. The flow became slowly due to the mechanical compaction.
2. From observing the flow color contour map, it can be understood that the flow within the fracture aperture is inhomogeneous, it is disturbed by different positions, especially around the fracture contact-area. The flow bypassed the fracture contact-area and changed the flow path. The flow became tortuous and random around the contact-area and concentrated on a relative aperture open position.
3. Reynolds number at different water heads shows the difference. From the simulation results, we can understand that Re number was larger than 10 at some positions. Therefore, Darcy's law is not suitable. Forchheimer flow regime may better illustrate when the Reynolds number is larger than 10. It also indicated that the flow within the fracture became random and turbulence.
4. Hydraulic aperture, which was calculated from the flow simulation, from the CT experimental results, and from the permeability test results were compared. Results show that the hydraulic aperture from the flow simulation is much close to the result measured from the CT observation. In contrast, the hydraulic aperture value obtained from the permeability tests shows lower. However, hydraulic aperture variations of these results are qualitatively match each other well. Flow was disturbed by the fracture contact-area is verified.

References

- Hirt,C.W., Cook,J.L.: Calculating three-dimensional flows around structures and over rough terrain. *Journal of Computational Physics*. 10.324-340.1972.
- Kishida, K., Ishikawa, T., Higo, Y., Sawada, A. and Yasuhara, H. :Measurements of fracture aperture in granite core using microfocus X-ray CT and fluid flow simulation. *49th US Rock Mechanics / Geomechanics Symposium*. San Francisco, CA, USA, 15-0485.2015.
- Kishida, K., Mgya, P., Ogura, K. and Hosoda, T. :Flow on a single rock fracture in the shear process and the validity of the cubic law examined through experimental results and numerical simulations. *Soils and Foundations*. 49(4): 597-610.2009.
- Kishida, K., Sawada, A. and Yasuhara, H.: Estimation of fracture flow considering the inhomogeneous structure of single rock fractures. *Soils and Foundations*. 53(1):105-116.2013.
- Li, B., Jiang, Y.J., Koyama, T., Jing, L.R. and Tanabashi, Y.: Experimental study of the hydro-mechanical behavior of rock joints using a parallel-plate model containing contact areas and artificial fractures. *International Journal of Rock Mechanics and Mining Sciences*. 45(3): 362-375.2008.
- Mgya, P., Kishida, K., Hosoda, T. and Yamamoto, A.: Estimation of flow behavior on rock joints using the depth averaged flow model. *Journal of Applied Mechanics*. JSCE. 7: 1013-1021.2004.
- Min, K.B., Rutqvist, J. and Elsworth, D.: Chemically and mechanically mediated influences on the transport and mechanical characteristics of rock fractures [J], *International Journal of Rock Mechanics and Mining Sciences*. 46(1): 80–89.2009.
- Okamoto, A.,Tanaka, H.,Watanabe, N.,Saishu, H.,Tsuchiya, N.: Fluid Pocket Generation in Response to Heterogeneous Reactivity of a Rock Fracture Under Hydrothermal Conditions. *Geophysical Research Letters* 44(20): 10,306-310,315.2017.
- Polak, A., Elsworth, D. and Liu, J. S. :Spontaneous switching of permeability changes in a limestone fracture with net dissolution [J], *Water Resources Research*. 40(W03502): 1029–1 038.2004.
- Pyrak, L.J. and Morris, J.P.:Single fractures under normal stress: the relation between fracture specific stiffness and fluid flow. *International Journal of Rock Mechanics and Mining Sciences*. 37:245–262.doi:10.1016/S1365- 1609(99)00104-5.2000.
- Raven, K.G. and Gale, J.E. : Water flow in a natural rock fracture as a function of stress and sample size. *International Journal of Rock Mechanics and Mining Sciences*. 22:251–61. 1985.
- Vafai, K. and Kim, S.J.: On the Limitation of the Brinkman-Forchheimer-Extended Darcy Equation. *International Journal of Heat Fluid Flow*, 16, 11-15.1995

Yasuhara, H., Elsworth D. and Polak, A.: Evolution of permeability in a natural fracture: Significant role of pressure solution. *Journal of Geophysical Research*. 109, B03204, doi:10.1029/2003JB002663.2004.

Yasuhara, H., Elsworth, D., Liu, J.S. and Halleck, P. : Spontaneous switching between permeability enhancement and degradation in fractures in carbonate: Lumped parameter representation of mechanically- and chemically mediated dissolution. *Transport in Porous Media*, 65, 385–409, doi:10.1007/s11242-006-6386-2. 2006.

Chapter 7 Chemical-Mechanical simulation of a single rock fracture under various conditions

7.1 Introduction

From experimental studies in **Chapter 3** and **Chapter 4**, it can be understood that permeability of a single granite fracture was changed under coupled (THMC) processes (Polak et al., 2004; Min et al., 2009; Ghassemi, 2012; Danko et al., 2012). The geochemical reactions within the rock fracture may significantly influence the permeability and aperture change in the long-term (Yasuhara et al., 2004; 2011; 2015). Several researchers ((Bernabé & Evans, 2014; Lang et al., 2015; Yasuhara et al., 2003; 2015) conducted the flow-through tests under different temperatures and confining pressures; pressure dissolution generates on the fracture asperities with an effective stress. Which will drive the to the chemical reaction. The dissolved minerals from the fracture asperities and the pore space change have been verified. Previous studies (Watanabe 2005; Taron et al., 2009; Lang et al., 2015) have been conducted to check the permeability evolution under mechanical-chemical coupled processes through numerical works. However, few laboratory works are used to compare with the simulation results. Moreover, internal fracture information such as the contact-area conditions under coupled processes needs to be checked further. Therefore, in this Chapter, the chemical-mechanical simulation was conducted to verify the aperture and the fracture contact conditions. CT data which were measured from the X-ray CT in **Chapter 4** was used. Then the simulation results are used to compare with the permeability evolution in the long-term. Finally, simulation results were discussed.

7.2 Matching the laboratory data

The schematic process of the chemical-mechanical simulation is shown in **Fig 7.1**. The initial aperture distribution and the fracture roughness surface without the confining pressure were measured from X-ray CT (i.e., **Chapter 4**, fracture down roughness surface and aperture value at 0 MPa). Then the aperture and the contact-area ratio changing with time can be evaluated, as illustrated in **Fig 7.2**. The mineral composition variation result from the simulation was used to compare with the experiment result. i.e., mineral composition variation which was measured in **Chapter 3**.

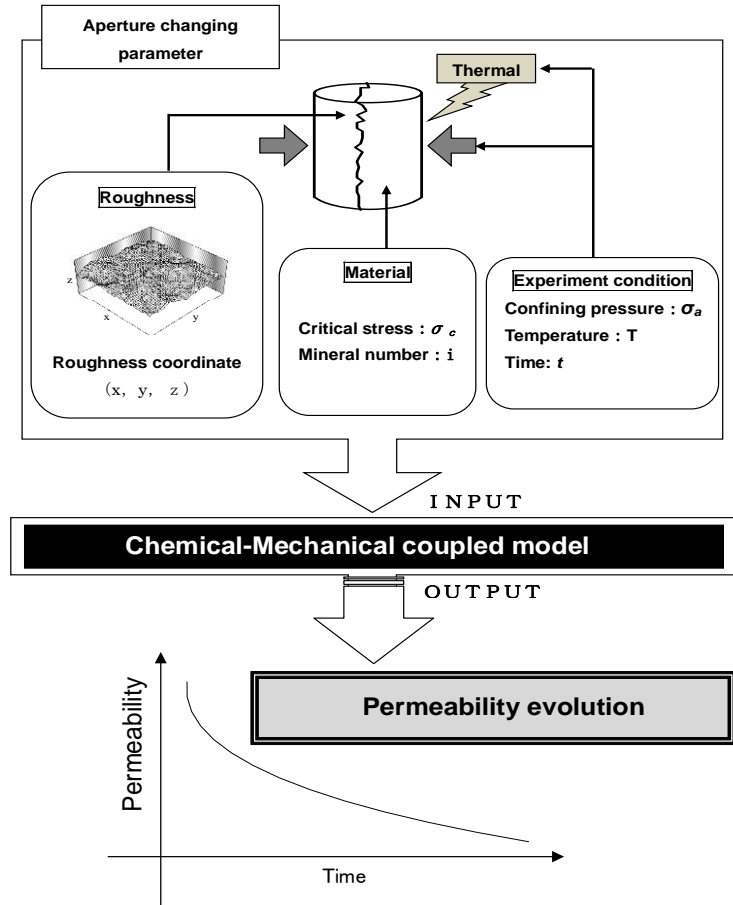


Fig.7.1 Schematic of permeability evolution under Chemical-Mechanical coupled processes

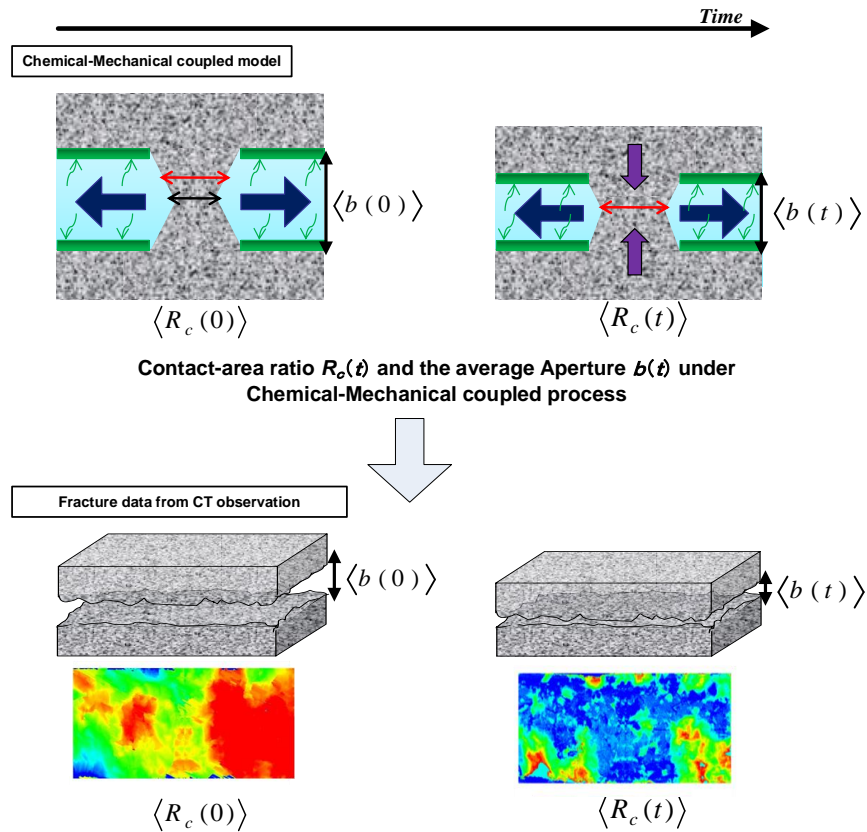


Fig.7.2 Conception figure of the prediction in aperture and the contact area change

7.3 Conceptual model

The chemical-mechanical process includes the pressure solution and the free-face dissolution happens within the aperture under various conditions (Yasuhara et al., 2003;2004). This process is described as follows:

- 1) The mineral dissolution happened on the fracture asperities
- 2) The mineral diffusion occurred along with the interfacial water film,
- 3) The mineral precipitation transports from the pore fluid to the pore wall.

Therefore, fracture aperture was altered through the interaction of the mineral dissolution, diffusion, and precipitation, as illustrated in **Fig 7.3** (Rutter,1976). The precipitation is not easy to happen because the pressure solution isn't easy to occur within a small pore space, while the pressure solution is easy to generate on the large pore space. The mineral elements are supposed as different composition. Previous study confirmed that the pressure solution is easy to happen under the conditions of 100 °C and 10.0 MPa (Yasuhara et al.,2013). Moreover, (Yasuhara et al.,2004; 2006;Polak et al.,2003) confirmed that the pressure solution was generating on the fracture contact asperities when the temperature and confining pressure were less than 150 °C and 10.0 MPa, respectively.

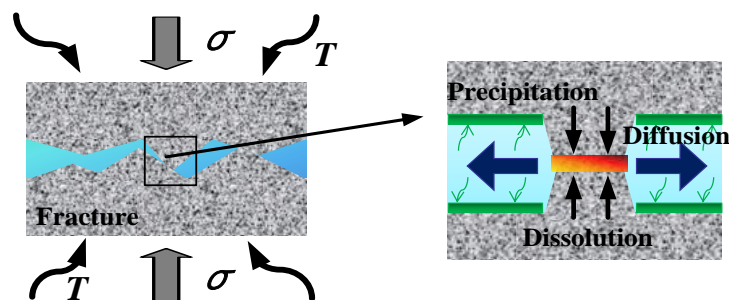


Fig.7.3 A schematic figure of pressure dissolution

7.3.1 Pressure solution • free-face dissolution

(Yasuhara et al.2004) defined the mass flux based on the process of dissolution, diffusion, and precipitation. Moreover, the thermodynamics under the non-hydrostatic and non-equilibrium states was also considered. The mass flux is defined by the difference between the chemical reactions on the fracture contact-area and on the free-face, and the dissolution generated on the fracture asperities. Moreover, the diffusion mass fluxes is described as the molecular diffusion phenomena based on the Fick's first law. The integral derivation was considered as the evolution on the fracture contact-area. Which indicated that the mass dissolved from the fracture contact asperities to the pore space. Then, the precipitation mass fluxes is defined as the secondary minerals production by the constant precipitation rate and the difference

between the solute solubility and concentration within the pore space. Therefore, the equations of dissolution, diffusion, and precipitation are shown below:

$$\dot{M}_{diss}^{PS} = \frac{3V_m^2(\sigma_a - \sigma_c)k_+\rho_g A_c}{RT} \quad (7.1)$$

$$\dot{M}_{diff} = \frac{2\pi\omega D_b}{\ln(d_c/2\varepsilon)} (C_{int} - C_{pore}) \quad (7.2)$$

$$\dot{M}_{prec} = k_- A_{pore} \rho_g V_m \left(\left(\frac{C_{pore}}{C_{eq}} \right)^p - 1 \right)^q \quad (7.3)$$

where, \dot{M}_{diss}^{PS} is the dissolution mass fluxes, \dot{M}_{diff} is the diffusion mass fluxes, \dot{M}_{prec} is the precipitation mass fluxes, V_m is the bulk volume, σ_a the stresses acting on the grain contact area, σ_c is the critical stress, $k_{+/-}$ is the dissolution and precipitation rate constant of quartz, ρ_g is the grain density (2650 kg m⁻³ for quartz), A_c is the grain contact area, R is the gas constant, T is the temperature of the system, ω is the thickness of the water film trapped at the interface, D_b is the diffusion coefficient, d_c is grain diameter, $(C_{int})_{x=\varepsilon}$ ($0 < \varepsilon < 1$) and $(C_{int})_{x=a}$ and $(C_{pore})_{x=dc/2}$ are concentrations in the interface and pore space, respectively. C_{eq} is the solubility of quartz (Fournier and Potter, 1982; Ragnarsdóttir and Walther, 1983), A_{pore} is the relative grain surface area, p and q is the constant number through the dissolution tests.

The interaction of the dissolution, diffusion, and precipitation processes depends on the constant parameter of Eq. (7.1) ~ (7.3), i.e., the dissolution, precipitation, the molecular diffusion, mineral composition, and the dissolved ion. Which has a great relationship to the temperature. Then the Arrhenius-type is written in Eq. (7.4) as follows:

$$x_i = x_i^0 \exp(-E_{x_i} / RT) \quad (7.4)$$

where x_i , $k_{+/-}$ or D_b , x_i^0 ($= k_{+/-}^0$ or D_b^0) is the pre-exponential factor, E_{x_i} ($= E_{k_{+/-}}$ or E_D) is the activation energy. The free-surface dissolution will happen when the material concentration is less than the solubility within the aperture.

$$\dot{M}_{diss}^{FF} = k_+ A_{pore} \rho_g V_m \left(1 - \left(\frac{C_{pore}}{C_{eq}} \right)^m \right)^n \quad (7.5)$$

The Eq. (7.1)~ (7.5) describe the pressure solution, diffusion, the free surface dissolution and the sedimentation mechanism of a single mineral composition within the rock fracture. However, the sample

was composed by the multiple minerals, then the volume contents of mineral i is x_i^V , and then the dissolution is written as Eq. (7.6). i.e., the roughness factor f_r , which represents the ratio of the microscopic surface area and the macroscopic surface area.

$$\dot{M}_{diss}^{PS} = f_{r,i} x_i^V \frac{3V_{m,i}^2 (\sigma_a - \sigma_c) k_{+,i} \rho_{g,i} A_c}{RT} \quad (7.6)$$

while,

$$f_{r,i} = \frac{S_{BET,i} \bar{d}_i \rho_{g,i}}{6} \quad (7.7)$$

S_{BET} is the specific surface area measured by BET method, ρ_w is the solvent density. \bar{d} is the average diameter of the grain, i means the mineral composition of the granite sample. Therefore, considering the whole mineral composition m , the dissolution mass flux can be changed as:

$$\begin{aligned} \dot{M}_{diss}^{PS} &= \sum_i^m \dot{M}_{diss,i}^{PS} \\ &= \frac{3(\sigma_a - \sigma_c) A_c}{RT} \sum_i^m f_{r,i} x_i^V V_{m,i}^2 k_{+,i} \rho_{g,i} \end{aligned} \quad (7.8)$$

The diffusion flux in Eq. (7.2) calculates the total diffusion of the contact-area by using the Fick's first law, which shows an integration from the contact center to the contact boundary. There is a singularity point around the contact center. Therefore, the exact solution cannot be obtained. An approximation process is performed when the integration is conducted with a slight departure from the contact center to the contact boundary. The more accurate diffusion can be calculated by the modification of the diffusion flux. Moreover, the diffusion is defined as the steady-state, then the diffusion in an axial domain is expressed as:

$$\frac{1}{r} \frac{d}{dr} \left(r \frac{dC}{dr} \right) + \frac{A_0}{D_b} = 0 \quad (7.9)$$

Here, the C is the material concentration around the diameter r . A_0 is the dissolution under the asperity contacts via the defined contact-area. It is assumed that the contact-area boundary concentration is equal to the pore space concentration. Therefore, after the integration within r , the formula is written as:

$$C(r) = C_{pore} + \frac{A_0}{D_b} (a_c^2 - r^2) \quad (7.10)$$

where a_c is the diameter around the contact-area. From Eq.(7.10), Eq. (7.11) can be written as:

$$\begin{aligned}
C_{\text{int}} \pi a^2 &= \int_0^a C(r) \cdot 2\pi r dr \\
\Rightarrow C_{\text{int}} &= C_{\text{pore}} + \frac{\dot{M}_{\text{diff}} / \pi a_c^2 \omega}{8D_b} a_c^2 \\
\Rightarrow \dot{M}_{\text{diff}} &= 8\pi D_b \omega (C_{\text{int}} - C_{\text{pore}})
\end{aligned} \tag{7.11}$$

It is considered that the ions dissolved to the pore space is not in a linear path. It diffused randomly to the pore space. Then the circuitous ratio (7.11) is considered as :

$$\dot{M}_{\text{diff}} = \frac{8\pi D_b \omega}{\tau} (C_{\text{int}} - C_{\text{pore}}) \tag{7.12}$$

where τ is the circuitous ratio of the material dissolved ions. Then the concentration is evaluated from the material dissolved ions j. If the total numbers of the dissolved masses which are composed by the mineral dissolution n, then the total diffusion mass fluxes is expressed as:

$$\dot{M}_{\text{diff}} = 8\pi \omega \sum_j^n \frac{D_{b,j}}{\tau} (C_{\text{int},j} - C_{\text{pore},j}) \tag{7.13}$$

Second, the free-face dissolution, precipitation within the aperture were considered. In this study, it is assumed that the influence of the precipitation is negligible, and the free-face dissolution flux is defined as follows:

$$\dot{M}_{\text{diss}}^{\text{FF}} = A_{\text{pore}} \sum_i^m f_{i,r} x_i^V V_{m,i} k_{+,i} \rho_{g,i} \left(1 - \frac{Q_i}{K_i} \right) \tag{7.14}$$

where Q_i is the activity product of ions, K_i is equilibrium constant number. Moreover, the activity product of ions, and the constant equilibrium number in Eq.(7.14) are the important parameters of the mineral and the dissolution ions. It mainly depends on the temperature, mineral concentration, and the charge number, which is shown as follows:

$$Q_i = \prod a_j = \prod r_j c_j \tag{7.15}$$

$$\begin{aligned}
K_i &= \alpha_1 + \alpha_2 T + \frac{\alpha_3}{T} + \frac{\alpha_4}{T^2} + \alpha_5 \log T + \alpha_6 T^2 \\
&+ \alpha_7 T^3 + \alpha_8 T^4 + \alpha_9 T^5 + \alpha_{10} T^6 + \alpha_{11} T^7
\end{aligned} \tag{7.16}$$

a_x ($x=1 \sim 11$) is constant, then the chemical reaction equation and the constant equilibrium based on the activity product ions are listed in **Table 7.1 and Table 7.2** (Stefán et al.,1982; Holland et al., 1998; Andri,2001):

Table 7.1 Chemical reaction formula of the ionic activity product

Name	Chemical reaction
(Quartz)	$\text{SiO}_2 + 2\text{H}_2\text{O} \rightarrow \text{H}_4\text{SiO}_4$
(Orthoclase)	$\text{KAlSi}_3\text{O}_8 + 8\text{H}_2\text{O} \rightarrow \text{K}^+ + \text{Al}(\text{OH})_4^- + 3\text{H}_4\text{SiO}_4$
(Albite)	$\text{NaAlSi}_3\text{O}_8 + 8\text{H}_2\text{O} \rightarrow \text{Na}^+ + \text{Al}(\text{OH})_4^- + 3\text{H}_4\text{SiO}_4$
(Anorthite)	$\text{CaAl}_2\text{Si}_2\text{O}_8 + 8\text{H}_2\text{O} \rightarrow \text{Ca}^{2+} + 2\text{Al}(\text{OH})_4^- + 2\text{H}_4\text{SiO}_4$
(Biotite)	$\text{KAl}_3\text{Si}_3\text{O}_{10}(\text{OH})_2 + 10\text{H}_2\text{O} + 2\text{OH}^- \rightarrow \text{K}^+ + 3\text{Al}(\text{OH})_4^- + 3\text{H}_4\text{SiO}_4$

Table 7.2 Coefficient of the equilibrium constant

Name	α_1	α_2	α_3	α_4	α_5
(Quartz)	4.1×10^{-1}	-1.3×10^3	0	0	0
(Orthoclase)	3.9×10	-4.6×10^{-2}	-1.7×10^4	1.0×10^6	0
(Albite)	3.7×10	-4.4×10^{-2}	-1.6×10^4	1.0×10^6	0
(Anorthite)	-8.2×10^2	1.2×10	0	0	0
(Biotite)	6.1×10^3	6.9×10^{-1}	-3.9×10^5	2.5×10^7	-2.1×10^3

Name	α_6	α_7	α_8	α_9	α_{10}	α_{11}
(Quartz)	0	0	0	0	0	0
(Orthoclase)	0	0	0	0	0	0
(Albite)	0	0	0	0	0	0
(Anorthite)	-8.1×10^{-2}	2.4×10^{-4}	-6.3×10^{-7}	8.2×10^{-10}	-5.8×10^{-13}	1.8×10^{-16}
(Biotite)	0	0	0	0	0	0

7.3.2 Relationship between the fracture aperture and the contact area

The fracture aperture (or permeability) will be affected by the interaction of the pressure solution, the surface diffusion, and the free-face dissolution. If the pressure solution at the asperity contact area is superior to the free-face dissolution, the fracture aperture will become closed with time, and the permeability will decrease. Conversely, if the free-face dissolution is greater than the pressure solution, the permeability will increase. Therefore, in order to accurately predict the interaction of the pressure solution and the free-face dissolution, it is necessary to grasp the relationship between the aperture and the fracture contact-area. (Yasuhara et al. 2003;2004;2006) measured the fracture aperture information of a single rock fracture by using a laser device. Then from the relationship between the average aperture and the contact-area ratio, the equation is expressed as follows:

$$\langle b \rangle = b_r + (b_0 - b_r) \exp(-(R_c - R_{c0})/a) \quad (7.17)$$

Where $\langle b \rangle$ is the average aperture, b_0 is the initial aperture, b_r is the residual aperture, R_{c0} is the initial contact area ratio, a is a constant number.

7.3.2.1 Fracture contact condition

It has a big difference between the contact-area and the noncontact-area within a single rock fracture. The aperture is changing with the contact-area ratio R_c , which has been described in Eq.(7.17). Then the simulation was conducted by a representative element of R_c . The contact area ratio is illustrated in Eq.(7.18), which shows the relationship between macroscopic and the microscopic. i.e., the ratio of the macroscopic contact-area and the fracture area A_c^l, A_c^t is equal to the ratio of the microscopic contact-area and the fracture area A_c^l, A_c^t , as depicted in **Fig 7.4**.

$$R_c = \frac{A_c^l}{A_c^t} = \frac{A_c^l}{A_c^t} \quad (7.18)$$

Moreover, d_c represents the diameter of the contact-area, which is written as follows.

$$d_c = \sqrt{\frac{4A_c^l}{\pi}} \quad (7.19)$$

The representative contact-area is assumed as an uniaxial compaction, then the average vertical stress σ_a is expressed as the ratio between the effective stress σ_{eff} and the contact-area ratio R_c , as shown in Eq.(7.20):

$$\begin{aligned} \sigma_{eff} \cdot A &= \sigma_a \cdot A_c^l \\ \Rightarrow \sigma_a &= \frac{\sigma_{eff}}{R_c} \end{aligned} \quad (7.20)$$

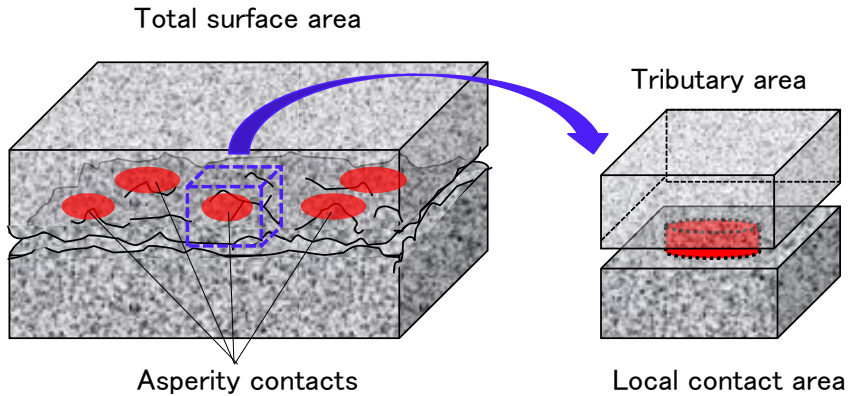


Fig.7.4 Illustration of the representative elements

7.3.2.2 Procedure of the simulation

The aperture evolution of a single rock fracture is considered as the interaction of the pressure solution on the fracture asperities, the mass dissolution and the free-face dissolution which has been illustrated in Eq. (7.8)~(7.16). During the time Δt , the dissolved mass ions on the contact-area boundary are calculated through the pressure solution mass flux in Eq. (7.8). Then, the diffusion mass flux on the contact-area is

calculated by Eq. (7.13), i.e., the mass ions concentration difference between the contact-area boundary and the pore space. Then the total diffusion volume V_t^c is changed with time t as shown bellow:

$$V_t^c = \int \dot{M}_{diff} / \rho_g dt \quad (7.21)$$

Moreover, V_t^c is equal to the removed volume of the aperture contact-area. Therefore, from the Eq.(7.18), the contact-area ratio is changed with time. Then the V_t^c can be expressed as in Eq. (7.21).

$$V_t^c = -A_c^l \int_{R_{c0}}^{R_c(t)} \frac{R_c}{1-R_c} \frac{d\langle b \rangle}{dR_c} dt$$

$$= (b_0 - b_r) A_c^l \exp\left(-\frac{1-R_c(t)}{a}\right) \left[\exp\left(\frac{1+R_{c0}}{a}\right) - \exp\left(\frac{1+R_{c(t)}}{a}\right) + \frac{\exp\left(\frac{R_{c0} + R_{c(t)}}{a}\right)}{a(E_i((1-R_{c0})/a) - E_i((1-R_{c(t)})/a))} \right] \quad (7.22)$$

$E_i(x)$ is an exponential integral function, if $x > 0$, the $E_i(x)$ is written as:

$$E_i(x) = \gamma + \ln x + \sum_{n=1}^{\infty} \frac{x^n}{n!n} \quad (7.23)$$

where $\gamma (=0.5772\dots)$ is a constant value of Euler – Mascheroni. Then Eq.(7.24) is written as follows:

$$V_t^c = (b_0 - b_r) A_c^l \exp\left(-\frac{1-R_c(t)}{a}\right) \left[\exp\left(\frac{1+R_{c0}}{a}\right) - \exp\left(\frac{1+R_{c(t)}}{a}\right) + \frac{\exp\left(\frac{R_{c0} + R_{c(t)}}{a}\right)}{a \left(\ln\left(\frac{1-R_{c0}}{1-R_{c(t)}}\right) + C \right)} \right] \quad (7.24)$$

$$C = \sum_{n=1}^{\infty} \frac{(1-R_{c0})^n - (1-R_{c(t)})^n}{a^n n!n}$$

V_t^c will increase when the aperture decrease. The aperture decrease means the contact-area ratio increase. Then the aperture can be defined as the relationship between the aperture and the contact-area ratio at different periods t . From Eq.(7.21), the relationship between aperture and contact-area ratio is written in (7.25):

$$\langle b(t) \rangle_c = b_r + (b_0 - b_r) \exp(-(R_c(t) - R_{c0})/a) \quad (7.25)$$

where, $\langle b(t) \rangle_c$ is the aperture change, it is altered when the pressure solution is acting on the fracture contact-area. It should be noticed that the free-face dissolution within the aperture also need to be considered. Then the relationship between the dissolved volume V_t^F on the fracture free-face and the aperture change $\langle b(t) \rangle_F$ is defined as:

$$V_t^F = \langle b(t) \rangle_F A_c^l = \int \left(\sum_i^m \dot{M}_{dssi}^{FF} / \rho_{g,i} \right) dt \quad (7.26)$$

V_t^F increase means the aperture is enlarged. Simultaneously, the contact-area ratio will decrease. Then the aperture changing at different period t is defined as the interaction process of the pressure solution happening on the contact asperities and the free-face dissolution generating on the pore space:

$$\langle b(t) \rangle = \langle b(t) \rangle_c + \langle b(t) \rangle_F \quad (7.27)$$

In order to solve Eq. (7.21) to (7.27), it is necessary to obtain the concentration of the contact asperities and the pore space from Eq.(7.13). Pressure solution and diffusion have effect on the concentration variation on the contact asperities. The free-surface dissolution and diffusion influence the concentration change on the pore space. Therefore, the relationship between them can be expressed as follows:

$$\begin{Bmatrix} q_{1,j} \\ q_{2,j} \end{Bmatrix} = 8\pi\omega D_{b,j} \begin{bmatrix} 1 & -1 \\ -1 & 1 \end{bmatrix} \begin{Bmatrix} C_{i\text{nt}j} \\ C_{porej} \end{Bmatrix}_\tau + \begin{bmatrix} V_{i\text{nt}} & 0 \\ 0 & V_{pore} \end{bmatrix} \begin{Bmatrix} \dot{C}_{i\text{nt}j} \\ \dot{C}_{porej} \end{Bmatrix}_t \quad (j=1,2,\dots,n) \quad (7.28)$$

Then, when $\tau = t + \Delta t$, it is calculated as:

$$\begin{Bmatrix} C_{i\text{nt}j} \\ C_{pore,j} \end{Bmatrix}_{t+\Delta t} = \begin{bmatrix} 8\pi\omega D_b + \frac{V_{i\text{nt}}}{\Delta t} & -8\pi\omega D_b \\ -8\pi\omega D_b & 8\pi\omega D_b + \frac{V_{pore}}{\Delta t} \end{bmatrix} \begin{bmatrix} q_{1,j} \\ q_{2,j} \end{bmatrix} + \begin{bmatrix} \frac{V_{i\text{nt}}}{\Delta t} & 0 \\ 0 & \frac{V_{pore}}{\Delta t} \end{bmatrix} \begin{Bmatrix} C_{i\text{nt}j} \\ C_{pore,j} \end{Bmatrix}_t \quad (7.29)$$

Where q_1 and q_2 are contributing to the pressure solution and the free-face dissolution happen. When the aperture became closed, the equation should be written as:

$$q_{1,j} = \sum_i^m \dot{M}_{diss,j}^{PS} \frac{\nu_{ij} \cdot m_{w,j}}{\rho_{g,i} \cdot V_{m,i}} \quad (7.30)$$

$$q_{2,j} = \sum_i^m \dot{M}_{diss,i}^{FF} \frac{\nu_{ij} \cdot m_{w,j}}{\rho_{g,i} \cdot V_{m,i}} \quad (7.31)$$

where ν_{ij} is the stoichiometric coefficient of j when the mineral constituent is i , $m_{w,j}$ is the molecular of j .

Then, the flow chart of the chemical-mechanical coupled simulation is illustrated in **Fig 7.5**.

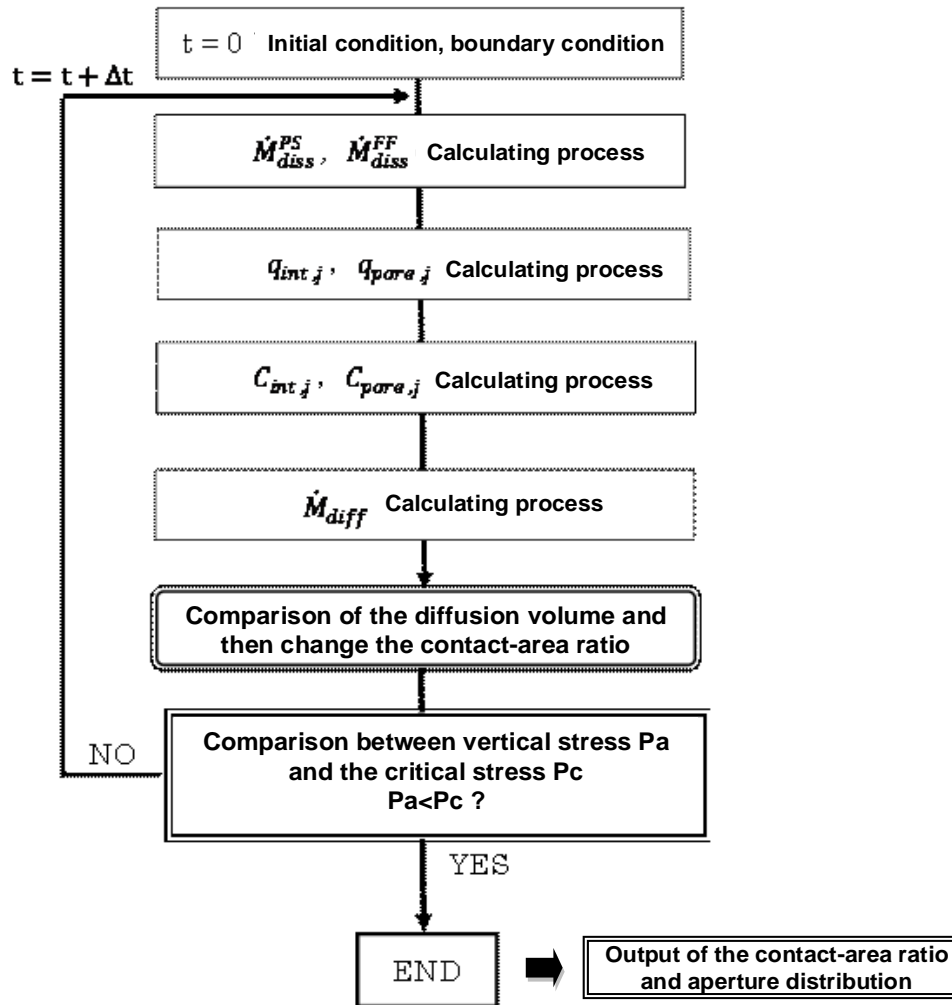


Fig.7.5 .Simulation procedure of the Chemical-Mechanical coupled model

7.3.2.3 Parameter a

In this study, the parameter a is defined based on the Eq. (7.17). Which represents the gradient of aperture closed. The initial aperture, initial contact-area ratio, the average aperture under the confining pressure, and the contact-area ratio variation which is obtained from the CT observation are used to calculate the value of a . The initial aperture and initial contact-area ratio were measured under the confining pressure of 0 MPa. Moreover, aperture and the contact-area variation are obtained from the long-term CT observation at 20 °C, which has been illustrated in **Chapter 4**.

7.4 Simulation results

The initial value of aperture and the contact-area ratio are shown in **Fig 4.14 (Chapter 4)**, which equal to 0.253 mm and 5.4%, respectively. Therefore, the parameter a can be predicted through a fitting curve, as shown in **Fig 7.6** i.e., relationship between the long-term aperture and contact-area ratio variation. In this prediction, $a = 0.08$. Then the chemical-mechanical simulation was conducted. The simulation

result is listed in **Table 7.3** Result shows that the aperture and mineral composition have no change. It can be guessed as two reasons. On the one hand, in this study, the confining stress 3.0 MPa, which acting on the fracture contact area, i.e., σ_a is much smaller than the critical stress, i.e., material strength σ_c , 140 MPa. Therefore, it may difficult to drive the chemical reaction to happen. On the other hand, geochemical response may not easy to happen under the room temperature. A higher temperature may easy lead to the geochemical response happen. Therefore, this coupled processed are needed to be further investigated, and the chemical-mechanical coupled model should be further modified.

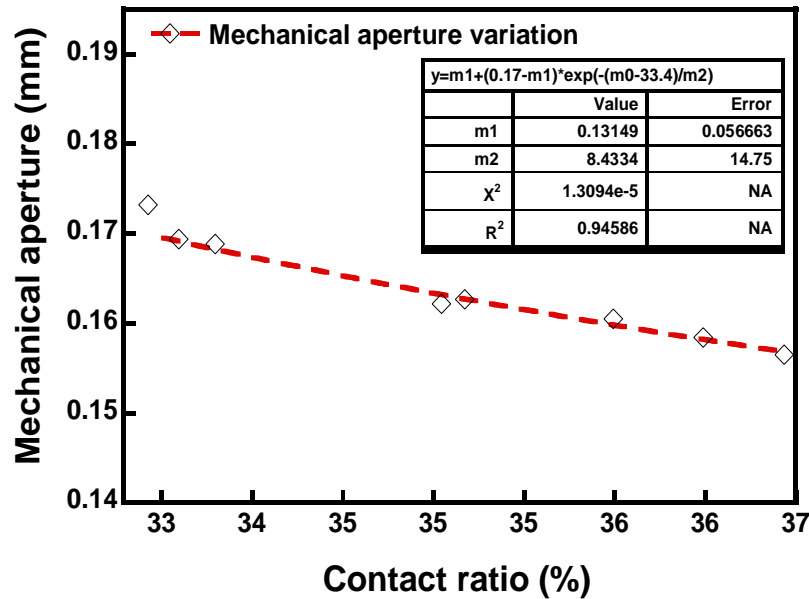


Fig.7.6 Relation between mechanical aperture and contact-area ratio. Circles are evaluated by using the profiling data which has measured from X-ray CT, and the dotted line is the regression curve of $\langle b(t) \rangle_c = b_r + (b_0 - b_r) \exp(-(R_c(t) - R_{c0})/a)$ initial $b_0=0.17$, $R_{c0}=33.4\%$ at 3.0 MPa, 0 day. with the correlation coefficient, $R^2 = 0.95$

Table 7.3 Simulation result by using the CT observation data

Mineral Concentration	Si [mol/L]	Al [mol/L]	K [mol/L]	Fe [mol/L]	Ca [mol/L]	Na [mol/L]	Mg [mol/L]
	0.4833×10^7	0.3768×10^7	0.2635×10^7	0.1091×10^7	0.8633×10^6	0.9447×10^6	0.4301×10^6
Aperture and contact condition	Aperture [mm]	Permeability [m ²]	Rc [%]	Flowrate [m ³]			
	0.14	0.166×10^{-10}	14.70 %	0.106×10^{-8}			

7.5 Summary

In this Chapter, numerical simulation was conducted to check the CT analysis result. The relation between aperture and contact-area ratio was measured. Which is satisfied with the previous studies that the aperture has an exponential decay. The gradient of the aperture decrease was obtained. However, simulation result shows that there is no significant change of the aperture and contact-area ratio variation under the current model. Moreover, The mineral concentration from the simulation result also has no change. Considering of the current model, the effective stress acting on the fracture contact-area is smaller; it cannot result in the chemical reaction occur. Moreover, the geochemical response may not easy to happen at 20°C. It is also corresponding to the permeability experiment result at 20 °C, which shows that the mineral concentration didn't have an obvious change. From the simulation result, it can be supposed as two reasons. On the one hand, the geochemical response may not generate at 20 °C. A higher confining stress and temperature conditions may easy to drive the chemical reactions happen. On the other hand, current model cannot be used to explain the experiment result, a redefined model is needed to verify the permeability decreasing at 20 °C. The permeability evolution under coupled conditions should be reconsidered.

References

- Andri, S. : Dissolution of primary minerals of basal t in natural waters : I. Calculation of mineral solubilities from 0 °C to 350°C, *Chemical Geology*, Vol .172, Issues 3 -4, 15, Pages 225-250.2001.
- Arnórsson, S., Sigurdsson, S., Svavarsson, H. : The chemistry of geothermal waters in Iceland. I. Calculation of aqueous speciation from 0° to 370°C, *Geochimica et Cosmochimica Acta*, vol. 46 , Issue 9,pp.1513-1532, 1982.
- Bernabé, Y., Evans, B.: Pressure solution creep of random packs of spheres. *J. Geophys. Res. Solid Earth*, 119, 4202–4218, doi:10.1002/ 2014JB011036.2014.
- Danko, G., Bahrami, D.: A new T-H-M-C model development for discrete-fracture EGS studies. *GRC Trans.* 36:383–392.2012.
- Fournier, R. O., and Potter II,R.W. : An equation correlating the solubility of quartz in water from 25_C to 900_C at pressure up to 10,000 bars, *Geochim. Cosmochim. Acta*, 46, 1969– 1973.1982.
- Ghassemi A. : A review of some rock mechanics issues in geothermal reservoir development.*Geotech Geol Eng.* 30:647–664.2012.
- Holland, T.J.B., and Powel, I.R. : An internally-consistent thermodynamic dataset for phases of petrological interest . *Journal of Metamorphic Geology.* 16, 309-344,1998.
- Lang, P.S., Paluszny, A., Zimmerman,R.W.: Hydraulic sealing due to pressure solution contact zone growth in silici- clastic rock fractures, *J. Geophys. Res. Solid Earth*, 120, 4080–4101, doi:10.1002/2015JB011968.2015.
- Min,K.B., Rutqvist,J., Elsworth, D.: Chemically and mechanically mediated influences on the transport and mechanical characteristics of rock fractures[J], *International Journal of Rock Mechanics and Mining Sciences.* 46(1): 80–89.2009.
- Polak, A., Elsworth, D., and Liu, J. S.: Spontaneous switching of permeability changes in a limestone fracture with net dissolution[J], *Water Resources Research*, 40(W03502): 1 029–1 038.2004.
- Polak, A., Elsworth,D., Yasuhara,H., Grader, A., and Halleck,P. : Permeability reduction of a natural fracture under net dissolution by hydrothermal fluids, *Geophys. Res. Lett.*, 30(20), 2020, doi:10.1029/2003GL017575, 2003.
- Ragnarsdóttir., Walther.: Pressure sensitive silica geothermometer determined from quartz solubility experiments at 250°C. *Geochim. Cosmochim. Acta*, 47, pp. 941-946.1983.
- Rutter, E. H. : The kinetics of rock deformation by pressure solution, *Philos. Trans., R. Soc. London, Ser. A.*283, pp. 203-219, 1976.
- Taron, J., Elsworth,D., Min,K.: Numerical simulation of thermal-hydrologic-mechanical-chemical processes in deformable, fractured porous media. *International Journal of Rock Mechanics and Mining*

Sciences. 46(5):842– 854.2009.

Watanabe, N. :Finite Element Method for Coupled Thermo-Hydro-Mechanical Processes in Discretely Fractured and Non-fractured Porous Media. PhD disserta- tion. Dresden University of Technology. Germany. 2005.

Yasuhara, H., Elsworth, D., Polak, A. : A mechanistic model for compaction of granular aggregates moderated by pressure solution. *J Geophys Res*. 108(11):2530. 2003.

Yasuhara, H., Elsworth, D., Polak, A.: Evolution of permeability in a natural fracture: the significant role of pressure solution. *J Geophys Res*. 109(B3):B03204. 2004.

Yasuhara, H., Elsworth, D.: A numerical model simulating reactive transport and evolution of fracture permeability. *Int J Numer Anal Mech Geomech*. 30:1039–1062.2006.

Yasuhara, H., Kinoshita, N., Ohfuji, H., Lee, D.S., Nakashima, S., Kishida, K.: Temporal alteration of fracture permeability in granite under hydrothermal conditions and its interpretation by coupled chemo-mechanical model. *Appl Geochem*. 26:2074–2088.2011.

Yasuhara,H., Hasegawa, D., Nakashima, S., Yano, T., Kishida,K.: Experimental evaluation of fracture permeability in granite under temperature and stress controlled conditions, *Japanese Geotechnical Journal*, 1880-6341, 10.3208/jgs.8.71.2013.

Yasuhara,H., Kinoshita,N., Ohfuji,H., Takahashi, M., Ito, K., Kishida,K.: Long-term observation of permeability in sedimentary rocks under high-temperature and stress conditions and its interpretation mediated by microstructural investigations, *Water Resources Research* ,1944-7973|0043-1397, 10.1002/2014WR016427.2015.

Chapter 8 Conclusions and Future Studies

8.1 Conclusions

In this study, the internal fracture information was clarified. Several long-term permeability tests and the X-ray CT observations were conducted under the coupled conditions. The permeability at different times shows different performances. Simultaneously, X-ray CT was utilized to observe the aperture distribution and the contact area ratio variation under different conditions. i.e., the condition was set the same with long-term permeability test at 20 °C. In order to verify the accuracy of the aperture extraction results from the CT images, different image analysis methods were utilized to check the influence of the image analysis results. i.e., different CT resolution and different image processing methods. Moreover, in order to further clarify the permeability and aperture evolution and contact-area condition in long-term, numerical simulations (flow simulation and chemical-mechanical coupled simulation) were also conducted to check the flow behavior and aperture change. From this study, several conclusions were summarized as follows:

Chapter 1 is a brief summary of the background and purpose.

Chapter 2 shows several literature reviews of the permeability evolution under different conditions and the utilized of the X-ray CT observation. The fracture aperture can be visualized through using X-ray CT; Internal fracture information needs to be further verified. Then, the flow simulation was described to check the effect factors of the flow behavior. It can be guessed that flow behavior was changed due to the contact-area variation and the permeability may be altered under the coupled conditions.

Chapter 3 introduced the primary experimental work. Several permeability tests under different conditions were conducted. First, short-term permeability tests were performed under three temperatures. i.e, 20,60 and 90 °C. Experiment results showed that the permeability was decreased as increasing the temperature. The permeability is sensitive to the confining pressure; it is altered with different confining pressures and temperatures. Irreversible behavior of the permeability can be confirmed. It should be noted that the permeability has different performance under the same loading-unloading confining pressure when the loading-unloading circle is different.

In the long-term permeability tests, three temperatures (20, 60, and 90 °C, the same temperature with the short-term tests) are adopted to demonstrate the effect of time dependence and the temperature on permeability. The experiment results show that the permeability decreased monotonically at 20 °C, while

there is an irregular permeability change at 60 °C and 90 °C. This is different from the previous experiment results, which were conducted by other researchers. Those researchers clarified that permeability always becoming lower at a higher temperature. The main reason for this irregular change is summarized as the interaction of the positive effect of mineral dissolution and the negative effect of thermal expansion on the permeability.

In addition, after the short-term test, the temperature was unloaded to 20 °C. The permeability at this long-term loading-unloading performance showed it has irreversible behavior. After a long-term randomly change of the permeability at 60 °C, the temperature was increased to 90 °C. The permeability showed it decreased sharply at 90 °C in comparing with 20 and 60 °C. The negative effect, i.e., thermal expansion, may reduce the aperture, and then the permeability decreased. Moreover, after 60 °C, another negative effect, i.e., the mineral elements, may dissolve from the fracture asperities due to the examination of the effluent within the fracture. The dissolved elements may obstruct the fluid path in a long-term mechanical and thermal interaction. Therefore, the permeability was reduced.

Permeability test results indicated the internal fracture contact asperities may altered under different conditions. However, it is difficult to grasp the internal fracture information at the previous research. Especially to grasp the fracture contact-area condition. Therefore, in **Chapter 4**, X-ray CT was used to grasp the fracture aperture and the contact-area ratio change in the long-term. At 20 °C, aperture distribution variation was used to compare with the permeability test results at the conditions of 3.0 MPa, 180 days. The variation of the permeability shows that it is congruent with the fracture aperture change. Aperture decreased sharply under two stages from observing the CT results. The first stage is that the confining pressure was added from 0 to 3.0 MPa, mechanical compaction reduced the aperture. The second stage is that the aperture was kept at 3.0 MPa for about 30 days, and it decreased with time, which is the same decreasing tendency with the permeability test results at 20 °C, 30 days. After 30 days, CT results showed that the aperture decreased again while the contact-area was enlarged. It indicated that the permeability decreased due to the fracture contact-area increase.

Then the temperature was increased to 60 °C. The aperture was observed under various confining pressures for 180 days. Results show that aperture first decreased, then it performed a random change at about dozens of days. The negative effect, such as the thermal expansion, reduced the aperture. Moreover, the fracture roughness surfaces were altered under higher temperatures and various effective confining stresses. Therefore, it shows an irregular variation.

In order to check the accuracy of the CT image analysis results, different CT resolution and different image processing methods were conducted. The CT resolution results indicated that it may generate some image analysis difference under different CT resolutions. Moreover, different CT image processing methods were further studied in **Chapter 5**.

In **Chapter 5**, previous studies showed that the threshold method has several misidentifications on the CT image segmentation. Therefore, different CT segmentation methods are needed to check the influence of the CT segmentation results. The region growing method has been introduced in **Chapter 4**. The edge detection method has a good capability to identify the boundary of the CT image. Therefore, the boundary of the fracture aperture can be identified successfully. The CT images from the different positions of the sample were extracted and were analyzed under these two methods. 2-D CT images at the confining pressure 0 and 3.0 MPa were analyzed and compared. At 0 MPa, CT images can be observed that the aperture position is almost discontinuity; both of the two methods can segment the CT images quite well. However, there are several slight differences in several CT images on a relatively lower grey value positions. Region growing method removed such kind of lower grey value positions while the edge detection method recognized this position as a rock continuity. Therefore, the recognition difference of the CT images has a great influence on the CT results. i.e., aperture distribution and the contact-area ratio. At 3.0 MPa, fracture aperture became much difficult to identify. Confining pressure reduced the aperture. It became much narrower. Region growing method has a large misidentification on identifying the lower grey value position due to the voxel connectivity. In contrast, edge detection can distinguish the aperture boundary successfully even though at a higher confining pressure. Which should be widely used in the rock mechanics field.

In **Chapter 6**, based on the permeability test results in **Chapter 3** and the CT observation results in **Chapter 4**, flow simulation was conducted to further verify the contact-area variation under coupled conditions. Aperture and roughness surface data at 0 and 3.0 MPa from the CT observation was chosen. Flow within the aperture at 3.0 MPa became slowly by comparing with the flow at 0 MPa. From observing the flow vector distribution on the color contour map, the fracture contact area at 3.0 MPa has a great influence on altering the flow direction. The flow bypassed the fracture contact-areas and concentrated on the aperture open position. The flow became tortuous and randomly around the fracture contact-areas. Moreover, Re number was also calculated under different confining stresses. Re value shows difference under different flow water heads. Re number became higher at a higher water heads. From observing the color contour map of Re distribution, the Re number larger than 10 at several aperture positions was confirmed. It indicates that Darcy's law may not be suitable. It is also corresponding to the irregular change of permeability within the fracture under different confining pressures. The variation of the fracture roughness surfaces have a great effect on the flow behavior.

Hydraulic aperture from the flow simulation was also calculated and compared with the value from CT and from the permeability test results. Results showed that the hydraulic aperture from the flow simulation is much closer to the CT results. However, it shows much higher than the value from the permeability tests. i.e., two orders of magnitude higher. It can be inferred that this difference may due to

the size of the two samples. Hydraulic aperture comparison shows that the variation tendencies of them are qualitatively match well. Therefore, experiment results were verified.

In **Chapter 7**, chemical-mechanical simulation was conducted to check the aperture and the mineral composition variation. The permeability changing in the long-term can be confirmed in **Chapter 3**. And CT observation results also showed that several aperture positions became contacted after two long-term permeability tests. Moreover, the geochemical response was considered on both permeability tests and the CT experiment results. The mineral composition variation at 20 °C and 60 °C were illustrated in **Chapter 3**. The mineral variation also indicated that the mineral might dissolve from the free-face at 60 °C. Then the aperture would become larger, and the permeability will show an increasing behavior at a higher temperature. However, simulation results at 20 °C show that the aperture and the mineral composition had no significant change. One reason is that the geochemical response may not easy happen at 20 °C. It may easily happen at a relatively high temperature. The other reason may attribute to the current model, that the effective stress which acted on the fracture was much lower than the critical stress. It cannot drive the mineral on the fracture asperities to dissolve. Therefore, the chemical-mechanical interaction within the fracture is needed to be a further investigation.

8.2 Recommendations for future works

Future works are summarized as below.

8.2.1 Long-term permeability tests

- (1) Higher confining pressure and temperature influence should be considered, especially on establishing the geothermal system. Permeability evolution may become more complexed, fracture may generate a plastic deformation.
- (2) Different types of samples should be considered. The permeability may be altered by different types of rock samples. Permeability evolution and the mineral composition of different types of fractured rock are needed to be checked;
- (3) Several different solutions should be used to check the permeability evolution, such as the acid or the alkaline solution. A significant difference of permeability evolution may occur by using different solutions.

8.2.2 CT observation on the fracture information

Aperture variation and fracture contact-area condition under coupled conditions are needed to be further understood. Internal fracture deformation should be explained further.

8.2.3 Image processing methods

From **Chapter 4** and **Chapter 5**, it can be noted that CT images are greatly affected by different CT image processing methods. The accuracy CT segmentation methods are needed to detect the aperture and contact-area evolution, Edge detection method should be extended on identifying different types of rock fractures, and other effective image analytical methods were also needed to be checked further.

8.2.4 Model construction and further investigation

From flow simulation results in **Chapter 6**, fracture contact-area variation and flow behavior were further verified. Fracture geometry deformation such as the chemical reaction may have a significant influence on the permeability evolution. The relation between aperture and contact-area ratio was also confirmed to satisfy with the permeability decreasing at 20 °C. From the chemical-mechanical simulation result, it can be noted that the mineral dissolution may not easy to occur at 20 °C under a relative low effective stress. Therefore, the chemical-mechanical interaction should be reconsidered to verify the permeability evolution at 20 °C, and the permeability evolution at a higher temperature also needs to be checked by the coupled model in the future.